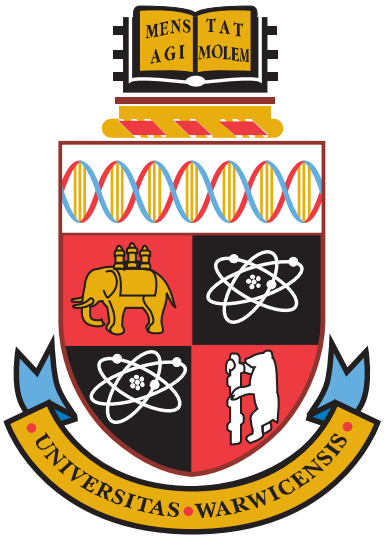

Charge Neutrality Level in Significantly Cation-Anion Mismatched Semiconductors

by

Philip David King

Thesis

Submitted to the University of Warwick

for the degree of

Doctor of Philosophy

Department of Physics

May 2009

THE UNIVERSITY OF WARWICK

Contents

Acknowledgments

There are many people that I would like to thank, without whom this work would not have been possible. First, thanks go to my supervisor, Prof. Chris McConville, for his constant support and encouragement. My time at Warwick has been a very happy one, and I thank him for welcoming me so warmly into his group. Especial thanks go to Dr. Tim Veal. He has given me enormous amounts of guidance and friendship throughout my Ph.D., and I have really enjoyed our many discussions.

I would like to thank Rob Johnston. He has provided invaluable technical support, enjoyable early-morning cups of 'brown', and is even helping me move to Scotland (Lagavulin's on its way...). Further cups of brown and other displacement activities wouldn't have been the same without the other members of the group: Paul, Stuart, Jim, Lolly, Wojtek, Sep, mini-Chris, Mark, Liam, and Gavin. In particular, thanks go to Dr. Paul Jefferson for his friendship, encouragement, Daresbury banter, and for never (quite) defenestrating me.

I spent many hours at facilities for this work, and would like to thank the fantastic scientists there for all of their assistance – in particular, Dr. Danny Law (NCESS), Dr. Iain McKenzie (ISIS), and Dr. Francesco Offi (ESRF). I am very grateful to Prof. Philip Hofmann from the University of Århus and his group (Dr. Emile Rienks, Maria Fuglsang Jensen, Dr. Ed Perkins, and also Marco Bianchi 'on loan' from Trieste) not only for their technical assistance, but also for illuminating discussions, and for welcoming me into their group during beam times at ASTRID. I would like to thank Dr. Frank Fuchs, André Schliefe, Prof. Dr. Friedhelm Bechstedt, and Dr. Jurgen Furthmüller for providing me with the results of their calculations, and for useful discussions. Further thanks go to Prof. Roger Lichti, Dr. Gurkan Celebi, and Prof. Steve Cox for their insights into the, what can only be described as the slightly-made-up, world of 'muonium'. This work would also not have been possible without the high-quality samples that were kindly provided by Dr. Bill Schaff (Cornell), Prof. Steve Durbin (Canterbury), Prof. Russ Egdell (Oxford), Dr. Jesus Zùñiga-Pérez (CRHEA), Prof. Vicente Muñoz-Sanjosé (Valencia), Prof. Mark Hopkinson (Sheffield), Dr. Volker Cimalla (Freiburg), Prof. Yasushi Nanishi (Ritsumeikan), Prof. Alex Georgakilas (Crete), and their co-workers.

Finally, I would like to thank my family, for their continued support and encouragement. In particular, I am indebted to my wife, Liz. Thank you for putting up with my long hours of work, trips away, and (slightly?!) insane tendencies. Doing this Ph.D. would not have been possible without you.

Declarations

I declare that this thesis contains an account of my research carried out in the Department of Physics at the University of Warwick between October 2006 and May 2009 under the supervision of Prof. C. F. McConville. The research reported here has not been submitted, either wholly or in part, in this or any other academic institution for admission to a higher degree.

The CdO helium ion implantation was performed at the Surrey Ion Beam Centre by Dr. N. H. Peng (University of Surrey, UK). Additionally, the bulk electrical properties of five of the irradiated samples were independently considered in the doctoral work of P. H. Jefferson (University of Warwick, UK). The single-field Hall effect measurements reported in Fig. 6.4 were performed by Dr. W. J. Schaff and Dr. H. Lu (Cornell University, USA). The *n*-type InGaN and *bcc*–In_2O_3 x-ray photoemission spectroscopy measurements (Figs. 7.3(a) and 8.5) were performed by Dr. T. D. Veal (University of Warwick, UK) and Dr. D. J. Payne (University of Oxford, UK), respectively. The density-functional theory calculations presented in this work were performed by Dr. Frank Fuchs, Mr. André Schleife, Prof. Dr. Friedhelm Bechstedt, and Dr. Jürgen Furthmüller (Friedrich-Schiller-Universität, Jena, Germany). All of the remaining data collection and calculations were performed by the author. The data analysis, simulation and interpretation was all performed by the author.

Philip King

May 2009

Several articles based on this research have been published:

P.D.C. King, T.D. Veal, P.H. Jefferson, C.F. McConville, Hai Lu, and W.J. Schaff, *Variation of band bending at the surface of Mg-doped InGaN: evidence of p-type conductivity across the composition range*, Phys. Rev. B **75**, 115312 (2007).

P.D.C. King, T.D. Veal, P.H. Jefferson, C.F. McConville, T. Wang, P.J. Parbrook, Hai Lu, and W.J. Schaff, *Valence band offset of InN/AlN heterojunctions measured by x-ray photoelectron spectroscopy*, Appl. Phys. Lett. **90**, 132105 (2007).

P.D.C. King, T.D. Veal, C.F. McConville, F. Fuchs, J. Furthmüller, F. Bechstedt, P. Schley, R. Goldhahn, J. Schörmann, D.J. As, K. Lischka, D. Muto, H. Naoi, Y. Nanishi, Hai Lu, and W.J. Schaff, *Universality of electron accumulation at wurtzite c- and a-plane and zinc-blende InN surfaces*, Appl. Phys. Lett. **91**, 092101 (2007).

P.D.C. King, T.D. Veal, P.H. Jefferson, S.A. Hatfield, L.F.J. Piper, C.F. McConville, F. Fuchs, J. Furthmüller, F. Bechstedt, Hai Lu, and W.J. Schaff, *Determination of the branch-point energy of InN: Chemical trends in common-cation and common-anion semiconductors*, Phys. Rev. B **77**, 045316 (2008).

P.D.C. King, T.D. Veal, Hai Lu, P.H. Jefferson, S.A. Hatfield, W.J. Schaff, and C.F. McConville, *Surface electronic properties of n- and p-type InGaN alloys*, Phys. Status Solidi B **245**, 881 (2008).

P.D.C. King, T.D. Veal, and C.F. McConville, *Non-parabolic coupled Poisson-Schrödinger solutions for quantized electron accumulation layers: Band bending, charge profile, and subbands at InN surfaces*, Phys. Rev. B **77**, 125305 (2008).

P.D.C. King, T.D. Veal, A. Adikimenakis, Hai Lu, L.R. Bailey, E. Iliopoulos, A. Georgakilas, W.J. Schaff, and C.F. McConville, *Surface electronic properties of undoped InAlN alloys*, Appl. Phys. Lett. **92**, 172105 (2008).

P.D.C. King, T.D. Veal, C.E. Kendrick, L.R. Bailey, S.M. Durbin, and C.F. McConville, *InN/GaN valence band offset: High-resolution x-ray photoemission spectroscopy measurements*, Phys. Rev. B **78**, 033308 (2008).

P.D.C. King, T.D. Veal, D.J. Payne, A. Bourlange, R.G. Egdell, and C. F. McConville, *Surface electron accumulation and the charge neutrality level in* In_2O_3, Phys. Rev. Lett. **101**, 116808 (2008).[1]

P.D.C. King, T.D. Veal, P.H. Jefferson, J. Zùñiga-Pérez, V. Muñoz-Sanjosé, and C.F. McConville, *Unification of the electrical behavior of defects, impurities, and surface states in semiconductors: Virtual gap states in CdO*, Phys. Rev. B **79**, 035203 (2009).

P.D.C. King, T.D. Veal, W.J. Schaff, and C. F. McConville, *Surface electronic properties of Mg-doped InAlN alloys*, Phys. Status Solidi (b), **246**, 1169 (2009).

P.D.C. King, T.D. Veal, and C. F. McConville, *Unintentional conductivity of indium nitride: transport modelling and microscopic origins*, J. Phys.: Condens. Matter special issue: Physics of III-V Nitrides (invited paper) **21**, 174201 (2009).

T.D. Veal, **P.D.C. King**, and C.F.McConville, *Surface electronic properties of InN and related alloys*, in *Indium Nitride and Related Alloys*, edited by T.D. Veal, C.F. McConville and W.J. Schaff (CRC press, Boca Raton, 2009).

[1]Featured in a Technology Research Review, *Materials – Indium oxide reveals secret surface charge*, Compound Semiconductor **14** (9), 36 (2008).

P.D.C. King, T.D. Veal, and C.F. McConville, *InN in brief: conductivity and chemical trends*, in *Indium Nitride and Related Alloys*, edited by T.D. Veal, C.F. McConville and W.J. Schaff (CRC press, Boca Raton, 2009).

P.D.C. King, T.D. Veal, F. Fuchs, Ch.Y. Wang, D.J. Payne, A. Bourlange, H. Zhang, G.R. Bell, V. Cimalla, O. Ambacher, R.G. Egdell, F. Bechstedt, C.F. McConville, *Band gap, electronic structure and surface electron accumulation of cubic and rhombohedral* In_2O_3, Phys. Rev. B **79**, 205211 (2009).

P.D.C. King, R.L. Lichti, Y.G. Celebi, J.M. Gil, R.C. Vilão, H.V. Alberto, J. Piroto Duarte, D.J. Payne, R.G. Egdell, I. McKenzie, C.F. McConville, S.F.J. Cox, and T.D. Veal, *Shallow donor state of hydrogen in* In_2O_3 *and* SnO_2*: implications for conductivity in transparent conducting oxides*, Phys. Rev. B Rapid Comm. **80**, 081201(R) (2009).

Additionally, the author has contributed to the following articles that have been published or are in press:

T.D. Veal, **P.D.C. King**, P.H. Jefferson, L.F.J. Piper, C.F. McConville, Hai Lu, W.J. Schaff, P.A. Anderson, S.M. Durbin, D. Muto, H. Naoi and Y. Nanishi, *In adlayers on c-plane InN surfaces: A polarity-dependent study by x-ray photoemission spectroscopy*, Phys. Rev. B **76**, 075313 (2007).

T.D. Veal, **P.D.C. King**, M. Walker, C.F. McConville, Hai Lu and W.J. Schaff, *In-adlayers on non-polar and polar InN surfaces: ion scattering and photoemission studies*, Physica B **401-402**, 351 (2007).

P.D.C. King, T.D. Veal, S.A. Hatfield, P.H. Jefferson, C.F. McConville, C.E. Kendrick, C.H. Swartz and S.M. Durbin, *X-ray photoemission spectroscopy determination of the InN/yttria stabilized cubic-zirconia valence band offset*, Appl. Phys. Lett. **91**, 112103 (2007).

P.D.C. King, T.D. Veal, Hai Lu, S.A. Hatfield, W.J. Schaff and C.F. McConville, *The influence of conduction band plasmons on core-level photoemission spectra of InN*, Surf. Sci. **602**, 871 (2008).

P.H. Jefferson, S.A. Hatfield, T.D. Veal, **P.D.C. King**, C.F. McConville, J. Zùñiga-Pérez and V. Muñoz-Sanjosé, *Bandgap and effective mass of epitaxial Cadmium Oxide*, Appl. Phys. Lett. **92**, 022101 (2008).

T.D. Veal, P.H. Jefferson, **P.D.C. King**, S.A. Hatfield, C.F. McConville, J. Zùñiga-Pérez and V. Muñoz-Sanjosé, *Response to "Comment on 'Bandgap and effective mass of epitaxial cadmium oxide'"*, Appl. Phys. Lett. **92**, 106104 (2008).

Martin Allen, Holger Von Wenckstern, Marius Grundmann, Stuart Hatfield, Paul Jefferson, **Philip King**, Timothy Veal, Chris McConville and Steven Durbin, *Mechanisms in the formation of high quality Schottky contacts to n-type ZnO*, Mater. Res. Soc. Symp. Proc. **1035**, L10-06 (2008).

P.D.C. King, T.D. Veal, C.F. McConville, F. Fuchs, J. Furthmüller, F. Bechstedt, J. Schörmann, D.J. As, K. Lischka, Hai Lu and W.J. Schaff, *Valence band density of states of zinc-blende and wurtzite InN from x-ray photoemission spectroscopy and first-principles calculations*, Phys. Rev. B **77**, 115213 (2008).

L.F.J. Piper, Leyla Colakerol, **P.D.C. King**, A. Schleife, J. Zùñiga-Pérez, Per-Anders Glans, Tim Learmonth, A. Federov, T. D. Veal, F. Fuchs, V. Muñoz-Sanjosé, F. Bechstedt, C.F. McConville, and Kevin E. Smith, *Observation of quantized subband states and evidence for surface electron accumulation in CdO from angle-resolved photoemission spectroscopy*, Phys. Rev. B **78**, 165127 (2008).

P.D.C. King, T.D. Veal, M.J. Lowe, and C.F. McConville, *Surface electronic properties of clean and S-terminated InSb(001) and (111)B*, J. Appl. Phys. **104**, 083709 (2008).

P.D.C. King, T.D. Veal, C.S. Gallinat, G. Koblmüller, L.R. Bailey, J.S. Speck and C.F. McConville, *Influence of growth conditions and polarity on interface-related electron density in InN*, J. Appl. Phys. **104**, 103703 (2008).

L.R. Bailey, T.D. Veal, **P.D.C. King**, C.F. McConville, J. Grandal, M.A. Sánchez-García, E. Muñoz, and E. Calleja, *Band bending at the surfaces of In-rich InGaN alloys*, J. Appl. Phys. **104**, 113716 (2008).

T.D. Veal, **P.D.C. King**, S.A. Hatfield, L.R. Bailey, C.F. McConville, B. Martel, J.C. Moreno, E. Frayssinet, F. Semond, and J. Zùñiga-Pérez, *Valence band offset of the ZnO/AlN heterojunction determined by x-ray photoemission spectroscopy*, Appl. Phys. Lett. **93**, 202108 (2008).

T.D. Veal, **P.D.C. King**, C.F. McConville, D.J. Payne, A. Bourlange, and R.G. Egdell, *MBE unmasks the real indium oxide*, Compound Semiconductor **14** (11), 27 (2008).

P.D.C. King, T.D. Veal, C.F. McConville, P.J.C. King, S.F.J. Cox, Y.G. Celebi, and R.L. Lichti, *Donor nature of muonium in undoped, heavily n-type and p-type InAs*, J. Phys.: Condens. Matter **21**, 075803 (2009).[2]

A. Bourlange, D.J. Payne, R.G. Palgrave, H. Zhang, J.S. Foord, R.G. Egdell, R.M.J. Jacobs, T.D. Veal, **P.D.C. King**, and C.F. McConville, *The influence of Sn doping on the growth of In_2O_3 on Y-stabilized ZrO_2(100) by oxygen plasma assisted molecular beam epitaxy*, J. Appl. Phys. **106**, 013703 (2009).

[2]Featured article in *IoP Select* (http://Select.iop.org), selected by the editors on the basis of one or more of the following criteria: substantial advances or significant breakthroughs; a high degree of novelty; significant impact on future research.

P.D.C. King, T.D. Veal, A. Schleife, J. Zùñiga-Pérez, B. Martel, P.H. Jefferson, F. Fuchs, V. Muñoz-Sanjosé, F. Bechstedt, and C.F. McConville, *Valence band electronic structure of CdO, ZnO, and MgO from x-ray photoemission spectroscopy and quasi-particle corrected density functional theory calculations*, Phys. Rev. B. **79**, 205205 (2009).

H.L. Zhang, D.J. Payne, R.G. Palgrave, V. Lazarov, A.T.S. Wee, W. Chen, C.F. McConville, **P.D.C. King**, T.D. Veal, G. Panaccione, P. Lacovig, and R.G. Egdell, *Surface structure and electronic properties of* $In_2O_3(111)$ *single crystal thin films grown on Y-stabilised* $ZrO_2(111)$, Chem. Mater. *in press.*

The author has also presented the research reported in this thesis at the following national and international conferences (January 2007 – July 2009).

Variation of band bending at the surface of Mg-doped InGaN: evidence of p-type conductivity across the composition range (poster presentation), UK Nitrides Consortium Meeting, January 2007, University of Cambridge, UK.

Electronic properties of InN and InGaN surfaces (oral presentation), UK Nitrides Consortium Meeting, July 2007, University of Warwick, UK.

Valence band offsets of group III-N semiconductors (oral presentation), UK Compound Semiconductors Conference, July 2007, University of Sheffield, UK.

Surface electronic properties of n- and p-type InN and InGaN alloys (oral presentation), 7th International Conference of Nitride Semiconductors, September 2007, MGM Grand Hotel, Las Vegas, Nevada, USA.

Charge neutrality level in InN (oral presentation), The Rank Prize Funds Mini-symposium on Physics and Applications of InN and InGaN Semiconductor Materials, June 2008, Wordsworth Hotel, Lake District, UK.[3]

Surface electronic properties of undoped and Mg-doped In(Ga,Al)N alloys (poster presentation), Gordon Research Conference on Defects in Semiconductors, August 2008, Colby-Sawyer College, New London, NH, USA.

The charge neutrality level in CdO: defects, doping and surface electronic properties (poster presentation), Gordon Research Conference on Defects in Semiconductors, August 2008, Colby-Sawyer College, New London, NH, USA.

Understanding the Extreme Electronic Properties of InN: Chemical Trends and the Charge Neutrality Level (oral presentation, plenary contribution), International Workshop on Nitride Semiconductors, October 2008, Montreux Convention Centre, Montreux, Switzerland.

Quantum Well States at Oxide and Nitride Surfaces (oral presentation, invited contribution), Quantum Processes and Nanostructured Surfaces meeting, April 2009, University of Birmingham, UK.

Surface electron accumulation in significantly cation-anion mismatched semiconductors (oral presentation), International Conference on the Formation of Semiconductor Interfaces, July 2008, Congress Centrum Neue Weimarhalle, Weimar, Germany.

Defects in In_2O_3 (oral presentation), 25th International Conference on Defects in Semiconductors, July 2009, St Petersburg State Polytechnical University, Russia.

[3]Awarded the Rank Prize Funds Optoelectronics committee prize for the best contibuted paper at the mini-symposium.

Unintentional conductivity of InN (oral presentation), 25th International Conference on Defects in Semiconductors, July 2009, St Petersburg State Polytechnical University, Russia.

Abstract

The fundamental bulk and surface electronic properties of a novel class of semiconductors, characterised by a significant mismatch between the size and electronegativity of the cation and anion (SCAMS), have been investigated. The characteristic examples of CdO, In_2O_3, and InN were studied using high-resolution x-ray photoemission spectroscopy, infrared reflectivity, optical absorption spectroscopy, and single-field Hall effect measurements. The behaviour of not only defects, dopants and impurities, which dominate the bulk electronic properties, but also surface states was shown to depend on the position of a single energy level, the charge neutrality level (CNL), unifying bulk and surface electronic properties of semiconductors.

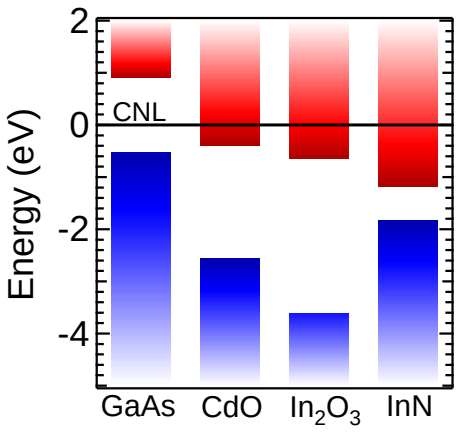

For the materials studied, the CNL was shown to be located within the conduction band (0.39 eV, ∼0.65 eV, and 1.19 eV above the conduction band minimum (CBM) in CdO, In_2O_3, and InN, respectively; see figure) in contrast to the vast majority of semiconductors where the CNL lies within the fundamental band gap (as, for example, in the classic case of GaAs). In CdO, this was shown to lead to native defects, hydrogen impurities and surface states all being donors, even in already n-type material. The donor surface states result in electron accumulation at the CdO surface. Such an electron accumulation is also present at InN surfaces, and this was shown to exhibit a remarkable independence on surface orientation, and to lead to inversion layers at the surface of p-type InN. The changes in surface space-charge regions were investigated across the In(Ga,Al)N composition range, for both undoped and Mg-doped alloys. The influence of the CNL position on interface properties and conductivity in InN was considered. Electron accumulation was observed in In_2O_3, in contrast to previous reports. Muonium, and by analogy hydrogen, was also shown to be a shallow donor in this material. The location of the CNL above the CBM in SCAMS was used to explain many of their striking bulk electronic properties, such as why materials like In_2O_3 are able to be conducting despite being optically transparent, two normally contradictory properties. The conclusions drawn from these studies are applicable to a wide variety of other materials, in particular other SCAMS such as ZnO or SnO_2.

Surface electron accumulation is treated here mainly within a one-electron semiclassical approximation. The final section of this work moves beyond this, using angle-resolved photoemission spectroscopy measurements and theoretical calculations to consider both the quantized nature of an electron accumulation layer, and the influence of many-body effects.

Abbreviations and common symbols

2DEG	Two-dimensional electron gas
ADM	Amphoteric defect model
AHC	Atomic hydrogen cleaning
ARPES	Angle-resolved photoemission spectroscopy
BZ	Brillouin zone
CBM	Conduction band minimum
CNL	Charge neutrality level
DFT	Density-functional theory
DOS	Density of states
EDC	Energy distribution curve
FTIR	Fourier-transform infrared
FWHM	Full width at half maximum
GGA	Generalized gradient approximation
IFIGS	Interface-induced gap states
IMFP	Inelastic mean free path
IR	Infrared
KS	Kohn-Sham
LDA	Local density approximation
LEED	Low energy electron diffraction
MB	Moss-Burstein
MDC	Momentum distribution curve
MIGS	Metal-induced gap states
MOVPE	Metal-organic vapour-phase epitaxy
MTFA	Modified Thomas-Fermi approximation
NP	Non-parabolic

OAS	Optical absorption spectroscopy
PAMBE	Plasma-assisted molecular-beam epitaxy
PES	Photoemission spectroscopy
PS	Poisson-Schrödinger
Q2DEG	Quasi two-dimensional electron gas
QPC	Quasiparticle-corrected
SCAMS	Significantly cation-anion mismatched semiconductors
TCO	Transparent conducting oxide
TD	Threading dislocation
TMM	Transfer matrix method
UHV	Ultra-high vacuum
UV	Ultraviolet
VB-DOS	Valence band density of states
VBM	Valence band maximum
VBO	Valence band offset
ViGS	Virtual gap states
XC	Exchange and correlation
XPS	X-ray photoemission spectroscopy
bcc	Body-centred cubic
rh	Rhombohedral
rs	Rock-salt
wz	Wurtzite
zb	Zinc-blende
α	Optical absorption coefficient
$\mathbf{A}$	Vector potential
$A(\mathbf{k}, E)$	Spectral function
c	Speed of light (2.998×10^8 ms^{-1})

Δ_{cr}	Crystal-field splitting
Δ_{so}	Spin-orbit splitting
δ	Kronecker delta function
E	Energy
E_B	Binding energy
E_C	Conduction band minimum energy
E_F	Fermi level
E_f	Final state energy
E_g	Band gap
E_i	Initial state energy
E_k	Kinetic energy
E_{mid}	Mid-gap energy
$\bar{E}_{mid}$	Average mid-gap energy
E_V	Valence band maximum energy
e	Electronic charge (1.602×10^{-19} C)
eV	Electron volts (1.602×10^{-19} J)
ε_0	Permittivity of vacuum (8.854×10^{-12} Fm^{-1})
$\varepsilon(0)$	Static dielectric constant
$\varepsilon(\infty)$	High-frequency dielectric constant
$f(E)$	Fermi-Dirac distribution function
$\mathbf{G}$	Reciprocal lattice vector
$G(\mathbf{k}, E)$	Single-particle Green's function
g	Density of states
Γ	Centre of Brillouin zone
$\mathcal{H}$	Hamiltonian
h	Planck's constant (6.626×10^{-34} Js)
$\hbar$	$h/2\pi$ (1.055×10^{-34} Js)

$\mathbf{k}$	Wavevector
λ	Wavelength *or* inelastic mean free path
M_{fi}	Matrix element connecting initial i and final f states
m_0	Free electron mass (9.109×10^{-31} Kg)
m^*	Effective mass
N	Sheet density
N_A^-	Ionized acceptor density
N_D^+	Ionized donor density
N_{ss}	Surface state density
n	Carrier density (electrons)
ξ	Valence band maximum to surface Fermi level separation
Ψ	Many-electron wavefunction
ψ	One-electron wavefunction
Φ_B	Barrier height
ϕ	Work function
P	Kane's matrix element
p	Carrier density (holes)
$\mathbf{p}$	Momentum operator ($-i\hbar\nabla$)
$\mathbf{q}$	Imaginary component of wavevector
$\mathbf{r}$	Position vector
S	Slope parameter (MIGS model)
$\Sigma(\mathbf{k}, E)$	Self-energy
V	Potential
ν	Frequency
X	Electronegativity
χ	Electron affinity

Chapter 1

Introduction

1.1 Significantly cation-anion mismatched semiconductors

Research on semiconductor materials has been intimately linked with technological developments. While silicon still dominates the microelectronics industry, III-V materials such as GaAs have become increasingly important as their generally direct band gaps give favourable properties for optoelectronic applications, and their low effective masses and high mobilities make them suitable for use in high-frequency electronic devices. Indeed, the development of heterostructure-based III-V devices can be regarded as one of the most important technological achievements of recent years [1, 2]. Research into semiconductors is not, however, limited to practical applications: they have also provided an opportunity to study fundamental physics. Perhaps most notably, studies of AlGaAs/GaAs heterostructures revealed a highly precise quantization of the Hall coefficient at values dependent only on fundamental physical constants [3].

The archetypal III-V semiconductor, GaAs, has been extensively studied and utilized. However, an ever increasing need for higher-speed/higher-power electronic and innovative photonic devices has spurred progressive investigation of new materials. A novel class of semiconductor compounds has emerged, characterised by a large size and electronegativity mismatch between the constituent atoms. The electronegativity and atomic radii of some group II, III, V and VI elements are shown in Fig. 1.1. In particular, N and O can be seen to be much more electronegative, and have much smaller atomic radii, than other group V and VI elements, respectively, as well as group II and III atoms.

One subset of such *highly mismatched compounds* results from the substitution of a dilute concentration of N or O in place of the anion of a III-V or II-VI semiconductor, respectively [5, 6]. Studies of these alloys, where an interaction of the localized N or O impurity levels and the host conduction band leads to a so-

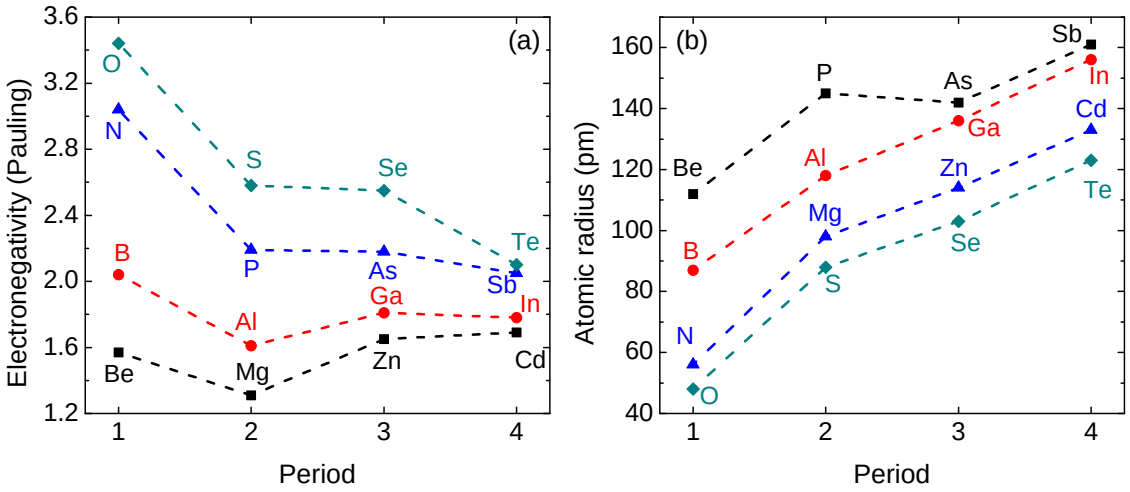

Figure 1.1: (a) Electronegativity (in Pauling units) from Ref. [4] and (b) atomic radii of some group II, III, V and VI elements.

called conduction band anticrossing, restructuring the conduction band into two subbands, revealed novel physical mechanisms involved in the formation of band structure. Concurrently with these fundamental insights, the materials also show technological promise, with high-efficiency multi-band solar cells just one suggested application [6].

Instead of incorporation in dilute concentrations, N or O can themselves be used as the anion of a compound semiconductor. These materials can be considered *significantly cation-anion mismatched semiconductors* (SCAMS) due to the large size and electronegativity mismatch between the anion (small, very electronegative atom) and the cation (much larger, less electronegative atom). The SCAM nature is most pronounced for compounds with large cations such as CdO, InN and In_2O_3, which are the focus of the current work. While these materials have already shown device potential, or indeed realisation, such as in high-frequency electronic, efficient photonic and transparent contact applications, relatively little is known or understood about their fundamental material properties. A number of striking phenomena have, however, already been discovered. For example, InN has previously been shown to support a surface accumulation of electrons [7], in contrast to the depletion layers observed at the majority of semiconductor surfaces, and CdO and In_2O_3 both exhibit high conductivity, despite their relatively wide band gaps and

optical transparency [8, 9]. It is of interest to investigate what gives rise to these seemingly unusual properties.

This thesis aims to develop a comprehensive understanding of the electronic properties of SCAMS, centred around the concept of the charge neutrality level (CNL), focussing specifically on the properties of CdO, InN and related alloys, and In_2O_3. This is motivated by the dual goals of furthering the knowledge and understanding of their material properties for potential use in device applications, and the investigation of novel physical phenomena in solid state physics.

1.2 Organisation of the thesis

The remainder of this chapter presents an introduction to the concept of virtual gap states, the CNL, electronic properties of surfaces, and defects in semiconductors. Chapters 2 and 3 detail the basic theoretical models (band structure and semiconductor space-charge calculations) and the core experimental techniques (photoemission spectroscopy, optical absorption, infrared reflectivity, and Hall effect measurements) used throughout this thesis. In Chapter 4, investigations of CdO are used to show that the CNL ultimately determines the charge character of surface states, defects and impurities in semiconductors, hence unifying bulk and surface electronic properties. These concepts are utilized in investigations of other materials systems in Chapters 5 to 8: the CNL position in InN is determined in Chapter 5, and its influence on the nature of InN's surface electron accumulation and interface-related electron density are investigated in detail in Chapter 6; the variation in surface electronic properties of the In(Ga,Al)N alloys are considered in Chapter 7; surface electron accumulation is also discovered in In_2O_3 in Chapter 8, and the determined CNL position is shown to be the overriding factor giving rise to conductivity in this transparent oxide. Throughout these chapters, surface electron accumulation is treated in a semi-classical single-electron approximation (detailed in Chapter 2). Chapter 9 moves beyond this approximation, considering the quantized nature of an accumulation layer, and the influence of many-body effects at semiconductor surfaces. Finally, the main findings of this work are summarised in Chapter 10.

1.3 Charge neutrality level

1.3.1 Virtual Gap States

In the solution of the Schrödinger equation in terms of Bloch functions (see Section 2.1.1), application of Born-von Karman periodic boundary conditions for the infinite crystal requires the Bloch wavevector to be real. However, at the surface of a material, the perfect periodicity of the structure is broken. This allows states with a complex Bloch wavevector, which are also solutions of the Schrödinger equation, to exist. Consequently, surface states are evanescent, that is, they decay exponentially into the vacuum and into the bulk of the semiconductor, and physically describe electronic levels that are localized near the surface. Due to a similar breaking of the full translational symmetry of the lattice at a metal–semiconductor interface, Heine [10] showed that the wavefunctions of the metal states can tunnel into the band gap of the semiconductor just as a surface state does. Inkson [11] argued that the same holds for deep (that is, localized) defects.

Much insight into these surface, interface, and defect states can be obtained by considering the complex band structure of a one-dimensional lattice within the nearly-free electron model [12]. An electron of mass m_0 in a constant potential V_0 must satisfy the one-electron Schrödinger equation (see Section 2.1 for a more thorough discussion of this)

$$\mathcal{H}_0 \left|\psi_{\mathbf{k}}(\mathbf{r})\right\rangle = E^0_{\mathbf{k}} \left|\psi_{\mathbf{k}}(\mathbf{r})\right\rangle \tag{1.1}$$

where $\mathcal{H}_0 = \frac{\mathbf{p}^2}{2m_0} + V_0$, the momentum operator $\mathbf{p} = -i\hbar\nabla$, and the one-electron wavefunctions $|\psi_{\mathbf{k}}(\mathbf{r})\rangle \propto e^{i\mathbf{k}\cdot\mathbf{r}}$, giving

$$E^0_{\mathbf{k}} = \frac{\hbar^2\mathbf{k}^2}{2m_0} + V_0. \tag{1.2}$$

A small periodic potential is introduced as a perturbation

$$\mathcal{H} = \mathcal{H}_0 + \mathcal{H}_1 \tag{1.3a}$$

$$\mathcal{H}_1 = \sum_{\mathbf{G}} V_1 e^{-i\mathbf{G}\cdot\mathbf{r}} \tag{1.3b}$$

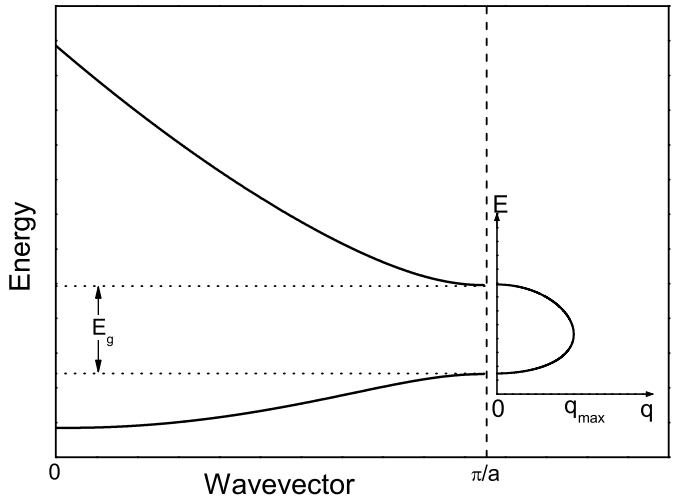

Figure 1.2: Complex band structure in the reduced zone scheme of a one-dimensional nearly-free electron solid with band gap E_g. The imaginary component of the complex band structure is plotted as a function of imaginary wavevector, q. The maximum wavevector, $q_{\max}$, occurs just below the middle of the energy gap.

where $\mathbf{G}$ is a reciprocal lattice vector. Writing the Hamiltonian in matrix form [13],

$$\mathcal{H}_{\mathbf{k}'\mathbf{k}} \equiv \langle \psi_{\mathbf{k}'} | \, \mathcal{H} \, | \psi_{\mathbf{k}} \rangle = E^0_{\mathbf{k}'} \delta_{\mathbf{k}\mathbf{k}'} + \langle \psi_{\mathbf{k}'} | \, \mathcal{H}_1 \, | \psi_{\mathbf{k}} \rangle \, . \tag{1.4}$$

The matrix elements

$$\begin{aligned} \langle \psi_{\mathbf{k}'} | \, \mathcal{H}_1 \, | \psi_{\mathbf{k}} \rangle &= \sum_{\mathbf{G}} V_1 \int \mathrm{d}^3\mathbf{r} \, e^{-i\mathbf{k}'\cdot\mathbf{r}} e^{-i\mathbf{G}\cdot\mathbf{r}} e^{i\mathbf{k}\cdot\mathbf{r}} \\ &= \begin{cases} V_1 & \mathbf{k} = \mathbf{k}' + \mathbf{G} \\ 0 & \text{otherwise.} \end{cases} \end{aligned} \tag{1.5}$$

The energy eigenvalues, $E(\mathbf{k})$, are therefore given by solution of the secular equation

$$\begin{vmatrix} \frac{\hbar^2\mathbf{k}^2}{2m_0} + V_0 - E(\mathbf{k}) & V_1 \\ V_1 & \frac{\hbar^2(\mathbf{k}-\mathbf{G})^2}{2m_0} + V_0 - E(\mathbf{k}) \end{vmatrix} = 0. \tag{1.6}$$

Considering the wavevector with respect to the Brillouin zone (BZ) boundary in one dimension, $\kappa = (\pi/a) - k$, where a is the lattice parameter,

$$E(\kappa) = V_0 + E_1 + \frac{\hbar^2\kappa^2}{2m_0} \pm \sqrt{V_1^2 + 4E_1\frac{\hbar^2\kappa^2}{2m_0}} \tag{1.7}$$

where

$$E_1 = \frac{\hbar^2}{2m_0}\left(\frac{G}{2}\right)^2, \tag{1.8}$$

the familiar dispersion shown in Fig. 1.2 results for real wavevectors, where an energy gap $E_g = 2\,|V_1|$ opens up at the BZ boundary.

However, as discussed above, it is not sufficient to consider only the band structure corresponding to real wavevectors, but also evanescent states with real

energies but complex wavevectors. Considering the imaginary component of the wavevector q, where $k = (\pi/a) + iq$, the dispersion becomes

$$E(q) = V_0 + E_1 - \frac{\hbar^2 q^2}{2m_0} \pm \sqrt{V_1^2 - 4E_1 \frac{\hbar^2 q^2}{2m_0}}. \tag{1.9}$$

This complex dispersion exists within the band gap of the bulk semiconductor, as shown in Fig. 1.2. As such states are meaningless within the bulk, they are termed virtual gap states (ViGS) [10]. Similar considerations, although somewhat less simple, hold in three dimensions [12, 14].

As the ViGS derive from the bulk band structure, their character changes from predominantly donor-like close to the valence band to predominantly acceptor-like close to the conduction band. The energy at which they have equal donor- and acceptor-like character is termed the branch-point energy of the ViGS, and occurs where the decay length of the ViGS wavefunctions is a minimum. In the one-dimensional example of Fig. 1.2, this occurs at $q_{\max}$, $V_1^2/4E_1$ below the mid-gap energy. As the ViGS are predominantly donor-like below this energy, and acceptor-like above this energy, this branch point can be identified as the charge neutrality level (CNL) of the semiconductor [15, 16].

The ViGS are highly localized in real space, and so their character is determined by contributions from a large proportion of the BZ, and not just around the Γ-point. Consequently, the branch point of the ViGS, and hence the CNL, will be located close to the mid-gap energy averaged across the BZ. Various theoretical schemes for estimating the CNL position have been developed. Tersoff [16–19] determined energy bands via linearized augmented plane-wave calculations within the local density approximation (LDA) for a wide range of semiconductors. Following a rigid shift of the conduction band to reproduce experimental band gaps, Tersoff determined the CNL as the energy at which the valence and conduction band contribution to the real-space Green's function is equal. The calculation was performed by averaging over 152 points within the first BZ, well representing the extended **k**-space behaviour of the ViGS but resulting in a rather expensive calculation. Cardona and Christensen [20] and Mönch [21] instead employed Baldereschi's [22] concept of mean-value points, which dictates that the value which any function periodic

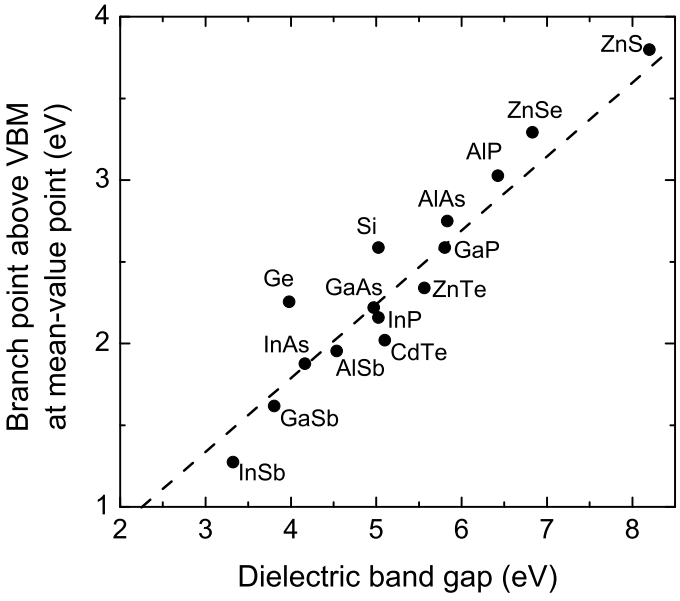

Figure 1.3: Calculated branch point of the ViGS above the VBM vs. the dielectric band gap. The dashed line is a linear fit with a slope 0.449 ± 0.007. Adapted from Mönch [21].

in wavevector assumes at this point is representative of the average value of that function across the BZ. Mönch [21] showed that the energy gap at the mean-value point of the BZ equals the dielectric band gap [23] of the semiconductor. Further, as shown in Fig. 1.3, he used emperical tight-binding calculations to demonstrate a linear relation between the position of the branch point of the ViGS above the valence band maximum (VBM) and the semiconductor dielectric band gap energy, with a slope parameter 0.449 ± 0.007. The CNL therefore lies slightly below the average mid-gap energy of the semiconductor, in agreement with the simple one-dimensional model discussed above. Tersoff [24] semi-empirically identified an alternative average mid-gap energy as

$$\bar{E}_{mid} = \frac{1}{2}\left(\bar{E}_V + \bar{E}_C\right) \tag{1.10}$$

where $\bar{E}_V = E_V - \frac{1}{3}\Delta_{so}$ is the position of the 'effective' VBM in the absence of spin-orbit splitting, Δ_{so}, and $\bar{E}_C$ is the indirect conduction band minimum (CBM). This gives a simple scheme for estimating the CNL position of a material.

The CNL is thought to be universal for all materials on an absolute energy scale [25]. However, while Walukiewicz [26] takes a value 4.9 eV below the vacuum level, based on the electron affinity of GaAs, Van de Walle and Neugebauer [25] employ a value of ~ 4.5 eV. Meanwhile, the equivalent level in the calculations of Kiliç and Zunger [27] is only 3 eV below the vacuum level. Despite these variations

in absolute energy, the alignment of relative CNL positions has proved very powerful in predicting electronic properties in different materials. Some implications of the CNL position in conventional semiconductors are discussed in the following sections.

1.3.2 Surface electronic properties

Surface electronic states distinct from those of the bulk were first considered theoretically by Tamm [28], although substantial insight was added by Shockley [29] who showed that localized levels deriving from the bulk bands exist within the semiconductor band gap. Maue [30] considered the existence of evanescent surface states within the nearly-free electron model discussed above. Provided boundary conditions are fulfilled for matching of the wavefunction tails of the surface states into both the vacuum and the semiconductor bulk [10, 12], these surface states can therefore be seen to derive from the ViGS of the complex band structure.

The ViGS inherent to a clean surface with full translational symmetry in two-dimensions (in the plane of the surface) are termed intrinsic surface states. The microscopic origin for such state formation is the dangling bonds formed when a surface is generated by truncating the bulk structure – each atom at the surface has fewer nearest neighbours than those in the bulk. The breaking of bonds at the surface costs energy, and so a rearrangement of the surface atoms in order to minimize this energy, that is, minimize the energy associated with dangling bonds, almost invariably results in a surface that is different to an ideally truncated bulk. Intrinsic surface states are specific to such surface reconstructions [12, 31].

Extrinsic surface states can also be formed when imperfections (for example adatoms or defects) cause electronic states to become localized at the surface. In the case of adatom induced states, charge transfer will occur between the semiconductor and the adatom dependent on their difference in electronegativity, although Mönch [12] incorporates this effect within the ViGS concept.

From the discussions in Section 1.3.1, the surface ViGS will either be donor-like or acceptor-like if they are below or above the CNL, respectively. These states can be occupied or unoccupied dependent on the Fermi level position at the sur-

face and are either neutral (occupied donor-like or unoccupied acceptor-like states), positively charged (unoccupied donor-like states) or negatively charged (occupied acceptor-like states). In the presence of charged surface states, the carriers in the near-surface region of the semiconductor rearrange in order to screen the macroscopic electric field induced by these states. This occurs over a distance determined by the Thomas-Fermi screening length. While this is very short in metals due to their extremely high free carrier concentration, it is appreciably longer in semiconductors leading to macroscopic regions of charge redistribution known as space-charge regions.

Consequently, the Fermi level shifts as a function of depth within the semiconductor, which can equivalently be viewed as a bending of the conduction and valence bands with respect to the Fermi level. The position of the Fermi level at the surface is determined by the condition of charge neutrality within the semiconductor: the total charge due to surface states, Q_{ss}, must be compensated by an equal but opposite charge within the space-charge region, Q_{sc},

$$Q_{ss} = -Q_{sc}. \tag{1.11}$$

For an n-type material, when the surface states are negatively (positively) charged, a positive (negative) space-charge region is therefore required to maintain charge neutrality. This is achieved by an upward (downward) bending of the bands in order to decrease (increase) the electron concentration at the surface with respect to the bulk values, resulting in a depletion (accumulation) of electrons at the surface. If there are sufficient negatively charged surface states, the band bending required to maintain charge neutrality can be so severe that the Fermi level at the surface moves below the middle of the direct band gap and a p-type surface layer of holes exists, separated from the n-type bulk region by a depletion layer. This is termed an inversion layer. In the situation where the Fermi level at the surface is located exactly at the CNL, there are on average no charged surface states, and so there is no band bending. This is referred to as the flat-band case. The preceding considerations are reversed when the bulk region has p-type conductivity. Schematic representations of the band bending and carrier concentration variation

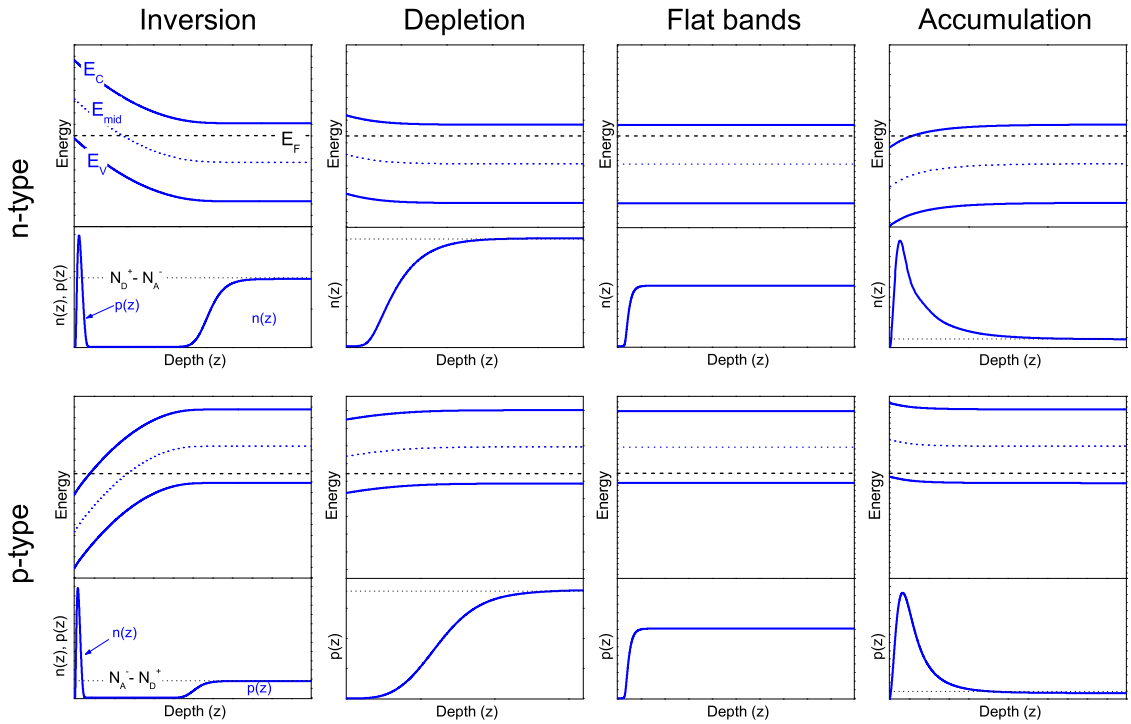

Figure 1.4: A schematic representation of the band bending and associated charge profiles for inversion, depletion, flat-bands and accumulation space-charge layers at the surface of n- and p-type semiconductors. The variation of the conduction and valence band edges (E_C and E_V) and the mid-gap energy (E_{mid}, dotted line) are shown. A schematic Fermi level (E_F) is also represented (dashed line). In the carrier concentration plots, the background net ionized donor density ($N_D^+ - N_A^-$) and net ionized acceptor density ($N_A^- - N_D^+$) is shown for n-type and p-type samples, respectively (dotted line).

as a function of depth in each of these space-charge regions is shown in Fig. 1.4.

Allen and Gobeli [32] investigated the clean Si(111) surface prepared in the (2×1) reconstruction by cleavage in ultra-high vacuum (UHV), and observed a strong pinning of the Fermi level at the surface by intrinsic states for a wide range of bulk Fermi level positions, with upward (downward) band bending observed for n-type (p-type) samples. This results in electron (hole) depletion layers, consistent with the CNL lying only a little below the middle of the direct band gap [24]. Similar space-charge layers result for the Si(100) $-$ (2×1) and Si(111) $-$ (7×7) surfaces [31, 33], consistent with the position of the CNL, but with differences in surface state distributions for the different crystal surfaces and reconstructions leading to small differences in the Fermi level pinning position. Meanwhile, a much larger tendency for upward band bending for n-type material than downward band bending for p-type material was observed at the cleaved Ge(111) $-$ (2×1) surface [34], consistent

with the CNL lying approximately at the VBM in Ge [24].

The situation is a little more complex for III-V compound semiconductors. While a pinning of the Fermi level a little below mid-gap was observed at the (001) surface of as-grown GaAs [35], consistent with the CNL position [24], flat-bands were observed at the perfectly cleaved (110) surface [36, 37]. However, the pinning of the Fermi level was recovered upon adsorption of a small quantity of O, or in the presence of step edges on the cleaved surface [37]. This was subsequently understood by theoretical predictions that a relaxation of the surface layer, where the Ga–As zigzag chains tilt with the As atoms being pushed outwards at the cleaved (110) surface, results in the intrinsic surface states related to dangling bonds being pushed out of the band gap. Thus, the pinning of the Fermi level in as-grown or ex-situ prepared GaAs(110) can be attributed to extrinsic surface states. This confirms that the CNL still represents the relevant energy level for discussing the electronic properties of surfaces where extrinsic, rather than intrinsic, surface states dominate. A final interesting example is the case of InAs, which has been observed to exhibit an accumulation of electrons at the clean surface of n-type material [38, 39]. This is because the CNL actually lies outside of the fundamental band gap in InAs, above the CBM [24]. A pinning of the Fermi level close to this energy leads to an increase in electron density approaching the surface. This example is of particular relevance for the materials considered in this thesis.

1.3.3 Metal-semiconductor and semiconductor-semiconductor interfaces

The first model to explain the behaviour of metal-semiconductor contacts was developed as early as 1931 by Schottky *et al.* [40]. They proposed that the so-called Schottky barrier height (that is, the separation of the Fermi level and CBM of the semiconductor at the interface, Φ_B) should simply be the difference between the work function of the metal, ϕ_M, and the electron affinity of the semiconductor, χ, both referenced to the vacuum level,

$$\Phi_B = \phi_M - \chi, \tag{1.12}$$

as shown in Fig. 1.5. While this successfully explained the rectifying nature of

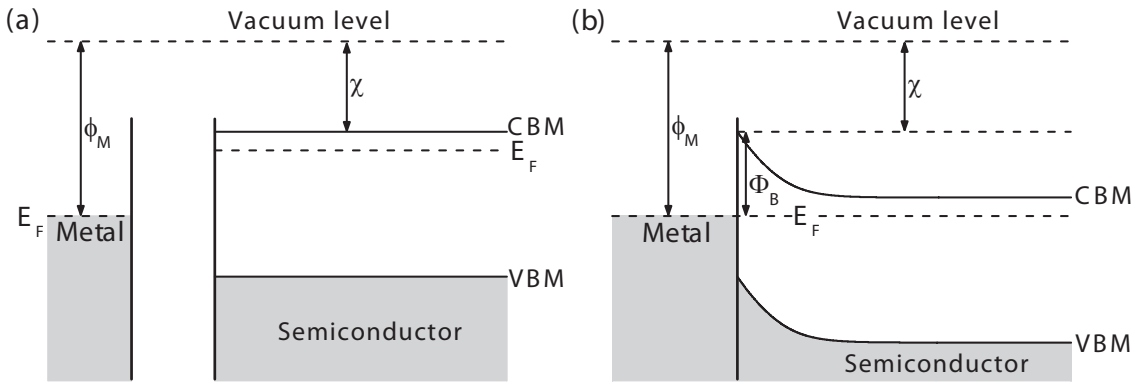

Figure 1.5: Schematic representation of metal-semiconductor contact behaviour within the Schottky model, (a) before and (b) after the junction is formed. Filled states are represented by shading. The semiconductor is assumed to have no surface states, and so the bands are flat up to the surface in (a). Equally, no interface states are considered once the contact is made. Figure adapted from Ref. [41].

Schottky contacts, as they were later termed, the dependence of the barrier height on the metal work function was generally found to be much weaker than predicted by this model. Bardeen [42] alternatively considered the role of a high density of interface states, effectively pinning the Fermi level at the interface. In this model, the barrier height is independent of the metal work function, dependent only on the relative difference between the CBM of the semiconductor and the pinning position of the Fermi level

$$\Phi_B = E_c - E_F^{pin}. \tag{1.13}$$

Very ionic (covalent) materials are better described within the Schottky (Bardeen) limit [43], whereas intermediate materials exhibit a degree of Fermi level pinning, although with changes in the barrier height observed as a function of the metal work function.

The microscopic origin of the interface states giving rise to Fermi level pinning was variously attributed to defects [44, 45] or to ViGS in the form of metal induced gap states (MIGS) [10,16]. Tersoff [24] showed that a linear relation existed between the CNL and the barrier height for gold contacts to a number of semiconductors, as shown in Fig. 1.6(a). This suggests that the MIGS model, where the Fermi level would pin at the CNL in the Bardeen limit, is likely key to understanding the formation of Schottky barriers. However, some variation in barrier height with metal work function would still be expected due to charge transfer between the

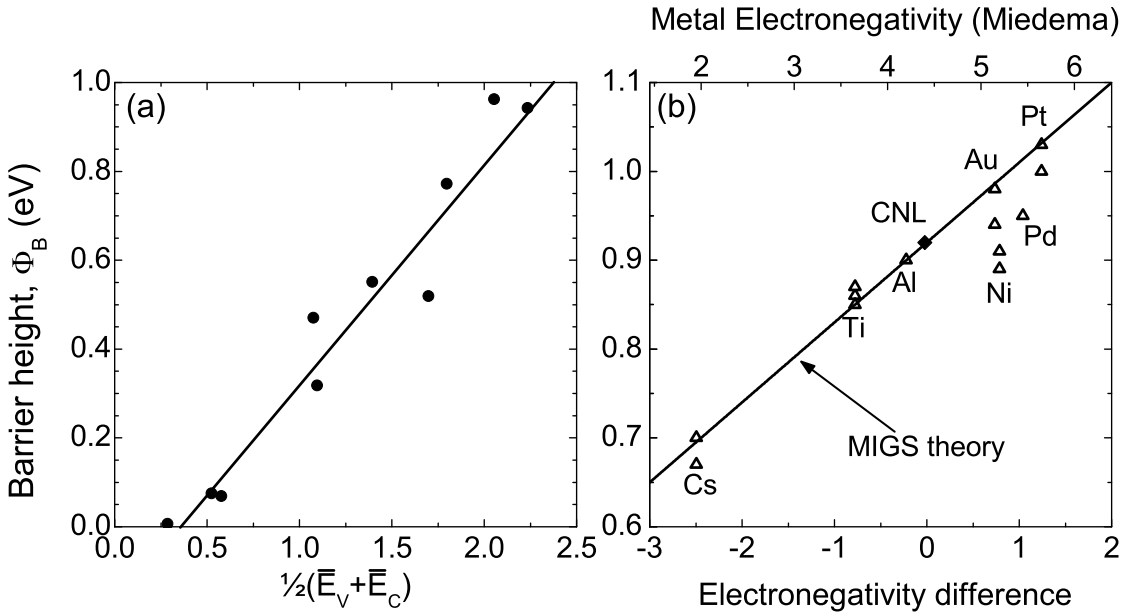

Figure 1.6: (a) Schottky barrier height, Φ_B, for gold on a number of semiconductors as a function of the CNL position calculated from Eqn. 1.10, adapted from Ref. [24]. The solid line is $\Phi_B = \frac{1}{2}\left(\bar{E}_V + \bar{E}_C\right) - 0.2$ eV. (b) Schottky barrier height, Φ_B, for different metals deposited on GaAs as a function of metal electronegativity in Miedema units, adapted from Ref. [4]. The solid line is Eqn. 1.14 with $\Phi_{CNL} = 0.92$ and $S_X = 0.08$ eV.

metal and the semiconductor; indeed, Tersoff found that the barrier height for these gold contacts was $\sim$0.2 eV below the value that would be obtained for pinning of the Fermi level at the CNL, consistent with a 'MIGS plus charge transfer' model.

Mönch [4] included the variation in barrier height with work function of the metal into the MIGS model via a slope parameter, S_X, giving the n-type barrier height

$$\Phi_B = \Phi_{CNL} + S_X(X_m - X_s) \tag{1.14}$$

where Φ_{CNL} is the barrier height obtained when the metal is of the same electronegativity as the semiconductor, and so the Fermi level pins at the CNL at the interface, and X_m and X_s are the metal and semiconductor electronegativities, respectively, in Miedema units. The metal and semiconductor electronegativities were shown to scale linearly with the metal work function and dielectric work function (vacuum level to CNL) of the semiconductor, respectively [46], making this electronegativity difference a suitable quantity to characterise charge transfer at the interface.

Mönch [46, 47] further determined the slope parameter to vary as

$$S_X = \frac{0.86}{1 + 0.1(\varepsilon(\infty) - 1)^2} \tag{1.15}$$

where $\varepsilon(\infty)$ is the high-frequency dielectric constant of the semiconductor. Thus, for very ionic (covalent) compounds where $\varepsilon(\infty)$ is small (large), S_X is large (small) leading to a weak (strong) pinning corresponding to the Schottky (Bardeen) limit. This explains the chemical trends observed by Kurtin *et al.* [43].

The barrier heights for a number of metals on GaAs are shown in Fig. 1.6(b), with the MIGS-plus-electronegativity model line. In general, good agreement is seen between the barrier heights from experimental measurements and those predicted theoretically. However, the points for Ni and Pd lie well below the model line. Ni and Pd are known to decompose GaAs even at room temperature [4], and so the Ni/Pd–GaAs interface may be somewhat defective. Mönch [48] showed that, while the MIGS model was the overriding mechanism determining the formation of barrier heights at metal-semiconductor contacts, a reduction in the barrier height below the MiGS value would be expected for contacts where a high density of defects exist. This reconciles the differing explanations of MIGS or defects as the microscopic origin of the interface states.

The natural band lineup of two semiconductors can also be determined from the locations of the CNL relative to the VBM in each material [15, 17], where interface induced gap states (IFIGS) are the important ViGS. The influence of charge transfer at the interface can often be neglected in this case due to the similar electronegativities of most semiconductors. Mönch [4] has also shown the alignment of CNLs to hold for metamorphic heterostructures, making this an excellent way to predict the valence band offset (VBO) between highly lattice-mismatched semiconductors such that the interface is characterised by a high density of strain-relieving misfit dislocations. The measured VBOs of a number of pseudomorphic and metamorphic semiconductor heterojunctions are plotted against the difference in their calculated CNL positions in Fig. 1.7, indicating the validity of the IFIGS model for determining VBOs of semiconductors.

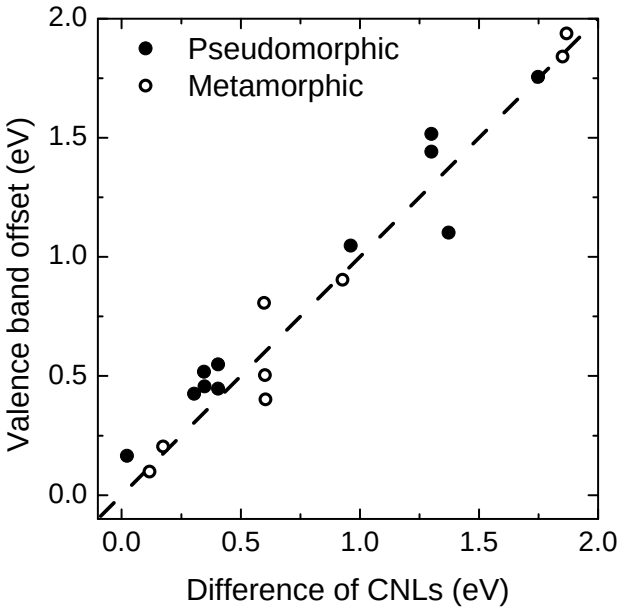

Figure 1.7: The VBO of a number of pseudomorphic and metamorphic semiconductor heterojunctions vs. the difference in their calculated CNL positions, adapted from Mönch [4].

1.4 Amphoteric defect model

In an attempt to explain the mechanisms of Schottky barrier formation, Spicer *et al.* [44, 49] proposed a 'unified defect model', where Fermi level pinning at a metal/semiconductor (or indeed oxide/semicondctor) contact was attributed to extrinsic defects at the interface. While numerically this model appears to predict the values of Schottky barrier heights rather well, there is evidence that a distribution of defects do not pin the Fermi level in Schottky barrier formation [4, 50] – the formation of Schottky barriers can be better understood in terms of the MIGS model, discussed above. However, the numerical agreement achieved between the two models suggests some intrinsic link exists between the energetics of native defect formation and that of surface/interface states. This will be considered further in Chapter 4.

The unified defect model was subsequently extended by Walukiewicz [45, 51], where it was termed the amphoteric defect model (ADM). While it still inaccurately assigns native defect states as the sole origin of the electronic properties of semiconductor interfaces, the ADM remains insightful in elucidating tendencies for their bulk electronic properties. Within this model, the formation energy for donor (acceptor) native defects, such as anion (cation) vacancies, increases (decreases) with increasing Fermi level, such that formation of donor (acceptor) native defects is most

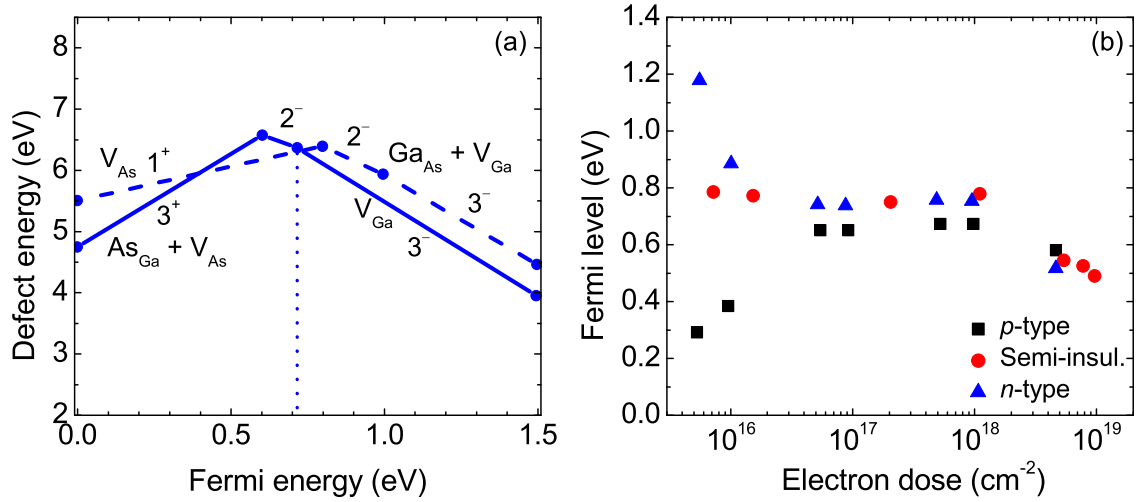

Figure 1.8: (a) Formation energies for Ga and As vacancies (V_{Ga}, V_{As}) and anti-site defect complexes ($\mathrm{As_{Ga}} + V_{\mathrm{As}}$, $\mathrm{Ga_{As}} + V_{\mathrm{Ga}}$) in GaAs, with the charge state as shown, adapted from Walukiewicz [51]. The vertical line represents E_{FS}. (b) Evolution of the Fermi level in *p*-type, semi-insulating and *n*-type GaAs upon high-energy electron irradiation, adapted from Walukiewicz [52].

favourable when the Fermi level is below (above) an energy known as the Fermi level stabilization energy (E_{FS}) in the nomenclature of the ADM. This is represented for GaAs in Fig. 1.8(a). Consequently in GaAs, for energies below E_{FS}, the donor As-vacancy has a low formation energy, whereas for energies above E_{FS}, the acceptor cation-on-anion defect complex, $\mathrm{Ga_{As}} + V_{\mathrm{Ga}}$, is more favourable. Conversely, above E_{FS}, the acceptor Ga vacancy can exist, although the donor anion-on-cation defect complex, $\mathrm{As_{Ga}} + V_{\mathrm{As}}$, becomes favourable as the Fermi level moves below E_{FS}.

Native defects can be deliberately introduced into a semiconductor, for example by high-energy particle irradiation. If the Fermi level is initially below E_{FS} (for example, in *p*-type GaAs), the production of donor defects will be more favourable (see Fig. 1.8(a)), acting to increase the Fermi level up towards E_{FS}. Conversely, for Fermi levels initially lying above E_{FS} (for example in *n*-type GaAs), acceptor defects will have the lower formation energy (Fig. 1.8(a)), resulting in a decrease of the Fermi level back down towards E_{FS}. As the Fermi level reaches E_{FS}, donor and acceptor native defects will be generated at the same rate, resulting in no net change in carrier concentration, and acting to stabilize the Fermi level at E_{FS} for high irradiation doses. This can be observed for GaAs is Fig. 1.8(b) [52].

The ADM can also be used to explain doping limits in semiconductors [53].

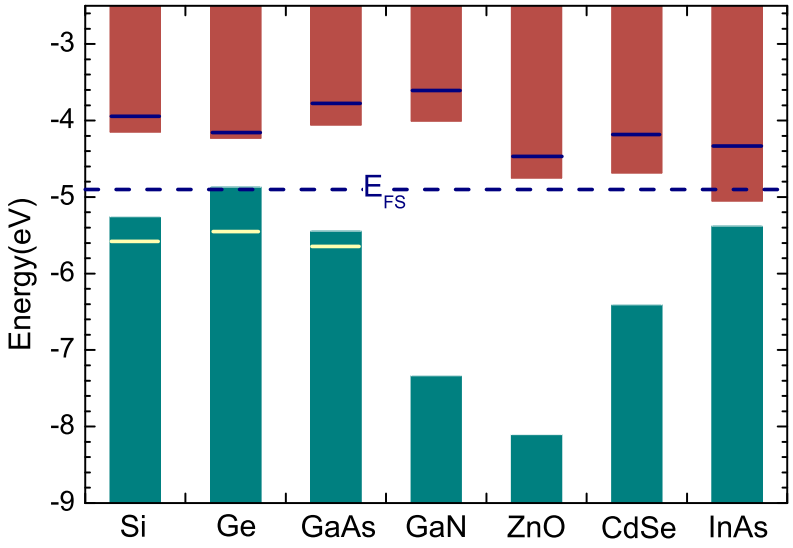

Figure 1.9: Band lineup relative to E_{FS} in a number of semiconductors. Doping limits are represented by bars in the valence (p-type doping) and conduction (n-type doping) bands, adapted from Khanal *et al.* [54].

As seen in Fig. 1.8(a), with increasing Fermi level away from E_{FS}, the formation energy of compensating defects decreases. Therefore, it is difficult to extrinsically dope semiconductors to move the Fermi level too far above or below E_{FS} due to the increasing prevalence of compensating defect centres. Experimental doping limits are represented for a number of semiconductors in Fig. 1.9. For materials where E_{FS} lies close to the valence band (for example, Ge), p-type doping is much more efficient, whereas for materials where E_{FS} lies close to the conduction band (for example, ZnO, InAs), n-type doping can be readily achieved, while p-type doping is difficult.

The above sections have revealed that the CNL and ADM are useful in the analysis and understanding of the electronic properties of semiconductor materials, including their bulk doping, surface space-charge, metal-semiconductor and semiconductor-semiconductor interface properties. In this thesis, these two models will be unified, and the influence of the CNL position on the electronic properties of a number of SCAMS will be investigated.

Chapter 2

Theoretical methods

This thesis is concerned with the electronic properties of semiconductors. As such, the relation between the electronic band structure and measurable/calculable parameters such as carrier densities and Fermi levels is of the utmost important. The materials considered here have non-parabolic conduction band dispersions, necessitating the use of band structure approximations beyond the simple parabolic model. The theoretical background and resulting expressions of such approximations are presented in Section 2.1 of this chapter. Furthermore, the solution of band bending potentials will form a large component of the work presented here, and the formulations used for this are discussed in Section 2.2 of this chapter.

2.1 Electronic structure calculations

The behaviour of electrons in a crystal solid is governed by the many-body Schrödinger equation

$$\mathcal{H}\left|\Psi\right\rangle = E\left|\Psi\right\rangle. \tag{2.1}$$

Neglecting magnetic effects, the Hamiltonian operator is given by

$$\mathcal{H} = \sum_{i=1}^{N} \frac{\mathbf{p}_i^2}{2m_i} + \frac{1}{2}\sum_{i=1}^{N}\sum_{j\neq i}^{N} \frac{Z_i Z_j}{4\pi\varepsilon_0\left|\mathbf{r}_i - \mathbf{r}_j\right|} \tag{2.2}$$

where the sums are over the N particles (electrons and nuclei) of charge Z_i, mass m_i, and spatial position $\mathbf{r}_i$ making up the system, the momentum operator

$$\mathbf{p}_i = -i\hbar\nabla_i \tag{2.3}$$

and $\Psi(\mathbf{r}_1, \mathbf{r}_2, \ldots, \mathbf{r}_N)$ is a N-body wavefunction.

It is generally appropriate to consider the electrons as either core or valence electrons. The core electrons are localized around the nuclei, and so the system can be treated as a number of valence electrons interacting with ion cores (nuclei and core electrons). Due to their significantly lower mass, the electrons can be assumed to react almost instantaneously to the motion of the ions – the ions appear stationary

to the electrons, whereas the ions only respond to the time-averaged behaviour of the electrons. This is the *Born-Oppenheimer* (or *adiabatic*) *approximation* [55], allowing the motion of the ions to be decoupled from that of the electrons. A simplified N-body electronic Hamiltonian results,

$$\mathcal{H}_e = \sum_i -\frac{\hbar^2}{2m_e}\nabla_i^2 + \frac{1}{2}\sum_i\sum_{j\neq i}\frac{e^2}{4\pi\varepsilon_0\,|\mathbf{r}_i-\mathbf{r}_j|} - \sum_i\sum_\ell \frac{Z_\ell\, e}{4\pi\varepsilon_0\,|\mathbf{r}_i-\mathbf{R}_{\ell_0}|} \tag{2.4}$$

where the indices i, j (ℓ) label the electrons (ions) at position $\mathbf{r}_{i/j}$ (equilibrium position $\mathbf{R}_{\ell_0}$), e is the electronic charge, Z_ℓ is the charge of the ion core and m_e the electron mass. The three terms in the above Hamiltonian physically represent the kinetic energy of the electrons, electron-electron and electron-ion interactions.

2.1.1 Simplified band structure approximations

The simplified electronic Hamiltonian, Eqn. 2.4, remains analytically intractable. In particular, the electron-electron interactions cause a correlation of the electronic motion, preventing the separation of the N-body problem into N one-electron problems. The following further simplifications of the many-electron Schrödinger equation are therefore often employed:

- *one-electron approximation*, where the electron-electron interaction is assumed to contribute a constant repulsive component to the Hamiltonian resulting from the averaged electron-electron interaction, and any deviations from this are regarded as small and neglected;
- *mean-field approximation*, where each electron is assumed to be in identical surroundings dependent on the interaction with the ions in their equilibrium position.

Thus, the electronic band structure can be approximated from a solution of the Schrödinger equation with the simplified Hamiltonian

$$\mathcal{H} = \frac{\mathbf{p}^2}{2m_e} + V_0(\mathbf{r}) \tag{2.5}$$

where $V_0(\mathbf{r})$ represents the periodic potential of the Bravais lattice. Invoking the translational symmetry of the lattice, it can be shown (see, for example, Ref. [56])

that the solutions to Eqn. 2.5 are Bloch wavefunctions

$$\psi_{\nu\mathbf{k}}(\mathbf{r}) = u_{\nu\mathbf{k}}(\mathbf{r}) \exp(i\mathbf{k} \cdot \mathbf{r}) \tag{2.6}$$

where ν labels the band, $\mathbf{k}$ is the wavevector of the electron in the first Brillouin zone and the Bloch wavefunction $u_{\nu\mathbf{k}}(\mathbf{r})$ has the full translational symmetry of the lattice

$$u_{\nu\mathbf{k}}(\mathbf{r} + \mathbf{T}) = u_{\nu\mathbf{k}}(\mathbf{r}) \tag{2.7}$$

where $\mathbf{T}$ is a primitive translation vector.

Parabolic approximation

Solution of the Schrödinger equation with the Hamiltonian given in Eqn. 2.5 is still, however, non-trivial. A simple approximation is to consider the electron or hole energy dispersion only close to the centre of the Brillouin zone (the Γ-point) where the extrema of the conduction and valence bands are located for most semiconductors [57]. Expanding the dispersion relations about the Γ-point as a Taylor series, it follows that they can be approximated by parabolic functions sufficiently close to the zone centre. By analogy with the free electron case, the dispersion relations for electrons or holes can be denoted

$$E_{e,h}(\mathbf{k}) = E_{e,h}(0) \pm \frac{\hbar^2 \mathbf{k}^2}{2m^*} \tag{2.8}$$

where m^* is an effective electron or hole mass and $E_{e,h}(0)$ defines the zero of the energy scale. The semiconductor band gap $E_g = E_e(0) - E_h(0)$.

As the electronic properties of a semiconductor are largely determined by the few states (electrons and holes) close to the Γ-point, this approximation holds well in non-degenerate wide band gap materials, where the interaction between the conduction and valence bands is small. However, in certain cases, such as for narrow band gap materials or where there is a large occupation of the conduction band, the interaction between the conduction and valence bands cannot be neglected and Eqn. 2.8 is no longer an appropriate approximation.

$\mathbf{k}\cdot\mathbf{p}$ perturbation theory

A more accurate method of band structure calculation is the $\mathbf{k}\cdot\mathbf{p}$ perturbation method of Kane [58]. Utilising the momentum operator (Eqn. 2.3) and the Bloch theorem, the one-electron Schrödinger equation can be written

$$\left[\mathcal{H}_0 + \frac{\hbar}{m}\mathbf{k}\cdot\mathbf{p} + V_{so} + V_{cr}\right] u_{\nu\mathbf{k}}(\mathbf{r}) = \tilde{E}_{\nu\mathbf{k}}(\mathbf{r}) u_{\nu\mathbf{k}}(\mathbf{r}) \tag{2.9}$$

where $\mathcal{H}_0 = \frac{\mathbf{p}^2}{2m} + V_0(\mathbf{r})$, $\tilde{E}_{\nu\mathbf{k}} = E_\nu(\mathbf{k}) - \frac{\hbar^2 k^2}{2m}$ and where magnetic effects have been included through V_{so} and V_{cr}, the spin-orbit and crystal-field potentials, respectively. At the Γ-point ($\mathbf{k} = (0,0,0)$), Eqn. 2.9 reduces to

$$\left[\mathcal{H}_0 + V_{so} + V_{cr}\right] u_{\nu\mathbf{0}}(\mathbf{r}) = E_{\nu\mathbf{0}}(\mathbf{r}) u_{\nu\mathbf{0}}(\mathbf{r}) \tag{2.10}$$

whose solutions form a complete orthonormal set. Thus, the energy eigenvalues and wavefunctions at any value of $\mathbf{k}$ close to the Γ-point can be expressed by treating the $\mathbf{k}\cdot\mathbf{p}$ interaction between the valence and conduction bands (and indeed the effects of higher lying bands) as perturbations.

In the original theory of Kane [58] for zinc-blende structures, the Hamiltonian describing the interaction of the (doubly degenerate) conduction and top three valence bands is given by

$$\mathcal{H} = \begin{pmatrix} \tilde{\mathcal{H}} & 0 \\ 0 & \tilde{\mathcal{H}} \end{pmatrix} \tag{2.11a}$$

where

$$\tilde{\mathcal{H}} = \begin{pmatrix} E_s & 0 & kP & 0 \\ 0 & E_p - \Delta_{so}/3 & \sqrt{2}\Delta_{so}/3 & 0 \\ kP & \sqrt{2}\Delta_{so}/3 & E_p & 0 \\ 0 & 0 & 0 & E_p + \Delta_{so}/3 \end{pmatrix} \tag{2.11b}$$

where E_s and E_p are the eigenvalues of the Hamiltonian at the Γ-point (Eqn. 2.10), Δ_{so} is the spin-orbit splitting of the valence band and P is the optical momentum matrix element

$$P = -i\left(\frac{\hbar}{m_e}\right)\langle S|\, p_z\, |Z\rangle \tag{2.12}$$

where $|S\rangle$ and $|Z\rangle$ are the s-like and p_z-like wavefunctions, having the symmetry properties of atomic s and p_z orbitals respectively. The material is assumed to be

isotropic, and have negligible crystal field splitting, which is a good approximation for all materials considered in this work.

The conduction band dispersion is described by

$$E_c(k) = E' + E_k \tag{2.13}$$

where

$$E_k = \frac{\hbar^2 k^2}{2m_0} \tag{2.14}$$

where m_0 is the free electron mass, and E' is the largest eigenvalue of the Hamiltonian (Eqn. 2.11), given by the largest solution of the algebraic equation

$$E'(E' + E_g)(E' + E_g + \Delta_{so}) - k^2P^2(E' + E_g + 2\Delta_{so}/3) = 0. \tag{2.15}$$

$E_s = 0$ and $E_p = -E_g - \Delta_{so}/3$ have been used here, defining the zero of energy at the conduction band minimum (CBM). Kane's matrix element (Eqn. 2.12) is given by

$$P^2 = \frac{3\hbar^2(1/m_0^* - 1/m_0)}{2[2/E_g + 1/(E_g + \Delta_{so})]} \tag{2.16}$$

where m_0^* is the conduction band-edge effective mass.

A useful simplifying approximation, applicable for the materials considered in this work as $\Delta_{so} \ll E_g$, is to neglect the spin-orbit splitting. In this case, solving Eqn. 2.15 gives the '2-band' $\mathbf{k} \cdot \mathbf{p}$ analytic form of the conduction band dispersion

$$E_c(k) = \frac{1}{2}\left[-E_g + \sqrt{E_g^2 + 4k^2P^2}\right] + E_k, \tag{2.17}$$

Kane's matrix element simplifies to

$$P^2 = \frac{\hbar^2}{2m_0}\left(\frac{m_0}{m_0^*} - 1\right)E_g, \tag{2.18}$$

the density of conduction band states is given by

$$\begin{aligned} g_c(k) &= \frac{k^2}{\pi^2}\left[\frac{\mathrm{d}E_c(k)}{\mathrm{d}k}\right]^{-1} \\ &= \frac{k/\pi^2}{2P^2\left[E_g^2 + 4k^2P^2\right]^{-1/2} + (\hbar^2/m_0)}, \end{aligned} \tag{2.19}$$

and the electron effective mass becomes energy dependent

$$\begin{aligned} m^*(E) &= \hbar^2 k\left[\frac{\mathrm{d}E_c(k)}{\mathrm{d}k}\right]^{-1} \\ &= \frac{\hbar^2}{2P^2\left[E_g^2 + 4k^2P^2\right]^{-1/2} + (\hbar^2/m_0)}. \end{aligned} \tag{2.20}$$

The electron density

$$n = \int_0^\infty \mathrm{d}E\, f(E) g_c(E) \tag{2.21}$$

where the Fermi-Dirac distribution function

$$f(E) = \frac{1}{1 + \exp\left[\beta(E - \mu)\right]} \tag{2.22}$$

where $\beta = \frac{1}{k_B T}$ and μ is the chemical potential (equal to the Fermi energy at zero temperature).

2.1.2 Density functional theory

In some cases, however, such band structure approximations are not sufficient. For example, knowledge of the electronic structure across the Brillouin zone, rather than just at the zone centre, may be required. Alternative calculation methods are therefore necessary. Density functional theory (DFT) is one widely used method.

In this, the electron density, which is a functional of the many-body wavefunction

$$n(\mathbf{r}) = \langle \Psi(\mathbf{r}) | \, \Psi(\mathbf{r}) \rangle \,, \tag{2.23}$$

is treated as the central variable, rather than the many-body wavefunction itself. Hohenberg and Kohn [59] showed that, for N interacting electrons in an external potential, V_{ext}, the external potential, and hence the Hamiltonian and the eigenstate energy is a unique functional of the electron density [59]

$$E[n] = F[n] + \int \mathrm{d}\mathbf{r}\, n(\mathbf{r}) V_{ext}(\mathbf{r}), \tag{2.24}$$

where $F[n]$ is a universal functional valid for any number of particles and any external potential. The ground state energy is obtained by minimizing the functional, corresponding to the ground state electron density, $E_0[n_0]$.

Kohn and Sham [60] (KS) separated the functional $F[n]$ into three parts to account for the kinetic energy of a non-interacting electron gas, and the Hartree (Coulomb) and exchange-correlation (XC) effects of the electron-electron interaction. They showed that the ground state energy could be obtained by solving N one-electron Schrödinger-like equations, self-consistently with the charge density.

The Hamiltonian of the one-electron equations is of the form given in Eqn. 2.5 but with the potential replaced by an effective KS potential including Hartree and XC parts. Therefore, while the individual solutions do not include inter-particle interactions (one-electron approximation), the KS particles do interact indirectly via the density dependence of the Hartree and XC parts of the potential within a mean-field approximation.

The theory discussed above is exact. However, the functional for XC is not known for all but a few simple situations (such as a homogeneous free-electron gas). A common approximation, the local density approximation (LDA), is therefore to approximate this functional by the energy of an electron in a uniform electron gas of the same density. Another approach, the generalized gradient approximation (GGA), also includes the gradient of the density in the calculation. Various more advanced approximations for the XC functional have subsequently been developed, but these are beyond the scope of the current discussion. However, the eigenvalues resulting from solution of the DFT equations are not the quasiparticle energies relevant for discussing the electronic structure of solids. In fact, the DFT-formalism, within the LDA and GGA approximations, is known to severely underestimate the fundamental band gap of many semiconductors, in some cases even leading to an absence of a fundamental gap. Hybertsen and Louie [61] showed that including quasiparticle (QP) corrections for the electron self-energy based on dressed Green's functions and a screened Coulomb interaction (GW) is a suitable method with which to overcome this band gap problem.

The DFT calculations utilised in this work were performed elsewhere by Dr. Frank Fuchs, Mr. André Schleife, Prof. Dr. Friedhelm Bechstedt, and Dr. Jürgen Furthmüller (Friedrich-Schiller-Universität, Jena, Germany), using a hybrid functional HSE03 for exchange and correlation [62]. The electron-ion interaction was treated in the framework of the projector-augmented wave method [63]. In this method, a plane-wave basis set is used to represent the wavefunctions, while close to the ion cores, a radial representation employing pseudopotentials is adopted. Within the pseudopotential approximation, valence electrons are considered to be

moving in a pseudopotential formed by the nuclei potential partially screened by the core electrons. In materials with shallow semi-core-levels, such as In or Cd $4d$ electrons, care must be taken to include the effects of these electrons on the valence band states [64]. Consequently, these were included as valence states in the calculations. QP effects were included in the calculations by a perturbative G_0W_0 correction of the HSE eigenvalues. As the HSE eigenvalues generally show much better agreement with experimental band structure than the LDA or GGA calculations (for example, the ordering of the bands is correct, even if their separation is not), first-order perturbation theory is generally applicable to include QP effects, allowing only G_0W_0 rather than full GW QP corrections. Full details of the quasiparticle-corrected density-functional theory (QPC-DFT) calculations utilised in this work are reported elsewhere [65].

2.2 Space-charge calculations

2.2.1 Poisson's equation

The spatial dependence of band bending in the space-charge region at a semiconductor surface (see Fig. 1.4) can be described by a potential, $V(z)$, which must satisfy Poisson's equation [12]

$$\frac{\mathrm{d}^2V}{\mathrm{d}z^2} = -\frac{e}{\varepsilon(0)\,\varepsilon_0}\left[N_D^+ - N_A^- - n(z) + p(z)\right] \tag{2.25}$$

where $\varepsilon(0)$ is the static dielectric constant, N_D^+ $[N_A^-]$ is the bulk ionized donor [acceptor] density, assumed constant throughout the sample, $n(z)$ $[p(z)]$ is the electron [hole] density, and z is the depth below the surface. The potential $V(z)$ satisfies the boundary conditions

$$V(z) \to 0 \;\text{ as }\; z \to \infty \tag{2.26a}$$

as there can be no band bending in the bulk of the semiconductor and

$$\left.\frac{\mathrm{d}V}{\mathrm{d}z}\right|_{z=0} = \frac{e}{\varepsilon(0)\,\varepsilon_0}N_{ss} \tag{2.26b}$$

where N_{ss} is the surface state (sheet) density. Alternatively, it is equivalent to consider the total band bending at the surface as a boundary condition.

In order to obtain the potential $V(z)$ and the carrier density, Poisson's equation (Eqn. 2.25) should be solved self-consistently with the one-electron Schrödinger equation (Eqns. 2.1 and 2.5). This is, however, non-trivial (especially for non-parabolic semiconductors) as the carrier concentrations in Eqn. 2.25 are themselves dependent on the potential via solution of the Schrödinger equation. Thus, the problem becomes highly non-linear.

2.2.2 Modified Thomas-Fermi approximation

A simplified approach is to use a modified Thomas-Fermi approximation (MTFA) [66], where the potential is calculated by solving the Poisson equation subject to the boundary conditions (Eqn. 2.26) with the carrier densities corresponding to the conduction and i^{th} valence bands calculated, respectively, from

$$n(z) = \int_0^{\infty} \mathrm{d}E\, g_c(E) f'(E) f_{MTFA}(z) \tag{2.27a}$$

$$p_i(z) = \int_{E_{V_i}}^{-\infty} \mathrm{d}E\, g_{v_i}(E) f'(E) f_{MTFA}(z) \tag{2.27b}$$

where $g(E)$ is the density of states, $f'(E)$ is the Fermi-Dirac function including the potential dependence

$$f'(E) = \frac{1}{1 + \exp[\beta(E - \mu + V(z))]}, \tag{2.28}$$

and the MTFA factor

$$f_{MTFA}(z) = 1 - \mathrm{sinc}\left[\frac{2z}{L}\left(\frac{E}{k_B T}\right)^{\frac{1}{2}}\left(1 + \frac{E}{E_g}\right)^{\frac{1}{2}}\right] \tag{2.29}$$

where, for non-degenerate semiconductors, L is the thermal length $L = \hbar/(2m_0^* k_B T)^{1/2}$ whereas for degenerate semiconductors, $L = \frac{1}{k_F}$ is the Fermi length. Physically, this correction factor $f_{MTFA}(z)$ represents the interference of incident and reflected wavefunctions due to the potential barrier at the surface and thus causes the carrier concentration to tend smoothly to zero right at the surface. The integral limit E_{V_i} in Eqn. 2.27b denotes the VBM of the i^{th} valence band allowing for spin-orbit and crystal-field splittings. The MTFA correction has been shown [66] to yield profiles that are in good agreement with those obtained from full self-consistent Poisson-Schrödinger calculations (see also Section 9.3.1).

The MTFA outlined here allows the important effect of the non-parabolicity (especially of the conduction band) on the density of states to be easily incorporated. Numerical solution of Eqns. 2.25 and 2.27 using a trial potential $V(z)$ and an interval bisection method is used here to converge to a solution of the band bending potential and the carrier concentration profiles as a function of depth. Note that, for accumulation and depletion layers, the minority carrier concentration can, without loss of information, be assumed to be zero in the calculations.

Chapter 3

Experimental techniques

Throughout this thesis, the techniques of photoemission spectroscopy, optical absorption spectroscopy, infrared reflectivity and the single-field Hall effect are used extensively. This chapter presents an introduction to both the theoretical background of these techniques, and also experimental and technical details about the specific instruments used in this work.

3.1 Photoemission spectroscopy

Photoemission spectroscopy (PES) relies on the photoelectric effect, first discovered by Hertz in 1887 [67] and explained by Einstein in 1905 [68], whereby an electron is emitted from a solid upon light-matter interaction. Stimulated largely by the work of Siegbahn [69], PES has been developed into one of the most important techniques for studying electronic and also chemical properties of solids. As such, it is one of the central techniques used in this work.

At its simplest, PES, shown schematically in Fig. 3.1, involves illuminating a sample with a flux of photons of energy $h\nu$ from an x-ray tube, gas discharge tube or a synchrotron radiation source. Photoelectrons are then emitted from both the core and valence levels of the solid via the photoelectric effect in some direction and with some kinetic energy

$$E_k = h\nu - \phi - E_B \tag{3.1}$$

where ϕ is the spectrometer work function, assuming the sample and spectrometer share the same ground, and E_B is the binding energy of the electron. The binding energy is given by the difference in total energy of the final $N-1$ electron state following ejection of the photoelectron and the initial N electron ground state of the system,

$$E_B = E_{f,tot}(N-1) - E_{i,tot}(N), \tag{3.2}$$

as will be discussed more rigorously below. Both the kinetic energy and emission (polar, θ, and azimuthal, ϕ) angles of the photoelectron can be detected, giving

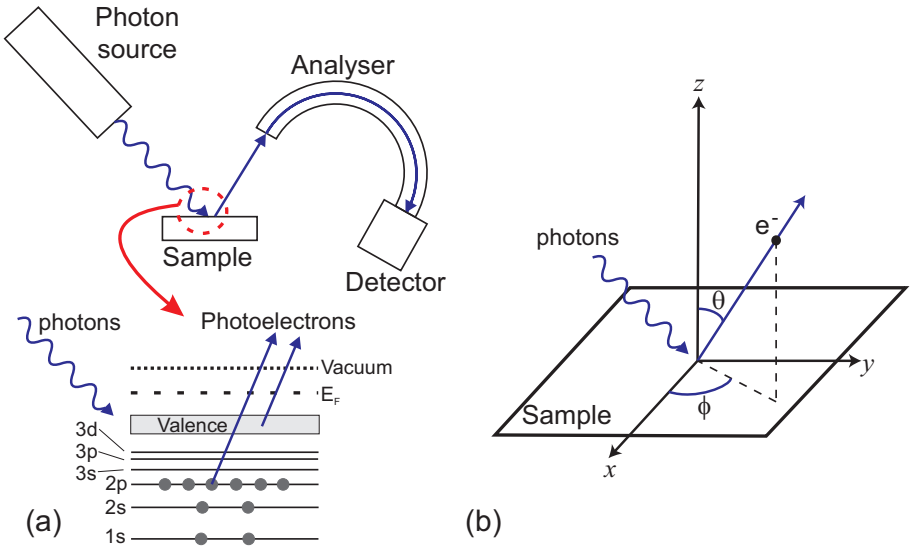

Figure 3.1: Schematic representation of PES showing (a) photoemission from core and valence states and (b) the angle of photoelectron emission referenced to the sample coordinate system.

information of both the binding energy and momentum of the electronic states within the solid.

3.1.1 Three-step model

The photoemission process can be considered using the so-called three-step model of Berglund and Spicer [70], consisting of: (i) the photo-excitation of an electron; (ii) its passage to the surface of the solid; and (iii) its penetration through the surface into the vacuum. The discussion here is based upon that of Hüfner [71].

In the first step, using Fermi's golden rule to give the transition probability between an initial state, $|i\rangle$, and final state, $|f\rangle$, the energy distribution of photoexcited electrons, $N(E)$, can be obtained as

$$N(E) \propto \sum_{f,i} |M_{fi}|^2 \, \delta\left(E_f - E_i - h\nu\right) \delta\left(E - (E_f - \phi)\right) \delta\left(\mathbf{k}_i + \mathbf{G} - \mathbf{k}_f\right). \tag{3.3}$$

In the presence of electromagnetic radiation, the Hamiltonian of the system [55]

$$\begin{aligned} \mathcal{H} &= \frac{1}{2m_e}\left[\mathbf{p} + \left(\frac{e\mathbf{A}}{c}\right)\right]^2 + V(\mathbf{r}) \\ &\approx \mathcal{H}_0 + \frac{e}{m_e c}\mathbf{A}\cdot\mathbf{p} \end{aligned} \tag{3.4}$$

where $\mathcal{H}_0 = \frac{\mathbf{p}^2}{2m_e} + V(\mathbf{r})$, $\mathbf{p}$ is the momentum operator, $\mathbf{A}$ is the vector potential, the Coulomb gauge has been used so that both the scalar potential and $\nabla \cdot \mathbf{A}$ are zero,

and terms $\mathcal{O}(A^2)$ have been neglected. Consequently, the transition matrix element

$$M_{fi} \propto \langle f | \mathbf{A} \cdot \mathbf{p} | i \rangle \propto \langle f | (\mathbf{E} \cdot \mathbf{r}) | i \rangle \tag{3.5}$$

where the final expression corresponds to the electric dipole approximation, appropriate if the photon wavevector is small. The first delta function in Eqn. 3.3 ensures conservation of energy during the excitation of the photoelectron, while the second ensures that the kinetic energy of the photoelectron in the vacuum is that of the final state inside the crystal minus the work function [71]. The third delta function ensures conservation of momentum, up to a reciprocal lattice vector.

The second step considers the transport of the excited photoelectrons to the surface of the solid, during which time the photoelectrons can be inelastically scattered, predominantly by other electrons, but also by phonons or ionized impurities. Such inelastic scattering events cause the photoelectrons to be emitted from the solid with a lower energy than would be expected from their initial state, and these therefore contribute to the background of photoemission spectra.

The total intensity of photoelectrons emitted from a distance d below the surface that have not been inelastically scattered by the time that they arrive at the surface follows the Beer-Lambert law

$$I(E) = I_0(E) e^{-d/\lambda \sin\theta} \tag{3.6}$$

where $I_0(E)$ is the initial intensity of photoemitted electrons of energy E, θ is the polar angle that the detector makes to the surface, so that $d/\sin\theta$ is the effective path length to the surface, and λ is the inelastic mean free path (IMFP) of the electrons. Consequently, PES is a surface specific technique with, in a normal emission geometry, 65% of the photoemission signal originating from within λ of the surface and 95% from within 3λ of the surface, with the majority of the signal originating from photoelectrons generated closest to the surface. The IMFP can be estimated for specific materials from semi-empirical means such as the TPP-2M predictive formula of Tanuma *et al.* [72]. However, Seah and Dench [73] showed that the IMFP for a very large number of elements and compounds all fit approximately on a 'universal curve' which shows a pronounced minimum in IMFP of $\lambda \approx 5$ Å for electron kinetic

energies of $\sim 30 - 70$ eV, with a marked increase towards both lower and higher kinetic energies. Consequently, PES measurements made in this energy range are the most surface sensitive.

A characteristic of the inelastic scattering events is a stepped background, with an increase in background intensity observed to the lower kinetic energy (higher binding energy) side of spectral features [74]. For non-monochromatic sources, photoemission due to Bremsstrahlung radiation can also give rise to a general background, in addition to satellite features due to lower intensity satellite lines of the photon source, although these two features do not need to be considered for monochromatic sources. The background can be accounted for using various methods. However, for most purposes, fitting a Shirley integrated iterative background [75] is sufficient.

The removal of the photoelectron from the solid into the vacuum is described by the final step of the three-step model. Assuming perfect two-dimensional translational symmetry in the plane of the surface, parallel momentum must be conserved in this step, up to a parallel reciprocal lattice vector, $\mathbf{G}_{\parallel}$, and so the momentum of the final electron in vacuum, $\mathbf{p}$, satisfies

$$\frac{\mathbf{p}_{\parallel}}{\hbar} = \mathbf{k}_{i,\parallel} + \mathbf{G}_{\parallel}. \tag{3.7}$$

Assuming a free electron dispersion of the final state bands, the parallel wavevector of the initial state can therefore be determined

$$\begin{aligned} k_{i,\parallel} &= k_{f,\parallel} \\ &= \left| sin(\theta)\left(\cos(\phi)\hat{\mathbf{x}} + \sin(\phi)\hat{\mathbf{y}}\right)\sqrt{\frac{2m_e E_k}{\hbar^2}} \right| \\ &= \sin(\theta)\sqrt{\frac{2m_e E_k}{\hbar^2}} \end{aligned} \tag{3.8}$$

where the coordinate system is defined in Fig. 3.1(b). This ability to determine the initial state wavevector simply from the angle of the photoemitted electrons is the central concept of angle resolved photoemission spectroscopy (ARPES). However, the wavevector is not simply conserved normal to the surface. Consequently, ARPES is most effective for looking at electronic features characteristic of two-dimensional

solids, such as surface states on metals or semiconductors. However, by applying various approximations, such as free-electron final state bands and a step function for the surface potential, it is possible to obtain information on the perpendicular momentum, allowing, for example, bulk band mapping of semiconductors [71, 76].

Including all steps of the three-step model, the total photocurrent, $\mathcal{I}(E, \mathbf{p}_\parallel)$, therefore becomes

$$\begin{aligned}\mathcal{I}(E, \mathbf{p}_\parallel) \quad \propto \quad & \sum_{f,i} |M_{fi}|^2 \, \delta\left(E_f - E_i - h\nu\right) \delta\left(E - (E_f - \phi)\right) \delta\left(\mathbf{k}_i + \mathbf{G} - \mathbf{k}_f\right) \\ & \times D(E) \times |T(E, \mathbf{p}_\parallel)| \, \delta(\mathbf{k}_{i,\parallel} + \mathbf{G}_\parallel - (\mathbf{p}_\parallel/\hbar)), \end{aligned} \tag{3.9}$$

where $D(E)$ accounts for the attenuation of the excited photoelectrons by inelastic scattering (step 2) and $T(E, \mathbf{p}_\parallel)$ is the transmission factor for photoelectrons penetrating the surface (step 3).

Although it has proved remarkably successful in explaining photoemission features, the treatment of each step separately in the three-step model is a simplification. A more accurate picture is the one-step model, where the photon induces an excitation from the initial state directly into a damped final state, which propagates in the vacuum, but decays away into the solid near the surface. In fact, the arguments leading to Eqns. 3.3 to 3.5 are appropriate for a one-step model, provided that the final state wavefunction is taken as the damped state propagating into the vacuum. However, theoretical treatments of this model, such as the inverse LEED formalism, are beyond the scope of this thesis, and the interested reader is referred to Refs. [71, 77].

3.1.2 Sudden approximation and the spectral function

The above has all been considered in a one-electron picture. However, a solid is a complex many-body system, and so the screening and relaxation effects of the other particles must also be considered. In the sudden approximation, where the photoemission process is assumed sufficiently fast that the photoelectron escapes from the solid before the system relaxes, the initial and final states of the N electron system can be written as a product of the states of the photoelectron, ϕ, and those

of the remaining $N-1$ electron system, ψ [78]

$$|i\rangle = |\phi_i\rangle\, a^- |\psi_i(N)\rangle \tag{3.10a}$$

$$|f\rangle = |\phi_f\rangle\, |\psi_{f,s}(N-1)\rangle \tag{3.10b}$$

where a^- is the electron annihilation operator, and the subscript s denotes the s^{th} excited state of the final $N-1$ electron system. Consequently, the transition matrix element (Eqn. 3.5) satisfies

$$|M_{fi}|^2 \propto |\langle\phi_f|\, \mathbf{A}\cdot\mathbf{p}\, |\phi_i\rangle|^2 \sum_s \left|\langle\psi_{f,s}(N-1)|\, a^- |\psi_i(N)\rangle\right|^2 . \tag{3.11}$$

The electronic behaviour of the many-body system is entirely incorporated within the so-called spectral function

$$A(\mathbf{k},E) = \sum_s \left|\langle\psi_{f,s}(N-1)|\, a^- |\psi_i(N)\rangle\right|^2 , \tag{3.12}$$

which has been related to the single-particle Green's function of the system [71]

$$A(\mathbf{k},E) = \frac{1}{\pi}\Im\left\{G(\mathbf{k},E)\right\}. \tag{3.13}$$

For a non-interacting system, $|\psi_f(N-1)\rangle = |\psi_i(N-1)\rangle$, and the spectral function is simply a delta function at $E = E^0_{\mathbf{k}}$ where $E^0_{\mathbf{k}}$ is the one-electron energy of the system. Consequently, the binding energy observed in the photoemission spectrum would be that of the non-interacting system. This is known as the Koopman's energy, although it is never observed in practice. In reality, many-body interactions such as electron-electron, electron-phonon and electron-ion interactions cause a renormalization of the electron energy by the self energy $\Sigma(\mathbf{k},E)$, and it is important to remember that it is this renormalized electronic structure that is observed in PES, which differs from the true ground state of the system by the self energy. The Green's function of the renormalized system,

$$G(\mathbf{k},E) = \frac{1}{E - E^0_{\mathbf{k}} - \Sigma(\mathbf{k},E)}, \tag{3.14}$$

yielding a spectral function

$$A(\mathbf{k},E) = \frac{1}{\pi}\frac{\Im\left\{\Sigma(\mathbf{k},E)\right\}}{\left[E - E^0_{\mathbf{k}} - \Re\left\{\Sigma(\mathbf{k},E)\right\}\right]^2 + \left[\Im\left\{\Sigma(\mathbf{k},E)\right\}\right]^2}. \tag{3.15}$$

The lifetime of the electronic states is therefore given by $\tau = [2\Im\{\Sigma(\mathbf{k}, E)\}]^{-1}$, giving rise to a finite width to the spectral features, $\Gamma \sim \hbar/\tau$. For a weakly interacting system, the Green's function can be recast into a so-called coherent part, which is very similar to the non-interacting system but with a slightly renormalized mass, a so-called quasiparticle, and an incoherent part. These can approximately be considered as the main photoemission line and satellite features occurring at higher binding energy due to screening by plasmons in the material [79], respectively.

3.1.3 Density of states measurements

Instead of detecting photoelectrons at a single angle, or more realistically within a small solid angle, as in ARPES, the photoelectrons can be collected over a large solid angle in an *angle-integrated* mode. At relatively low photon energies, the transitions must still be direct, and so integrating over all wavevectors yields the joint density of states between initial and final states [71]. In reality, the acceptance angle of a spectrometer will be limited, which may restrict the portion of the Brillouin zone sampled in the measurement.

However, if x-ray photons are used, several other factors become important. First, for photoelectrons with high kinetic energies, small angles of emission still correspond to high values of wavevector, and so even for relatively modest acceptance angles, it is possible to sample the entire Brillouin zone. Second, assuming the Debye factor is not too large, the influence of phonon scattering at higher energies can become very significant, meaning that direct transitions are no longer required. It should also be noted that the wavevector of the photon can no longer be considered negligible for x-rays, resulting in the breakdown of the dipole approximation introduced in Eqn. 3.5, and the necessity to include a term for the photon wavevector in the overall wavevector conservation term. Integrating Eqn. 3.9 over $\mathbf{k}_i$ and $\mathbf{k}_f$ independently yields the total photocurrent

$$\mathcal{I}(E) \propto \left|\bar{M}_{fi}\right|^2 N(E_i) N(E_f) D(E) T(E) \tag{3.16}$$

where $N(E_i)$ and $N(E_f)$ denote the initial and final density of states, respectively, and $\bar{M}_{fi}$ is an averaged transition matrix element. To a good approximation, both

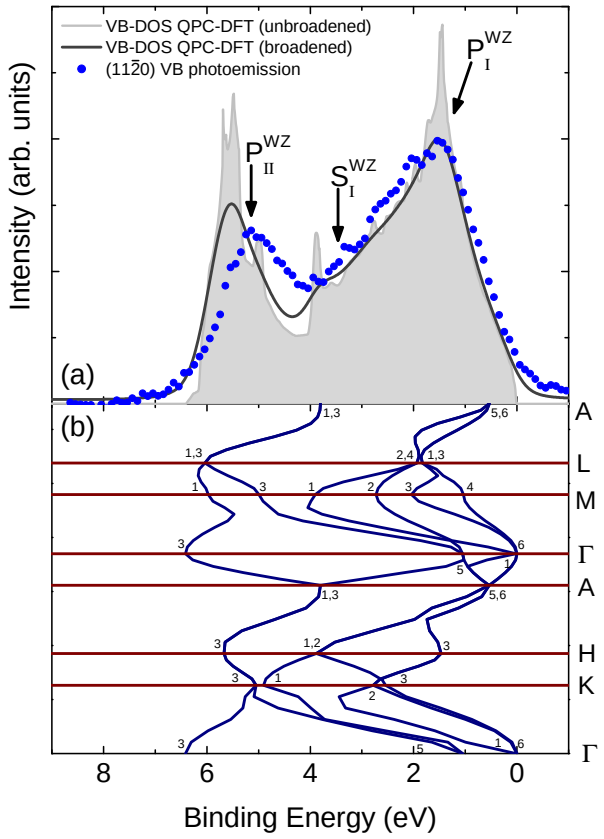

Figure 3.2: Shirley-background-subtracted valence band x-ray photoemission spectrum and QPC-DFT VB-DOS calculations shown without (shaded) and with lifetime and instrumental broadening for wurtzite InN(11$\bar{2}$0). The main features in the VB-DOS are identified, after Ley *et al.* [82]. The measured valence band photoemission is rigidly shifted to lower energies by 1.53 eV to align the VBM at 0 eV binding energy as for the calculations. The XPS and QPC-DFT spectra are normalized to the peak P^{WZ}_{I} intensity. The corresponding QPC-DFT valence band structure for wurtzite InN is shown in (b). High symmetry points are denoted using double group symmetry notation, although the symmetry point label has been dropped for clarity of presentation. Therefore, for example, at the valence band maximum the label 6 denotes Γ_6 symmetry. The XPS spectrum was measured at the National Centre for Electron Spectroscopy and Surface Analysis, Daresbury Laboratory, UK, using a photon energy $h\nu = 1486.6$ eV. For more details, see Ref. [83].

the matrix element and the final density of states, as well as terms due to the second and third steps of the three-step model, can be treated as constant over the range of the measurement, and so valence-band x-ray photoemission spectroscopy (XPS) approximates well the initial density of states of the material. While in rare cases, direct transition effects can be observed in XPS measurements [80], these can normally be neglected, at least at room temperature and above. Indeed, Shirley [75] found excellent agreement between broadened valence band density of states (VB-DOS) calculations and valence band XPS measurements from gold, while Pollak *et al.* [81] and Ley *et al.* [82] showed that this holds for a range of group IV, III-V and II-VI semiconductors. Subsequent investigations have also shown excellent agreement between theoretical calculations and XPS measurements for the VB-DOS of many other materials. An example of this, for the case of InN, is shown in Fig. 3.2 [83].

The energy reference is generally taken to be the Fermi level in a PES measurement. It should be noted that, in a semiconductor where space-charge regions can exist, the reference Fermi level is that at the surface due to the surface speci-

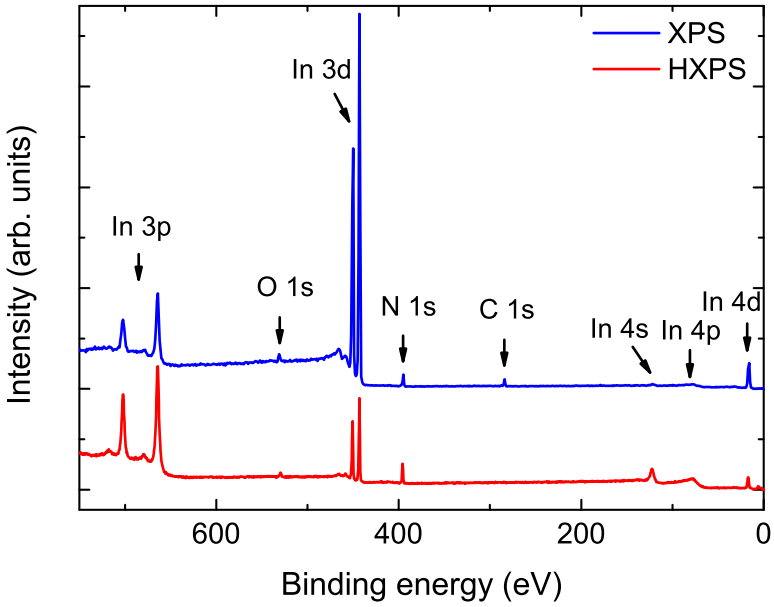

Figure 3.3: XPS ($h\nu = 1486.6$ eV) and HXPS ($h\nu = 7600$ eV) wide energy scans from InN($11\bar{2}0$), performed at the National Centre for Electron Spectroscopy and Surface Analysis, Daresbury Laboratory, UK, and beamline ID16, European Synchrotron Research Facility, Grenoble, France, respectively. The positions of several core-level peaks are shown. The Fermi level is defined as the zero of the binding energy scale, and the spectra are vertically offset for clarity.

ficity of the technique. Consequently, by either extrapolating the leading edge of the valence band photoemission to the background level, or by aligning it with VB-DOS calculations, the surface Fermi level of a semiconductor can be determined. This will be used extensively in this work. While XPS is not as surface sensitive as PES performed with lower photon energies, it is still dominated by the signal from the surface. Additionally, interpretation of valence band photoemission spectra obtained using lower photon energies is complicated by final state effects and also the presence of surface states. Consequently, XPS measurements are perhaps the most suitable for determining the surface Fermi level position in semiconductors.

3.1.4 Core-levels

At higher binding energies, PES can be used to investigate the core levels of a material, provided a high enough photon energy is utilized. XPS measurements performed over a large energy range from an 'as-loaded' InN($11\bar{2}0$) sample are shown in Fig. 3.3, utilizing monochromated Al-K_α radiation ($h\nu = 1486.6$ eV) and hard x-rays (HXPS, $h\nu = 7600$ eV). A series of peaks due to different elemental core-

levels are observed, separated due to their different binding energies, sitting on a stepped background due to inelastic scattering, as discussed above. The core-level peaks are labelled by their element and orbital angular momentum quantum number ($\ell = s, p, d, f, \ldots$). A number of points deserve further comment.

The s-levels are characterised by a single peak, whereas core-levels for which $\ell \neq 0$ exhibit a doublet structure due to spin-orbit coupling. The orbit of a charged electron around a nucleus induces a magnetic field, which can couple with the spin moment of the electron, $\hat{\mathbf{s}}$. As the final state of the atom is singly ionized in photoemission, the j–j coupling scheme is appropriate for use, where $\hat{\mathbf{j}}$ is the total angular momentum, $\hat{\mathbf{j}} = \hat{\boldsymbol{\ell}} + \hat{\mathbf{s}}$. For the s state, $\ell = 0$ and the only source of angular momentum is the spin moment. Consequently, $j(\ell = 0) = \frac{1}{2}$ as the electron is a spin-$\frac{1}{2}$ particle. In contrast, for all other orbital angular momenta, $j = \ell \pm \frac{1}{2}$. This spin-orbit coupling causes a shift of the energy level by an amount

$$\Delta E_{so} \propto \xi(n\ell)\left[j(j+1) - \ell(\ell+1) - s(s+1)\right] \tag{3.17}$$

where $\xi(n\ell)$ is the spin-orbit coupling constant [84]. Consequently, doublets are observed in the core-level spectra, for example $p_{\frac{3}{2},\frac{1}{2}}$ or $d_{\frac{5}{2},\frac{3}{2}}$ levels, with the lower j level occurring at higher binding energy. The intensity ratio of the spin-orbit split components, after accounting for the background intensity, must be equal to the ratio of their relative degeneracies, $(2j+1)$ [74], namely 1:2 for a $p_{3/2}:p_{1/2}$-level, 3:2 for a $d_{5/2}:d_{3/2}$ level, and so on.

The photoionization cross-sections are determined by the matrix elements discussed above (Eqn. 3.5), and so will clearly vary significantly with atomic number and core level via changes in the initial state wavefunction. However, it is also clear from Fig. 3.3 that the relative ratio between the different core-levels shows a marked dependence on photon energy. This can be understood by a change in the coupling between the initial and final state wavefunctions with changes in the wavelength of the free electron final states, although a detailed discussion of this is beyond the scope of this thesis. Cross-sections can be calculated assuming one-electron wavefunctions, and in practice their effect on measured spectra can be incorporated using tabulated sensitivity factors, making quantitative analysis possible. As dis-

cussed above, the Lorentzian linewidth of core-levels arises due to the many-body interactions of the solid, although these must be convolved with a, typically Gaussian, instrumental response function to account for instrumental broadening effects such as a natural linewidth of the photon beam and a finite resolution of the electron analyser, to give the measured spectral linewidth. Consequently, XPS core-levels tend to have Voigt (mixed Lorentzian-Gaussian) lineshapes. In general, the width of an inner core-level such as a $1s$ level will be larger than for an outer core-level, reflecting the fact that an inner core-hole can be filled more rapidly.

A very useful feature of XPS core-levels for chemical analysis is that their binding energy is sensitive to the exact local environment of the atom, as a change in the valence charge of an atom changes the potential in which the core-level electrons reside. For example, if an atom is bonded to another more electronegative one, the valence charge of the original atom is effectively reduced, causing the core-level electron to become more deeply bound. In contrast, if bonded to a less electronegative species, the atom in question will effectively become more negatively charged, and the core-level electron will become less tightly bound. Consequently, when bonded to a more (less) electronegative element, the emitted photoelectron exhibits a chemical shift to higher (lower) binding energy. While this picture is complicated by many-body interactions, it proves a useful guide. In particular, due to the surface specificity of XPS, chemical shifts provide a very useful way to probe the chemical nature of the surface of materials.

3.1.5 XPS measurements – Scienta ESCA-300 spectrometer

High-resolution XPS measurements were performed using a Scienta ESCA300 spectrometer at the National Centre for Electron Spectroscopy and Surface analysis, Daresbury Laboratory, UK. The spectrometer consists of a high intensity rotating anode Al-K_α x-ray source, a 7-crystal monochromator, a 300 mm mean radius hemispherical electron energy analyser, and a multi-channel CCD detection system, as shown schematically in Fig. 3.4. The main features of the system are summarised in this section. More details about the spectrometer and its performance can be found

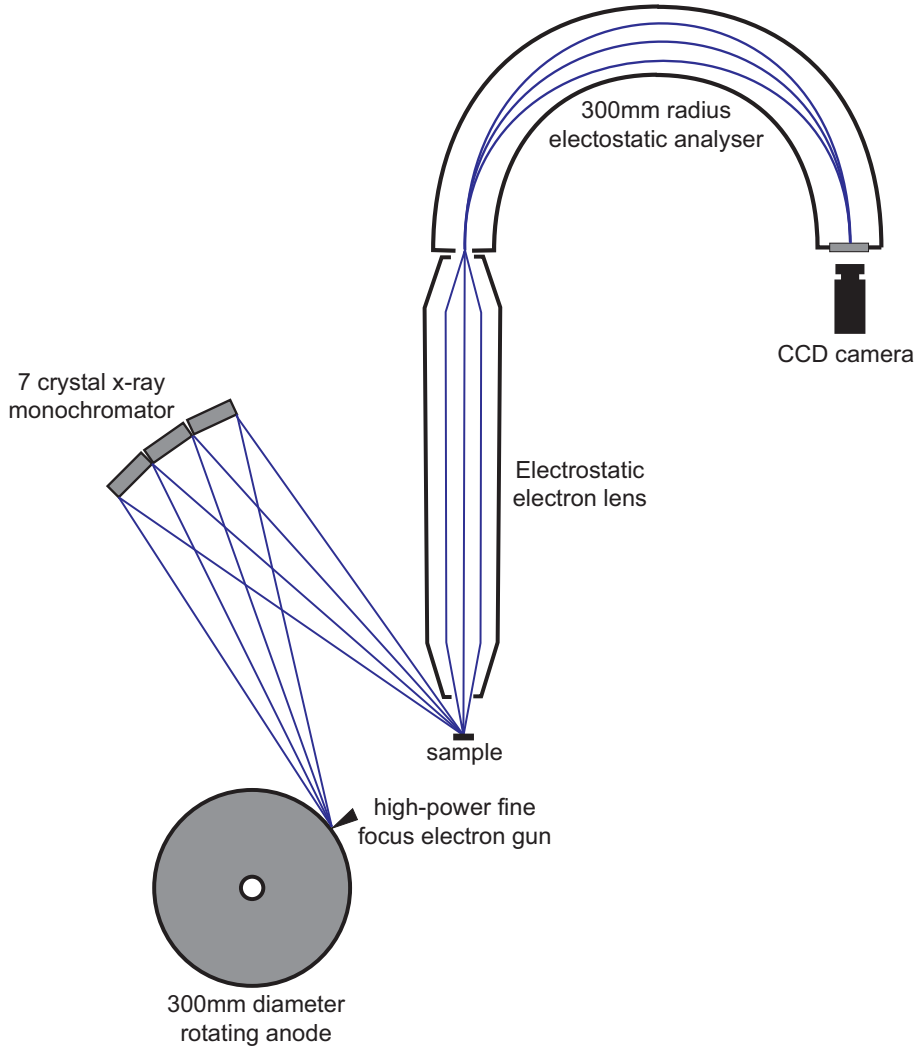

Figure 3.4: Schematic of the Scienta ESCA-300 spectrometer, adapted from Ref. [85].

in Refs. [85, 86].

The rotating anode x-ray source consists of an electron gun focussed on an Al band around the edge of a water-cooled titanium alloy disc, which rotates at $\sim$10000 revolutions per minute. The emitted x-rays (predominantly Al-K_α, $h\nu = 1486.6$ eV) pass into the monochromator chamber through a thin beryllium window which prevents any secondary high-energy electrons from reaching the monochromator crystals. Bremsstrahlung radiation and satellite x-ray lines are removed by monochromation using the $(10\bar{1}0)$ plane of seven α-quartz crystals, arranged on a Rowland circle of 650 mm diameter. A combination of the finite width of the electron beam on

the anode and the diffraction width of the α-quartz crystals yields a total linewidth of the x-ray source of ~ 0.26 eV [86]. The whole monochromator chamber is temperature stabilized by a quartz lamp to prevent changes in the lattice spacing of the monochromator crystals in order to maintain a constant photon energy. The monochromator chamber is separated from the analysis chamber by a thin Al window in order to maintain a good vacuum in the analysis chamber and prevent any secondary electrons from the x-ray source impinging on the sample. The sample is mounted on a precision four-axis manipulator. The geometry is arranged so that the emission angle to the analyser can be varied from normal to grazing angles, while still maintaining x-ray illumination of the sample. The footprint of the x-ray spot on the sample is $\sim 4 \times 0.5$ mm^2.

If a sample is insulating, the emission of photoelectrons leaves the surface of the sample positively charged, which can both shift and distort the XPS peaks, making analysis impossible. To neutralise this charge, the sample can be irradiated with low energy electrons simultaneously to the photon illumination, correcting the spectral distortion and much of the peak shifts, although care must be taken with the exact energy referencing of the spectra [87]. A low energy (up to 9 eV) electron flood gun is incorporated into the analysis chamber, allowing such charge compensation to be performed. Note, many of the samples investigated here are conducting but were grown on insulating substrates. For these samples, an electrical contact was made to the top of the sample to ensure that it was properly grounded.

Emitted photoelectrons are collected by a five-element electrostatic electron lens and focussed onto the entrance slit of a 300 mm mean radius, 100 mm inner electrode gap, hemispherical electron energy analyser. The analyser can be operated with a pass energy of 20 to 1000 eV, with eight different slit widths from 0.2 mm to 4 mm. All spectra presented in this work were recorded with 0.8 mm slits at a pass energy of 150 eV, giving a good compromise between resolution and count rates. During each set of experiments, the Fermi edge of an ion-bombarded silver reference sample was measured. This was fitted by a Gaussian-broadened Fermi function, from which the Fermi level position and instrumental resolution were calibrated.

The instrumental resolution determined in this way was 0.40 ± 0.05 eV, derived from the convolution of the analyser broadening and the natural linewidth of the x-ray source.

The multichannel electron detector contains two 40 mm diameter microchannel plates, of which the electron cascade from the second plate is incident on a phosphor screen, imaged by a CCD camera. The position on the CCD array is then converted into energy and the total counts accumulated by a computer.

Samples are mounted on stubs, and transferred using wobble sticks and rack and pinion railway transfer systems. Samples are introduced into the system via a fast entry load lock, pumped by a turbomolecular pump to a base pressure of $\sim 10^{-6}$ mbar. There is also a preparation chamber, where samples can be annealed by radiative heating or electron-beam heating. The temperature is calibrated by a thermocouple spot-welded close to the sample stub position. The preparation chamber also has ports where an ion gun and a thermal gas cracker can be installed for sample preparation. The spectrometer and preparation chambers are all pumped by separate oil diffusion pumps with liquid nitrogen cooled traps. The base pressure of the analyser and analysis chambers is $\sim 5 \times 10^{-10}$ mbar, and the preparation chamber $\sim 1 \times 10^{-9}$ mbar.

3.1.6 ARPES measurements – SGM3 beamline, ASTRID

ARPES measurements were performed on the SGM3 undulator beamline at the Århus STorage Ring In Denmark (ASTRID) synchrotron, Århus, Denmark. ASTRID is a small (40 m circumference), 580 MeV electron storage ring, although it can also be operated in an ion beam mode, with five bending magnet and three undulator beamlines. Electron injection is achieved from a 100 MeV rack-track Microtron, accelerated by eighteen passes through a linac before being extracted at full energy. The storage ring is pumped by a total of 20 ion pumps and 24 sublimation pumps, resulting in a typical pressure of 1×10^{-10} mbar.

The undulator (DanFysik) consists of 30 periods of permanent magnets with a 55 mm period length. The first and third harmonic of the undulator are used to yield

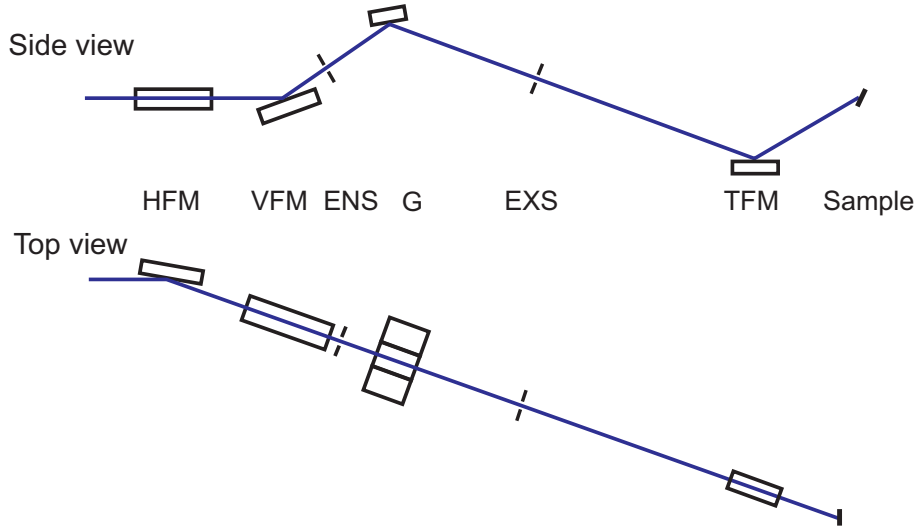

Figure 3.5: Schematic of SGM3 beamline layout, adapted from Ref. [88], showing the horizontal (HFM), vertical (VFM), and toroidal (TFM) focussing mirrors, entrance (ENS) and exit (EXS) slits and the three spherical gratings (G).

photon energies in the range 12–130 eV. The beam from the undulator is reflected from a spherical horizontal focussing mirror and a spherical vertical focussing mirror which focus the beam into an entrance slit. The light is then directed onto one of three spherical grating monochromators: a low-energy grating (10–27 eV), medium-energy grating (22–60 eV) or a high-energy grating (55–130 eV). The beam then passes through an exit slit, which can be moved by 500 mm in order to position the slit in the beam focus over the whole energy range covered by the gratings. Finally, a toroidal mirror re-focusses the beam onto the sample. A schematic of the beamline layout is shown in Fig. 3.5. More details of the beamline construction and specification can be found in Ref. [88].

PES measurements were performed using a Specs PHOIBOS 150 mm mean radius hemispherical energy analyser, which has a theoretical resolution limit of 0.5 meV. The chamber where the analyser is installed and the analyser itself are constructed from μ-metal in order to prevent stray magnetic fields influencing the low energy photoelectrons. The analyser can be operated with a pass energy up to 660 eV, and a kinetic energy range from 0 to 3500 eV, with a range of entrance and exit slit sizes. Using a 2D CCD detector, both angle and spatially resolved measurements can be performed. In particular, the angular dispersive modes of operation allow parallel recording up to $\pm 13^\circ$ acceptance angle. For the best res-

olution, a small photon spot size is required. Unfortunately, the beam spot size on the ASTRID synchrotron is optimised for the bending magnet beamlines, and is rather large for the undulator beamlines. Consequently, the beam spot size is reduced by inserting a pinhole just before the sample, resulting in a spot size on the sample of a few tenths of a mm diameter. The sample is mounted on a high-precision four-axis cryo-manipulator, on which the sample can be cooled to $\sim$60 K. Measurements at higher temperature are performed by radiative heating from a filament mounted behind the sample. The heating is 'chopped' so that measurements are only performed when the filament is off, to prevent electric fields influencing the measurements. The temperature is controlled by a Eurotherm controller, via a thermocouple spot-welded to the sample plate. The rotation of the manipulator is controlled by a stepper motor, so that automated Fermi surface/constant energy contour ARPE spectra can be recorded. The spectrometer chamber also contains low-energy electron diffraction optics. The spectrometer chamber is pumped by an ion pump and a titanium sublimation pump, and has a typical base pressure of $\sim 1 \times 10^{-10}$ mbar.

There is also a preparation chamber attached to the spectrometer chamber, in which the sample can be radiatively heated to $\sim$ 850 K, and ion bombarded if required. The manipulator from the preparation chamber can be driven into the main spectrometer chamber for sample transfer. The preparation chamber is pumped by a turbomolecular pump, an ion pump and a titanium sublimation pump, and reaches a typical base pressure of $\sim 1 \times 10^{-10}$ mbar. Finally, there is a small load lock chamber, pumped by a turbomolecular pump to a base pressure of $\sim 1 \times 10^{-8}$ mbar, for insertion of samples. All sample transfer is performed using wobble sticks.

3.2 Optical absorption

Optical absorption spectroscopy (OAS) can be used to obtain information on the band gap of semiconductor materials and, in certain cases, their bulk doping level. As in photoemission, an incoming photon is absorbed, exciting an electron from

some initial occupied state of the material to an unoccupied final state. Unlike photoemission, however, the final state is typically a conduction band state just above the band gap, and it is the transmission of the light that is monitored as the photon energy is varied, from which the absorption is determined. A brief introduction to this technique is given here.

3.2.1 Absorption coefficient

The one-electron Hamiltonian in the presence of electromagnetic radiation discussed in Section 3.1.1 (Eqn. 3.4) is the relevant Hamiltonian again. Using Fermi's golden rule as above, the number of transitions from an initial to a final state per unit volume and time due to photon absorption

$$N(h\nu) = \frac{2\pi}{\hbar} \sum_{c,v} |M_{fi}|^2 \, \delta(E_f(\mathbf{k}_f) - E_i(\mathbf{k}_i) - h\nu) \tag{3.18}$$

where the delta-function ensures initial and final states are separated by an energy equal to the photon energy. The transition matrix element

$$M_{fi} = \langle c | \, \mathbf{E} \cdot \mathbf{r} \, | v \rangle \tag{3.19}$$

where the initial and final states, $|v\rangle$ and $|c\rangle$, are Bloch states of the valence and conduction bands, respectively, and the electric dipole approximation is valid as the photon wavevector is small [55]. In practice, the magnitude of the matrix element can often be treated as independent of $\mathbf{k}$ over the range of the measurement, yielding

$$|M_{fi}|^2 \propto |P_{cv}|^2 \, \delta(\mathbf{q} - \mathbf{k}_c + \mathbf{k}_v) \tag{3.20}$$

where P_{cv} is a constant representing the coupling strength of the initial and final states, and the delta-function ensures that these states have the same wavevector, neglecting the small photon wavevector, $\mathbf{q}$, yielding so-called *direct* transitions shown schematically in Fig. 3.6(a). The absorption of light is defined as the energy removed from the beam, as a fraction of the incident flux

$$\begin{aligned} \alpha(h\nu) &= \frac{h\nu N(h\nu)}{\varepsilon\omega^2 A_0^2/2} \\ &\propto \frac{1}{h\nu} \sum_{c,v} |P_{cv}|^2 \, \delta(E_f(\mathbf{k}_f) - E_i(\mathbf{k}_i) - h\nu) \, \delta(\mathbf{q} - \mathbf{k}_c + \mathbf{k}_v). \end{aligned} \tag{3.21}$$

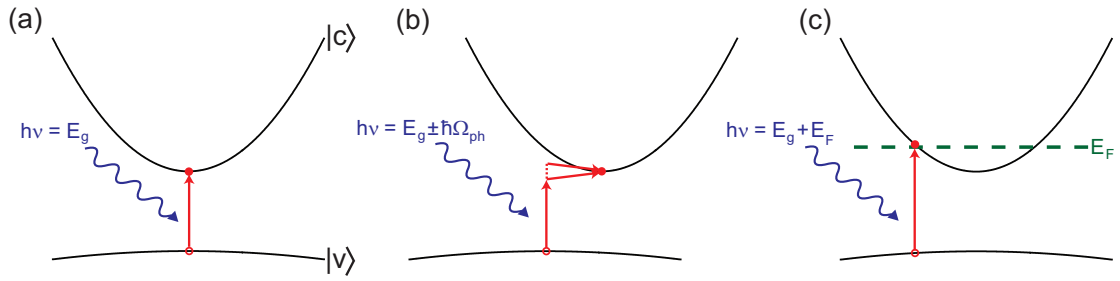

Figure 3.6: Schematic representation of (a) direct and (b) indirect absorption, and (c) the Moss-Burstein shift.

Treating E as a continuous function, changing the sum to an integral [89], Eqn. 3.21 can be written

$$\alpha(h\nu) \propto \frac{1}{h\nu} |P_{cv}|^2 g_j(E_c - E_v) \tag{3.22}$$

where

$$g_j(E_c - E_v) = \frac{k^2}{\pi^2} \left[\frac{\mathrm{d}E_c(k)}{\mathrm{d}k} - \frac{\mathrm{d}E_v(k)}{\mathrm{d}k} \right]^{-1} \tag{3.23}$$

is the joint density of states over the conduction and valence bands. Assuming parabolic dispersion relations for the conduction and valence bands, the coefficient of direct interband absorption

$$\alpha(h\nu) \propto (h\nu - E_g)^{1/2}. \tag{3.24}$$

The band gap of the semiconductor can, in this limit, be determined by a linear extrapolation of α^2 to the background level. This expression is modified, and in fact an analytical solution can often not be given, for non-parabolic bands, where the non-parabolic dispersions and potentially **k**-dependent matrix elements should be considered [90]. However, a linear extrapolation of α^2 can often still yield sufficiently accurate results.

In an indirect semiconductor, the direct transition model discussed above suggests that there will be no onset of absorption until the photon energy is equal to the direct band gap energy, rather than the fundamental band gap energy. However, indirect transitions can occur, where a change of momentum is provided by either emission or absorption of a phonon, as shown schematically in Fig. 3.6(b). In this case, the energy separation of initial and final states is given by the photon energy, $h\nu$, plus (absorption) or minus (emission) the phonon energy, $\hbar\Omega_{ph}$, causing the

delta-function in Eqn. 3.18 to become $\delta(E_f(\mathbf{k}_f) - E_i(\mathbf{k}_i) \pm \hbar\Omega_{ph} - h\nu)$, and momentum conservation is ensured by modifying the delta function in Eqn. 3.20 to $\delta(\mathbf{q} - \mathbf{k}_c + \mathbf{k}_v + \mathbf{k}_{ph})$. Considering the density of phonons within Bose-Einstein statistics, it can be shown [91] that the absorption coefficient for indirect transitions

$$\alpha_i(h\nu) \propto (h\nu - E_g \pm \hbar\Omega_{ph})^2. \tag{3.25}$$

However, this process requires both the absorption of a photon and absorption or emission of a phonon, and so the strength of absorption due to indirect transitions is rather low. Consequently, a pronounced increase in absorption coefficient is still observed when the photon energy becomes large enough to allow direct interband transitions.

In the above, it has been assumed that all of the valence band states are filled, and all of the conduction band states empty. However, for heavily doped semiconductors, the Fermi level can move into one of the bands. Consider a degenerately doped n-type semiconductor. Now, the lowest energy corresponding to direct interband transitions from initially occupied valence band states to initially unoccupied conduction band states is no longer given by the band gap energy, but rather by the energy separating the valence band at the Fermi wavevector and the Fermi level, as shown schematically in Fig. 3.6(c). Consequently, the absorption edge is shifted to higher energies compared to non-degenerate samples. Such an effect was first observed independently by Moss [92] and Burstein [93] in InSb, and so the shift of the absorption edge due to band-filling is commonly termed the Moss-Burstein shift. Formally, it can be accounted for by including conduction and valence band Fermi functions in the matrix element discussed above.

Another effect can become important for heavily doped materials, where charged impurities can induce a local change of the band edge potential due to Coulombic interactions. Additionally, a change in local strain state due to the presence of an impurity atom or vacancy in the host lattice can induce a similar perturbation of the band edge energies. As these impurities/vacancies are randomly distributed in space, the spatial variations in band edge potential can be averaged into an exponential-like tailing of the density of states of the conduction and valence

bands into the band gap. Consequently, optical transitions can occur from or into band-tail states, leading to an exponential increase in absorption coefficient below the fundamental onset of absorption [89], known as an Urbach tail [94]. Also, in heavily doped materials, phonon-assisted transitions can occur from an electron in a partially occupied band to an empty state higher in that band. This can lead to a peak in the absorption coefficient at photon energies significantly below the band gap. This 'free-carrier absorption' will be considered in more detail in Section 3.3.

3.2.2 Measurements of the absorption coefficient

In practice, optical absorption is monitored by the transmission of light through a sample,

$$T(h\nu) = \frac{(1-R)^2 \exp(-\alpha(h\nu)d)}{1-R^2 \exp(-2\alpha(h\nu)d)} \tag{3.26}$$

where R is the reflection coefficient of the air/semiconductor interface and d is the thickness of the sample. At normal incidence, the reflection coefficient,

$$R(h\nu) = \left| \frac{\tilde{n}(h\nu)-1}{\tilde{n}(h\nu)+1} \right|^2 \tag{3.27}$$

where $\tilde{n}(h\nu) = \eta(h\nu) + i\kappa(h\nu)$ is the complex refractive index. In practice, however, the refractive index is often treated as real and independent of frequency in this conversion,

$$R \approx \left[\frac{\eta-1}{\eta+1} \right]^2 . \tag{3.28}$$

Under this assumption, Eqn. 3.26 can be rearranged to yield the absorption coefficient of the sample. The presence of additional layers in the sample (for example, substrate and buffer layers) can complicate the picture further, leading to features such as Fabry-Pérot interference fringes, and substrate absorption features, but it is usually possible to obtain quantitative information about the semiconductor layer of interest.

FTIR measurements

Measurements at infrared (IR) wavelengths were performed here by Fourier-transform IR (FTIR) spectroscopy. In this technique, light from a polychromatic IR source is

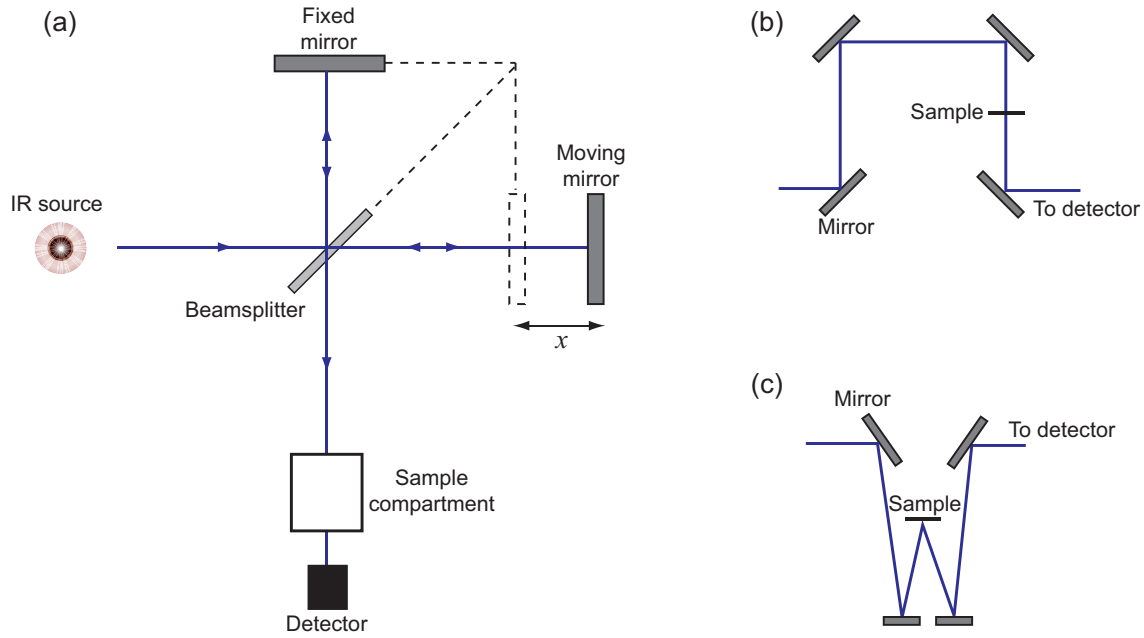

Figure 3.7: Schematic of an FTIR spectrometer showing (a) the beam path and Michelson interferometer and the beam path in the sample compartment for (b) transmission and (c) reflectivity measurements.

passed through a Michelson interferometer before being directed onto the sample, as shown schematically in Fig. 3.7(a). In the Michelson interferometer, a beamsplitter ensures that 50% of the light is reflected up to a fixed mirror, while the other 50% of the light is transmitted, and subsequently reflected from a moveable mirror. The light from the two paths recombines at the beamsplitter, before entering the sample compartment. After interaction with the sample, the light reaches a detector, whose response must be 'slow', that is, it averages over a long time compared to the coherence time of the light.

If the electric-field amplitude from one path reaching the detector at time t is $V(t)$, that from the other (shorter) arm is $V(t+\tau)$ where $\tau = 2x/c$ is the time by which the wavetrain is advanced by travelling a shorter distance by $2x$. Consequently, the 'slow' detector measures an intensity [95]

$$I(\tau) \propto \left\langle V(t)^2 \right\rangle + \langle V(t)V(t+\tau) \rangle \tag{3.29}$$

where the second term is the autocorrelation function

$$\langle V(t)V(t+\tau) \rangle = \frac{1}{T} \int_{-T/2}^{T/2} V(t)V(t+\tau)\, \mathrm{d}t. \tag{3.30}$$

From Eqn. 3.29, $I(\tau = 0) \propto 2\langle V(t)^2 \rangle$. The interferogram

$$W(\tau) \equiv I(\tau) - \frac{1}{2} I(0) \propto \langle V(t) V(t+\tau) \rangle \tag{3.31}$$

can be recorded as the moveable mirror distance, x, and consequently the time delay, τ, is scanned. From the Wiener-Khintchine theorem, the frequency spectrum of the light following interaction with the sample can then be obtained simply from a Fourier transform of the interferogram [95],

$$\left| \tilde{V}(\omega) \right|^2 \propto \int_{-\infty}^{\infty} \langle V(t) V(t+\tau) \rangle \, e^{i\omega\tau} \, \mathrm{d}\tau \propto \int_{-\infty}^{\infty} W(\tau) e^{i\omega\tau} \, \mathrm{d}\tau. \tag{3.32}$$

As all frequencies are measured simultaneously, this leads to quick measurements, and hence a good signal to noise ratio compared to measurements performed using dispersive spectrometers. Additionally, the light throughput can be comparatively large as there are not the slits that cut out most of the light that are required for dispersive instruments. However, there are some disadvantages. Most importantly, care must be taken when performing the Fourier transform not to introduce additional structure into the spectrum, for example due to poor windowing of the interferogram. Additionally, as FTIR spectrometers are single-beam instruments, a background spectrum must be taken in advance without the sample present to account for the spectral response of the source, mirrors, beamsplitter, detector and any absorption by the atmosphere. The spectral response of the sample is then given by the ratio of the measured spectrum with the sample present to the background spectrum. However, atmospheric absorption features may change over the course of a long scan due to a change in atmospheric conditions, which could adversely affect the measured spectrum.

The optical transmission measurements reported in this work were performed using a Perkin Elmer Spectrum GX FTIR spectrometer. A spectral range of 0.04 to 1.24 eV is available using a cadmium mercury telluride detector and potassium bromide and quartz beamsplitters. The sample compartment arrangement for transmission measurements is shown in Fig. 3.7(b), resulting in transmission of the beam through the sample. A small aperture mask is used to ensure that the beam size does not exceed the sample size. Nitrogen gas is flowed along the beam path and

into the sample compartment to minimize changing absorption features due to a change in atmospheric conditions.

UV-Visible measurements

For transmission measurements in the visible and ultraviolet (UV), a UV-Visible spectrophotometer is used. In this instrument, the transmission of a sample is measured as a function of the frequency of the light, determined by a monochromator. In this work, a Perkin Elmer Lambda 25 UV-Visible spectrophotometer was used to cover the spectral range from 1.1 to 6.5 eV. The light is provided by deuterium and tungsten sources, and monochromated by a Seya Namioka Holographic concave grating.

3.3 IR reflectivity

Instead of considering the transmission of light, it is possible to investigate the reflection of light from a sample (Eqn. 3.27). At mid-IR frequencies, this yields particularly useful information about phonons and free carriers in the material. Note, this is the reflectivity analogue of free-carrier absorption discussed in Section 3.2.1.

A free electron gas can be described as a plasma which supports a collective excitation of the electrons at a frequency known as the plasma frequency, ω_p. The plasma frequency is related to the carrier concentration, n, and momentum effective mass, m^*, via

$$\omega_p^2 = \frac{ne^2}{\varepsilon_0 \varepsilon(\infty) \langle m^*(E) \rangle}. \tag{3.33}$$

As this is a collective excitation of all of the electrons in the free-electron gas, the energy-dependent effective mass should be averaged over the density of states

$$\langle m^*(E) \rangle = \frac{\int_0^\infty g(E) m^*(E) f(E)\, \mathrm{d}E}{\int_0^\infty g(E) f(E)\, \mathrm{d}E}, \tag{3.34}$$

where $g(E)$ is the density of states and $f(E)$ is the Fermi-Dirac factor. Thus, determination of the plasma frequency yields the value of $n/\langle m^*(E) \rangle$. If the band edge effective mass and its energy dependence are known, the carrier concentration can be determined. Otherwise, if the carrier concentration is determined by independent means, the plasma frequency gives information on the effective mass of the carriers.

3.3.1 Two-oscillator dielectric function

Within a two-oscillator approximation, the complex dielectric function (square of the complex refractive index),

$$\tilde{\varepsilon}(\omega) = \varepsilon'(\omega) + i\varepsilon''(\omega) = [\tilde{n}(\omega)]^2 \tag{3.35}$$

is given by the sum of lattice (phonon) and free-carrier (plasmon) terms [96]

$$\begin{aligned} \tilde{\varepsilon}(\omega) &= \tilde{\varepsilon}_L(\omega) + \tilde{\varepsilon}_e(\omega) \\ &= \varepsilon(\infty) + \frac{[\varepsilon(0) - \varepsilon(\infty)]\omega_{TO}^2}{\omega_{TO}^2 - \omega^2 - i\omega\Gamma} - \frac{\varepsilon(\infty)\omega_p^2}{\omega(\omega + i/\tau)} \end{aligned} \tag{3.36}$$

where $\varepsilon(0)$ and $\varepsilon(\infty)$ are the static and high-frequency dielectric constants of the material, respectively, ω_{TO} (Γ) is the frequency (damping) of the transverse optical phonon and ω_p (τ) is the frequency (lifetime) of the plasmon. Considering just the electronic term in the absence of damping, the reflectivity tends to unity at the plasma frequency, giving rise to a Restrahlen band. However, this is modified by damping and by interactions with the phonons of the lattice (if the plasma and phonon frequencies are sufficiently close, the plasmon and phonon couple, forming a collective mode known as a plasmaron). It is therefore necessary to simulate the reflectivity spectra, which can be done using Eqns. 3.27, 3.35 and 3.36 and compared to a measured spectrum.

Experimentally, the spectra are recorded here using the Perkin Elmer Spectrum GX FTIR spectrometer described above. The geometry in the sample compartment is shown in Fig. 3.7(c). In this arrangement, the angle of incidence is not normal, but rather a specular reflection is used. Additionally, the sample is often made up of several layers, and it is necessary to account for all of these in the analysis. These features can be effectively incorporated using a transfer matrix method (TMM).

3.3.2 Transfer matrix formalism

The TMM utilised here is based upon that of Katsidis and Siapkas [97]. Consider the electric field amplitudes within an arbitrary N-layer structure, shown schematically

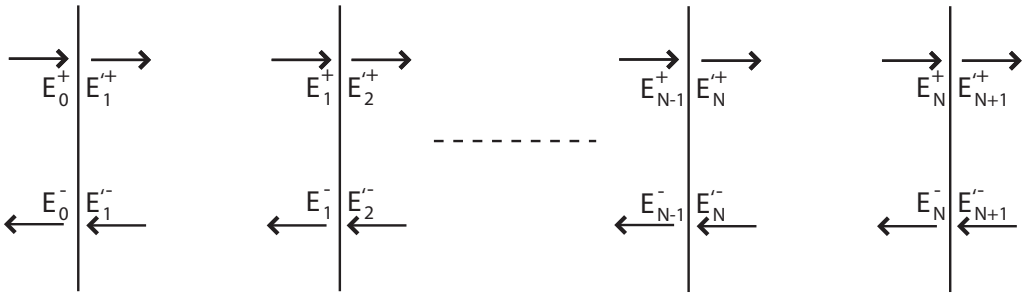

Figure 3.8: Schematic representation of electric field amplitudes within an arbitrary N-layer structure.

in Fig. 3.8. The subscript denotes the medium, $+/-$ the direction of travel (to the right/left). The electric field amplitudes just to the left of an arbitrary interface, $E^{\pm}_{m-1}$, can be related to those just to the right of that interface, $E'^{\pm}_{m}$ by a dynamical matrix that describes the reflection and transmission at the interface

$$\begin{pmatrix} E^{+}_{m-1} \\ E^{-}_{m-1} \end{pmatrix} = \mathbf{D}^{-1}_{m-1}\mathbf{D}_{m} \begin{pmatrix} E'^{+}_{m} \\ E'^{-}_{m} \end{pmatrix}. \tag{3.37}$$

The elements of the 2×2 dynamical matrix D_{ij} can be related to the complex Fresnel coefficients for transmission and reflection at the interface

$$r_{m-1,m} = \left.\frac{E^{-}_{m-1}}{E^{+}_{m-1}}\right|_{E'^{-}_{m}=0} = \frac{D_{21}}{D_{11}} \tag{3.38a}$$

$$t_{m-1,m} = \left.\frac{E'^{+}_{m}}{E^{+}_{m-1}}\right|_{E'^{-}_{m}=0} = \frac{1}{D_{11}} \tag{3.38b}$$

$$r_{m,m-1} = \left.\frac{E'^{-}_{m}}{E'^{+}_{m}}\right|_{E^{+}_{m-1}=0} = -\frac{D_{12}}{D_{11}} \tag{3.38c}$$

$$t_{m,m-1} = \left.\frac{E^{-}_{m-1}}{E'^{+}_{m}}\right|_{E^{+}_{m-1}=0} = \frac{\det(\mathbf{D}^{-1}_{m-1}\mathbf{D}_{m})}{D_{11}} \tag{3.38d}$$

where $\det(\mathbf{D}^{-1}_{m-1}\mathbf{D}_{m})$ denotes the determinant of the dynamical matrix. As light propagation occurs at an arbitrary angle θ to the surface normal, the complex Fresnel coefficients must be treated separately for s-polarised (transverse electric) and p-

polarised (transverse magnetic) light, and are given [98] by

$$r^s_{m-1,m} = \frac{\tilde{n}_{m-1}\cos\theta_{m-1} - \tilde{n}_m\cos\theta_m}{\tilde{n}_{m-1}\cos\theta_{m-1} + \tilde{n}_m\cos\theta_m} \tag{3.39a}$$

$$r^p_{m-1,m} = \frac{\tilde{n}_m\cos\theta_{m-1} - \tilde{n}_{m-1}\cos\theta_m}{\tilde{n}_{m-1}\cos\theta_m + \tilde{n}_m\cos\theta_{m-1}} \tag{3.39b}$$

$$t^s_{m-1,m} = \frac{2\tilde{n}_{m-1}\cos\theta_{m-1}}{\tilde{n}_{m-1}\cos\theta_{m-1} + \tilde{n}_m\cos\theta_m} \tag{3.39c}$$

$$t^p_{m-1,m} = \frac{2\tilde{n}_{m-1}\cos\theta_{m-1}}{\tilde{n}_{m-1}\cos\theta_m + \tilde{n}_m\cos\theta_{m-1}}. \tag{3.39d}$$

The electric field amplitudes at the left and right of a medium m can be related by a propagator matrix

$$\begin{aligned}\begin{pmatrix} E'^+_m \\ E'^-_m \end{pmatrix} &= \mathbf{P}_m \begin{pmatrix} E^+_m \\ E^-_m \end{pmatrix} \\ &= \begin{bmatrix} \exp(-i\delta_m) & 0 \\ 0 & \exp(i\delta_m) \end{bmatrix} \begin{pmatrix} E^+_m \\ E^-_m \end{pmatrix}\end{aligned} \tag{3.40}$$

where, using Snell's law,

$$\delta_m = \frac{2\pi}{\lambda}\tilde{n}_m d_m \cos\theta_m \tag{3.41}$$

is the phase change of light travelling once through the medium m of thickness d_m. The total transfer matrix (TM) for the N layer system, $\mathbf{T}$, satisfying

$$\begin{pmatrix} E^+_0 \\ E^-_0 \end{pmatrix} = \mathbf{T} \begin{pmatrix} E'^+_{N+1} \\ E'^-_{N+1} \end{pmatrix}, \tag{3.42}$$

can then be determined by concatenating the relevant dynamical and propagation matrices

$$\mathbf{T} = \begin{bmatrix} T_{11} & T_{12} \\ T_{21} & T_{22} \end{bmatrix} = \mathbf{D}_0^{-1} \left[\prod_{m=1}^{N} \mathbf{D}_m \mathbf{P}_m \mathbf{D}_m^{-1} \right] \mathbf{D}_{N+1}. \tag{3.43}$$

The total reflection coefficient can be directly determined from the total TM (*cf.* Eqn. 3.38a)

$$r = \frac{T_{21}}{T_{11}}. \tag{3.44}$$

If unpolarised light has been used, as in the experimental arrangement used here, the total reflectivity is given by the incoherent average of the two polarisations of light

$$R = \frac{1}{2}\left(R^s + R^p\right) = \frac{1}{2}\left(|r^s|^2 + |r^p|^2\right). \tag{3.45}$$

There is one final complication that should be considered. If the multilayer structure of interest contains a thick layer, such as a substrate, it is more appropriate to think of incoherent interference in this layer rather than the coherent interference treated above. This is included in this TMM as follows. Assume that there is an incoherent layer m in an N layer structure. The TMs up to and beyond layer m are given, as before, by

$$\mathbf{T}_{0,m} = \frac{1}{t_{0,m}} \begin{bmatrix} 1 & -r_{m,0} \\ r_{0,m} & t_{0,m}t_{m,0} - r_{0,m}r_{m,0} \end{bmatrix} \tag{3.46}$$

and the equivalent for $\mathbf{T}_{m,N+1}$. These are then converted to intensity TMs

$$\mathbf{T}^{int}_{0,m} = \frac{1}{|t_{0,m}|^2} \begin{bmatrix} 1 & -|r_{m,0}|^2 \\ |r_{0,m}|^2 & |t_{0,m}t_{m,0}|^2 - |r_{0,m}r_{m,0}|^2 \end{bmatrix} \tag{3.47}$$

and the equivalent for $\mathbf{T}^{int}_{m,N+1}$. The total TM is then given by concatenating these intensity TMs with a propagator matrix for incoherent propagation in medium m,

$$\mathbf{T}^{int} = \mathbf{T}^{int}_{0,m}\mathbf{P}^{int}_{m}\mathbf{T}^{int}_{m,N+1} \tag{3.48}$$

where

$$\mathbf{P}^{int}_{m} = \begin{bmatrix} |\exp(-i\delta_m)|^2 & 0 \\ 0 & |\exp(i\delta_m)|^2 \end{bmatrix}. \tag{3.49}$$

Given that this is already a TM relating intensities, the total reflectivity is given by

$$R = \frac{T^{int}_{21}}{T^{int}_{11}}. \tag{3.50}$$

This correctly represents all of the multiple interference within the multi-layer sample. In particular, it allows the fitting of both the plasma edge and Fabry-Pérot interference fringes of a reflectivity spectrum to yield the correct plasma frequency and thickness of a sample of interest atop a buffer and substrate layer structure.

3.4 Hall effect

Hall effect measurements are the most widely used method with which to determine carrier concentrations in semiconductors. A semiconductor sample is placed in a magnetic field $\mathbf{B}$, with a current flowing normal to the magnetic field. This

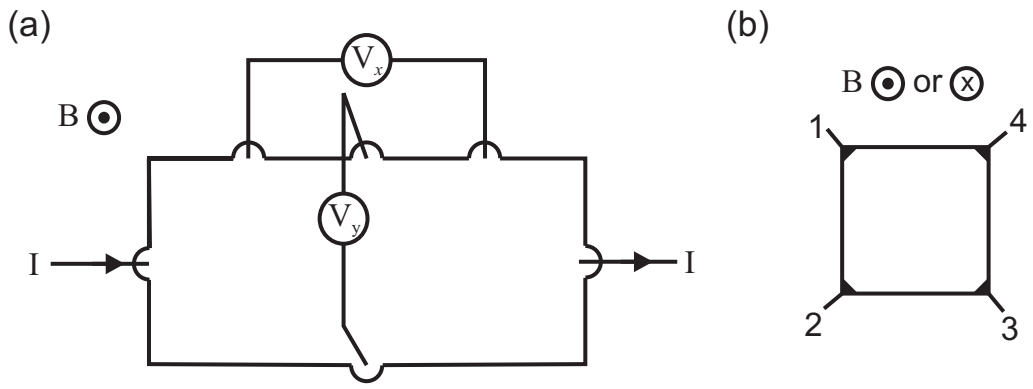

Figure 3.9: Geometries for Hall effect measurements: (a) Hall bar; (b) van der Pauw.

generates a transverse electric field due to the action of the Lorentz force. In the 'Hall bar' geometry, shown in Fig. 3.9(a), the magnetic field is applied along the z-direction, $\mathbf{B} = (0, 0, B)$, the current is driven in the x-direction, and transverse and longitudinal voltages are measured to deduce the electric field, $\mathbf{E} = (E_x, E_y, 0)$, assumed to have no component in the z-direction.

Within the relaxation-time approximation [99], the drift velocity of a carrier in the semiconductor, $\mathbf{v}_j$, satisfies the relation

$$m_j^* \left(\frac{\mathrm{d}\mathbf{v}_j}{\mathrm{d}t} + \frac{\mathbf{v}_j}{\tau_j} \right) = q_j(\mathbf{E} + \mathbf{v}_j \times \mathbf{B}) \tag{3.51}$$

where q_j, m_j^* and τ_j^{-1} are the charge, effective mass, and scattering rate of the carrier respectively. In the steady-state, $\mathrm{d}\mathbf{v}/\mathrm{d}t = 0$, and Eqn. 3.51 becomes

$$v_{y,j} \left(1 + \omega_{c,j}^2 \tau_j^2\right) = \frac{q_j \tau_j}{m_j^*} \left(E_y - \omega_{c,j} \tau_j E_x\right) \tag{3.52}$$

where the cyclotron frequency $\omega_{c,j} = qB/m_j^*$. For typical Hall-effect measurements, rather small magnetic fields are employed, and so terms or order $\omega_c^2 \tau^2$ can be neglected. The total net transverse current from all carriers must be zero

$$\sum_j n_j v_{y,j} q_j = 0, \tag{3.53}$$

where n_j is the density of carrier type j. From this, the Hall coefficient, $R_H = E_y/J_x B$ where J_x is the current density in the x-direction, can be determined, and, in the presence of both electrons and holes, is given by

$$R_H = \frac{1}{|e|} \frac{(p\mu_h^2 - n\mu_e^2)}{(p\mu_h + n\mu_e)^2} \tag{3.54}$$

where n (μ_e) and p (μ_h) are the electron and hole concentrations (mobilities), respectively. The hole signal is usually dominated by the heavy hole component. Furthermore, either electrons *or* holes are usually dominant, and so Eqn. 3.54 simplifies to $R_H = -1/ne$ (n-type semiconductors) or $R_H = 1/pe$ (p-type semiconductors). In reality, the current, rather than current density, flowing through the sample is known, and a Hall voltage, rather than electric field strength, is measured. Consequently, an areal density of carriers is determined, although this can be converted to a volume density upon division by the film thickness. The resistivity of a semiconductor

$$\rho = \frac{1}{e(n\mu_e + p\mu_h)}. \tag{3.55}$$

From measurements of the sheet density and sheet resistance, the mobility of the majority carriers can therefore also be determined.

3.4.1 Van der Pauw geometry

A common geometry used for measurements of the sheet resistance and Hall voltage of a sample, and that used in this work, is the van der Pauw geometry, shown schematically in Fig. 3.9(b).

If a current is passed between contacts 1 and 2, I_{12}, and a voltage measured across contacts 3 and 4, V_{34}, the resistance

$$R_{12,34} = \frac{V_{34}}{I_{12}}. \tag{3.56}$$

Van der Pauw [100,101] showed that, for a flat continuous lamina of arbitrary shape, the sheet resistance R_s satisfies

$$\exp(-\pi R_{12,34}/R_s) + \exp(-\pi R_{23,41}/R_s) = 1, \tag{3.57}$$

allowing the sheet resistance to be determined from simple electrical measurements. From the reciprocity theorem, $R_{12,34} = R_{34,12} = R_{21,43} = R_{43,21}$, and so these quantities can be averaged to yield a much more accurate determination of the sheet resistance, cancelling out any offset voltages.

In a similar way, the reciprocity theorem can be used to yield accurate values of the Hall voltage. A current can be applied between a set of contacts on opposite

corners, for example I_{13}, in the presence of either a positive or negative magnetic field, and a Hall voltage is measured between the other two corners, for example $V_{24}^{\pm}$, where $\pm$ denotes the polarity of the magnetic field. The average Hall voltage is then given from

$$V_H = \frac{V_{13}^{+} - V_{13}^{-} + V_{24}^{+} - V_{24}^{-} + V_{31}^{+} - V_{31}^{-} + V_{42}^{+} - V_{42}^{-}}{8}. \tag{3.58}$$

Using each set of currents and voltages for the Hall voltage and sheet resistance measurements, it is therefore possible to obtain an accurate value for the sheet density and mobility of the sample.

3.4.2 Hall effect measurements – HMS-3000 system

Hall effect measurements reported in this work were performed using an Ecopia HMS-3000 Hall effect measurement system. Contacts are made to the samples in the van der Pauw geometry discussed above. The system includes a 0.55 T permanent magnet, and the polarity of the field is changed by rotating the magnet through 180°. The system can pass a current up to 20 mA. Current–voltage ($I-V$) measurements can also be taken between each set of contacts, and Hall effect measurements were only made if a linear $I-V$ curve was obtained, indicating Ohmic contacts had been formed to the material. During measurements, the sample sits in a container that can be filled with liquid nitrogen for performing measurements at 77 K if required.

Chapter 4

Unification of the electrical behaviour of defects, impurities and surface states in semiconductors: Virtual Gap States in CdO

4.1 Introduction

The presence of even small concentrations of native defects or impurities in semiconductors has a profound effect on their bulk electronic properties; for example, hydrogen almost always counteracts the prevailing conductivity [25]. Similarly, surface electronic properties, crucial when forming contacts to the material, are generally dominated by a small number of charged surface states of acceptor-like character in n-type and donor-like character in p-type semiconductors, leading to a depletion of charge carriers at the surface. In rare cases, however, such native defects, localised impurities and surface states can be donors in n-type or acceptors in p-type material [7, 102, 103]. Understanding this unconventional behaviour is crucial to advancing the functionality of current and future semiconductors.

The group II-oxide materials represent a rapidly emerging class of semiconductors, where recent advances in growth resulting in high quality single-crystalline material present opportunities for their use in a wide range of devices. Research in these materials has largely focussed on ZnO which, with its similar band gap to GaN but substantially larger exciton binding energy, has enormous promise for devices such as light emitting diodes [104]. However, the smaller band gap compound CdO ($E_g \sim$2.2 eV at the Brillouin zone centre [105]) has received far less attention, despite its importance when alloyed with ZnO to extend the operation of ZnO-based devices into the visible spectral range [106, 107].

In this chapter, surface states and intentionally introduced impurities and native defects are all shown to be donors in n-type CdO. While these properties have important consequences for CdO's use in practical applications, more importantly it serves as a model system in which to probe the fundamental origins of bulk and

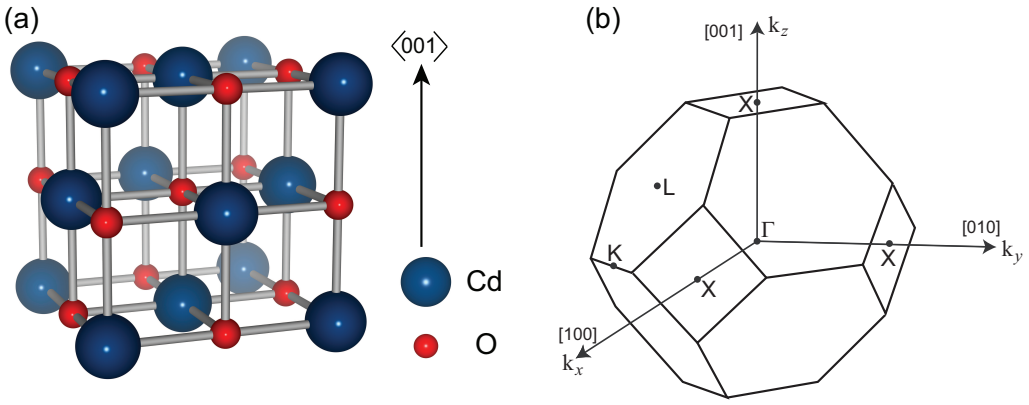

Figure 4.1: (a) Single unit cell of the rock-salt crystal structure of CdO and (b) corresponding Brillouin zone.

surface electronic properties. In particular, it is shown that the electrical behaviour of native defects, hydrogen and surface states can all be understood from the position of a single energy level, the charge neutrality level (CNL), unifying bulk, surface and interface electronic properties of semiconductors, and giving insight into possibilities for future engineering of materials with specific electrical characteristics.

4.1.1 Crystal and electronic structure

CdO crystallises in the rocksalt crystal structure (space group $Fm3m$), shown in Fig. 4.1(a). It is a six-fold coordinated, face centred cubic structure with a two-atom basis – a Cd atom at $(0, 0, 0)$ and an O atom at $(\frac{1}{2}, \frac{1}{2}, \frac{1}{2})$ – and a lattice parameter $a = 4.695$ Å [108]. The corresponding Brillouin zone of the face centred cubic lattice is shown in Fig. 4.1(b).

Quasiparticle-corrected density-functional theory (QPC-DFT) band structure calculations for CdO are shown in Fig. 4.2. The three topmost valence bands have largely O $2p$ character, and these are separated from the fourth valence band (of predominantly O $2s$ character), by a large ionicity gap of $\sim$15 eV. Very shallow localised Cd $4d$ levels occur within this ionicity gap, visible in Fig. 4.2 at around 8 eV below the valence band maximum (VBM). For the octahedral point symmetry of CdO's rock-salt structure, a p–d interaction between the Cd $4d$ and O $2p$ orbitals, which pushes the VBM to higher energies, is symmetry forbidden at Γ [110, 111] ($\Gamma_{15}^{v}(p)$ states in the valence band, $\Gamma_{12}(d)$ and $\Gamma_{25'}(d)$ states for the d-levels). This

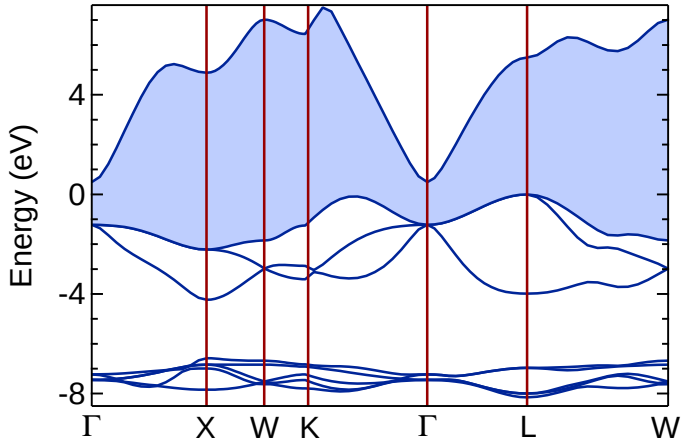

Figure 4.2: QPC-DFT band structure calculations for CdO [109]. The fundamental energy gap across the Brillouin zone is represented by shading.

causes the valence bands to disperse upwards along the $\Gamma \rightarrow$ L and $\Gamma \rightarrow$ K directions and downwards along the $\Gamma \rightarrow$ X direction, leading to an indirect band gap between the VBM and the Γ_1^c conduction band minimum (CBM).

4.1.2 Band parameters

The fundamental electronic parameters of CdO have received relatively little attention. The most widely quoted value of the direct bandgap is 2.28 eV, determined by Koffyberg from thermoreflectance measurements at 100 K [112]. Koffyberg also used an effective mass of $0.14m_0$, although without experimental justification. However, Jefferson *et al.* [105] showed that non-parabolicity could not be neglected, as had been done in previous studies. From a combination of infrared (IR) reflectivity, optical absorption and Hall effect measurements, the room temperature direct band gap and conduction band-edge effective mass were given as 2.16 ± 0.02 eV and $0.21 \pm 0.01m_0$, respectively. Here, the investigation of Jefferson *et al.* has been extended to both lower and higher carrier density samples, as shown in Fig. 4.3. The position of the direct absorption onset is determined by a linear extrapolation of the squared absorption coefficient, while the plasma frequency is determined from simulation of IR reflectivity spectra as discussed in Section 3.3. The room temperature direct bandgap obtained here is in good agreement with that of Jefferson *et al.*, although a slightly higher value for the effective mass of $0.24 \pm 0.02m_0$ is determined. These parameters are used for the following investigations.

There is a large spread in the experimental values for the indirect gap. Al-

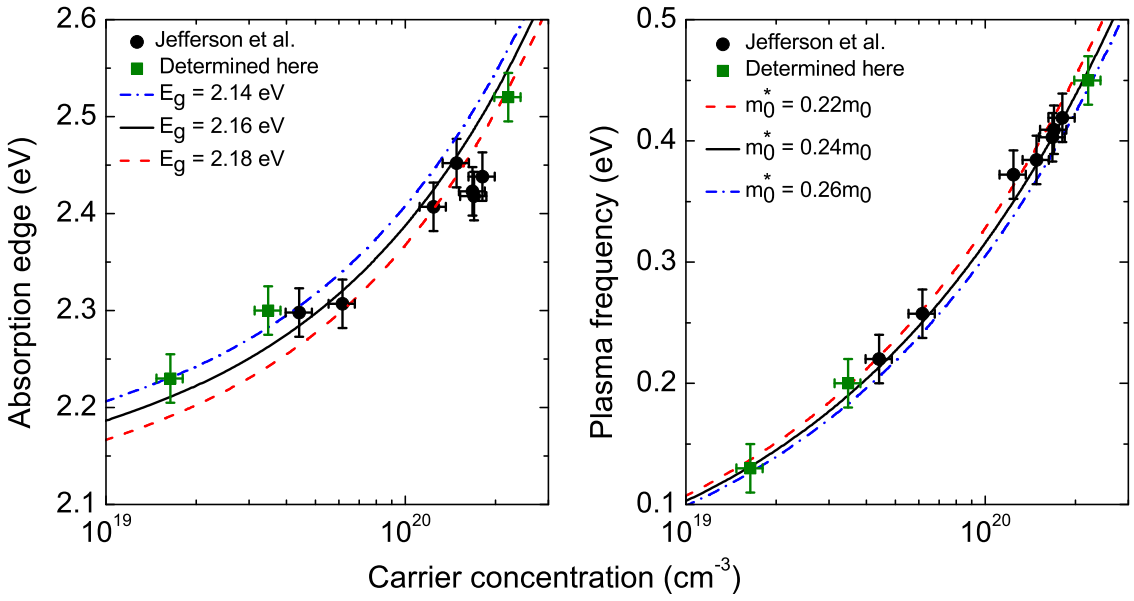

Figure 4.3: (a) Absorption edge and (b) plasma frequency, determined from optical absorption and IR reflectivity, respectively, vs. Hall electron density for a range of CdO samples, as determined by Jefferson *et al.* [105] and determined here. Model calculations for the variation of (a) the absorption edge for different band gap values, and (b) the plasma frequency for different band edge effective masses, as a function of bulk carrier concentration, are also shown.

though DFT calculations can be unreliable for predicting band gaps accurately, dispersions are normally determined more accurately. Therefore, the separation of the Γ-point and L-point of the valence band is taken as 1.2 eV here, from the QPC-DFT calculations. This is supported by comparisons of the QPC-DFT calculated density of states with photoemission and x-ray emission spectroscopy measurements [109, 113].

4.2 Experimental details

Single-crystalline CdO(001) samples were grown at the Universitat de València by metal-organic vapour phase epitaxy (MOVPE) on *r*-plane $(1\bar{1}02)$ sapphire substrates at a growth temperature of 400°C, using tertiary butanol and dimethlycadmium as the oxygen and cadmium growth precursors, respectively. Further details of the growth and materials characterisation are reported elsewhere [108]. The electron density and mobility of the as-grown samples were $\sim 1.5 \times 10^{20}$ cm^{-3} and ~ 60 cm^{2}V^{-1}s^{-1}, respectively, from single-field Hall effect measurements. Particle irradiation was performed with 1 MeV ^{4}He$^+$ ions with a fluence ranging from

6.4×10^{13} cm^{-2} to 8.6×10^{16} cm^{-2}. The irradiation damage is characterised here by the displacement damage dose (product of the calculated non-ionising energy loss with the particle fluence) [114]. The stopping distance of the high energy particles was sufficiently large to ensure that they penetrated through the CdO layer into the substrate [115]. Atomic hydrogen diffusion into nominally undoped CdO was performed by annealing samples at $\sim$350°C in an ultra-high vacuum (UHV) system at a background pressure of 5×10^{-6} mbar of molecular hydrogen passed through a thermal gas cracker with a cracking efficiency of approximately 50%. Single-field Hall effect, optical transmission, 35° specular IR reflectivity and x-ray photoemission spectroscopy (XPS) measurements were performed as described in Chapter 3. All measurements were performed at room temperature.

4.3 Fermi level stabilization

As-grown CdO samples were irradiated with 1 MeV $^4He^+$ particles to introduce native defects. To accurately obtain the volume electron concentration from Hall effect measurements following the irradiation, each sample thickness was determined from simulations of the Fabry-Pérot interference fringes in IR reflectivity spectra, as shown in Fig. 4.4. The reflectivity spectra were simulated, as discussed in Section 3.3, using a transfer-matrix method to model transmission through the CdO epilayer and reflections at the air/CdO and CdO/sapphire (substrate) interfaces, as well as incoherent reflections from the back of the sapphire substrate. A two-oscillator dielectric theory model was used to account for lattice and free-carrier contributions.

Fig. 4.5 shows the evolution of electrical properties, as determined from Hall effect measurements, of CdO when native defects are introduced by this high-energy particle irradiation. The free-electron plasma frequency was also determined from the simulations of the IR reflectivity spectra discussed above. The carrier concentrations derived from these plasma frequencies gave values consistent with the Hall effect measurements. The mobility of the samples, determined both from the Hall effect measurements and from the scattering time of the conduction band plasmon

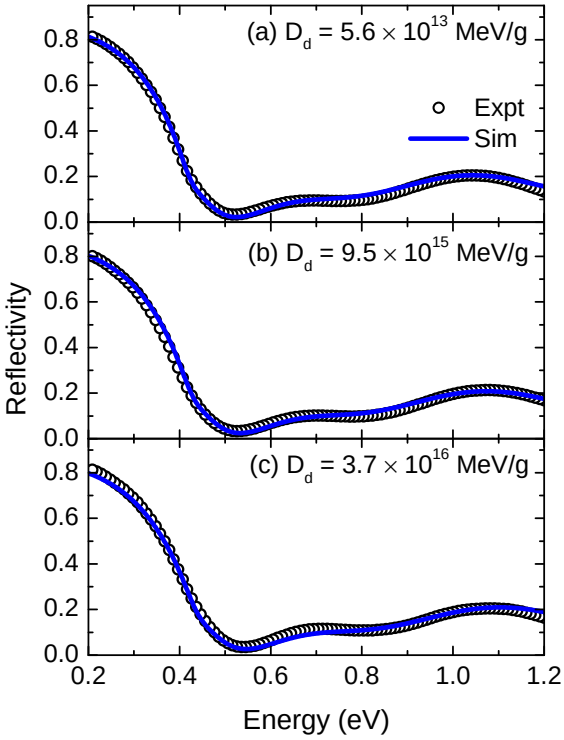

Figure 4.4: Measured (points) and simulated (line) IR reflectivity spectra of CdO following high energy particle irradiation for a displacement damage dose, D_d, of (a) 5.6×10^{13} MeV/g, (b) 9.5×10^{15} MeV/g, and (c) 3.7×10^{16} MeV/g.

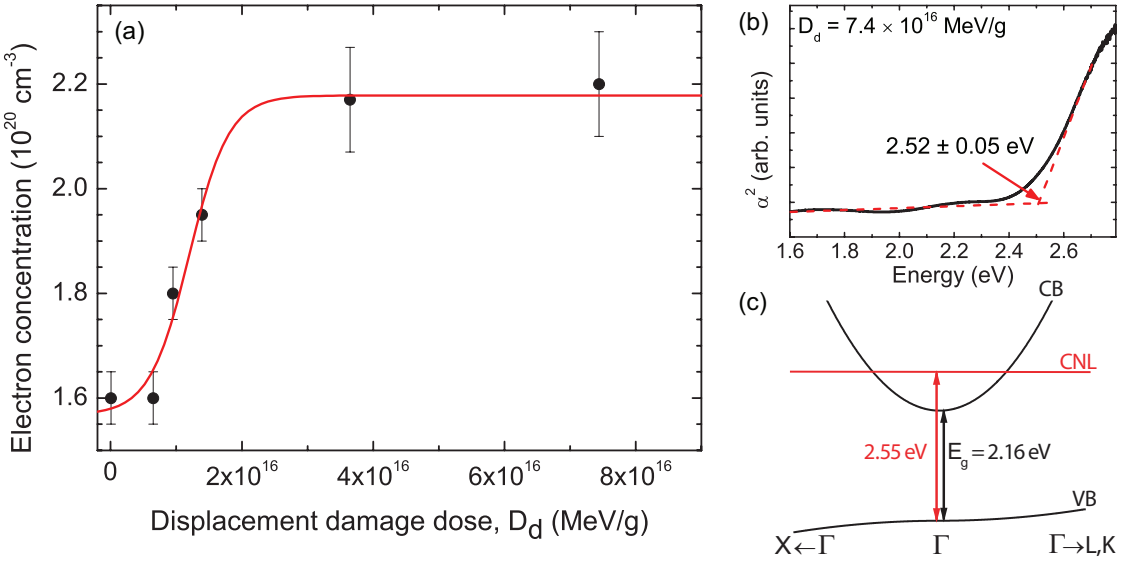

Figure 4.5: (a) Electron concentration of $^4He^+$ ion irradiated CdO as a function of displacement damage dose, D_d, with a sigmoidal fit to guide the eye. (b) Square of the optical absorption coefficient for the most heavily irradiated sample. (c) Schematic representation of the conduction (CB) and valence (VB) band edges in CdO close to Γ, indicating the position of the CNL above the CBM.

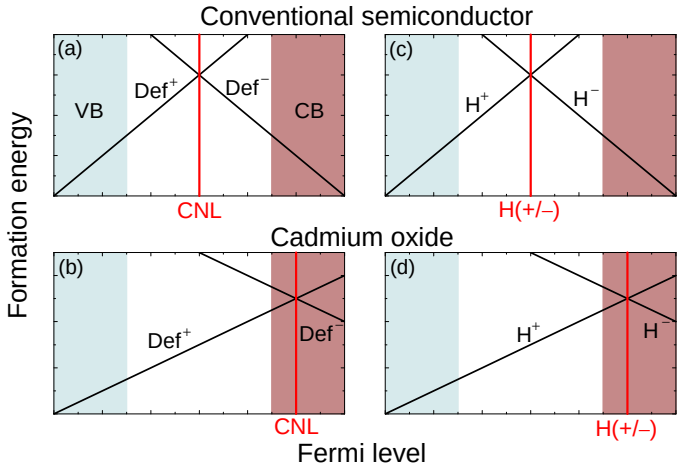

Figure 4.6: Schematic representation of the formation energy as a function of Fermi level for (a,b) irradiation-induced donor (Def^+) and acceptor (Def^-) defects, relative to the CNL, and (c,d) donor (H^+) and acceptor (H^-) hydrogen, relative to the H(+/−) level, in conventional semiconductors ((a) and (c)) and in CdO ((b) and (d)). The conduction (CB) and valence (VB) bands are represented by shading.

derived from the IR reflectivity simulations, decreased with increasing damage dose, indicating the more defective nature of the samples, and potentially increased carrier compensation.

Initially, the electron concentration increases with increasing displacement damage dose: the defects introduced are predominantly donors in nominally undoped, although already heavily n-type, CdO. With further increase in damage dose, however, the carrier concentration stabilizes at $n = 2.2 \times 10^{20}$ cm^{-3}. The stabilized carrier concentration corresponds to a bulk Fermi level 2.57 eV above the Γ-point VBM from non-parabolic carrier statistics calculations. This is in agreement (within experimental error) with optical absorption of the most heavily irradiated sample, where the Fermi level is determined to lie 2.52 ± 0.05 eV above the Γ-point VBM, as shown in Fig. 4.5(b). From the average of these values, the Fermi level is therefore determined to stabilize 2.55 ± 0.05 eV above the Γ-point VBM, and hence well above the CBM, following extremely heavy irradiation.

Within the amphoteric defect model (ADM) introduced in Section 1.4, the formation energy for donor (acceptor) native defects, such as anion (cation) vacancies, increases (decreases) with increasing Fermi level, as shown in Fig. 4.6(a). Consequently, the formation of donor native defects is most favourable when the Fermi level is below, and the formation of acceptor native defects most favourable when the Fermi level is above, an energy level known as the Fermi level stabilization energy [51]. However, the behaviour of such native defects can, more generally, be

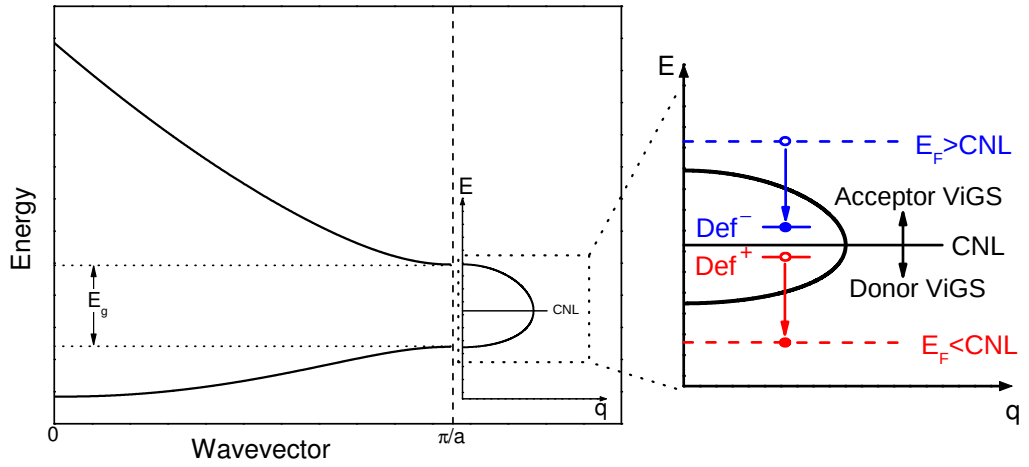

Figure 4.7: One dimensional nearly-free electron model complex band structure (see Section 1.3.1), illustrating the existence of virtual gap states (ViGS) characterised by complex wavevectors, and a schematic representation of the ADM in terms of ViGS.

considered from the charge character of the associated Virtual Gap States (ViGS), introduced in Section 1.3.1. Indeed, Inkson [11] previously showed that a deep impurity can be characterised by a localised evanescent state, that is, a ViG state.

Using the one-dimensional ViGS model described in Section 1.3.1 (see also Fig. 4.7), the ADM can be understood within the ViGS concept. This is represented schematically on the right of Fig. 4.7. If the Fermi level lies below the CNL, an energy gain can occur by an electron from a donor ViG state 'dropping down' to the Fermi level, creating a positively charged, that is, ionized, donor defect, Def^{+}. In contrast, an acceptor ViG state must remain unoccupied, and therefore neutral, as it would cost energy to promote an electron from the Fermi level up into this state. Consequently, for Fermi levels below the CNL, it is more favourable to create positively charged donor defects, acting as a source of n-type conductivity and increasing the Fermi level. In contrast, for the Fermi level above the CNL, an energy gain can occur by an electron at the Fermi level 'dropping down' into an acceptor ViG state, leaving a negatively charged ionized acceptor defect, Def^{-}. However, the Fermi level lies above the donor ViGS, and so these must remain filled, and cannot contribute to the conductivity. Consequently, for Fermi levels above the CNL, it is more favourable to create negatively charged acceptor defects, acting as a source of p-type conductivity and decreasing the Fermi level. With significant introduction of defects, the Fermi level will therefore move to the CNL,

at which point the formation energy for creating donor and acceptor native defects will become equal; no net change in carrier density will occur upon further creation of native defects, resulting in the Fermi level stabilizing at this energy [52]. Thus, the Fermi level stabilization energy within the ADM can be equated with the CNL. This explains why the ADM has previously been successful in describing the barrier height of metal-semiconductor contacts [45], as these too are determined by ViGS as discussed in Section 1.3.3.

In the majority of semiconductors, the CNL is located close to the middle of the fundamental band gap. Ion irradiation therefore preferentially produces donor defects in p-type material, whereas for n-type material, acceptor defects have the lower formation energy, as represented schematically in Fig. 4.6(a). However, donor defects are created here in already heavily n-type samples, indicating that the CNL must be located substantially above the CBM in CdO (Fig. 4.6(b)). From the above discussions and the position of the stabilized Fermi level following significant irradiation, the CNL is determined to lie 2.55 ± 0.05 eV above the Γ-point VBM, and consequently 0.39 ± 0.05 eV above the CBM, in CdO, as illustrated schematically in Fig. 4.5(c).

In addition to the behaviour of intentionally introduced defects, this has important implications for unintentionally introduced defects, and indeed doping of this material. As the CNL lies well above the CBM in CdO, and therefore above typical Fermi level positions, unintentionally introduced native defects will tend to be donors, acting to drive the Fermi level up towards the CNL and providing a source of unintentional n-type conductivity. Furthermore, the formation energy of compensating acceptor (donor) defects when n-type (p-type) doping CdO will be relatively high (low) [Fig. 4.6(b) compared with (a)] for Fermi levels above the CBM (below the VBM), allowing CdO to be extrinsically doped very heavily n-type, as has been observed experimentally [116], whereas p-type doping will be difficult.

As the ViGS are gap states, it seems counter-intuitive that the CNL can lie outside of the fundamental band gap. However, they are very localised, and so have an extended k-space character, derived from the complex band structure across the

entire Brillouin zone, rather than just at the Γ-point, with the CNL lying close to the mid-gap energy averaged across the Brillouin zone [12]. Due largely to the significant size and electronegativity mismatch of Cd and O, the CBM at the Γ-point is significantly lower than across the rest of the Brillouin zone in CdO, as confirmed by the band structure calculations shown in Fig. 4.2. Additionally, as discussed above, the valence bands disperse upwards along the $\Gamma \rightarrow$ L and $\Gamma \rightarrow$ K directions moving the valence band extrema away from Γ. The mid-gap energy averaged across the Brillouin zone, and therefore the CNL, consequently occur above the CBM at the zone centre.

4.4 Hydrogen in CdO

Hydrogen is a ubiquitous impurity in semiconductors, present in many growth environments and normally being electrically active. Interstitial hydrogen is generally considered to be a 'negative-U' defect, where the formation energy for the neutral charge state (H^0) always lies above that of either the positive donor (H^+) or negative acceptor (H^-) centre [25]. Hydrogen, therefore, primarily forms either donor or acceptor states when the Fermi level lies below or above an energy, H(+/−), respectively. Similar to the native defects discussed above, hydrogen forms a very localised impurity centre; it is therefore appropriate to also consider this within the ViGS framework. Indeed, the theoretical work of Van de Walle and Neugebauer [25] argued that hydrogen in the positive charge state can be associated with the creation of a cation dangling bond, whereas for hydrogen in the negative charge state, an anion dangling bond will exist. Through the discussions of native defects above, the H(+/−) transition should therefore occur at the CNL of the material.

To investigate this experimentally, atomic hydrogen was diffused into nominally undoped CdO for 1 and 3 h, as described in Section 4.2. Optical absorption spectra of the untreated sample and following diffusion of hydrogen are shown in Fig. 4.8. The incorporation of hydrogen within the semiconductor causes an increased Moss-Burstein shift of the absorption edge, associated with the Fermi level increasing in the conduction band, as represented schematically in the inset of

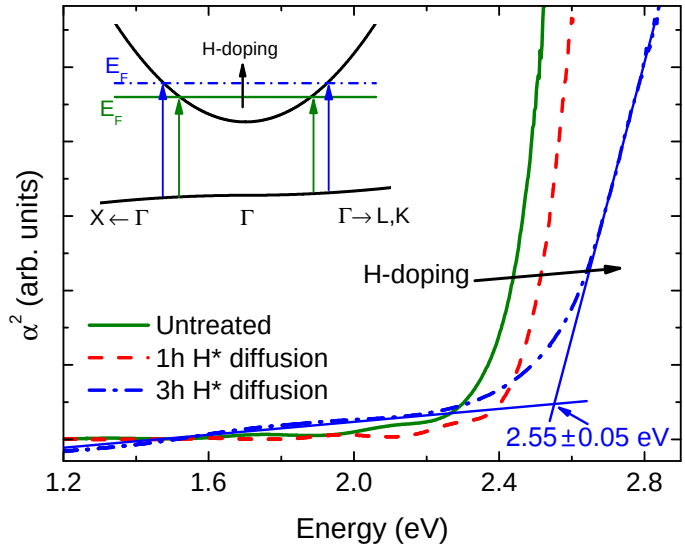

Figure 4.8: Squared optical absorption coefficient for untreated CdO and CdO following diffusion of atomic hydrogen for 1 and 3 h. An increased Moss-Burstein shift is evident with increased hydrogen doping, represented schematically inset.

Fig. 4.8. This is supported by Hall effect measurements which reveal an increase in carrier concentration from 1.4×10^{20} cm^{-3} to 2.2×10^{20} cm^{-3} upon diffusion of hydrogen. Following the 3 h treatment, the measured carrier density equates to a Fermi level 2.57 eV above the Γ-point VBM, in agreement with the value of 2.55 ± 0.05 eV determined from optical absorption.

Hydrogen therefore forms an electrically active donor, even in highly n-type CdO. This is in agreement with spectroscopic evidence for the shallow donor nature of muonium, a light isotope analogue of hydrogen, in CdO [117]. However, this is in contrast to the situation in most materials where hydrogen forms an acceptor (H^-) in n-type, or a donor (H^+) in p-type, material [25], as represented schematically in Fig. 4.6(c). In rare cases, however, perhaps most notably in ZnO, hydrogen has been predicted to act solely as a donor [102], independent of whether it occurs interstitially or substitutionally, where it forms a multicentre bond [118]. As for ZnO, the H(+/−) transition must be above the CBM in CdO (Fig. 4.6(d)). In this work, the Fermi level is observed to be located at the same energy as the CNL after significant diffusion of hydrogen. This provides the first experimental evidence of the equality of the CNL and the H(+/−) level, providing a common origin governing the electrical behaviour of both native defects and hydrogen in semiconductors.

Given its prevalence in common growth environments, in particular in MOVPE as used for the growth of the samples investigated here, hydrogen is certainly a plau-

sible candidate for the unintentional dominant donor giving rise to the high n-type conductivity of nominally undoped CdO samples, in addition to the donor native defects discussed above. Indeed, annealing in UHV has previously been observed to reduce the carrier concentration in MOVPE-grown CdO samples [105]. This is also observed here for a sample annealed at 600°C in UHV for 2 h, before (after) which the carrier concentration and mobility were determined from Hall effect measurements to be 1.7×10^{20} cm^{-3} (1.6×10^{19} cm^{-3}) and 59 cm^{2}V^{-1}s^{-1} (106 cm^{2}V^{-1}s^{-1}) respectively. The carrier density determined by Hall effect measurements following annealing is in agreement with the Fermi level determined from optical absorption measurements and the plasma frequency determined from IR reflectivity measurements, shown in Fig. 4.10 (b) and (c), respectively. Thermal de-bonding and removal of hydrogen is a likely cause for this dramatic improvement in electrical properties upon annealing. In all materials where the CNL, and consequently the H(+/−) level, is above the CBM, hydrogen must certainly be considered as a potential cause of unintentional n-type conductivity in addition to donor-type native defects. Conversely, when the CNL lies below the VBM, hydrogen is a plausible candidate for unintentional p-type conductivity.

4.5 Surface electron accumulation

To investigate the importance of the CNL in determining surface electronic properties, the surface Fermi level position in a CdO sample, prepared by annealing in UHV at 600°C for 2 h (discussed above), has been investigated. Information on the chemical nature of the surface was obtained from core-level XPS measurements, shown in Fig. 4.9. Prior to annealing, a pronounced multiple peak structure was observed for the Cd $3d_{5/2}$ core level. The lower binding energy component is attributed to Cd–O bonding in the CdO, with the higher binding energy components attributed to bonding to more electronegative species such as in CdO_2 (peroxide), $Cd(OH)_2$ (hydroxide) and $CdCO_3$ (carbonate) compounds, present due to atmospheric surface contamination and potentially remnants of the growth precursors. Equivalently, the low binding energy component of the O $1s$ peak is attributed to

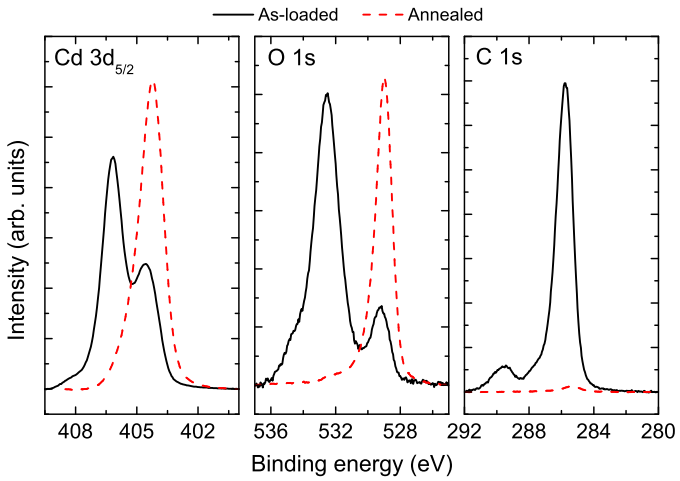

Figure 4.9: Cd $3d_{5/2}$, O $1s$ and C $1s$ XPS core-level peaks from CdO before (solid line) and after (dashed line) annealing the sample at 600°C in UHV. The intensities have been normalized relative to the Cd $3d_{5/2}$ intensity.

Cd–O bonding, with the higher binding energy components due to the peroxide, hydroxide and carbonate species. A large C $1s$ peak was also observed, with a low binding energy component due to adventitious physisorbed hydrocarbon, and higher binding energy components due to carbonate and alcohol species. Following annealing, the components in the XPS core level peaks due to peroxide, hydroxide and carbonate species were quenched, with only a negligible peak due to adventitious hydrocarbon remaining (Fig. 4.9). A slight asymmetry to higher binding energies was observed on the core level peaks. However, CdO is shown below to exhibit electron accumulation at its surface. The asymmetry in the core level peaks is attributed to satellite features due to conduction band plasmons in the accumulation layer, as was observed for the analogous compound InN [119].

Valence band XPS measurements following annealing of the sample are shown in Fig. 4.10(a). A linear extrapolation of the leading edge of the valence photoemission, to account for the finite resolution of the spectrometer [120], gives the L-point (indirect) VBM to surface Fermi level separation as $\xi = 1.29 \pm 0.05$ eV. From Hall effect, optical absorption and IR reflectivity measurements (Fig. 4.10(b) and (c)), the Γ-point VBM to bulk Fermi level separation was determined as $\eta = 2.23 \pm 0.05$ eV. Taking the separation of the Γ-point and L-point of the valence band as 1.2 eV as discussed above, the Fermi level lies higher relative to the band extrema at the surface than in the bulk, implying a downward bending of the bands at the surface. The calculated band bending is shown in Fig. 4.10(d). Below the CNL, surface

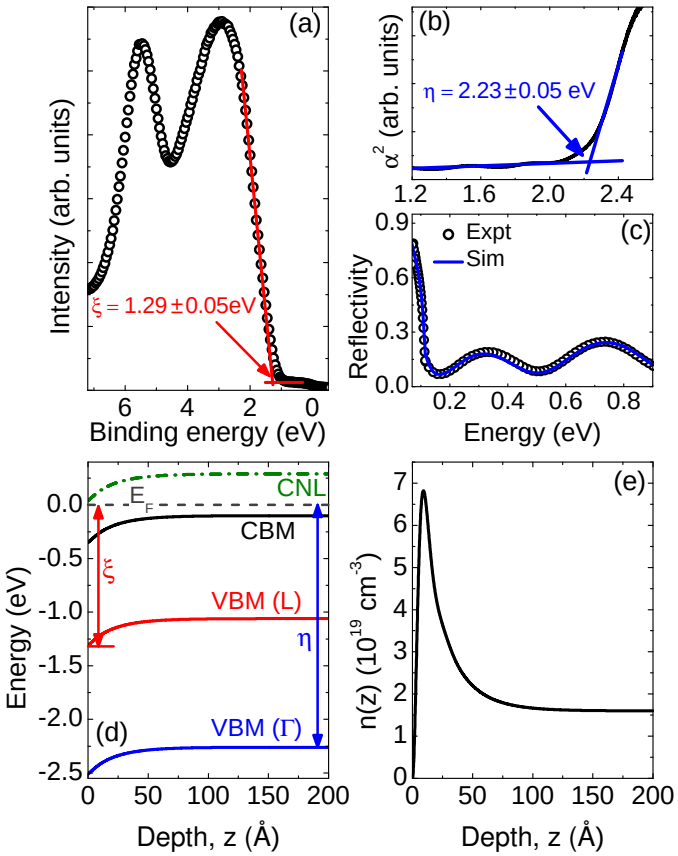

Figure 4.10: (a) Valence band photoemission, (b) squared optical absorption coefficient and (c) measured (points) and simulated (line) IR reflectivity spectrum for an undoped CdO sample following annealing at 600°C in UHV for 2 h. (d) Band bending (CBM, indirect (L-point) and direct (Γ-point) VBM) and (e) carrier concentration as a function of depth below the surface in the electron accumulation layer.

states can be described by ViGS which are predominantly donor-like (see Chapter 1). As the surface Fermi level pins slightly below the CNL value determined above (Fig. 4.10(d)), a number of these donor-like ViGS are unoccupied, and therefore ionized, leading to a positive surface charge. As the CNL is above the CBM in CdO, these ViGS are able to donate their electrons directly into the conduction band. This leads to a large accumulation of electrons in the near-surface region, as shown in Fig. 4.10(e), which screen the surface charge, maintaining charge neutrality. The CNL lying above the CBM in CdO can therefore be understood as the overriding mechanism driving the accumulation of electrons at the CdO surface. Some more features of the electron accumulation in CdO will be discussed in Chapter 9.

4.6 Implications and prospects

The above investigations have shown that a single energy level, fundamentally deriving from the bulk band structure of a material, dictates the favourable charge state

for native defects, hydrogen impurities and surface states in semiconductors. When the Brillouin zone averaged mid-gap energy, and hence the CNL, lie in the conduction band, as for CdO investigated here, the material exhibits properties such as: donor nature of hydrogen; high unintentional n-type conductivities; ease of n-type but difficulty of p-type doping; and surface electron accumulation. Similar properties would be expected for other semiconductors with a large size and electronegativity mismatch between the cation and anion, leading to particularly low Γ-point CBMs lying below the CNL. This explains, for example, why the oxide materials such as ZnO, SnO_2 and indeed CdO can have very high n-type conductivities, despite being optically transparent.

Conversely, in a material such as GaSb, the critical points of the conduction band edge are all located at similar energies, whereas the downwards dispersion of the valence bands away from Γ is rather pronounced [121]. Consequently, the CNL would be expected to lie at or even below the VBM in this material, explaining its propensity for unintentional p-type conductivity, surface hole accumulation [122] and the recent theoretical predictions of the acceptor nature of hydrogen even in p-type material [103]. Another interesting example is the Cu-containing delafossite materials. In these, the very high Cu p-orbital energy pushes the VBM upwards in energy, and so the CNL will lie relatively close to the VBM. High p-type conductivity can therefore be achieved, even in wide band gap materials as has previously been observed experimentally [123], explaining the use of Cu in p-type transparent conducting oxide semiconductors.

In general, band structure engineering of semiconductors involves the alloying of several compounds in order to control basic optoelectronic and structural properties (for example, the band gap and lattice constant). Using the insights gained here, this can be extended to tailor the electrical properties of the material by considering not only the band gap and lattice constant of the constituent compounds, but also the position of the band extrema relative to the CNL. For example, if an alloy is formed incorporating a material with a low Γ-point CBM, elements with low s–orbital energies, or dilute impurities which cause an anti-crossing interaction

lowering the conduction band edge [5], the CBM of the alloy will be pushed down with respect to the CNL, increasing its tendency towards n-type conductivity and surface electron accumulation. If, on the other hand, a high Γ-point VBM material is used, elements are incorporated with high p-orbital energies or a valence band anti-crossing interaction [124] is introduced pushing the VBM upwards with respect to the CNL, the proclivity towards acceptor defects, impurities and surface states will be increased.

4.7 Conclusions

The nature of the charge state of native defects, hydrogen and surface states has been unified via a single energy level deriving from the bulk band structure, the charge neutrality level. In CdO, this level was shown to be located 2.55 ± 0.05 eV above the Γ-point VBM, and consequently 0.39 ± 0.05 eV above the CBM, resulting in not only native defects but also hydrogen impurities and surface states being donors even in already n-type material. The unification of bulk and surface electronic properties presented here facilitates a general understanding of the electronic properties of all semiconductors, and allows the possibility of band structure engineering of materials to obtain not only the desired band gap and lattice constant, but also to tailor their bulk and surface electrical characteristics.

Chapter 5

Charge neutrality level in InN

5.1 Introduction

Initial research on InN suggests that this material has enormous potential for use in a range of device applications. It has excellent potential transport characteristics, such as high electron mobilities [125], small electron effective mass [126], high peak drift velocities [127], and high frequency transient drift velocity oscillations [128]. These suggest potential application for InN in high frequency electronic devices, operating up to the THz range. InN has also been suggested as a suitable material for light emission in the THz frequency range [129], with emission intensities already reported that exceed those from p-type InAs [130], which was previously thought to be the most efficient THz emitter. Further increases in emission intensity have recently been reported for a-plane InN [131] and from InN nanorod arrays [132]. InN has also shown potential for use as a chemical sensing device, with a chemically selective 'fast capture, slow response' modification of its electrical properties observed upon exposure to a number of solvents [133], and has also been proposed as a suitable material for biological sensing applications [134] and for anion concentration measurements [135,136]. In addition, In-containing III-N alloys have attractive properties for a range of optoelectronic device applications, discussed in Chapter 7.

Irrespective of these potential applications, InN remains probably the least understood of the III-V semiconductor materials, despite an intense recent research effort. A number of seemingly unusual properties have, however, already been identified. In particular, InN has a propensity for high n-type conductivity [137], with nominally undoped material typically having carrier concentrations in the range $10^{17} - 10^{21}$ cm^{-3}. This n-type conductivity increases still further approaching the surface of the material, where InN is known to exhibit a surface electron accumulation layer [7,138]. This surface electron accumulation is much more extreme than in InAs [39], the only other III-V material in which this phenomenon has been ob-

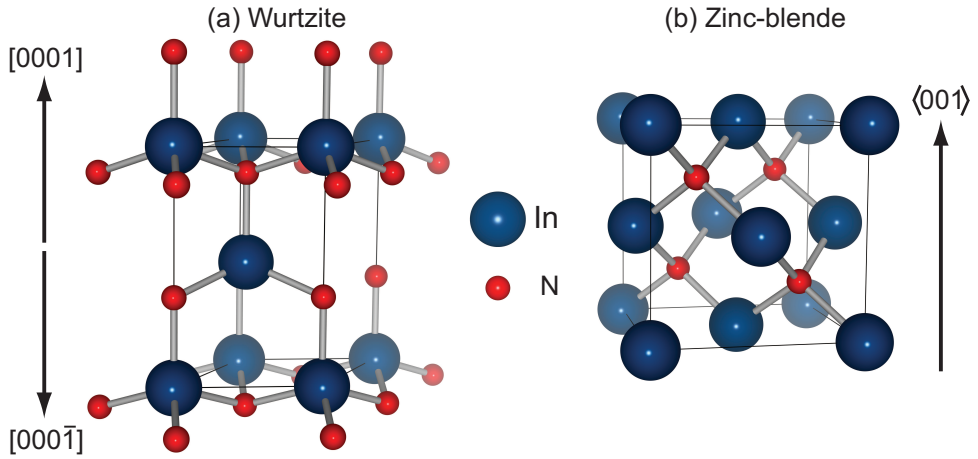

Figure 5.1: (a) Wurtzite and (b) zinc-blende crystal structure of InN. The unit cell is shown as a thin black line. The corresponding Brillouin zones are shown in Fig. 5.2.

served. Consequently, metal contacts to InN surfaces have been found to exhibit almost exclusively Ohmic behaviour [138, 139]. This has important implications for a variety of device architectures.

From the considerations presented in Chapter 4, these properties would seem to be consistent with the charge neutrality level (CNL) lying above the conduction band minimum (CBM), as was observed for CdO, the II-VI equivalent of InN. This is shown to be the case in this chapter from studies of Si-doped InN samples (and an undoped reference sample) using a combination of high-resolution x-ray photoemission spectroscopy (XPS), optical absorption spectroscopy (OAS), infrared (IR) reflectivity, and theoretical calculations employing quasiparticle-corrected density-functional theory (QPC-DFT). The rather extreme location of the CNL in InN, determined as lying 1.83 ± 0.10 eV above the valence band maximum (VBM), is rationalised within chemical trends, and is used to explain the striking fundamental bulk, surface and interface electronic properties of this material.

5.1.1 Crystal and electronic structure

The thermodynamically stable phase of InN, and indeed GaN, AlN and (In,Ga,Al)N alloys, is the wurtzite (wz) polymorph with space group $P6_3mc$, shown in Fig. 5.1(a). In this structure, the In and N atoms are arranged in hexagonally close packed planes which alternate along the crystal c-axis. As for the zinc-blende (zb) structure,

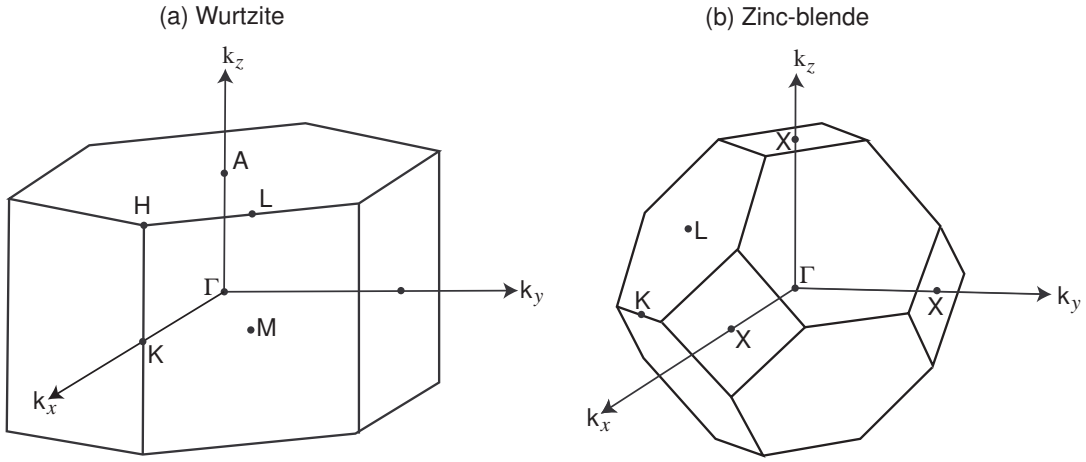

Figure 5.2: Brillouin zone of the (a) wurtzite and (b) zinc-blende structure.

most common amongst III-V semiconductors, the atoms are tetrahedrally bonded. However, due to a reduced symmetry compared to the *zb* structure, the [0001] and [000$\bar{1}$] crystallographic directions are inequivalent, and so the nitrides are polar materials. The In- (N-) polarity is defined as the orientation of the crystal such that there is a single bond from the In (N) atom directed towards the surface along the *c*-axis, and three bonds in the direction away from the surface, that is, upwards (downwards) in Fig. 5.1(a). The *a*-plane (11$\bar{2}$0) and *m*-plane (1$\bar{1}$00) surfaces are both non-polar. The lattice constants for *wz*–InN are $a = 3.5377$ Å and $c = 5.7037$ Å [140]. The Brillouin zone for the *wz* structure is shown in Fig. 5.2(a).

The QPC-DFT calculated band structure for *wz*-InN is shown in Fig. 5.3(a). In the tetrahedrally bonded configuration, there are eight valence electrons per unit cell. In a simple tight-binding picture, these form four doubly spin-degenerate valence bands of *p*–orbital character (the highest 3 bands) and of *s*–orbital character. Neglecting spin-orbit and crystal-field splitting, the three *p*–bands are degenerate at the VBM, with Γ_{15}^{v} symmetry. Including the spin-orbit and crystal-field (due to the non-isotropic wurtzite structure) interactions splits the Γ_{15}^{v} bands into an upper Γ_{9}^{v} and two lower $\Gamma_{7\pm}^{v}$ bands. Localized energy levels due to the In 4*d* orbitals can be seen $\sim$15 eV below the VBM, which hybridize with the N 2*s*–like orbitals (bottom valence band), as discussed elsewhere [83, 141]. A highly non-parabolic Γ_{15}^{c} conduction band is also present, necessitating the use of the non-parabolic band structure approximations discussed in Section 2.1.1. The higher lying conduction bands are

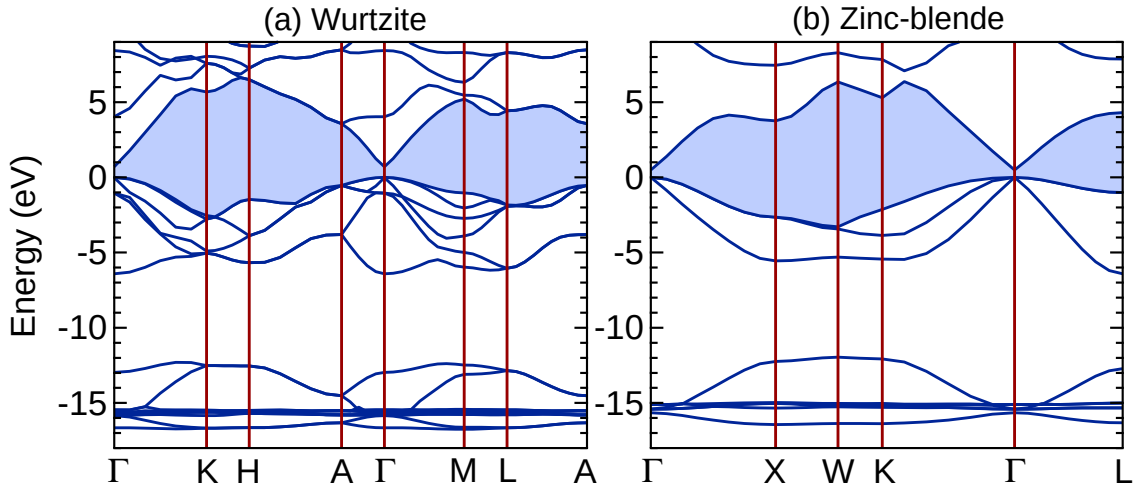

Figure 5.3: QPC-DFT band structure calculations for (a) *wz* and (b) *zb* InN [65]. The fundamental energy gap across the Brillouin zone is represented by shading.

well separated in energy from the lowest conduction band, and so the influence of the higher lying bands on the dispersion around the CBM will be minimal, suggesting the 2-band $\mathbf{k} \cdot \mathbf{p}$ approach outlined in Section 2.1.1 is generally adequate for InN.

Formation of the *zb* polymorph of InN, shown in Fig. 5.1(b), is calculated to cost only an extra ~ 20 meV of energy per cation-anion pair compared to the *wz* polymorph [64]. Consequently, judicious choice of substrate material, orientation, and growth conditions allows growth of *zb*-InN [142–145]. It is thought that the *zb* polymorph may be preferable to the *wz* one for potential device applications due to the smaller predicted band gap [64] and higher degree of symmetry, removing the anisotropy present in wurtzite structures. However, structural quality is unlikely to be as high as for *wz*–InN, with *wz* inclusions likely within a *zb* sample. The Brillouin zone and calculated band structure are shown for *zb*–InN in Figs. 5.2(b) and 5.3(b), respectively. The electronic band structure is similar to that for the *wz* structure, although somewhat simpler in this case due to the lack of crystal field splitting. The lattice constant of *zb*-InN is 5.01 Å [144]. While at standard temperature and pressure, the rocksalt (*rs*) structure (the stable polymorph for CdO considered in Chapter 4) has a very high formation energy [64], a high-pressure ($\sim$12 GPa) *wz*–*rs* phase transition occurs [146]. However, as this phase is only stable at high pressures, this structure will not be considered further here.

At a surface, the atomic arrangement can differ from that of the bulk material

in order to minimise energy. The III-N materials are known to reconstruct to form a metal-rich surface. This has been extensively studied for GaN [147–149], where the Ga-polar (N-polar) material has been found to be terminated by ~ 2.4 (~ 1) monolayers (ML) of Ga following Ga-rich growth. Recent theoretical [150] and experimental [151,152] investigations have also revealed In-adlayers as the favourable reconstruction at InN surfaces with ~ 2, ~ 3 and ~ 3.4 ML of In observed at the surface of N-polar, a-plane and In-polar InN, respectively.

5.1.2 Band parameters

The most fundamental property of any semiconductor is the size of its band gap. One of the most important occurrences in the development of InN to date was the revision of its accepted fundamental band gap value from ~ 2 eV [153] to less than 0.7 eV [154]. Early material was typically sputter-grown, and generally had very high electron densities leading to a large Moss-Burstein (MB) shift in the absorption edge, and hence the incorrect assignment of the band gap as ~ 2 eV. Improved growth of InN, largely by plasma-assisted molecular beam epitaxy (PAMBE), led to a dramatic reduction in electron concentration of nominally undoped material (see, for example, Fig. 18 in Ref. [137]), reducing the MB shift and consequently allowing the much lower value of the fundamental band gap to be revealed [154–158]. The revision of the InN band gap proved very controversial [159–161], although the debate has been almost entirely settled now (up to the second decimal place in the band gap value) [140]. Here, the extrapolated zero-temperature, zero-density band gap value and Varshni parameters derived by Wu *et al.* [154] are employed, giving a room temperature band gap of 0.64 eV.

Due to the highly non-parabolic nature of the conduction band, the effective mass varies rapidly with energy. Consequently, for samples with high carrier concentration, it is difficult to determine the band edge effective mass value. Wu *et al.* [162] used the variation of the plasma frequency determined from simulation of IR reflectivity spectra of a number of samples with differing carrier concentrations to obtain a value of $0.07m_0$. Fu and Chen [126] employed the same approach,

Table 5.1: Material parameters (a and c lattice constants, zero temperature band gap and Varshni parameters, spin-orbit and crystal-field splitting, and conduction band minimum effective mass) for wurtzite InN, GaN and AlN.

	a (Å)	c (Å)	$E_g(T=0)$ (eV)	α (meV/K)	β (K)	Δ_{so} (meV)	Δ_{cr} (meV)	m_0^* (m_0)
InN	3.538	5.704	0.69	0.414	454	5	24	0.048
GaN [170]	3.189	5.185	3.410	0.909	830	17	10	0.20
AlN [170]	3.112	4.982	6.25	1.799	1462	19	-169	0.31

although included a lower carrier density sample, determining a value of $0.05m_0$, while Hofmann *et al.* [163] determined a value of $0.047m_0$ from IR magneto-optic generalized ellipsometry measurements. Recently, Miller *et al.* [164] determined a value of $\sim 0.05m_0$ from modelling of thermopower measurements. In light of this scatter, a value of $0.048m_0$ is used here, determined from the empirical relationship $m_0^* \sim 0.07E_g$ [165], which is very close to the values determined from the most recent experimental studies. For the valence bands, the crystal-field and spin-orbit splitting are taken as 24 meV and 5 meV respectively [166]. The hole effective masses are not known, with only theoretical estimates having been provided [167–169]. The parameters of Fritch *et al.* [168] are therefore used here. The main materials parameters discussed above for InN, and the equivalent parameters for GaN and AlN, are summarised in Table 5.1.

5.2 Experimental and theoretical details

Wurtzite InN(0001) samples were grown on c-plane sapphire substrates by PAMBE at Cornell University, USA. Details of the growth and materials characterisation are reported elsewhere [171]. The InN layer thicknesses ranged from 250 to 2000 nm and the growth temperature was ∼480°C. The carrier concentrations and mobilities (from single-field Hall effect measurements) vary from 2.0×10^{18} cm^{-3} to 6.6×10^{20} cm^{-3} and 1100 cm^{2}V^{-1}s^{-1} to 38 cm^{2}V^{-1}s^{-1}, respectively. All except the lowest carrier concentration sample were doped with Si. Single-field Hall effect, optical transmission, IR reflectivity, and XPS measurements were performed as described in Chapter 3. All measurements were performed at room temperature. QPC-DFT calculations were performed elsewhere, as discussed in Section 2.1.2. For comparison

with the experimental results, the QPC-DFT valence band density of states (VB-DOS) is broadened by a 0.2 eV full width at half maximum (FWHM) Lorentzian and a 0.4 eV FWHM Gaussian to account for lifetime and instrumental broadening, respectively.

5.3 Determination of the CNL position

5.3.1 Results and analysis

The carrier concentration of the samples, determined from single-field Hall effect measurements, increases with increasing Si cell temperature during growth, indicating that Si is being incorporated into the InN host and is electrically active, acting as a donor. This is confirmed by XPS measurements of the Si 2*p* core-level peak (Fig. 5.4(a)), which increases in intensity with increasing carrier concentration. Additionally, the binding energy of the peak ($\sim$102 eV) is indicative of Si–N bonding [172] (the peak is chemically shifted from its elemental position in Si of $\sim$99 eV) confirming that the Si preferentially occupies the In–site, therefore acting as a donor. The increase in carrier density of the samples with increasing Si cell temperature was also confirmed from an increase in the conduction electron plasma frequency determined from IR reflectivity measurements, shown in Fig. 5.4(b). The reflectivity spectra were simulated using a two-oscillator dielectric theory model to account for lattice and free-carrier contributions. The transfer-matrix method discussed in Section 3.3 was used to model the effects of the InN epilayer as well as the GaN and AlN buffer layers, and the sapphire substrate. The plasma frequencies determined from these simulations gave carrier densities in reasonable agreement with those from Hall effect measurements.

OAS spectra, shown in Fig. 5.4(c), also indicate the effects of the increase in free-carrier concentration as an increase in free-carrier absorption at low photon energies. Additionally, the OAS spectra directly indicate the effects of doping on the bulk Fermi level: a significant increase in the absorption edge energy is observed with increasing doping, attributed to the MB band-filling effect, whereby the (de-

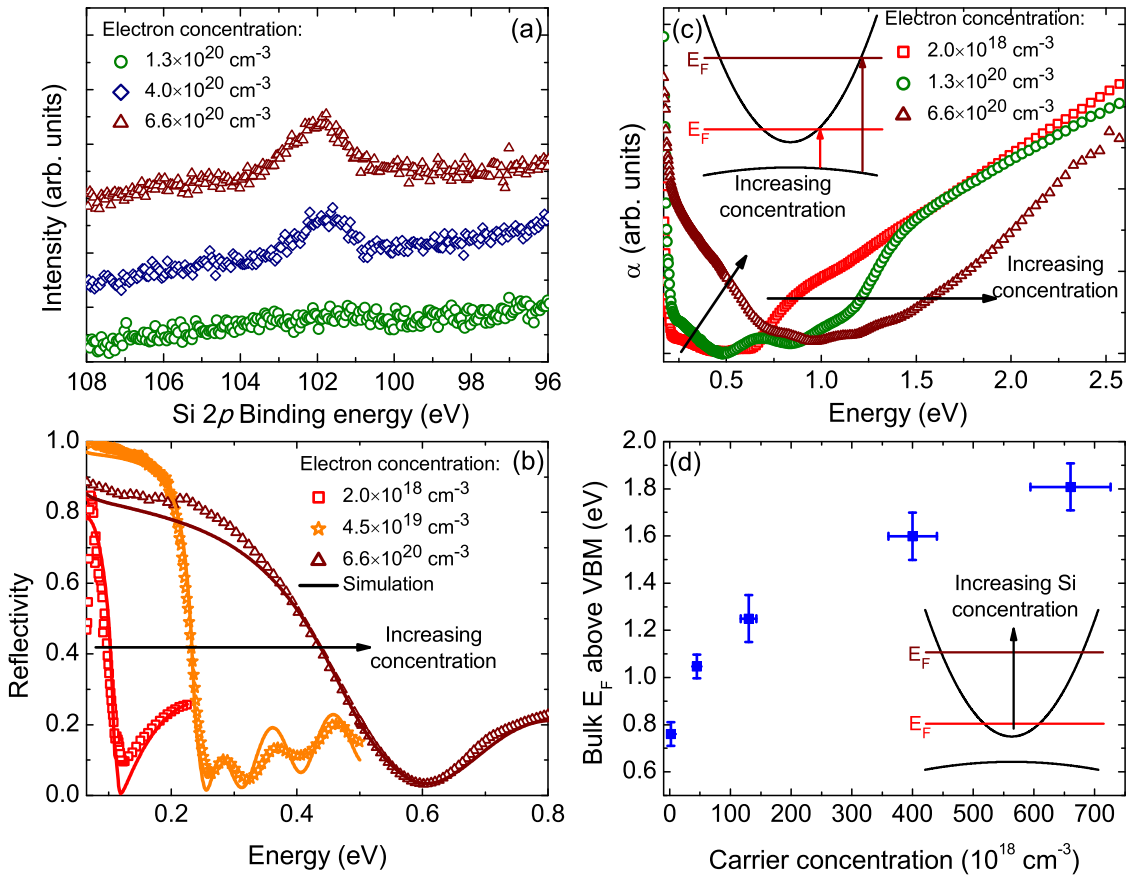

Figure 5.4: (a) Si 2*p* core-level XPS spectra, (b) IR reflectivity spectra, and (c) OAS spectra of a selection of undoped and Si-doped InN samples. A schematic of the Moss-Burstein shift of the optical absorption edge is shown inset in (c). (d) Bulk Fermi level versus carrier density for the samples investigated here. A schematic of the shift of bulk Fermi level with increasing Si concentration is shown inset.

generate) Fermi level shifts to higher energies with increasing doping, represented schematically inset. An exponential Urbach tail is seen below the absorption edge, and the extent of this tail increases with doping concentration due to the increase in band-tailing effects.

This Urbach tail limits the accuracy of the Fermi level position that can be determined from the OAS measurements. Instead, the bulk Fermi level position is determined here from the measured electron concentration and carrier statistics calculations. However, due to the very high doping levels involved, resulting in the Fermi level lying over 1 eV above the CBM in the most heavily doped samples, even non-parabolic band structure approximations (such as the $\mathbf{k} \cdot \mathbf{p}$ model introduced in Section 2.1) are limited in accuracy for the most heavily doped samples.

Consequently, carrier statistics calculations employing the conduction band dispersion from QPC-DFT calculations have been used to determine the bulk Fermi levels from the measured carrier concentrations; these are shown in Fig. 5.4(d). The values determined using the conduction band dispersion from QPC-DFT calculations agree well with those from $\mathbf{k} \cdot \mathbf{p}$ carrier statistics calculations for the lower doped samples, but diverge somewhat for the more heavily doped samples. It should be noted that the electron concentrations determined from the single-field Hall effect measurements contain a contribution from a surface electron accumulation region and an increase in electron density approaching the interface in addition to the bulk (see below and Chapter 6). This introduces a small error in calculating the bulk Fermi level based on the single-field Hall effect concentrations for the lower carrier concentration samples. This, along with the small discrepancies between the carrier density determined from Hall effect and IR reflectivity measurements, is represented by the error bars in Fig. 5.4(d). The bulk Fermi level positions are also consistent with the optical absorption edge positions in Fig. 5.4(c), although as discussed above, the large extent of Urbach tailing for the very heavily doped samples prevents an accurate determination of the bulk Fermi level position being made from the OAS measurements of these samples.

XPS was employed to determine the pinning position of the Fermi level at the surface as a function of bulk carrier concentration. The leading edges of the valence band photoemission spectra are shown in Fig. 5.5(a). The surface Fermi level position can be obtained by extrapolating the leading edge of the valence band photoemission to the baseline in order to take account of the finite resolution of the spectrometer [120]. The values determined in this way are shown in Fig. 5.5(b). For the nominally undoped sample, the surface Fermi level position lies well above its position in the bulk of the semiconductor (*cf.* Fig. 5.4(d)). Consequently, a pronounced downward bending of the conduction and valence bands relative to the Fermi level occurs at the surface of the nominally undoped InN, consistent with previous observations of a surface electron accumulation layer in this material [7]. Increasing the doping shifts the leading edge of the valence band photoemission to

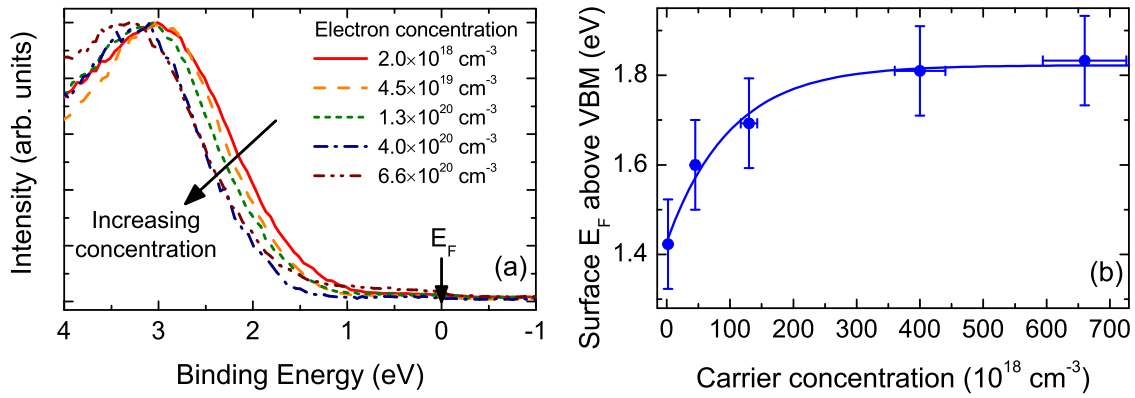

Figure 5.5: (a) Valence band photoemission spectra and (b) corresponding VBM to surface Fermi level separation evaluated by extrapolating the leading edge of the XPS spectra to the baseline to account for the finite resolution of the spectrometer. The solid line is an exponential fit to the data, to guide the eye.

higher binding energies indicating an increase in the VBM to Fermi level separation at the surface with increasing bulk doping. With continued increase in bulk doping, a stabilization of the surface Fermi level occurs at 1.83 ± 0.10 eV above the VBM.

For low bulk doping levels, the presence of such a significant band bending can cause the linear extrapolation method of analysis of the valence band photoemission to slightly underestimate the VBM to surface Fermi level separation [173]. An alternative method of analysis is to compare the position of spectral features in the valence band photoemission with those of a calculated VB-DOS which shows good spectral agreement with the photoemission results. This has been demonstrated for the QPC-DFT VB-DOS calculations of InN employed here [83]. The VBM is defined as 0 eV in the QPC-DFT calculations, and so the energy separation of the lowest energy peak in the VB-DOS and the corresponding peak in the XPS spectra gives the VBM to surface Fermi level separation. The valence band XPS spectra are shown, compared to the QPC-DFT VB-DOS, in Fig. 5.6(a), and the VBM to surface Fermi level separation determined by this method is shown as a function of bulk carrier concentration in Fig. 5.6(b).

For the lowest bulk carrier concentration sample, the Fermi level is pinned a little higher at the surface than was determined using the linear extrapolation method due to the significant downward band bending present and the finite escape depth of photoelectrons [173]. The surface Fermi level positions for the higher

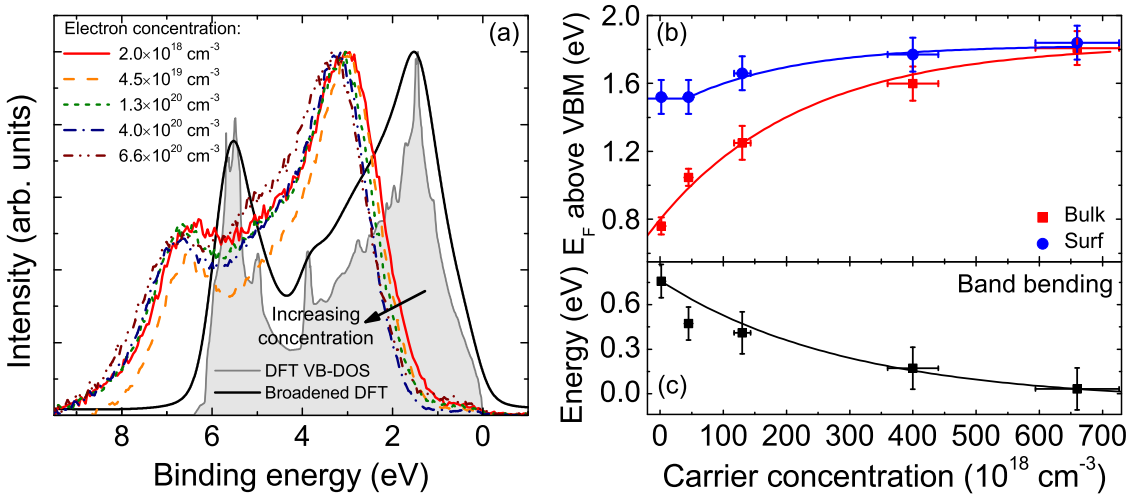

Figure 5.6: (a) QPC-DFT VB-DOS shown without (shaded) and with lifetime and instrumental broadening, and the Shirley-background-subtracted valence-band photoemission spectra, offset from the calculated VB-DOS due to Fermi level shifts. (b) VBM to bulk and surface Fermi level separation, with fits shown to guide the eye, and (c) resulting band bending.

bulk carrier concentration samples agree within experimental error between the two methods of analysis. This analysis reveals that the surface Fermi level is virtually static with increasing bulk carrier concentration below a value of $\sim 5 \times 10^{19}$ cm^{-3}. Further increase in bulk carrier concentration again leads to an increase and then saturation of the surface Fermi level position. Any difference between the bulk and surface Fermi level positions must be incorporated via a bending of the bands relative to the Fermi level, shown in Fig. 5.6(c), which tends smoothly to zero with increasing bulk carrier concentration.

5.3.2 Discussions

For a given bulk Fermi level, the surface Fermi level position is determined by the considerations of charge neutrality. If the surface Fermi level is located below the CNL, some donor surface states will be unoccupied and hence positively charged. This surface charge must be balanced by a space-charge due to downward band bending, leading to an increase in the near-surface electron density (an accumulation layer). For nominally undoped (low carrier concentration) InN, an extreme downward band bending was observed: the Fermi level must therefore be pinned some way below the CNL in these samples, as represented schematically in Fig. 5.7(a).

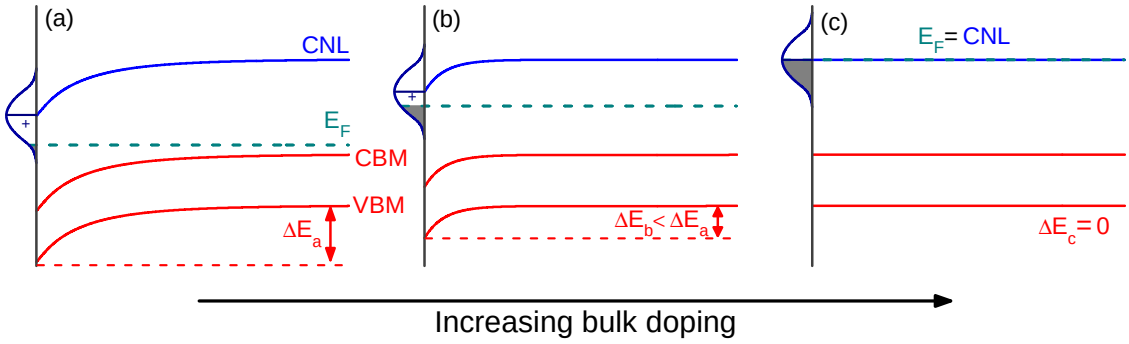

Figure 5.7: Schematic representation of the decrease in downward band bending ΔE, corresponding reduction in unoccupied surface-state density as the Fermi level moves closer to the CNL at the surface, and eventual stabilization of the bulk and surface Fermi levels at the CNL with increasing doping ((a) to (c)) in InN.

As the bulk Fermi level is increased, the amount of downward band bending must necessarily decrease, reducing the space charge. However, if this was all that happened, charge neutrality would no longer be maintained, as the surface charge would no longer balance the space charge. Consequently, as the bulk Fermi level increases, the surface Fermi level must move closer to the CNL so that a smaller density of donor surface states are unoccupied, reducing the surface charge to that of the new space charge, as represented in Fig. 5.7(b). For initial increases in bulk Fermi level, the change in the space-charge can be accommodated by very small shifts in the surface Fermi level position; the Fermi level is strongly *pinned* at the surface, seen by the virtually static position of the surface Fermi level for the two lowest carrier concentration samples in Fig. 5.6(a). However, as the bulk Fermi level increases further, larger reductions of the surface-state density, achieved by shifting of the surface Fermi level towards the CNL, are required to maintain charge neutrality (Fig. 5.7(b)). As the bulk Fermi level approaches the CNL, the surface Fermi level must also therefore approach the CNL, causing the band bending to tend to zero (Fig. 5.7(c)). Consequently, for the most heavily doped sample, there is zero space charge, as there is no band bending, and zero surface charge as the surface Fermi level is pinned at the CNL leading to zero density of charged surface states: charge neutrality is maintained.

The stabilization of the Fermi level at the CNL can be understood within the amphoteric defect model (ADM), introduced in Section 1.4. When the bulk

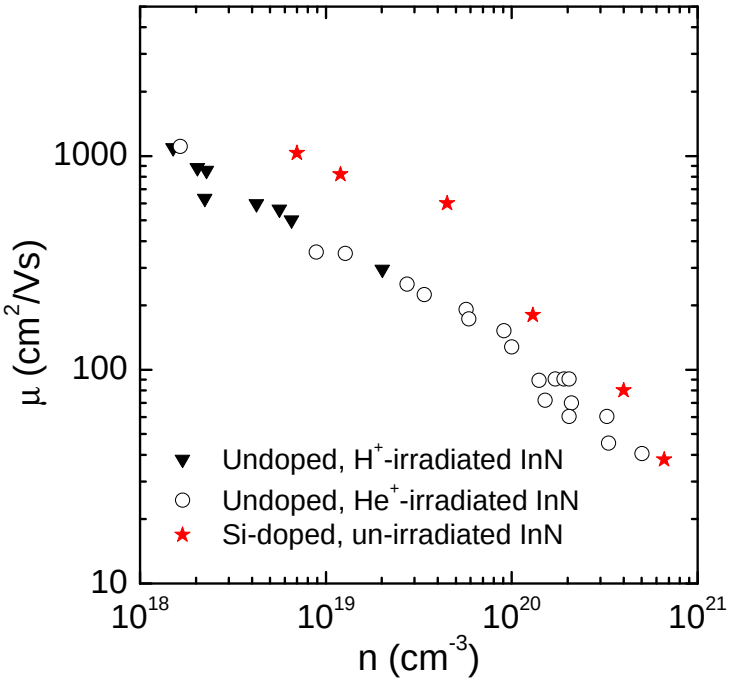

Figure 5.8: Mobility of undoped H^+ and He^+ ion-irradiated InN from Jones *et al.* [176] compared to un-irradiated Si-doped samples, including those investigated here.

Fermi level is well below the CNL, Si preferentially occupies the In–site (Si_{In}^{+}), acting as a donor, and any native defects preferentially have donor-character, increasing the bulk conductivity. As the Fermi level increases, acceptor defects such as triply charged In–vacancies (V_{In}^{3-}), Si on the N–site (Si_{N}^{-}) and acceptor-type defect complexes become more favourable, preventing further increase in Fermi level and acting to stabilize it at the CNL. In–vacancies have previously been observed to provide partial compensation in Si-doped InN [174]. Initial results from positron annihilation spectroscopy measurements also suggests that the same is true in these samples, with the density of In–vacancies increasing with increasing bulk carrier concentration [175]. Additionally, the low measured mobilities (by the single-field Hall effect) and large Urbach tailing observed in the most heavily doped samples (Fig. 5.4(c)) suggest the presence of significant concentrations of compensating native defects and impurities. Indeed, a comparison of the Hall mobilities of Si-doped samples, including those investigated here, with nominally undoped samples that have been irradiated [176] with high energy H^+ and He^+ ions is shown in Fig. 5.8. Irradiation of the samples introduces native defects, which acts to increase the electron concentration [177]. The mobility of the undoped reference sample used here (1100 $cm^2V^{-1}s^{-1}$) is very similar to those of the irradiated samples with the lowest

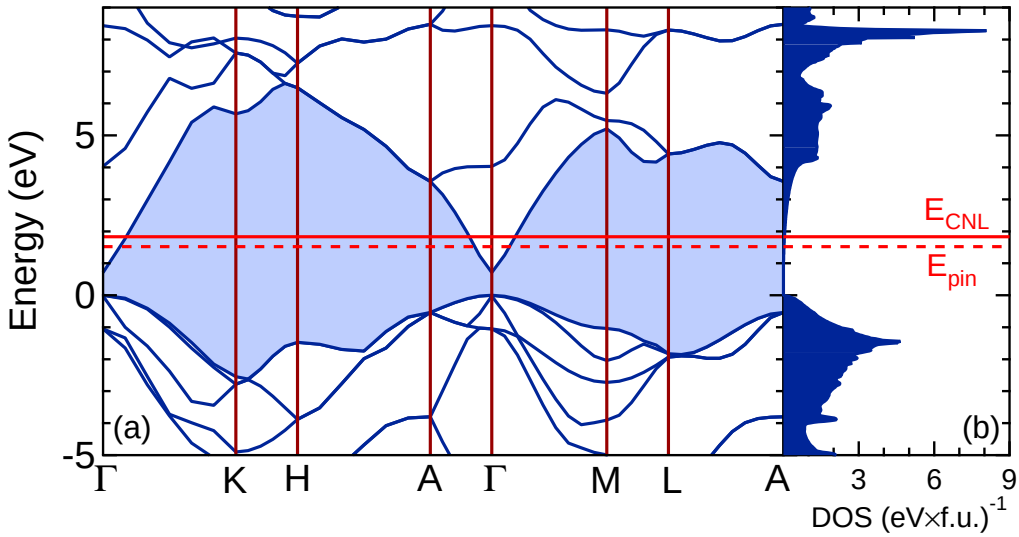

Figure 5.9: QPC-DFT (a) band structure across the Brillouin zone and (b) total DOS with the determined CNL, E_{CNL}, and surface Fermi level pinning, E_{pin}, positions shown.

carrier concentration, and hence smallest radiation dose. In both of these cases, the mobility is likely to be limited by native defects or impurities. However, for slightly higher bulk carrier concentrations, the mobility is significantly lower for the implanted samples as compared to equivalent Si-doped samples. This indicates that Si-doping may cause an increase in the electron concentration without the introduction of as many native defects as in the irradiated samples. However, for the highest concentration Si-doped sample, the mobility becomes equivalent to that of the most heavily irradiated samples, suggesting that it is more indicative of a native-defect controlled behaviour again. This supports the above arguments for stabilization of the Fermi level at the CNL upon heavy Si-doping.

Both methods of analysis of the XPS data presented above reveal a stabilization with heavy doping of the surface Fermi level at 1.83 ± 0.10 eV: the CNL is therefore determined as lying 1.83 ± 0.10 eV above the VBM, as illustrated in Fig. 5.9, slightly above the pinning position for moderately doped samples. In particular, the linear extrapolation method of analysis (Fig. 5.5) allows a direct experimental determination of the CNL position without recourse to theoretical calculations or detailed knowledge of the bulk Fermi level in the samples.

As discussed in Chapters 1 and 4, the CNL is located close to the average mid-gap energy across the entire Brillouin zone [12]. Employing Tersoff's criterion

for estimating the average mid-gap energy (Eqn. 1.10) [24], and taking the indirect conduction band minimum at the A-point, the CNL can be estimated from the QPC-DFT band structure calculations to lie close to 1.78 eV above the VBM, in agreement with the measured value. From Fig. 5.9, the conduction band edge is significantly lower at Γ than across the rest of the Brillouin zone: the CNL in InN therefore lies well above the conduction band minimum (CBM), in contrast to almost all other III-V semiconductors where the CNL is located below the CBM. In effect, the position of the CNL can be considered as a weighted average over the material's DOS around the band gap [178]. In InN, while there is a high DOS in the valence band, shown in Fig. 5.9(b), the highly dispersive conduction band at Γ, which lies well below the other conduction band valleys, results in only a small spectral weight in the DOS around the bottom of the conduction band. Consequently, the effective 'centre-of-mass' of the DOS around the band gap occurs well away from the VBM, resulting in the CNL actually lying above the CBM in InN.

The CNL energy determined here also agrees very well with previous theoretical calculations. Van de Walle and Neugebauer [25] locate the CNL at 1.88 eV above the VBM in InN using *ab initio* calculations. Additionally, Green's functions calculations by Robertson and Falabretti [178] give the CNL lying 1.87 eV above the VBM, while they determine a value of 1.88 eV using the theoretical calculations of Wei and Zunger [179].

5.4 Chemical trends

The seemingly unusually high location of the CNL relative to the CBM in InN, compared to other III-V semiconductors, can be explained within chemical trends by considering the band alignment of the common-anion III–N and the common-cation In–V compounds, shown in Fig. 5.10(a). Appealing to a simple tight-binding model, the valence (conduction) band edge derives mainly from the bonding (anti-bonding) state of anion and cation p– (s–) orbitals [185]. Due to the very small energy differences in the cation p–orbitals (Fig. 5.10(b)), the predominant factor in determining the valence band edge variation in the III–Ns is the interaction between

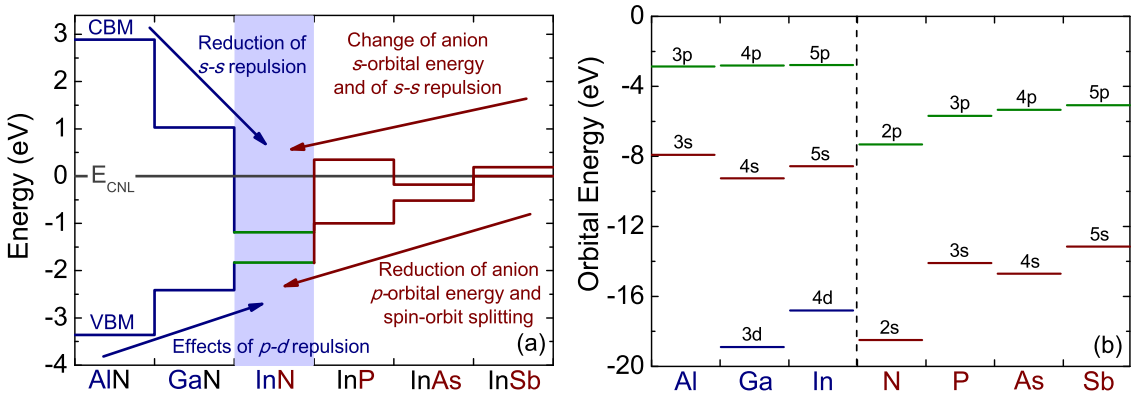

Figure 5.10: (a) Band lineup relative to the CNL in InN and common-cation and common-anion semiconductors determined from experimentally measured valence band offsets [180, 181], and experimentally determined values of the CNL position [182, 183, this study]. The locations of the constituent atom orbital energies (b), taken from Wei *et al.* [184], and anion-cation state couplings explain the chemical trends in the band offsets.

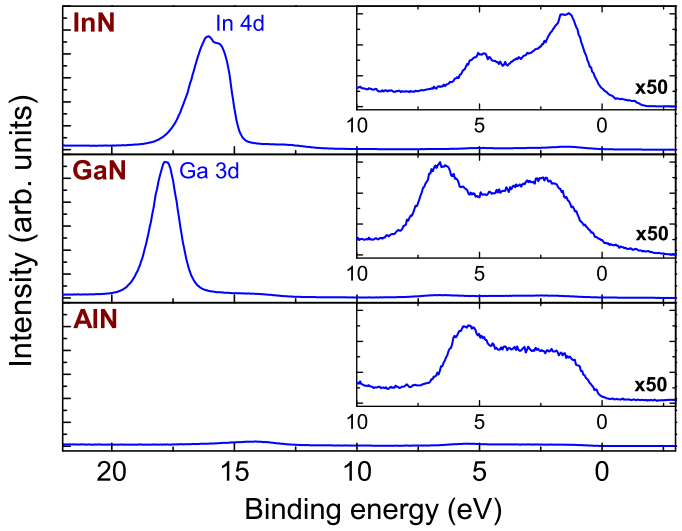

Figure 5.11: XPS spectra from InN, GaN and AlN showing the occupied cation *d*-levels in InN and GaN and their absence in AlN. A small peak due to N 2*s*-like states is seen in the AlN spectrum. These hybridize with the *d*-levels forming shoulders above and beloww the In 4*d* and Ga 3*d* peaks in the InN and GaN spectra, respectively. A magnified view of the valence band photoemission is shown inset for each material.

the cation *d*–orbitals and the N 2*p*–orbital [186]. In GaN and InN, shallow occupied Ga 3*d* and In 4*d* orbitals are located close to the VBM, whereas no such occupied cation *d*–orbitals are present in AlN, as shown by XPS measurements in Fig. 5.11. The occupied Ga 3*d* and In 4*d* orbitals hybridize with the N 2*p*–orbital. This causes a *p*–*d* repulsion which pushes the VBM to higher energies in GaN and InN with respect to AlN. The smaller cation *d* to N 2*p* orbital separation in InN compared with GaN results in the VBM lying highest in InN. The reduction of the CBM with increasing cation atomic number results from the change in cation *s*-orbital energy coupled with a decrease in the *s*–*s* repulsion strength between the cation and anion *s*–orbitals with increasing cation-anion bond length (on moving from AlN to InN).

Similar considerations hold for the common-cation compounds. The VBM follows the trend of the anion p–orbitals, causing a lowering of the band edge energy with decreasing anion atomic number. Furthermore, the spin-orbit splitting, which pushes the VBM upwards in energy, decreases with decreasing anion atomic number. The movement of the CBM results from the combined effects of the anion s–orbital energy shifts (Fig. 5.10(b)) and the change of s–s coupling with cation–anion bond length and energy separation of the In $5s$ and anion s–orbitals. In particular, the narrow band gap and very low position of the band extrema relative to the CNL in InN results from the large size and electronegativity mismatch of In and N, resulting in a large In–N bond length and low energy of the N $2s$–orbital. This is equivalent to the situation for CdO investigated in Chapter 4.

5.5 Implications for electronic properties

The position of InN at the intersection of these chemical trends, with the CNL located very high relative to the CBM, can be used to understand many of InN's striking electronic properties, as outlined in this section.

5.5.1 Surface electronic properties

As the Fermi level at the surface pins close to the CNL, but on the same side as the bulk Fermi level, the high location of the CNL relative to the conduction band edge in InN means that it will almost always exhibit a downward band bending, and consequently an extreme electron accumulation, at the surface. Such an electron accumulation would be expected to be present at the surface of p-type material also, explaining the presence of the recently reported [187] inversion layer, and the difficulty in determining p-type conductivity in InN. This is very similar to the situation in InAs, where the CNL is also located above the CBM (Fig. 5.10(a)), and electron accumulation (inversion) layers are present at the surface of n-type (p-type) material [39,188]. However, due to the smaller separation between the CBM and the CNL in InAs than in InN, the surface state densities are significantly lower than for InN accumulation layers, and so the electron accumulation is less extreme. Electron

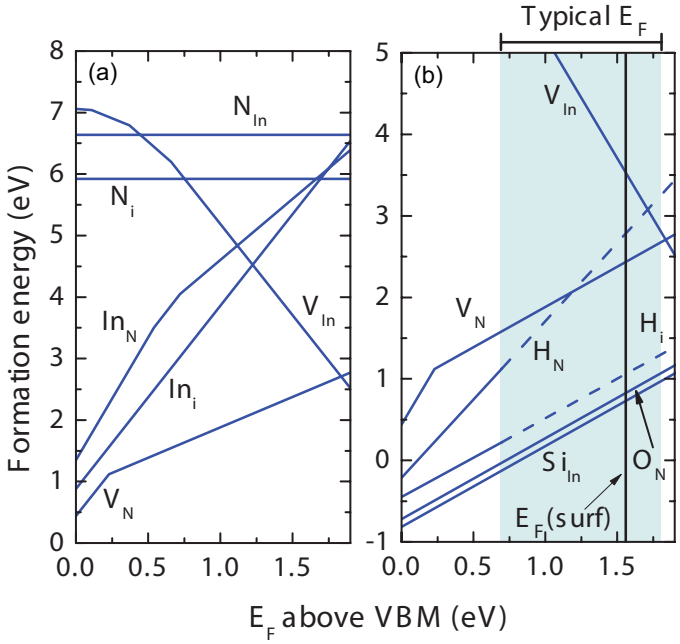

Figure 5.12: Formation energy for (a) native point defects and (b) additionally impurities, as a function of Fermi level, E_F, from the calculations of Stampfl *et al.* [190] and Janotti and Van de Walle [191]. The dashed lines indicate an extrapolation of the calculated values of Janotti and Van de Walle [191] to higher Fermi levels (above the CBM). Typical Fermi level positions in InN are represented in (b) by shading, and the pinning position of the surface Fermi level, as determined here, is also shown (vertical line).

accumulation layers at InN surfaces are investigated in more detail in Chapter 6.

In contrast, in GaN for example, the CNL is located below the CBM (Fig. 5.10(a)), and so in typical samples, the surface Fermi level will tend to be pinned below the bulk Fermi level for n-type material. Consequently, electron depletion layers are observed at the surface [189]. A transition from electron accumulation (for In-rich) to depletion (for Ga-rich) would therefore be expected at some composition of InGaN alloy. This is investigated in Chapter 7.

5.5.2 Propensity for n-type conductivity

Within the ADM, when the bulk Fermi level lies below the CNL, donor-type native defects are most favourable, tending to increase the Fermi level towards the CNL. Conversely, for bulk Fermi levels above the CNL, acceptor-type native defects have the lower formation energies, tending to reduce the net electron concentration and lower the Fermi level towards the CNL. Indeed, first-principles calculations of the formation energy of native defects in InN by Stampfl *et al.* [190], reproduced in Fig. 5.12(a), indicate a transition from the donor-like nitrogen vacancy, V_N^+, to the acceptor-like indium vacancy, V_{In}^{3-}, being the most favourable charge state at an energy very close to the CNL determined here. The high CNL position relative to the CBM in InN means that unintentional native defects will preferentially form as

donors, generally resulting in a high unintentional n-type bulk conductivity. These effects are also responsible for the observed stabilization of the Fermi level when native defects are intentionally introduced in InN by high energy particle irradiation [177]. The calculations also predict that both Si on the In site and O on the N site are effective donors in InN, as observed here and elsewhere [192, 193]. Consequently, native defects and impurities are all possible candidates for the high unintentional n-type conductivity of InN.

As discussed in Section 5.1.2, although the zero temperature InN band gap is now generally accepted to be ~ 0.7 eV [154], it was previously thought to be $\sim$ 1.9 eV [153]. These early measurements were largely performed by OAS on sputter-grown InN samples, which are likely to contain many native defects driving the Fermi level towards the CNL. A Moss-Burstein shift to the CNL position determined here is likely an important factor in explaining these previously observed high optical gap values.

Note also that the CNL still lies above mid-gap in GaN, making n-type conductivity more favourable than p-type, whereas for AlN, where the CNL lies a long way from both the CBM and VBM, n- and p-type doping are both difficult [53]. The position of the CNL relative to the band edges well explains the individual doping characteristics of the different III-N materials.

5.5.3 Hydrogen in InN

Hydrogen can form a positive or negative charge state in semiconductors, and usually acts to counteract the prevailing conductivity, so that it is a donor (acceptor) in p-type (n-type) material [25]. However, as discussed in Chapter 4, the H(+/−) transition energy is the CNL, and so for materials where the CNL lies above the CBM, as here, hydrogen can be a donor even in n-type samples. Indeed, hydrogen has been theoretically predicted [191, 194] (see Fig. 5.12(b)) and experimentally observed [195, 196] to be a donor in n-type InN, also consistent with the behaviour of muonium (a light isotope analogue of hydrogen) in this material [197]. Hydrogen must certainly, therefore, be considered as another potential source of n-type

conductivity in InN.

Discriminating between which of the native defects and impurities is responsible for the unintentional n-type conductivity in InN has proved controversial. Due to the lower calculated formation energies of impurities, such as oxygen and hydrogen, as compared to native defects (Fig. 5.12(b)), these have been suggested as the dominant donors [191, 198]. However, in some cases, these do not appear to be present in sufficient quantities to account for the total conductivity [199], and native defects and dislocations were suggested as important sources of electrons. Hydrogen, being present in most growth environments, is certainly a promising candidate, at least for a background concentration of electrons. However, it should also be noted that interstitial hydrogen, with the lower formation energy of the hydrogen impurities, may not be stable at growth temperatures [191]. Additionally, an extrapolation of the formation energy calculations of Janotti and Van de Walle [191] to Fermi levels above the CBM (Fig. 5.12(b)) reveals that the formation energy for substitutional hydrogen and nitrogen vacancies may be expected to cross if H_N^{2+} remains the favourable charge state for substitutional hydrogen for Fermi levels well into the conduction band. At Fermi levels typical for InN samples, in particular at the surface where impurities are incorporated during growth, hydrogen impurities and native defects could both, therefore, be important.

5.5.4 Interface-related electron density

An increase in electron density approaching the InN/buffer layer interface is also thought to occur [200–208], although the microscopic origin of this is still debated. As the lattice mismatch between InN and typical buffer layers is very large ($\sim$11% for GaN, $\sim$14% for AlN), the interface is characterised by a large density of threading dislocations (TDs) acting as a strain relieving mechanism [202,203,209,210]. Piper *et al.* [200] and Cimalla *et al.* [202] independently proposed these dislocations as the microscopic origin of the interface-related electron density. Due to the Γ-point CBM lying below the CNL in InN, point defects along or impurities localized at the TDs will preferentially have donor character, supporting the assignment of TDs as the

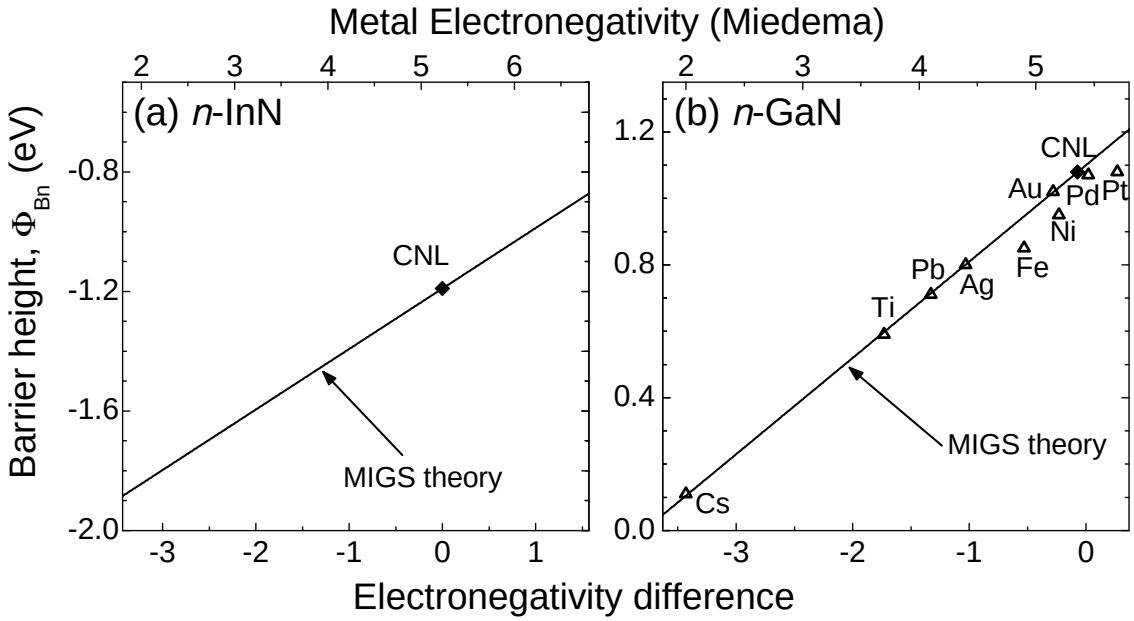

Figure 5.13: (a) n-type barrier height, Φ_{B_n}, for metal contacts on InN as a function of metal electronegativity. (b) The equivalent plot for GaN, adapted from Kampen and Mönch [182].

microscopic origin of an increase in electron density approaching the InN/buffer layer interface, as for the similar case of InAs/GaP interfaces [211]. This will be discussed in detail in Chapter 6.

5.5.5 Metal contacts to InN

Virtually all attempts to form metal/InN contacts have resulted in Ohmic, rather than rectifying (Schottky), behaviour [139]. This can be understood within Mönch's metal-induced gap states (MIGS) model, discussed in Section 1.3.3. Taking the CNL to lie 1.83 eV above the VBM (as determined here) and $\varepsilon(\infty) = 6.7$ [212], Eqns. 1.14 and 1.15 give the variation of n-type barrier height with metal electronegativity shown in Fig. 5.13(a). For a wide range of metal electronegativities, the barrier height is negative, indicating Ohmic behaviour for a laterally homogeneous metal contact. In contrast, for GaN shown in Fig. 5.13(b), the zero-charge-transfer barrier height is positive, allowing a range of metals to make Schottky contacts to GaN [182]. The differing location of the CNL in InN and GaN explains the opposing tendencies of their metal-semiconductor contact behaviour.

5.6 Conclusions

The CNL in InN has been located 1.83 ± 0.10 eV above the VBM, well above the Γ-point CBM. This was determined directly from experimental energy measurements of the surface Fermi level position stabilized at the CNL by heavy Si-doping, and confirmed using a combination of photoemission and optical measurements and QPC-DFT calculations. The location of the CNL above the band extrema was understood by the particularly low Γ-point CBM value compared to the average band edge across the Brillouin zone.

Many of the fundamental properties of the material which are often considered unusual, such as an extreme electron accumulation at the surface, inversion layer formation at the surface of p-type material, the propensity for high unintentional n-type conductivity, the donor nature of hydrogen even in n-type material, and the Ohmic behaviour of metal/InN contacts, were explained by the position of the CNL relative to the band edges. Far from being anomalous, therefore, the fundamental electronic properties of InN are governed by the same overriding mechanism as in other semiconductors, namely the position of the band edges relative to the CNL. This position follows from the chemical trends of common-cation and common-anion semiconductors, providing an understanding of the striking electronic properties of this material.

Chapter 6

Surface and interface-related electron density in InN

6.1 Introduction

As discussed in Chapter 5, InN exhibits an extreme accumulation of electrons at the surface, in contrast to all other III-V semiconductors except for InAs, which exhibit a depletion of electrons at the surface. This has many important implications for the use of InN as a material in device applications, in particular for the properties of contacts that can be made to the surface, its role as a material for chemical sensing applications and its potential for emission of THz radiation. Previous experimental studies of this electron accumulation have focussed on wurtzite (wz) c-plane surfaces [7, 138, 201], although first-principles calculations [213] have predicted electron accumulation at non-polar surfaces in the presence of In-adlayer surface reconstructions. Experimentally, however, studies of non-polar wurtzite surfaces and indeed studies of other polymorphs of InN have been largely neglected.

In this chapter, high-resolution x-ray photoemission spectroscopy (XPS) is used to investigate electron accumulation at cleaned wurtzite a- and c-plane surfaces, as well as at the (001) surface of zinc-blende (zb) material. A remarkable universality is observed between the degree of electron accumulation at different surfaces of wurtzite material, and this is discussed in terms of the conduction band minimum (CBM) position relative to the charge neutrality level (CNL). An interface-related electron density in InN is also probed both via a comparison of surface and bulk sensitive measurements, and by transport modelling of single-field Hall effect results. Finally, the implications of electron accumulation on the growth and characterisation of p-type InN are investigated.

6.2 Experimental details

Wurtzite c-plane InN samples were grown on c-plane sapphire substrates by plasma assisted molecular-beam epitaxy (PAMBE) with In- and N-polarity [(0001), grown at Cornell University, USA, and $(000\bar{1})$, grown at Ritsumeikan University, Japan, respectively]. GaN/AlN and low-temperature InN buffer layers were used for the In- and N-polarity samples, respectively. An a-plane $(11\bar{2}0)$ sample was grown on an r-plane sapphire$(1\bar{1}02)$ substrate incorporating a GaN/AlN buffer layer at Cornell University. Zinc-blende InN(001) samples were grown on 3C-SiC(001) substrates incorporating a zb–GaN buffer layer at Universität Paderborn, Germany. As zb–InN is not the most energetically favourable polymorph, wz inclusions are present in the zb–InN film. The results presented here are from the sample with the lowest density of wz inclusions – the sample was estimated to be approximately 95% zb phase InN from x-ray diffraction reciprocal space mapping [144], allowing experimental studies of almost phase pure zb–InN to be undertaken. Details of the various growth methods and materials characterisation are reported elsewhere [144, 214–216]. Mg-doped InN was also grown at Cornell University on c-plane sapphire by PAMBE, incorporating a GaN buffer layer [214]. Secondary ion mass spectroscopy (SIMS) measurements revealed a doping concentration of $[\mathrm{Mg}] = 3 \times 10^{19}$ cm^{-3}, calibrated from the Mg-SIMS profile of an undoped InN sample implanted with Mg_{25} to a dose of 1×10^{14} cm^{-2}. Mg_{25} was utilized for the calibration sample to prevent false counts from C_2 fragments. The natural isotope abundances were used to determine the total Mg-concentration in the InN:Mg sample.

Single-field Hall effect and XPS measurements were performed at room temperature as described in Chapter 3. Sample preparation, performed in a preparation chamber connected to the XPS chamber, was achieved by atomic hydrogen cleaning (AHC), which has been shown to effectively clean surfaces of InN without causing electronic damage [217]. The AHC consisted of annealing the samples at $\sim$200°C under exposure to a 10–20 kilo-Langmuir dose of molecular hydrogen passed through a thermal gas cracker with a cracking efficiency of approximately 50%, followed by a 1–2 hour anneal at $\sim$275°C. Core-level XPS was performed before and after surface

preparation. Before treatment, a large O signal was observed for all samples, with a corresponding significant oxide component in the In and N core level peaks chemically shifted to higher binding energies than the In–N bonding component. The surface oxide was seen to be largely quenched with the AHC treatment, although small concentrations (estimated to be submonolayer) of adventitious carbon and oxygen were still observed following the surface preparation. Scanning electron microscopy was used to ensure that the AHC had not resulted in In-droplet formation at the surface.

Quasiparticle-corrected density-functional theory (QPC-DFT) calculations were performed elsewhere, as discussed in Section 2.1.2. For comparison with the experimental results, the QPC-DFT valence band density of states (VB-DOS) is broadened by a 0.2 eV full width at half maximum (FWHM) Lorentzian and a 0.4 eV FWHM Gaussian to account for lifetime and instrumental broadening, respectively. The surface Fermi level position was determined by the shift in spectral features between the valence band photoemission and the QPC-DFT calculated VB-DOS, as performed in Chapter 5.

6.3 Universality of electron accumulation

6.3.1 Wurtzite InN

Valence band photoemission spectra from *wz* In- and N-polarity *c*-plane, and *a*-plane InN samples, following surface preparation by AHC, are shown with QPC-DFT VB-DOS calculations in Fig. 6.1. The differences in intensity of the ~ 3 eV binding energy peak between the samples has been shown to be a signature of the film polarity [151, 152]. Apart from this difference, the valence band photoemission spectra are very similar for the different samples. In particular, all of the photoemission spectra are coincident in energy, indicating the same valence band maximum (VBM) to surface Fermi level separation. This is determined, from the shift in peak position compared to the QPC-DFT calculations, to be 1.53 ± 0.10 eV for all three samples, revealing that the surface Fermi level is pinned ~ 0.9 eV above the CBM

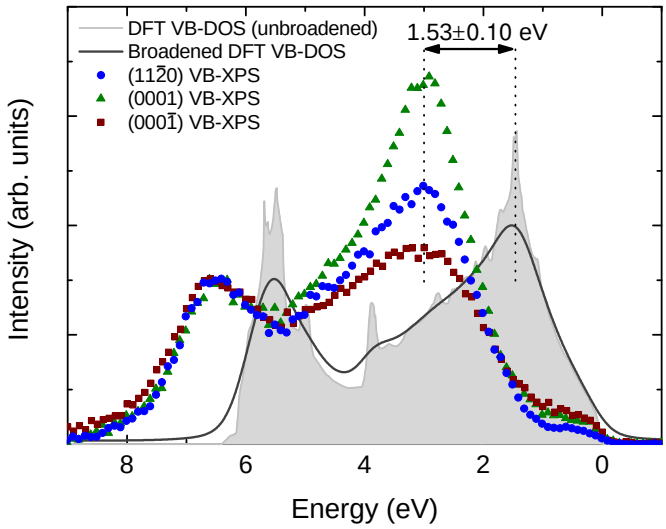

Figure 6.1: Valence band photoemission spectra for InN(11$\bar{2}$0), (0001) and (000$\bar{1}$) surfaces, relative to the surface Fermi level. QPC-DFT VB-DOS is shown without (shaded) and with lifetime and instrumental broadening. The indicated shift in peak position gives the VBM to surface Fermi level separation.

Table 6.1: Bulk carrier density, n, determined from single-field Hall effect measurements, and corresponding bulk Fermi level above the CBM, E_{F_b}, calculated using non-parabolic carrier statistics (Chapter 2). The band bending, V_{bb}, is calculated from the relative surface and bulk Fermi level positions. Poisson-MTFA calculations give the surface-state density, N_{ss}.

Orientation	n (cm^{-3})	E_{F_b} (eV)	V_{bb} (eV)	N_{ss} (cm^{-2})
(11$\bar{2}$0)	4.8×10^{18}	0.164	-0.725	1.66×10^{13}
(0001)	3.0×10^{18}	0.124	-0.765	1.64×10^{13}
(000$\bar{1}$)	6.7×10^{18}	0.200	-0.689	1.65×10^{13}

in all of the wz samples. Note also that the leading edge of the valence band photoemission extrapolates to the same value for all three samples, which is very close to, but slightly below, that determined by comparison with the calculated VB-DOS, consistent with the findings presented in Chapter 5.

The bulk electron densities in the samples, determined from Hall effect measurements (see Table 6.1) give Fermi levels 0.12–0.20 eV above the CBM from non-parabolic carrier statistics calculations. As the position of the surface Fermi level is located substantially further above the CBM than the bulk Fermi level in all samples, a downward band bending relative to the Fermi level at the surface is present, leading to electron accumulation in all cases. To investigate this further, the band bending profile and corresponding electron accumulation in the surface space-charge region was determined by solving Poisson's equation numerically within the modified Thomas-Fermi approximation (MTFA) as described in Chapter 2. The resulting profiles are shown in Fig. 6.2, and the relevant parameters listed in Table 6.1.

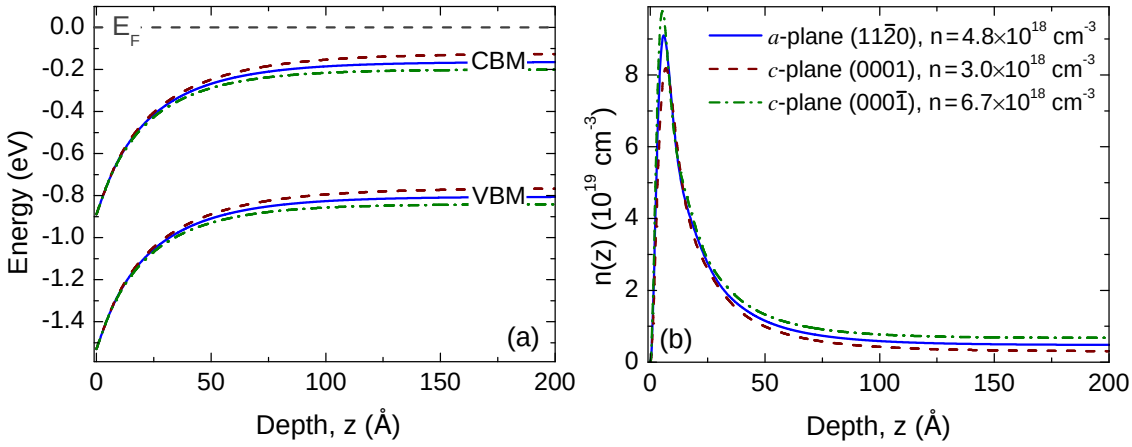

Figure 6.2: (a) Band bending relative to the Fermi level and (b) resulting carrier concentration variation in the accumulation layer at wz–InN surfaces.

Despite small differences in bulk Fermi level positions, the pinning of the surface Fermi level at the same energy for a-plane and both polarities of c-plane InN means that the band bending close to the surface is very similar (Fig. 6.2(a)), resulting in similar charge profiles (Fig. 6.2(b)). Indeed, the calculated surface-state density is essentially the same for all samples (Table 6.1), indicating the universality of the electron accumulation at wz–InN surfaces. Electron accumulation has also recently been observed at the non-polar m-plane surface of InN nanocolumns [218, 219], although a surface-state density for comparison with the values determined here for epitaxial films has not yet been determined.

This universality of the electron accumulation can be understood by considering the location of the CNL high above the CBM, as determined in Chapter 5. As discussed, the Fermi level pins slightly below the CNL at the surface leading to a positive surface charge from unoccupied donor surface states, resulting in the electron accumulation. While the exact microscopic nature of these surface states may vary between different surfaces, the position of the CNL is a bulk band structure property, dictating that all surfaces will exhibit a pronounced tendency towards electron accumulation, provided the bulk Fermi level lies below the CNL. As the density of conduction band states is so high at the energy of the CNL, charge neutrality can be maintained despite any small variations in surface-specific microscopic surface-state density by only very small movements in the Fermi level: it is strongly 'pinned' at

the surface of InN. This explains the universal nature of the electron accumulation observed here at both polarities of *c*-plane and at *a*-plane InN surfaces.

Several microscopic origins of the surface electron accumulation have been suggested. Theoretical calculations predict that In-rich surface reconstructions involving In-adlayers are energetically favourable for all In chemical potential values [150], which have been experimentally confirmed under In-rich conditions from core-level photoemission [151] and ion scattering [152] measurements, and additionally from reflection high energy electron diffraction intensity oscillations [220, 221]. In-In bonds in such an In-adlayer reconstruction have been predicted as a microscopic origin of the surface states giving rise to the electron accumulation in InN [213]. However, native defects [177] and impurities [201] have also been suggested as possible mechanisms for providing the donor surface charge in oxidised samples.

Certainly, analysis of the XPS core-level peak intensities supports the presence of In-adlayers at the surface of the samples investigated here, consistent with In-In bonds in such adlayers being the microscopic origin of the electron accumulation. Furthermore, the absence of In-adlayers on a perfect non-polar surface was predicted to lead to an absence of electron accumulation [213]. This has recently been observed by Wu *et al.* [222] who performed microscopic-area photoemission spectroscopy on a pristine *a*-plane surface following cleavage in ultra-high vacuum. This is, in fact, the usual situation for non-polar surfaces of III-V semiconductors, where a perfect cleave causes the surface states to relax out of the band gap, leading to flat-bands [36, 37]. Note, this does not contradict the CNL arguments given here – while for a perfect cleave, the microscopic situation may lead to zero charged intrinsic surface states, the tendancy for any extrinsic surface states to be donors is still there. Consequently, an imperfect cleave, resulting in any step edges, for example, or any contamination of the surface would all be expected to result in a pronounced electron accumulation again.

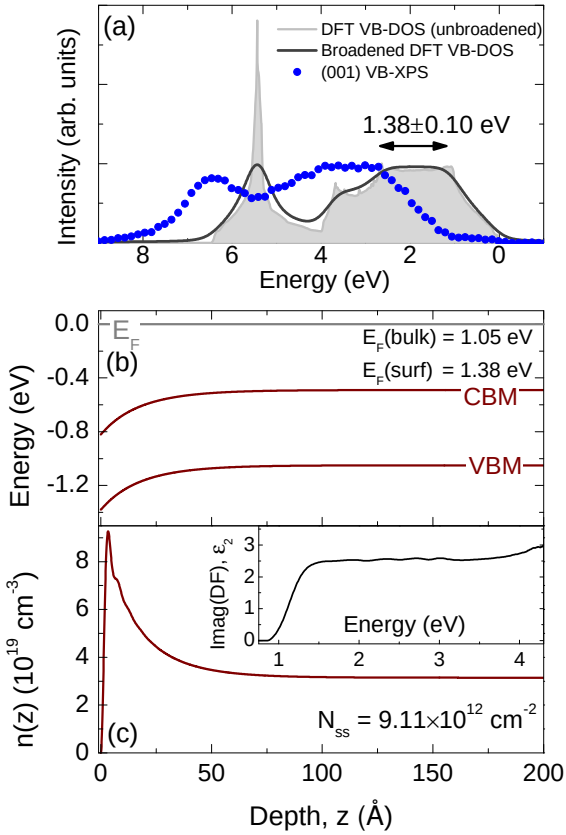

Figure 6.3: (a) Valence band photoemission spectrum for *zb*–InN(001) and corresponding QPC-DFT VB-DOS shown without (shaded) and with lifetime and instrumental broadening. Poisson-MTFA calculations yield (b) band bending and (c) carrier concentration profiles. The bulk Fermi level was determined from the imaginary part of the dielectric function, determined by spectroscopic ellipsometry (shown inset).

6.3.2 Zinc-blende InN

Valence band photoemission from *zb*–InN(001) is shown in Fig. 6.3(a). The DOS is somewhat different for zinc-blende compared to wurtzite polymorphs, and the detailed agreement of the XPS with the QPC electronic structure calculations is discussed elsewhere [83], although good agreement is seen when incorporating a VBM to surface Fermi level shift of 1.38 ± 0.10 eV.

Poisson-MTFA calculations for InN(001), using a room temperature band gap of 0.56 eV [144] and a band-edge electron effective mass of $0.039m_0$ (based on the empirical relation $m^* \approx 0.07E_g$ [165]), are shown in Fig. 6.3. Due to growth on a conducting substrate, single-field Hall effect measurements did not yield an accurate carrier concentration for the InN layer. The bulk Fermi level was therefore estimated from the imaginary part of the dielectric function (determined by spectroscopic ellipsometry [144]), shown inset in Fig. 6.3, to be 1.05 eV above the VBM. This corresponds to a bulk electron concentration (from non-parabolic carrier statistics calculations) of 3.2×10^{19} cm^{-3}.

Despite the higher bulk carrier density than in the wurtzite samples, a distinct electron accumulation is still observed. However, the Fermi level appears to pin slightly lower above the VBM, and the surface-state density from Poisson-MTFA calculations ($N_{ss} = 9.11 \times 10^{12}$ cm^{-2}) is somewhat lower, for the zinc-blende than the wurtzite cases. Although it has not been determined for InN, the valence band offset (VBO) between wurtzite and zinc-blende GaN is less than 100 meV [223, 224], and would be expected to decrease with increasing ionicity of the semiconductor [225]. Thus, the VBO between wurtzite and zinc-blende InN is expected to be small, and consequently the band edges in zinc-blende InN will still occur significantly below the CNL. Indeed, using the Tersoff method (Eqn. 1.10, which gave good agreement with the measured CNL in *wz*–InN, as discussed in Chapter 5) for the calculated zinc-blende band structure (Fig. 5.3(b)), the CNL can be estimated to lie 1.88 eV above the VBM in *zb*–InN, and so well above the Γ-point CBM as for the *wz* polymorph. Thus, while the detailed surface state distribution may be rather different to the previous cases, leading to the differences in observed surface Fermi level pinning position, the bulk band structure still dictates that electron accumulation will occur at the surface for this polymorph, as observed here.

6.3.3 Influence of growth conditions?

Fehlberg *et al.* [226] investigated the transport properties of In-polarity *wz*–InN films grown under In-rich, stoichiometric and N-rich conditions by multiple-field Hall effect measurements. Their interpretations of the results suggested that the sheet density associated with the surface electron accumulation layer increases with decreasing In-flux during growth, attributed to the increasing roughness of the surface. Additionally, an investigation of the film-thickness dependence of the sheet density determined from single-field Hall effect measurements of In- and N-polarity samples grown under optimised In-rich conditions [198, 227] revealed a different excess sheet density in each case, interpreted as a change in the surface electron accumulation. These interpretations are seemingly in contrast to the universality of the surface electron accumulation observed here. However, King *et al.* [207] performed

an XPS investigation of samples grown under identical conditions to those used in these transport measurements, showing that the surface Fermi level exhibited no dependence on film polarity or growth conditions.

The invariance of the surface Fermi level position of InN grown under different conditions can be reconciled with the differing properties suggested by previous electrical characterisation by considering an increase in electron density approaching the InN/buffer layer interface (introduced in Section 5.5.4) which was not previously considered in the interpretation of the electrical measurements. This supports the universality of the electron accumulation at as-grown and *ex-situ* prepared InN surfaces, but indicates the necessity to consider the interface related electron density when attempting to extract the surface electron contribution from electrical measurements of InN.

6.4 Interface-related electron density

Further evidence for an interface-related electron density in InN is considered in this section. Previous analysis of single-field Hall effect results from a large number of samples grown by PAMBE on GaN and AlN buffer layers revealed some interesting trends. A marked increase in carrier density was obtained with decreasing film thickness, along with a corresponding decrease in Hall mobility [171, 200, 202, 214], shown for samples grown by PAMBE on GaN buffer layers in Fig. 6.4.

The universal electron accumulation discussed above provides a possible mechanism for a variation in average electron concentration with film thickness, as the surface electron accumulation contributes a constant sheet density, independent of the film thickness. To investigate the effect of this on the single-field Hall results, a parallel conduction analysis [187, 228] has been performed here, where the Hall sheet density, N_H, and mobility, μ_H, satisfy

$$N_H \mu_H = N_s \mu_s + N_b \mu_b \tag{6.1a}$$

$$N_H \mu_H^2 = N_s \mu_s^2 + N_b \mu_b^2 \tag{6.1b}$$

where N_s (N_b) and μ_s (μ_b) are the surface (bulk) sheet density and mobility, re-

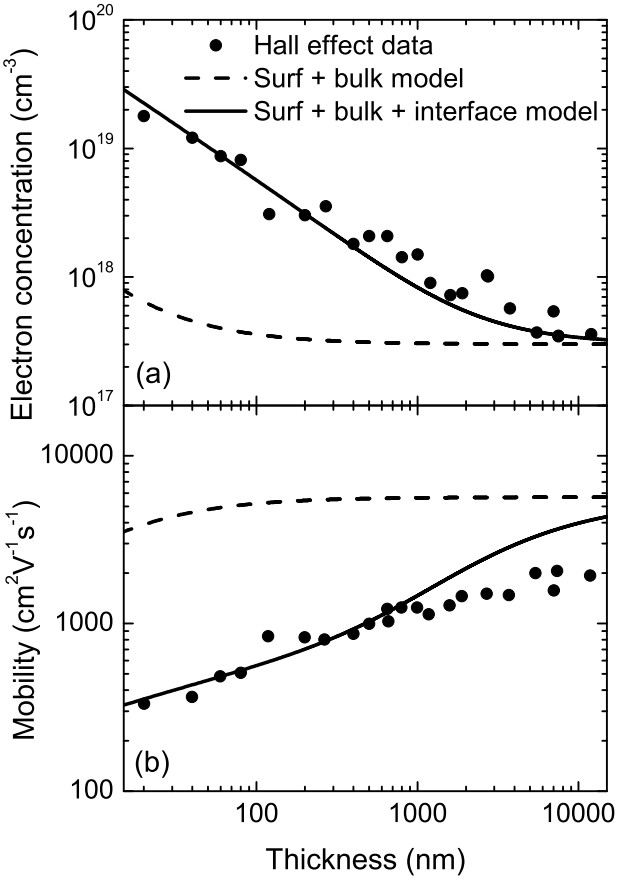

Figure 6.4: (a) Volume electron concentration and (b) mobility determined by single-field Hall effect measurements of a number of InN samples of varying thickness grown by PAMBE on GaN buffer layers on sapphire substrates [171, 214]. A parallel conduction model, described in the text, considering bulk and surface (dashed line) and additionally interface (solid line) contributions is also shown.

spectively. The surface sheet density is taken as the universal value of $N_s = 1.65 \times 10^{13}$ cm^{-2} determined above, and the mobility of these surface electrons is estimated as $\mu_s \approx 100$ cm^{2}V^{-1}s^{-1} from previous multiple-field Hall effect measurements [229]. A uniform background 'bulk' volume density of $n_b = 3 \times 10^{17}$ cm^{-3} is taken from the slope of the sheet density as a function of film thickness for In-polar InN grown under In-rich conditions on a GaN template [198], from the 'bulk' electron density determined by multiple-field Hall effect measurements on a 7.5 μm thick InN sample [229], and from the volume electron concentration determined by single-field Hall effect measurements of thick samples (Fig. 6.4). This is converted into a sheet density $N_b = n_b d$, where d is the film thickness. The bulk carrier mobility was calculated from the ionized impurity scattering time calculated using the non-parabolic formalism of Zawadzki and Szymanska [230], as described elsewhere [176].

The results of this parallel conduction model are shown in Fig. 6.4 (dashed line). The electron concentration is clearly underestimated, and the mobility overestimated, for all thicknesses of sample. Even though very high carrier densities

are present in the peak of the accumulation layer ($\sim 10^{20}$ cm^{-3}, Fig. 6.2), the band bending occurs over a distance determined by the Thomas-Fermi screening length, with the band bending potential reducing to zero over a distance of approximately 10 nm in InN. Consequently, the high carrier densities are very localized at the surface, and so do not contribute significantly to the measured electron density, except for very thin films. Additionally, as the carriers associated with the surface electron accumulation have a lower mobility than those in the bulk, their influence on the single-field Hall effect measurements is reduced further. It should be noted, however, that even if the mobility of the surface electrons is assumed to be as high as that of the bulk electrons, this model is still insufficient to reproduce the variation in measured electron density with film thickness [200]. Another explanation is therefore required to explain the single-field Hall effect results.

InN has a large lattice mismatch with typical substrate and buffer layer materials, for example 11% and 14% with GaN and AlN, respectively. Consequently, the InN/buffer layer interface is characterised by a large number of strain-relieving threading dislocations (TDs), whose density falls off exponentially with distance from the interface [209, 210, 231, 232]. By analogy with GaN [233], charged dislocation scattering was suggested as a mechanism to explain the reduction in mobility with decreasing film thickness [214]. However, dislocations in GaN are known to act as acceptors, and this was originally assumed to be the case for InN also [209], and so this mechanism was not thought to explain the dependence of the electron density on film thickness. However, Piper *et al.* [200] and Cimalla *et al.* [202] suggested that if dislocations at the interface acted as a source of donors, as for InAs/GaP [211] and InAs/GaAs [234], this would give an effective mechanism with which to explain the thickness dependence of the single-field Hall effect results. The resulting model for electron density in InN films is shown schematically in figure 6.5(a), and is characterised by three contributions – I: the background 'bulk' density resulting from defects or impurities uniformly distributed throughout the film; II: surface electron accumulation; and III: donors due to dislocations, whose density falls off exponentially away from the interface.

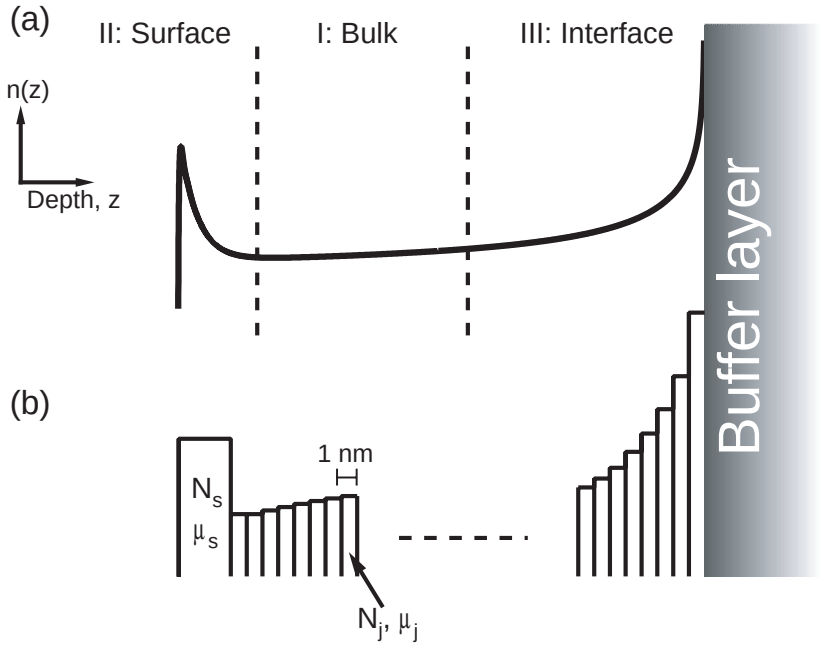

Figure 6.5: (a) Schematic representation of the 'three-region' model for conductivity in InN, indicating the I: bulk, II: surface, and III: interface contributions to the total electron concentration, n, as a function of depth. (b) Representation of the quantized layer model used for the full parallel conduction analysis described in the text.

Previous modelling of these three contributions was able to reproduce the film-thickness dependence of the carrier concentration determined from single-field Hall effect results for InN films grown on both GaN [200] and AlN [202, 203] buffer layers, but the analysis was performed assuming the same mobility for carriers in each region. To validate this model, it is necessary to reanalyze the data incorporating varying mobilities of the different contributions, within a full parallel conduction treatment. Such an analysis is presented here. In this model, the sample is divided up into slabs of 1 nm thickness, shown schematically in figure 6.5(b). The volume density in the j^{th} slab

$$n_j = n_b + D_j/C, \tag{6.2}$$

where n_b is the background 'bulk' concentration considered previously, D_j is the areal density of dislocations in the slab, assumed to follow the relation $D(x) = A(10^{-\log_{10} x})$ with distance x from the interface [235], and C is the separation of charged centres along a dislocation. The constant A is treated as a fit parameter to reproduce the experimentally measured dislocation densities of 5.0×10^{10} cm^{-2} [209] and 2.2×10^{10} cm^{-2} [210] at 450 nm and 760 nm away from the InN/GaN interface,

respectively. The mobility in the j^{th} slab is given by

$$\mu_j^{-1} = \mu_{dis_j}^{-1} + \mu_{ion_j}^{-1} \tag{6.3}$$

from Matthiessen's rule, where the ionized impurity scattering is calculated as described above, and scattering from dislocations is included via the formalism of Look *et al.* [209]

$$\mu_{dis_j} = \frac{4(3^{2/3})eC^2 n_j^{2/3}}{\pi^{8/3}\hbar D_j}\left[1 + y(n_j)\right]^{3/2}, \tag{6.4}$$

where

$$y(n_j) = \frac{2(3^{1/3})\pi^{8/3}\hbar^2\varepsilon(0)n_j^{1/3}}{e^2 m^*}, \tag{6.5}$$

where $\varepsilon(0) = 9.7$ is the static dielectric constant and m^* the effective mass. Although these relations assume parabolic band dispersion, conduction band non-parabolicity, important in InN, is approximately included by replacing the effective mass in these relations by the effective mass calculated at the Fermi level in each slab using the non-parabolic relations discussed in Section 2.1.1. The parallel conduction model introduced in Eqn. 6.1 is extended to incorporate the surface, bulk and interface-derived carriers:

$$N_H\mu_H = N_s\mu_s + \sum_j (n_j\ell)\mu_j \tag{6.6a}$$

$$N_H\mu_H^2 = N_s\mu_s^2 + \sum_j (n_j\ell)\mu_j^2 \tag{6.6b}$$

where $\ell = 1$ nm is the thickness of each slab.

The calculated volume electron concentration and mobility, assuming singly charged scattering centres, a compensation ratio of 0.5, an impurity centre every three unit cells along a dislocation, and the surface and bulk parameters used above, are shown in Fig. 6.4 (solid lines). The thickness dependence of the volume electron density is well reproduced using this parallel conduction treatment, validating the results of previous studies [200, 202] where variations in mobility were not considered. Further, it allows a calculation of the Hall mobility, which, as shown in Fig. 6.4(b), exhibits good agreement with the measured values at sample thicknesses below $\sim$1 μm. Above this, however, the experimental mobility is somewhat below

that of the calculated values. Hsu *et al.* [236] have shown that, while at high carrier concentrations, the mobility is limited virtually solely by Coulomb scattering, at lower electron densities, other mechanisms such as polar optical and acoustic phonon scattering become important, reducing the mobility below that of the Coulomb scattering limited value. For films thicker that ~ 1 μm, the electron density is relatively low, below 10^{18} cm^{-3}, and so it is likely that, in addition to Coulomb and dislocation scattering, phonon scattering also becomes important. This would reduce the mobility below the calculated value, explaining the discrepancy between the calculated and measured values for thick films. Notwithstanding these slight discrepancies, the good general agreement between the calculated and measured electron concentrations and mobilities supports the three-region model for conductivity in InN, with the bulk, surface and particularly interface-related carriers all being important.

The highly n-type nature of an interface-related contribution is also supported by the infrared reflectivity measurements of Ishitani *et al.* [237] and the modelling of electrolyte-gated Hall effect measurements of Brown *et al.* [238], who estimated a sheet density of $\sim 10^{13}$ cm^{-2} and 7.5×10^{13} cm^{-2} electrons associated with the interface, respectively. Further, combined structural and electrical studies show a correlation between the TD density and the average (Hall) electron concentration in samples grown by both MBE [239] and MOVPE [206]. Variations in the interface-related electron density with buffer layers, growth polarity and growth conditions are also important. The extrapolated 'excess' sheet density for zero-thickness samples determined from single-field Hall effect results has been shown to be slightly larger when using AlN rather than GaN buffer layers [138, 240], and for In- rather than N-polar InN samples, while the density of low-mobility electrons, not associated with the background 'bulk' carriers, in multiple-field Hall effect measurements has been shown to increase with decreasing In-flux during growth [226]. Any change in the sheet density of the surface electron accumulation with buffer layer, polarity, or growth conditions has been ruled out (see above) leaving the interface contribution as the only remaining plausible cause of these changes. Each increase in interface-related electron density can be correlated with an increase in the expected density

of TDs, due to the larger lattice mismatch of InN with AlN than with GaN, or with differing polarity and growth condition as previously inferred from x-ray diffraction studies [227].

Recently, Darakchieva *et al.* [241] have questioned the interpretation of dislocations as a source of interface-related electron density in InN from magneto-optic generalised ellipsometry (MOGE). They analysed their MOGE data based on a two-layer model including a surface electron accumulation and bulk layer, determining a more pronounced variation in bulk concentration than might be expected from the dislocation model presented here, along with potential small variations in surface electron density. However, there are a number of significant problems with their analysis: they did not include the possibility of any interface-related electron density in their model of the MOGE data; they modelled smoothly varying carrier concentration profiles as two step functions; they did not consider bulk carrier concentration dependence of the thickness of the surface electron accumulation due to changing screening lengths; the obtained carrier concentrations are the result of very complex multi-parameter fits; and their analysis was limited to a very small sample set. In contrast, Lebedev *et al.* [203] presented a very convincing correlation between the directly measured variation in dislocation density as a function of film thickness and the free-electron concentration. From the modelling of single-field Hall effect data presented here, and the observations of interface-related electron density in InN discussed above, donors localized at dislocations certainly seem a probable candidate. However, the exact microscopic origins of the electrons (whether they be donor-type native defects localized at, or impurities decorating, dislocations), and whether there are any additional sources of the observed film-thickness dependence of electron concentration, warrant further investigation.

6.5 Inversion layers

As for *n*-type InN, the Fermi level would be expected to pin slightly below the CNL at the surface of *p*-type InN, again leading to a positive surface charge. This positive surface charge must still be balanced by a negative space charge in order

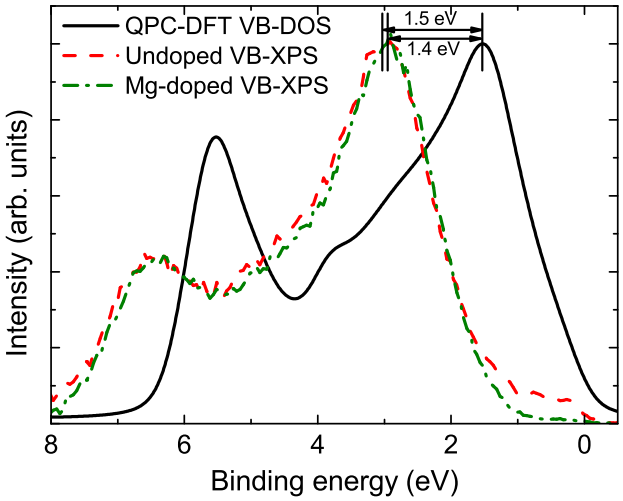

Figure 6.6: Broadened QPC-DFT VB-DOS (solid line) and Shirley-background-subtracted valence-band photoemission spectra for undoped (dashed line) and Mg-doped (dot-dashed line) InN.

to maintain charge neutrality. As the Fermi level approaches the CNL from below for both n- and p-type InN, the pinning position would be expected to be similar. This is confirmed by valence band photoemission measurements for an undoped and a Mg-doped InN sample, following surface preparation by AHC, shown in Fig. 6.6. Comparing with the VB-DOS from QPC-DFT calculations, as above, the VBM to surface Fermi level separation is determined as 1.4±0.1 eV for the Mg-doped sample, slightly lower than the value of $1.5(3) \pm 0.1$ eV for the undoped sample (discussed above). Due to the relative positions of the bulk Fermi levels, a greater degree of band bending occurs for Mg-doped (p-type) compared to undoped (n-type) InN, resulting in a greater space charge. For charge neutrality to be maintained, this space charge must be balanced by a larger surface-state charge, requiring the Fermi level to be located slightly further below the CNL at the surface of Mg-doped than undoped InN so that more donor surface states are unoccupied. This explains the slight difference in pinning position of the Fermi level observed here at the surface of undoped and Mg-doped InN.

Despite this small difference, the surface Fermi level still pins well above the CBM for p-type InN, resulting in an n-type surface region (electron accumulation) separated from the p-type bulk by a depletion layer. Determination and characterisation of a bulk p-type conductivity in InN are therefore very difficult. Direct measurements, such as the single-field Hall effect, are dominated by the surface electron accumulation, revealing only n-type conductivity. Several recent works have

used alternative techniques to infer the presence of a p-type bulk in some Mg-doped InN samples. Jones *et al.* [187] investigated Mg-doped InN using a combination of electrochemical capacitance-voltage (ECV) profiling and the effects of 2 MeV He^+ ion irradiation. The principal evidence for a bulk p-type conductivity came from the ECV profiling, where a turnover in $\frac{\partial(C^{-2})}{\partial V}$ with increasing bias voltage, V, was interpreted as evidence for a p-type region below the n-type surface. However, ECV yields information on the acceptor density, rather than the density of free holes in the material. Furthermore, Yim *et al.* [242] have shown that the turnover in $\frac{\partial(C^{-2})}{\partial V}$ occurs even in n-type samples at sufficient bias voltages, and modelling is important to determine if a p-type bulk conductivity is present. ECV profiling seems to have been adopted as the primary method to study p-type conductivity in InN [243]. However, even with modelling, it is very difficult to distinguish between a p-type bulk and a heavily compensated n-type bulk. Recent thermopower measurements [164, 244] seem somewhat more conclusive, with a positive Seebeck coefficient measured giving a clear indication of mobile holes in the material. Anderson *et al.* [245] have additionally employed multiple-field Hall effect measurements, using quantitative mobility spectrum analysis and multiple carrier fitting to reveal both electron and hole signals with differing mobilities in Mg-doped InN. However, this technique requires a complex fitting procedure, and does not have any depth resolution. The unambiguous determination and characterisation of bulk p-type conductivity in InN, therefore, remains a very active challenge.

For the Mg-doped sample investigated here (GS1810), the bulk acceptor density has been estimated as $N_A = 2.1 \times 10^{19}$ cm^{-3} from ECV modelling [242], consistent with high concentrations of mobile holes estimated from thermopower measurements [244]. This density has been used here to determine the bulk Fermi level in Poisson-MTFA calculations, yielding band bending and carrier concentration profiles as a function of depth below the surface as shown in Fig. 6.7.

The propensity for high n-type conductivity in InN (discussed in Section 5.5.2), combined with the difficulty associated with p-type doping GaN [246], has resulted in the assumption that p-type doping of InN will be extremely difficult [247]. Despite

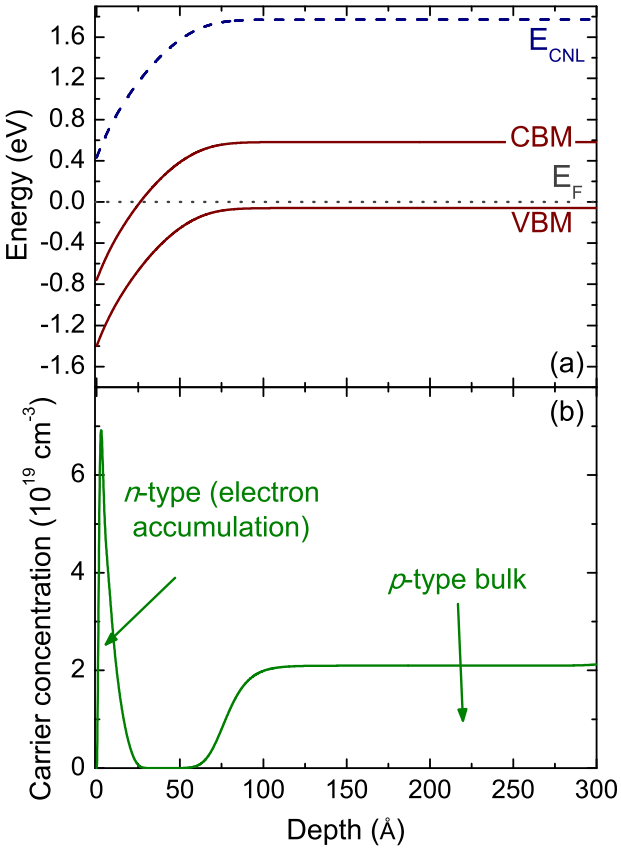

Figure 6.7: Poisson-MTFA calculations of (a) band bending and (b) carrier concentration variation in the inversion layer of the Mg-doped sample investigated here.

this, the investigations discussed above have suggested that InN has successfully been p-type doped with acceptor densities [187, 243] and heavy hole concentrations [245] estimated to be in excess of 10^{19} cm^{-3}, and possibly even degenerate concentrations of free holes have been identified [244]. The pinning of the Fermi level well into the conduction band at the surface may actually provide an intrinsic mechanism that increases the efficiency of p-type doping InN with Mg. The formation energy of the singly-charged acceptor formed by Mg substitutionally occupying the In site (Mg_{In}^{-}) is shown (after Stampfl *et al.* [190]) in Fig. 6.8(a). The formation energy decreases with increasing Fermi energy, indicating that it is easier to incorporate Mg-acceptors into the InN sample in regions of high n-type conductivity, where the Fermi level is high.

As seen above, the bulk conductivity has relatively little effect on the Fermi level position at the surface. The variation in Fermi level with depth for n- and p-type InN determined from Poisson-MTFA solutions for the samples considered above, with bulk carrier concentrations of $n = 3 \times 10^{18}$ cm^{-3} for the n-type sample

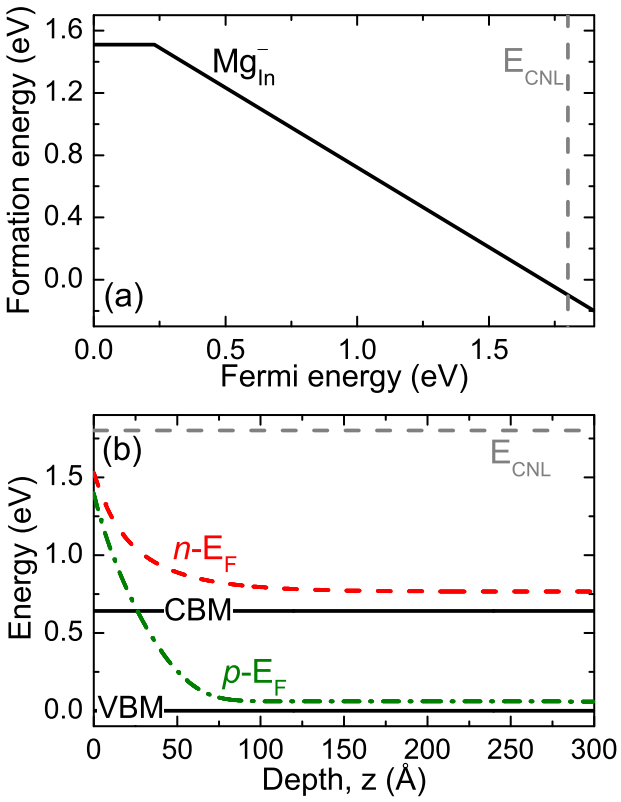

Figure 6.8: (a) Formation energy of the Mg_{In}^{-} acceptor in InN after Stampfl *et al.* [190]. (b) Fermi level above the VBM as a function of depth below the surface in the electron accumulation layer at n-type (n-E_F, dashed line) and p-type (p-E_F, dot-dashed line) InN surfaces. The CNL is located at 1.83 eV from Chapter 5.

and $p = 2 \times 10^{19}$ cm^{-3} estimated for the p-type sample, are shown in Fig. 6.8(b). Irrespective of the bulk conductivity or net donor/acceptor concentration, the Fermi level is very high at the surface. Consequently, the formation energy for incorporation of Mg_{In}^{-} acceptors is substantially lower at the surface than in the bulk of the material. During epitaxial growth, the Mg can therefore be incorporated more easily (as it is at the surface) than would be expected from considering the bulk properties of the material alone. Thus, despite masking its presence in conventional electrical characterisations, the p-type doping efficiency of InN may actually be enhanced by the presence of electron accumulation at the surface, explaining the high acceptor and hole densities that have previously been identified in InN:Mg films.

6.6 Conclusions

Electron accumulation has been shown to occur universally at InN surfaces due to the low position of the band extrema with respect to the charge neutrality level. The surface Fermi level pinning was shown to be the same for a-plane and for both polarities of c-plane wurtzite InN, although the pinning position was slightly

lower for zinc-blende InN(001). In addition to an accumulation of electrons at the surface, evidence was presented for an increase in electron density approaching the InN/buffer layer interface. A 'three-region' model was discussed, including contributions from background donors, interface-related electrons and the surface electron accumulation layer. A parallel conduction analysis of this model was performed, incorporating both ionized impurity scattering and charged dislocation scattering, reproducing the film-thickness dependence of carrier concentration and mobility determined from single-field Hall effect measurements of a large number of samples.

The surface electron accumulation layer was shown to lead to inversion layers in p-type InN. The Fermi level at the surface is pinned well above the CBM for both n-type and p-type InN, with only a slightly higher pinning position for the n-type case. From previous calculations of the formation energy for Mg_{In}^{-} acceptors, and from the pinning of the Fermi level at the surface determined here, the electron accumulation layer was shown to enhance the dopability of InN with Mg during epitaxial growth, explaining the high acceptor densities determined in some of the InN:Mg samples grown to date.

Chapter 7

Electronic properties of III-N alloys

7.1 Introduction

The III-nitrides present enormous promise for a range of electronic and optoelectronic device applications. This perhaps became most apparent with the introduction of high-brightness blue light emitting and laser diodes based around Ga-rich InGaN alloys [248–250], which have since stimulated a multi-billion dollar industry with implementation into many commercial technologies such as 'Blu-ray' DVD players.

The revision of the band gap of InN to less than 0.7 eV (see Section 5.1.2) extends the spectral range covered by this material system well into the infrared. Combined with GaN and AlN, which have fundamental band gaps of $\sim$3.5 eV and $\sim$6.2 eV respectively [170], In(Ga,Al)N alloys have a range of band gaps that covers an extremely large spectral window. As shown in Fig. 7.1, these band gaps are almost perfectly matched to the solar spectrum, suggesting potential application in full solar-spectrum high-efficiency photovoltaic devices. The range of band gaps offered by the III-N materials may, in fact, allow a multi-junction solar cell to be constructed from a single material system with an efficiency in excess of 50% at one sun illumination [251]. Wu *et al.* [252] have further shown that the optoelectronic properties of In-rich InGaN alloys show a higher degree of resistance to damage by high-energy irradiation than materials such as GaAs and GaInP that are presently used in photovoltaics, suggesting the application of In-rich III-N materials in solar cells for operation in hostile environments such as outer space. Given the high luminescence efficiency of InGaN, despite being characterised by high defect and dislocation densities [253], intense research effort has also been focussed on the III-N materials for use in high-performance light-emitting and laser diodes [250, 253, 254], including their potential application in solid state lighting [255].

Despite their importance for device applications, the electronic, and especially

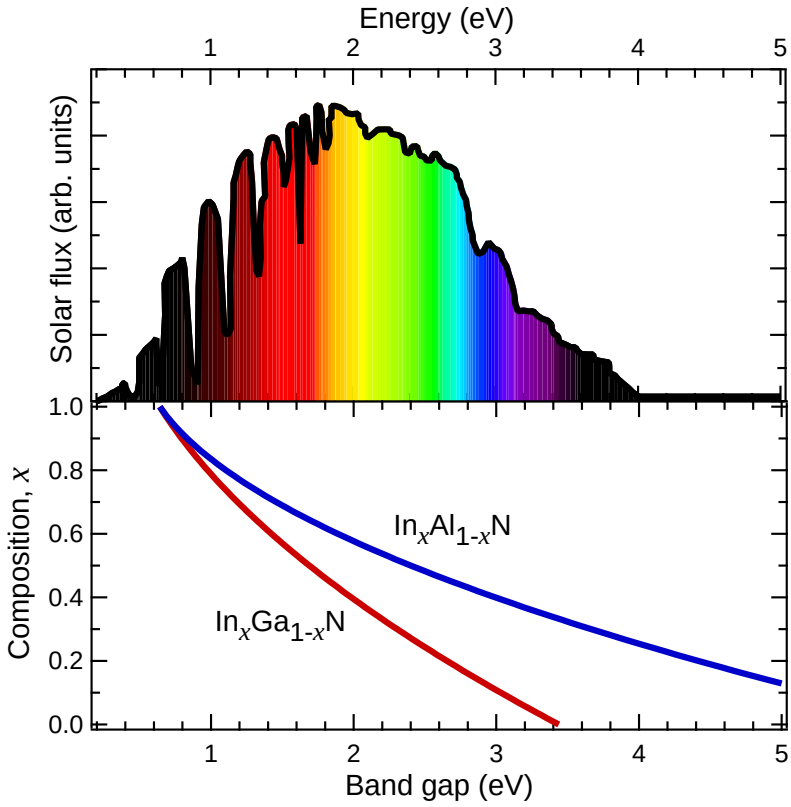

Figure 7.1: Fundamental band gaps of the InGaN and InAlN alloy systems, showing their good matching to the solar spectrum.

surface electronic, properties of (particularly In-rich) In(Ga,Al)N alloys are still not well characterised or understood. In order to achieve functioning devices, the surface electronic properties need to be understood across the composition range. In particular, they are crucial in determining the properties of metal/semiconductor and semiconductor/semiconductor contacts, which are fundamental components of the majority of device architectures. For example, to extract current from high-efficiency multi-junction solar cells, tunnel junctions must be formed between the active regions. This is not possible at InN surfaces, for example, where an electron accumulation generally results in ohmic contacts.

InAs is the only other III-V semiconductor which has been observed to exhibit electron accumulation at its surface [39]. Consequently, when InAs and InN are alloyed with other III-V materials, a transition from electron accumulation (inversion) to electron (hole) depletion for n- (p-) type material would be expected. This has previously been investigated via the variation in Au barrier heights on

n-InGaAs alloys [256], where such a transition was observed. Similar variation in surface electronic properties on moving from In-rich to Ga/Al-rich alloy compositions require investigation for In(Ga,Al)N alloys, across the composition range. Such an investigation, for undoped and Mg-doped alloys, is presented here, utilising high-resolution x-ray photoemission spectroscopy (XPS), single-field Hall effect measurements, and solutions of Poisson's equation within a modified Thomas-Fermi approximation (MTFA), as described in Section 2.2.2.

7.1.1 III-N band alignment

As discussed in the previous chapters, the overriding mechanism determining whether an accumulation or depletion of charge carriers occurs at the surface is the position of the band extrema relative to the charge neutrality level (CNL). To determine this across the composition range, detailed knowledge of the conduction and valence band offsets between InN, GaN and AlN is required. In addition, these quantities are themselves crucial to the design of heterostructure-based In(Ga,Al)N optoelectronic devices, and have consequently received considerable interest in recent years, both experimentally [257–263] and theoretically [21,25,178,186,264]. However, there is a large variety both within and between these studies. The reasons for this are discussed in detail in Ref. [180], but can, at least partly, be ascribed to the use of In 4*d* and Ga 3*d* levels in the determination of the valence band offset (VBO) by photoemission spectroscopy in a number of previous investigations. These levels, however, are very shallow in the nitrides, and so hybridize with the valence band structure [83]. This makes peak fitting of these features using conventional spectral functions impossible, yielding them inappropriate for use in the VBO measurement.

For this work, an investigation of the InN/GaN and InN/AlN VBOs, using XPS but with an alternative choice of core-levels to those that have adversely affected previous measurements, was therefore undertaken, and is reported in detail elsewhere [180,181]. The valence (conduction) band offset of InN/GaN and InN/AlN was identified as 0.58 eV (2.22 eV) and 1.52 eV (4.00 eV), respectively, as shown in Fig. 7.2, in good agreement with both theoretical predictions and the relative

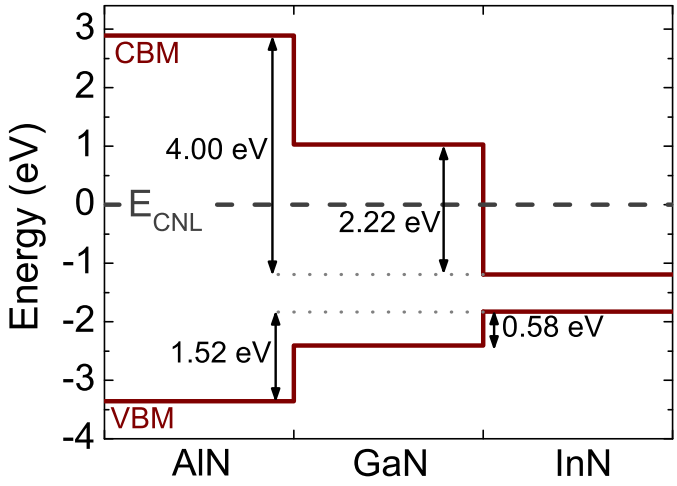

Figure 7.2: Band lineup of the III-N materials, relative to the CNL. The measured VBOs and calculated conduction band offsets (using the room temperature band gaps for each material) are shown. The VBM in InN is located 1.83 eV below the CNL as derived in Chapter 5.

locations of the CNL [182, this work (Chapter 5)]. From the transitivity rule, this gives the GaN/AlN VBO as $\sim$0.9 eV, in agreement with previous results [170]. As discussed in Section 5.4, the predominant factor in determining the alignment of the valence band edges in the common-anion III-N material system is a hybridization (or p–d repulsion) between the cation d–orbitals and N $2p$–orbital [186, 264], which pushes the valence band maximum (VBM) to higher energies [265]. Al has no occupied d–orbitals, whereas Ga and In both have occupied d–orbitals, explaining the relatively smaller VBO between InN and GaN than between AlN and (In/Ga)N. Taking the CNL position in InN from Chapter 5, the band lineup of the III-N semiconductors relative to the CNL can therefore be derived, as shown in Fig. 7.2.

7.1.2 Band-gap bowing

In addition to the binary band offsets, it is also necessary to know the variation in bulk properties such as band offsets and band gaps across the alloy composition range. In the simplest approximation, the so-called virtual crystal approximation, the parameters for any In(Ga,Al)N alloy is determined from a linear interpolation between the parameters of the binary semiconductors. This is used here for the VBO variation across the composition range, in agreement with the theoretical calculations of Mönch [21]. Other parameters, however, show a deviation from this linear behaviour. The variation in In(Ga,Al)N band gap across the composition range has previously been investigated [266–270], and was found to be well described

by a standard bowing equation

$$E_g^{AB}(x) = (1-x)E_g^A + xE_g^B + bx(1-x), \tag{7.1}$$

where the bowing parameter $b = 1.4$ eV for $In_xGa_{1-x}N$ alloys [266] and $b = 4.0$ eV for $In_xAl_{1-x}N$ alloys [269]. Due to the linear variation in valence band edge on an absolute energy scale, all of the band gap bowing occurs in the conduction band. The variation of other parameters, such as the effective mass, have not been investigated in detail across the composition range. However, given the empirical relation for the effective mass discussed in Section 5.1.2, an effective mass bowing parameter of $b_m = 0.07b$, where b is the band gap bowing parameter, seems a reasonable assumption, and will be used here.

7.2 Experimental details

Undoped $In_{0.14}Ga_{0.86}N$ and GaN samples were grown on *c*-plane sapphire substrates by metal-organic vapour phase epitaxy at the University of Liverpool, UK, utilizing a low-temperature (~ 550°C) GaN buffer layer. The substrate temperature was increased to 1050°C (830°C) for the GaN ($In_{0.14}Ga_{0.86}N$) epilayer growth. The remaining undoped and Mg-doped $In_xGa_{1-x}N$ samples were grown on *c*-plane sapphire substrates by plasma-assisted molecular-beam epitaxy (PAMBE) at Cornell University, USA, incorporating AlN (grown at 800°C) and/or GaN (grown at 750°C) buffer layers. The $In_xGa_{1-x}N$ layer thicknesses ranged from 100 to 1000 nm and growth temperatures from 480°C to 740°C. The Mg cell temperature was approximately 350°C for all Mg-doped sample growths. The $In_xAl_{1-x}N$ alloys were grown by PAMBE on *c*-plane sapphire substrates incorporating AlN buffer layers at the University of Crete, Greece (Al-rich undoped samples) and Cornell University, USA. The $In_xAl_{1-x}N$ layer thicknesses ranged from 190 nm to 4600 nm. Further details of the growth methodologies are reported elsewhere [171, 214, 271].

The InGaN and undoped InAlN alloy compositions were determined elsewhere by x-ray diffraction (XRD) using the GaN (0002) or AlN (0002) buffer layer peak as a reference peak and assuming a linear dependence of the lattice constant,

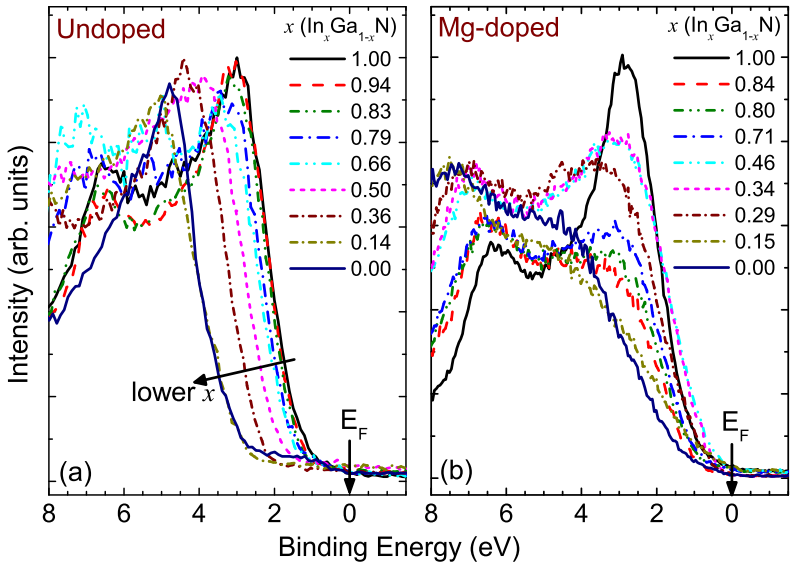

Figure 7.3: Valence-band XPS spectra for (a) undoped and (b) Mg-doped $In_xGa_{1-x}N$ alloys with respect to the Fermi level, E_F.

c, on alloy composition (Vegard's law)

$$c\left[\mathrm{In}_x(\mathrm{Ga/Al})_{1-x}\,N\right] = c\left[(\mathrm{Ga/Al})\mathrm{N}\right] - x\left\{c\left[(\mathrm{Ga/Al})\mathrm{N}\right] - c\left[\mathrm{InN}\right]\right\}. \tag{7.2}$$

The compositions determined from XRD also agreed well with those determined elsewhere from Rutherford Backscattering (RBS) measurements. The Mg-doped InAlN alloy compositions were all determined from RBS measurements.

Single-field Hall effect and XPS measurements were performed as described in Chapter 3. However, the Al-rich samples were insulating and so required charge compensation during the XPS measurements via a low-energy electron flood gun. For these alloys, the calibration of the Fermi level was achieved via a referencing of the binding energy of the C 1s core-level peak (from physisorbed carbon) to the average C 1s binding energy for the In-rich InAlN samples where no flood gun had been used.

7.3 InGaN Alloys

7.3.1 Results and Analysis

The position of the surface Fermi level as a function of alloy composition was investigated using valence band XPS measurements, shown in Fig. 7.3. For the undoped

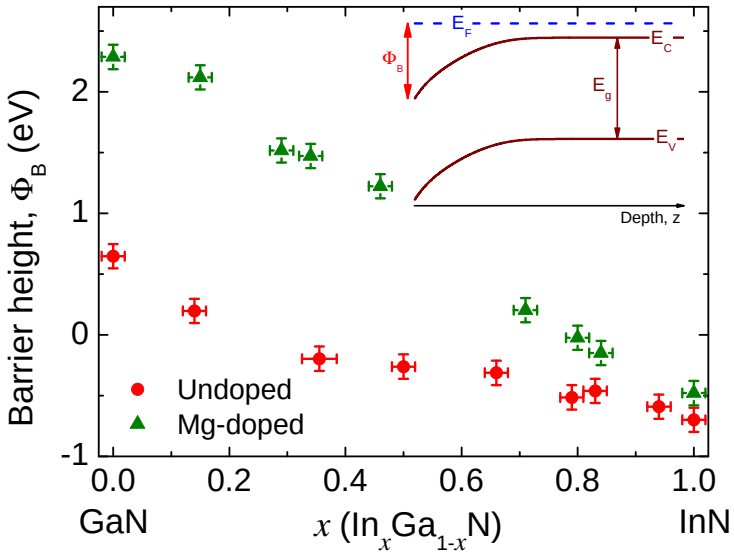

Figure 7.4: Barrier height, Φ_B, for undoped and Mg-doped $In_xGa_{1-x}N$ samples. The barrier height, represented schematically inset, is taken as negative if the Fermi level is above the CBM at the surface and positive if the Fermi level is below the CBM at the surface. A band gap bowing parameter of $b = 1.4$ eV [266] has been used to determine the barrier height from the VB-XPS measurements.

$In_xGa_{1-x}N$ samples, an increase in VBM to surface Fermi level separation is observed with increasing Ga-fraction, although no such monotonic trend is observed for the Mg-doped alloys. However, it is also necessary to consider the effects of the increasing band gap upon moving from In-rich to Ga-rich alloys. This is achieved by determining the barrier height, Φ_B (analogous to the n-type Schottky barrier height of a semiconductor-metal junction), defined as the conduction band minimum (CBM) to surface Fermi level separation, shown in Fig. 7.4. A clear trend in barrier height is evident across the composition range for both undoped and Mg-doped alloys, with the Mg-doped alloys exhibiting higher values of Φ_B compared to the undoped alloys for all alloy compositions, with the largest differences for Ga-rich alloys. This difference in barrier height provides initial evidence that Mg-doping is acting to induce a bulk p-type conductivity across the entire InGaN alloy composition range.

The bulk carrier density in the undoped samples was measured by the single-field Hall effect, and these values were used to determine (via non-parabolic carrier statistics calculations) the position of the bulk Fermi level. The surface and bulk Fermi level positions relative to the semiconductor band edges and the CNL are shown in Fig. 7.5.

For the most In-rich alloys, the surface Fermi level position is pinned well above the bulk Fermi level, indicating an extreme electron accumulation as for

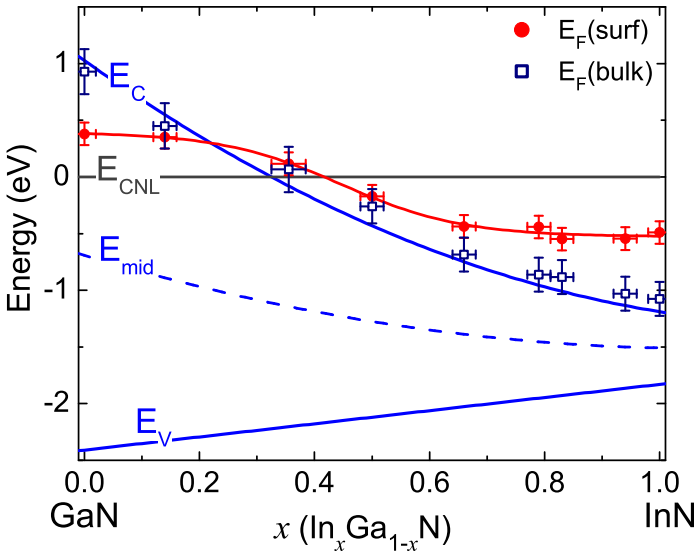

Figure 7.5: Surface (filled circles) and bulk (open squares) Fermi level (E_F) for undoped $In_xGa_{1-x}N$ alloys relative to the CNL (E_{CNL}), and InGaN band edges (E_C, E_V) and mid-gap position (E_{mid}). The CNL is located 1.83 eV above the VBM in InN (Section 5.3). The variation in valence band edge is assumed to be linear after Mönch [21], with the measured valence band offset of 0.58 eV (Section 7.1.1) and a band gap bowing parameter of 1.4 eV [266] (entirely in the conduction band due to the linear variation of the valence band edge) used to define the band edges relative to the CNL.

InN. In contrast, for the Ga-rich alloys, the surface Fermi level is pinned below the bulk Fermi level, indicating an upward band bending and electron depletion at the surface, as known for GaN [189]. For alloys closer to the middle of the composition range, the surface and bulk Fermi level positions move closer together, leading to a reduction in the degree of space-charge characteristics towards flat-band conditions. This is illustrated by Poisson-MTFA calculations, shown in Fig. 7.6, which show a pronounced electron accumulation for InN, virtually no electron accumulation for $In_{0.5}Ga_{0.5}N$ and a large electron depletion layer for GaN.

The surface Fermi level positions determined from the XPS measurements for the Mg-doped alloys, along with those for the undoped alloys, are shown in Fig. 7.7. The pinning position of the surface Fermi level for the Mg-doped and undoped material diverges with increasing Ga-content, as seen from the barrier heights discussed above. Accurate determination of the bulk carrier density is not possible due to the inversion layers for In-rich alloys. However, assuming that Mg-doping causes bulk p-type conductivity, the bulk Fermi level will be located close to the VBM. Consequently, the surface Fermi level is located above the bulk Fermi

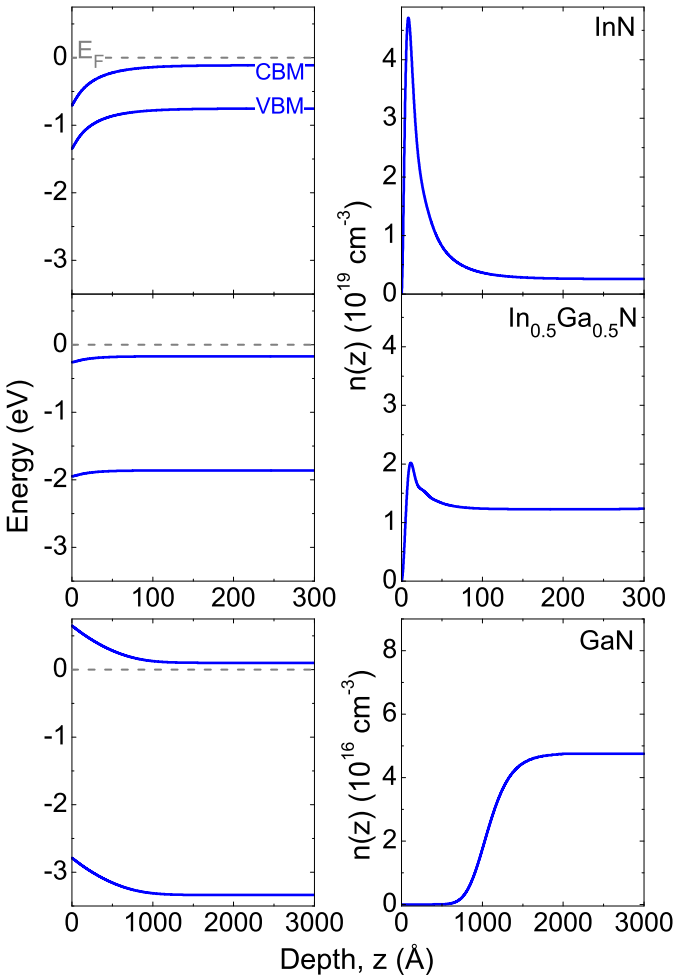

Figure 7.6: Band bending and carrier concentration profiles as a function of depth from Poisson-MTFA calculations for InN, $In_{0.5}Ga_{0.5}N$, and GaN.

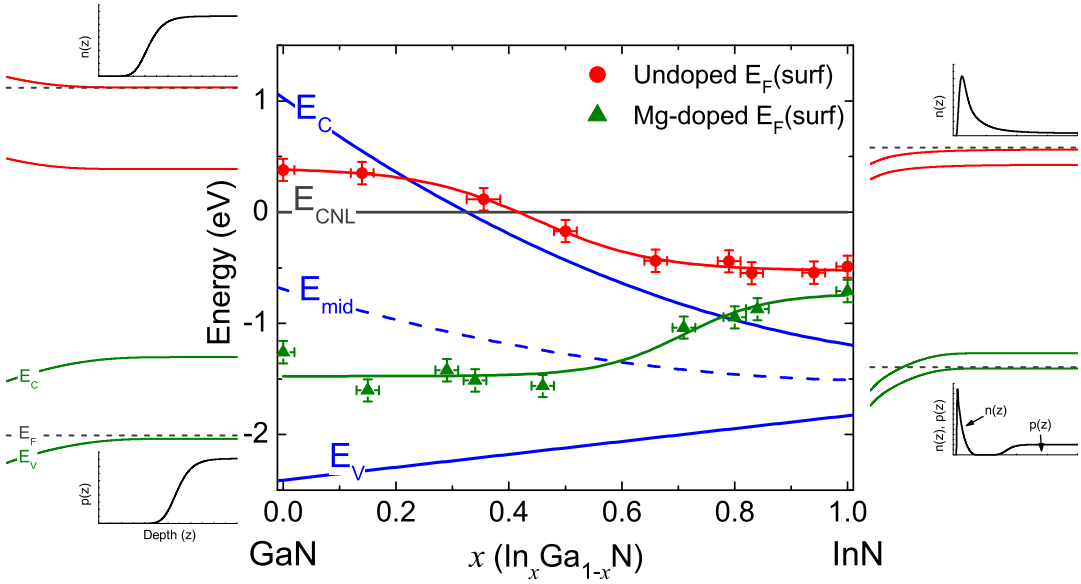

Figure 7.7: Surface Fermi level (E_F) for undoped (circles) and Mg-doped (triangles) $In_xGa_{1-x}N$ alloys relative to the CNL (E_{CNL}), and InGaN band edges (E_C, E_V) and mid-gap position (E_{mid}). The band edges are constructed as in Fig. 7.5. A schematic representation of the space-charge characteristics of each of the end points is also shown.

level across the composition range, indicating that downward band bending occurs for all alloy compositions. For the Ga-rich alloys, this leads to a hole depletion layer occurring at the surface, as shown schematically in Fig. 7.7. However, for the In-rich alloys, the surface Fermi level is pinned above the mid-gap position; electrons are the dominant carrier species at the surface, creating an inversion layer where the p-type bulk is separated from an n-type surface region by a depletion layer, as represented schematically in Fig. 7.7.

7.3.2 Discussion

The space-charge regions discussed above are consistent with the theory of virtual gap states (ViGS) and the variation of the CNL position relative to the band edges across the alloy system. The Fermi level approaches the CNL from below for both n- and p-type InN bulk conductivities. Consequently, the surface Fermi level pinning position is similar in both cases. This leads to extreme electron accumulation at the surface of both n- and p-type InN, which balances a positive surface charge due to unoccupied donor ViGS. For p-type InN, this electron accumulation leads to the formation of an inversion layer, as discussed in Section 6.5.

With increasing Ga fraction, the surface Fermi level for the n-type alloys remains pinned close to the CNL. However, as the CBM approaches, and typical Fermi levels move above, this energy, the surface Fermi level becomes pinned above the CNL (Fig. 7.5), causing some acceptor ViGS to be occupied and hence negatively charged. This surface charge is balanced by a reduction in near-surface electron density manifested as an upward bending of the bands with respect to the Fermi level. Thus, Ga-rich n-type alloys have electron depletion regions at the surface, as represented schematically in Fig. 7.7. The $In_xGa_{1-x}N$ composition marking the transition from surface electron accumulation (In-rich alloys) to electron depletion (Ga-rich alloys) can be estimated, to first order, as the crossing of the surface Fermi level pinning position and the CNL. From Fig. 7.7, this is estimated to occur at $x \approx 0.41$, although this will show some variation dependent on exact bulk Fermi levels in individual samples. Further, if an element is deposited on the surface (for

example if making a metal/semiconductor contact), charge transfer between the semiconductor and the metal will cause the Fermi level pinning position to vary somewhat dependent on their relative electronegativities.

The behaviour of the Mg-doped alloys is rather different (Fig. 7.7). The surface Fermi level is pinned below the CNL across the composition range, indicating that unoccupied (and hence negatively charged) ViGS are present, leading to downward band bending for all alloy compositions. With increasing Ga fraction, the VBM and hence the Fermi level in the p-type bulk, move further away from the CNL, requiring the surface Fermi level to pin at lower energies to maintain charge neutrality. The large difference between the n- and p-type surface Fermi level pinning positions for Ga-rich alloys can be attributed to the Fermi level approaching the CNL from above for n-type alloys and below for p-type alloys. The measured differences in GaN are consistent with previous results [189, 272]. For the Ga-rich alloys, the positively charged donor surface states are compensated by the background negatively charged acceptors in the hole depletion region. For the In-rich alloys, however, the CNL is above the CBM, allowing the ViGS to donate electrons directly into the conduction band, leading to a large accumulation of electrons causing an inversion layer at the surface. The transition from inversion (In-rich) to hole depletion (Ga-rich) surface space-charge regions occurs, to first order, when the surface Fermi level crosses the mid-gap position, and electrons are no longer the dominant carrier species at the surface. From Fig. 7.7, this can be estimated to occur at an $In_xGa_{1-x}N$ alloy fraction of $x \approx 0.59$. This p-type transition is, however, somewhat different from the n-type transition. In the former case, downward band bending occurs across the composition range, the transition simply marking a change in relative magnitude of the band bending leading to a change in the dominant surface carrier type. Conversely, in the latter case, the transition marks a change in the direction of band bending and hence a change in the type of contact (that is, Schottky or Ohmic) that could be made at the surface.

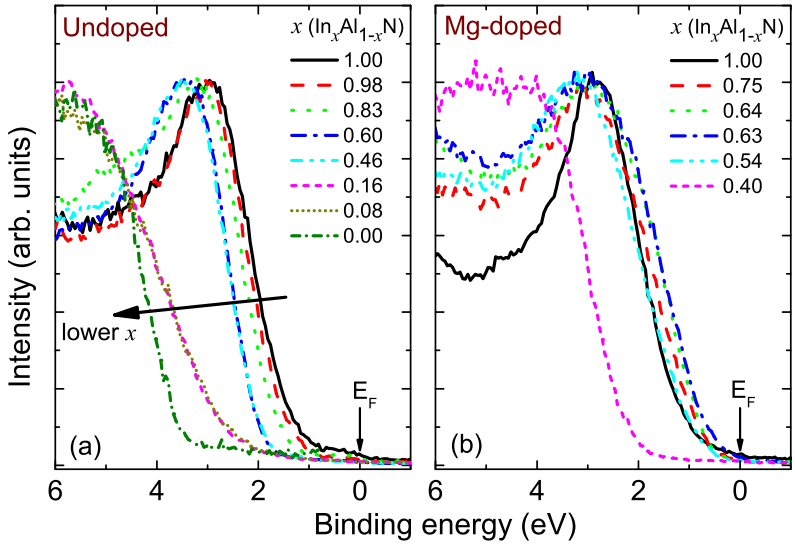

Figure 7.8: Valence-band XPS spectra for (a) undoped and (b) Mg-doped $In_xAl_{1-x}N$ samples with respect to the Fermi level, E_F.

7.4 InAlN Alloys

7.4.1 Results and Analysis

Valence band photoemission spectra from undoped and Mg-doped InAlN samples are shown in Fig. 7.8. Again, the leading edge of the valence band photoemission shifts to higher binding energies with increasing Al-content for the undoped InAlN alloys, indicating an increase in the VBM to surface Fermi level separation with increasing Al-content. However, as for the InGaN:Mg alloys, the change in VBM to surface Fermi level separation is non-monotonic with alloy composition for the InAlN:Mg alloys. The barrier heights, Φ_B, are also shown in Fig. 7.9. A similar difference in the barrier height between the undoped and Mg-doped InAlN samples is seen here for In-rich alloy compositions, as was observed for the InGaN alloys (Fig. 7.4), again suggesting that Mg-doping is causing bulk p-type conductivity in the In-rich InAlN alloys. However, the barrier height for the Mg-doped and undoped samples become very similar for Al-rich alloys, suggesting that p-type bulk conductivity has not been achieved in these samples.

The surface Fermi level positions, determined from the XPS measurements, are shown relative to the semiconductor band edges and the CNL in Fig. 7.10. The carrier density, from single-field Hall effect measurements, was again used to

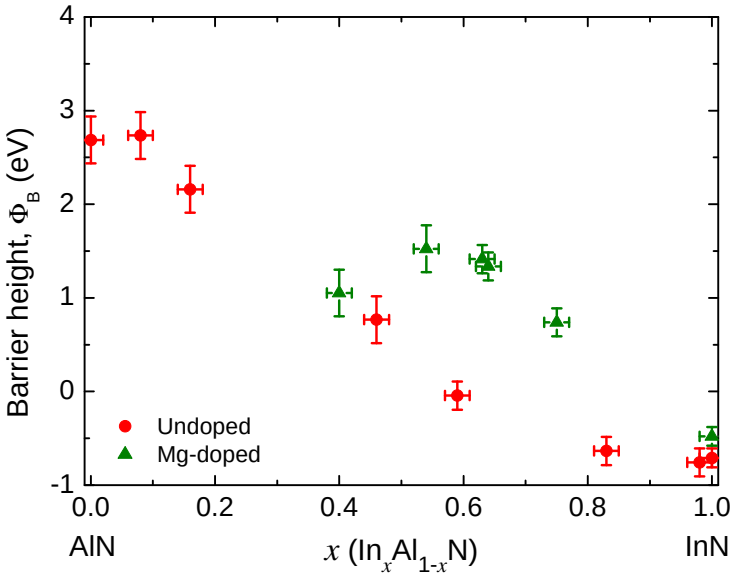

Figure 7.9: Barrier height, Φ_B, for undoped and Mg-doped $In_xAl_{1-x}N$ samples.

determine the bulk Fermi level, which is shown for the In-rich samples in Fig. 7.10. The Al-rich samples were insulating from single-field Hall effect measurements, and so, although a precise value of the bulk Fermi level could not be determined, it is expected to lie significantly below the CBM, approaching the mid-gap position. The insulating nature of the Al-rich samples was confirmed by the necessity of using a low-energy electron flood gun to achieve charge compensation in the XPS measurements.

For the most In-rich samples, the surface Fermi level lies significantly above the bulk Fermi level, implying an extreme electron accumulation is present at the surface. However, the surface and bulk Fermi levels do move closer together with increasing Al-content, indicating a reduction in the amount of band bending and hence a reduction in the degree of electron accumulation at the surface, as is clearly evident from comparing the Poisson-MTFA calculations for InN and $In_{0.83}Al_{0.17}N$, shown in Fig. 7.11. On further increase of the Al content to 41% ($In_{0.59}Al_{0.41}N$), the bulk and surface Fermi levels are virtually coincident in energy, leading to almost no electron accumulation as shown in Fig. 7.11. A reduction of the amount of electron accumulation upon increasing the Al-content in In-rich n-InAlN alloys has therefore been observed, as was observed above upon increasing the Ga-content in In-rich n-InGaN alloys.

With further increase in Al-content, the samples become insulating. The bulk

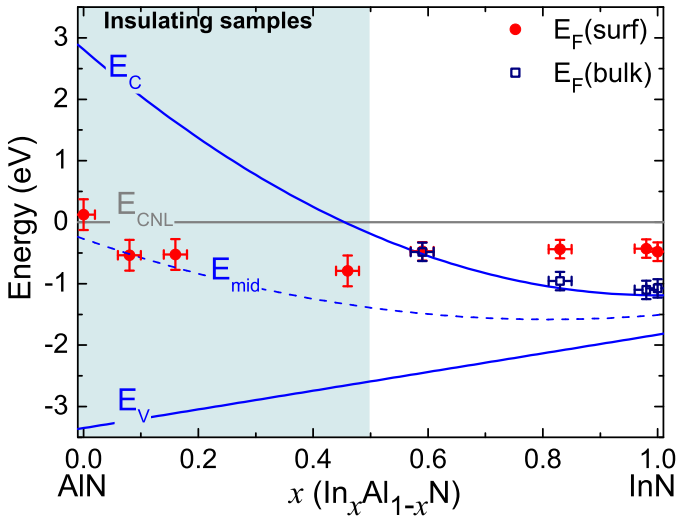

Figure 7.10: Surface (filled circles) and bulk (open squares) Fermi level (E_F) for undoped $In_xAl_{1-x}N$ alloys relative to the CNL (E_{CNL}), and InAlN band edges (E_C, E_V) and mid-gap position ($E_{\rm mid}$). The CNL is located 1.83 eV above the VBM in InN (Section 5.3). The variation in valence band edge is assumed to be linear after Mönch [21], with the measured valence band offset of 1.52 eV (Section 7.1.1) and a band gap bowing parameter of 4 eV [269] (entirely in the conduction band due to the linear variation of the valence band edge) used to define the band edges relative to the CNL.

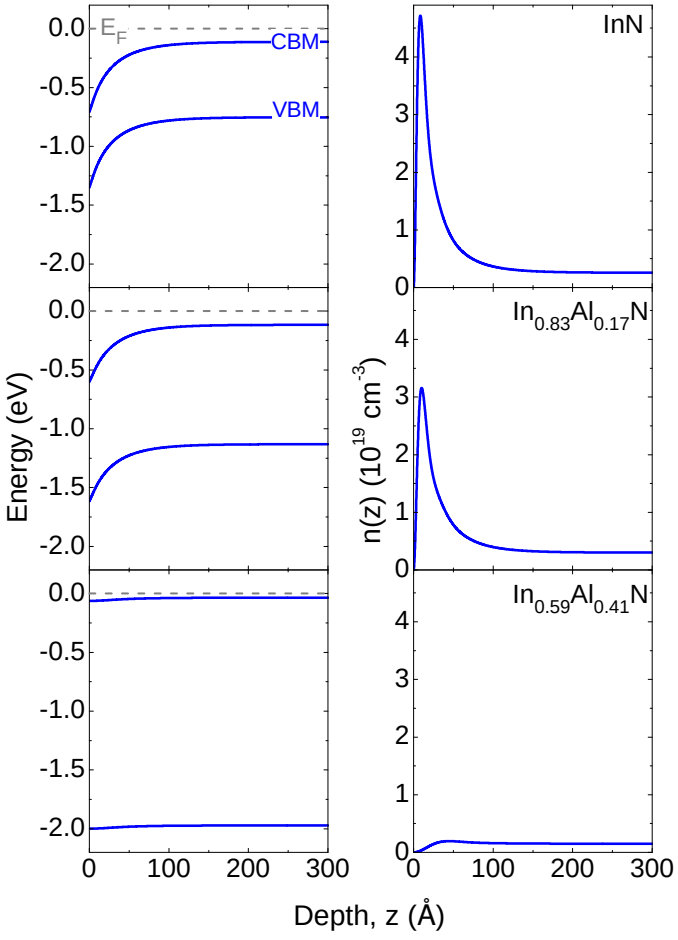

Figure 7.11: Band bending and carrier concentration profiles as a function of depth from Poisson-MTFA calculations for InN, $In_{0.83}Al_{0.17}N$ and $In_{0.59}Al_{0.41}N$.

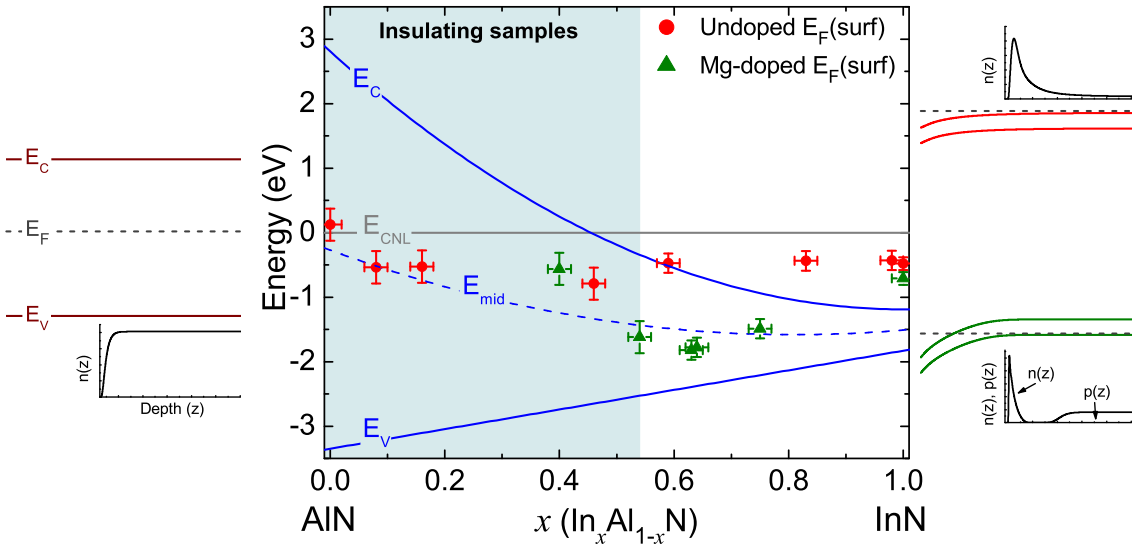

Figure 7.12: Surface Fermi level (E_F) for undoped (circles) and Mg-doped (triangles) $In_xAl_{1-x}N$ alloys relative to the CNL (E_{CNL}), and InAlN band edges (E_C, E_V) and mid-gap position (E_{mid}). The band edges are constructed as in Fig. 7.10. A schematic representation of the space-charge characteristics of each of the end points is also shown.

Fermi level is expected to lie close to the mid-gap position, and as evident from Fig. 7.10, the surface Fermi levels also tend towards the mid-gap energy, suggesting approximately flat-band behaviour for the Al-rich samples. Small amounts of band bending may be present at these surfaces dependent on the exact relative position of the bulk and surface Fermi levels, but this is not expected to be a large effect.

The surface Fermi level positions determined from the XPS measurements for the Mg-doped alloys, along with the undoped values, are shown in Fig. 7.12. For InN, an inversion layer exists as discussed above. However, similar to InGaN, a reduction in the surface Fermi level to below the mid-gap position, resulting in hole depletion, occurs with increase of Al-content. From Fig. 7.12, this is estimated to occur at an alloy composition of $x \sim 0.7$. With further increase in Al-content, however, the surface Fermi level pins close to that of the undoped alloys, and the samples are insulating giving rise to approximately flat-band conditions, as represented schematically in Fig. 7.12.

7.4.2 Discussion

As for the InGaN alloys, the surface Fermi level pins somewhat below the CNL for In-rich InAlN alloys, leading to a number of unoccupied donor ViGS, a positive

surface charge, and hence downward band bending to maintain charge neutrality. As the Al-content is increased, the CNL moves towards the CBM. The resulting decrease in the density of states around the CNL energy causes the surface and bulk Fermi levels to move closer together, as was observed experimentally.

The insulating nature of the Al-rich samples can also be understood by considering the CNL position relative to the band edges. Within the amphoteric defect model introduced in Section 1.4 [45], the favourable charge state of native defects is determined by the position of the Fermi level relative to the CNL, so that native defects act to drive the Fermi level towards the CNL. As the Al-composition increases, the CNL moves closer towards the middle of the direct band gap. Native defects therefore drive the Fermi level lower in the band gap, leading to insulating samples. Theoretical calculations [273] for Mg acting as an acceptor in AlN also show a pronounced increase in formation energy as the Fermi level moves towards the valence band; the resulting formation energy lies above that of the triply charged donor nitrogen vacancy, indicating donor-type native defects will act to compensate the Mg-doped samples, again leading to insulating samples. The approximately flat-band behaviour observed for the Al-rich samples can be considered as a compromise between, as was observed for InGaN, pinning of the surface Fermi level above the CNL, close to the CBM, for n-type alloys and pinning of the surface Fermi level well below the CNL, close to the VBM, for p-type alloys.

7.5 Conclusions

The surface electronic properties of undoped and Mg-doped $In_xGa_{1-x}N$ alloys have been investigated. The surface Fermi level pinning position for the undoped and Mg-doped alloys was seen to diverge with increasing Ga content, explained within the concept of virtual gap states, which gives evidence that Mg-doping induces a p-type bulk conductivity across the composition range. This divergence indicates a stronger pinning of the surface Fermi level in In-rich alloys due to the high location of the CNL relative to the CBM. A change in band bending direction causing a transition from surface electron accumulation (In-rich) to depletion (Ga-rich) oc-

curs at $x \approx 0.41$ for n-type alloys, whereas downward band bending occurs across the composition range for p-type alloys with a transition from surface inversion to hole depletion at $x \approx 0.59$. A similar investigation for $In_xAl_{1-x}N$ alloys revealed the surface electron accumulation reduced with increasing Al-content for the In-rich alloys, with approximately flat bands observed for $x = 0.59$. Upon further increase in Al-content, the samples became insulating resulting in the surface Fermi level pinning close to the mid-gap energy with little surface space-charge characteristics. For Mg-doped In-rich alloys, a transition from inversion to hole depletion was inferred at an alloy composition of $x \sim 0.7$. For Al-rich alloys, the surface Fermi level pinning position tended to that of insulating undoped samples due to the difficulty of p-type doping Al-rich InAlN alloys because of the increasing formation energy of Mg-acceptors and compensation by native point defects. The charge neutrality level was identified as crucial for understanding both the bulk and surface electronic properties of In(Ga,Al)N alloys across the composition range.

Chapter 8

Surface electron accumulation and the charge neutrality level in In_2O_3

8.1 Introduction

Transparent conducting oxides (TCOs), such as In_2O_3, SnO_2, ZnO, and indeed CdO (discussed in Chapter 4), along with their alloys, represent an important class of materials with applications including transparent electronics, contacts for photovoltaic devices, liquid crystal displays, light emitting diodes and chemical sensors [9, 274–276]. Recently, there has been increased interest in considering single-crystalline thin-film and nanostructured TCO materials as semiconductors in their own right, with potential applications in electronic, short wavelength photonic, and chemical and biological sensor devices [104, 277–282]. In_2O_3, the ubiquitous TCO material, has received much attention, and indeed implementation [9]; however, even basic material quantities such as its fundamental band gap have proved controversial. Its direct band gap was long thought to be ~ 3.75 eV from the onset of significant optical absorption, with a low intensity onset of absorption attributed to indirect optical transitions [283, 284]. This indirect band gap hypothesis was not, however, supported by theoretical calculations, which found no significant indirect nature of the band gap [285–289]. These experimental and theoretical results have recently been reconciled [288, 289], with In_2O_3 shown to have a direct band gap $E_g \lesssim 3$ eV. The weak nature of optical absorption around this energy can be attributed to transitions between the highest valence band states and states at the conduction band minimum (CBM) being dipole forbidden or having only minimal dipole-intensity. While the direct band gap of In_2O_3 is now known to be much smaller than previously thought, an accurate determination of its value is still required. This is performed here from a comparison of measured and calculated optical absorption coefficients.

In order to fully realise the range of potential device applications, in particular

for its use as contacts, sensors and in nanoscale material where the surface to bulk ratio is much higher than in conventional films, it is also crucial to understand the surface electronic properties of this material. In_2O_3 has been reported to exhibit a pronounced depletion of electrons at the surface [290, 291]. However, following the revision of the fundamental band gap and improvements in growth resulting in high-quality single-crystalline In_2O_3 films [292, 293], these surface space-charge regions need to be reinvestigated. This chapter reports an investigation of the surface electronic properties of epitaxial undoped and Sn-doped In_2O_3 using a combination of high-resolution x-ray photoemission spectroscopy (XPS), single-field Hall effect, and infrared (IR) reflectivity measurements, combined with space-charge layer calculations. In contrast to previous results, electron accumulation is identified at the surface of undoped In_2O_3 films. Additionally, from a combination of measurements performed on undoped and heavily Sn-doped samples, the charge neutrality level (CNL) is shown to lie $\sim$0.65 eV above the CBM in In_2O_3, explaining the electron accumulation at the surface of undoped material, the propensity for n-type conductivity, and the ease of n-type doping In_2O_3, and hence its use as a TCO material. Finally, the implications of the CNL position on the electrical behaviour of hydrogen in In_2O_3 are investigated via muon spin rotation and relaxation (μSR) spectroscopy.

8.1.1 Crystal and electronic structure and band parameters

The stable structure of In_2O_3 is the body centred cubic (*bcc*) bixbyite structure with space group $Ia\bar{3}$, shown in Fig. 8.1(a), with a lattice parameter of $a = 10.1$ Å. The corresponding Brillouin zone is shown in Fig. 8.1(b). The band structure of bixbyite In_2O_3, from density-functional theory (DFT) calculations [289], is shown in Fig. 8.2. Due to the large number of atoms within the unit cell (each cell containing sixteen units of In_2O_3), the band structure is rather complex. Of particular note, however, is the single, rapidly dispersing conduction band state around the CBM, and the fact that both the top valence band and bottom conduction band states are of the same parity [288]. This is important for the optical properties of this material, discussed below. The conduction band minimum effective mass of $0.35m_0$, and the static and

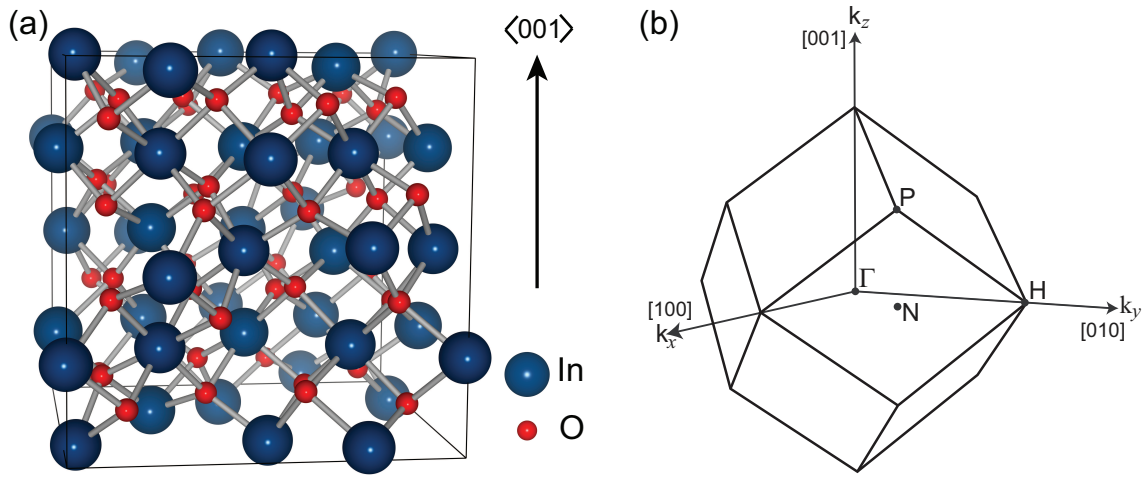

Figure 8.1: (a) Unit cell of the bixbyite crystal structure of In_2O_3, and (b) Brillouin zone of the *bcc* lattice.

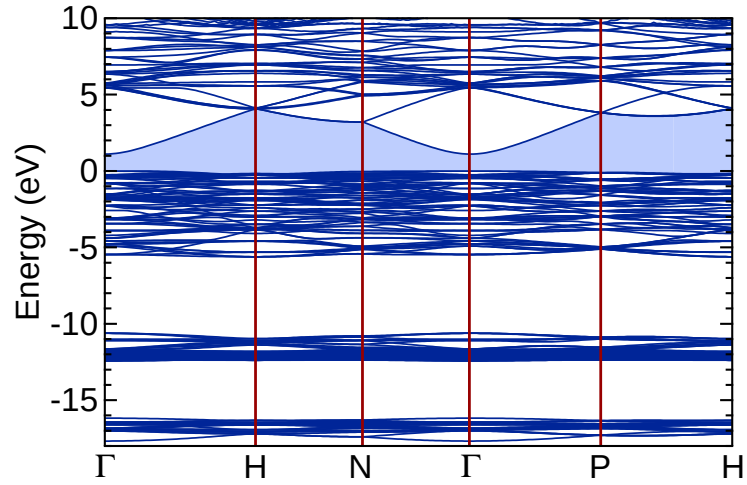

Figure 8.2: DFT band structure calculations for bixbyite In_2O_3 [289]. The fundamental energy gap across the Brillouin zone is represented by shading.

high frequency dielectric constants are 8.9 and 4.0, respectively, are used here from Ref. [275].

In addition, by judicious choice of substrate, trimethylindium flow rate, and growth temperature during metal-organic vapour phase epitaxy (MOVPE), growth of the metastable rhombohedral (rh) phase of In_2O_3 has been demonstrated [294]. The crystal and electronic structure of this polymorph of In_2O_3 are shown in Fig. 8.3. While slightly simpler, due to the smaller number of atoms in the unit cell (30 rather than 80), the electronic structure is similar to that of the *bcc* polymorph.

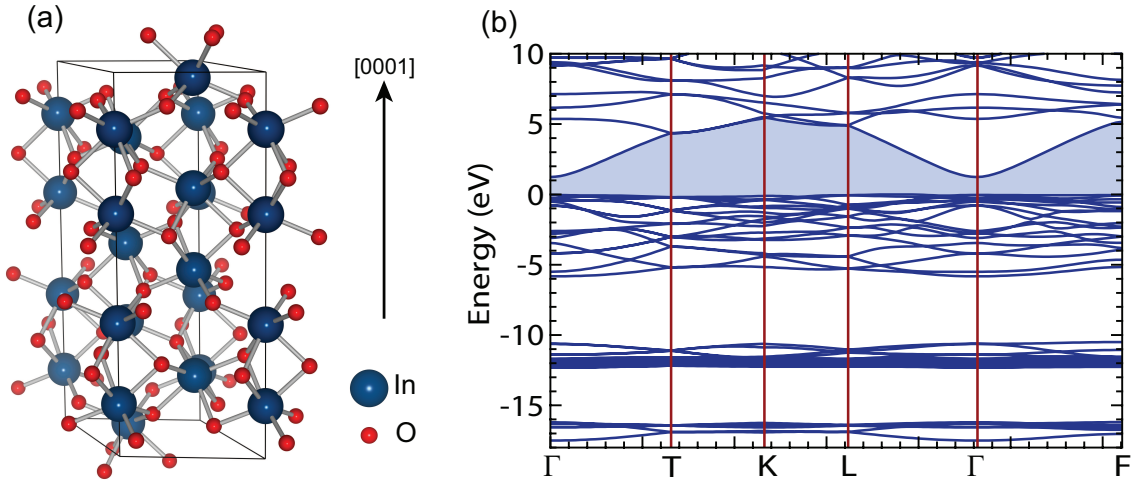

Figure 8.3: (a) Crystal structure of *rh*–In_2O_3, showing the unit cell, and (b) corresponding band structure from DFT calculations [289].

8.2 Experimental and theoretical details

Undoped and Sn-doped *bcc*–In_2O_3(001), and undoped *bcc*–In_2O_3(111) samples were grown at the University of Oxford, UK, by oxygen plasma-assisted molecular beam epitaxy (PAMBE) at a growth temperature of 650°C on yttria stabilized cubic-zirconia (YSZ) (001) and (111) substrates, respectively. The In_2O_3 layer thicknesses were 120 nm determined from growth rate calculations, which were themselves calibrated from cross-sectional transmission electron microscopy (TEM) measurements of films grown under identical conditions. No evidence of secondary phases was observed from TEM measurements. Further details of the growth and structural characterisation are reported elsewhere [293]. Undoped *bcc*–In_2O_3(111) and *rh*–In_2O_3(0001) films were grown at Technical University Ilmenau, Germany, by MOVPE. Trimethylindium and H_2O were used as growth precursors. The *bcc*–In_2O_3 was grown at 400°C on a sapphire substrate incorporating InN, GaN and AlN buffer layers. The *rh*–In_2O_3 was grown at 600°C directly on a sapphire substrate, and was estimated to contain less than 10% cubic inclusions. Further details of the growth and structural characterisation are reported elsewhere [292, 294]. Single-field Hall effect, XPS, optical absorption and IR reflectivity measurements were performed as described in Chapter 3. These measurements were performed at room temperature.

μSR measurements were performed using the EMU spectrometer on the

pulsed muon beamline at ISIS, Rutherford Appleton Laboratory, UK. Muons are generated from the decay of pions, following the interaction of a proton beam with a graphite target. The muon beam is 100% spin-polarised prior to being injected into the sample (a 99.999% purity In_2O_3 powder). The sample was mounted in a closed-cycle refrigerator, which was subsequently placed in a transverse magnetic field of 10 mT. Measurements were performed over the temperature range of 10–150 K.

DFT calculations were performed elsewhere, as described in Section 2.1.2. The large size of the In_2O_3 unit cell, especially for the *bcc* polymorph, made this system very computationally expensive. The valence band density of states (VB-DOS) was therefore calculated using the HSE03 functional, but neglecting quasiparticle (QP) effects. For comparison with the photoemission measurements, the calculated VB-DOS was convolved with a 0.4 eV full width at half maximum (FWHM) Gaussian and a 0.4 eV FWHM Lorentzian to account for instrumental and lifetime broadening, respectively. For the *rh* polymorph, the theoretical band gap was calculated by employing G_0W_0 QP corrections to the HSE03 eigenvalues. However, this proved too computationally expensive for the *bcc*–In_2O_3 polymorph. Consequently, the gap opening caused by QP corrections for the *rh* polymorph was applied as a rigid shift for the *bcc* polymorph, therefore approximately including QP effects. Optical spectra were calculated from the band structure determined within the local density approximation, treated within the independent QP approximation using scissor shifts to correct the band gap to that obtained from the HSE+QP calculations. Further details of the calculations are described elsewhere [289].

8.3 Band gap

The measured optical absorption coefficient from *bcc*–In_2O_3 is shown in Fig. 8.4(a). Significant onset of absorption in the measured spectrum occurs above ~ 3.5 eV, consistent with previous observations [283, 294]. A pronounced low energy tail is seen below this absorption edge. In previous reports, this was attributed to indirect optical absorption [283], in contrast to the results of theoretical band structure calculations [285–287]. However, as discussed in the introduction, an alternative

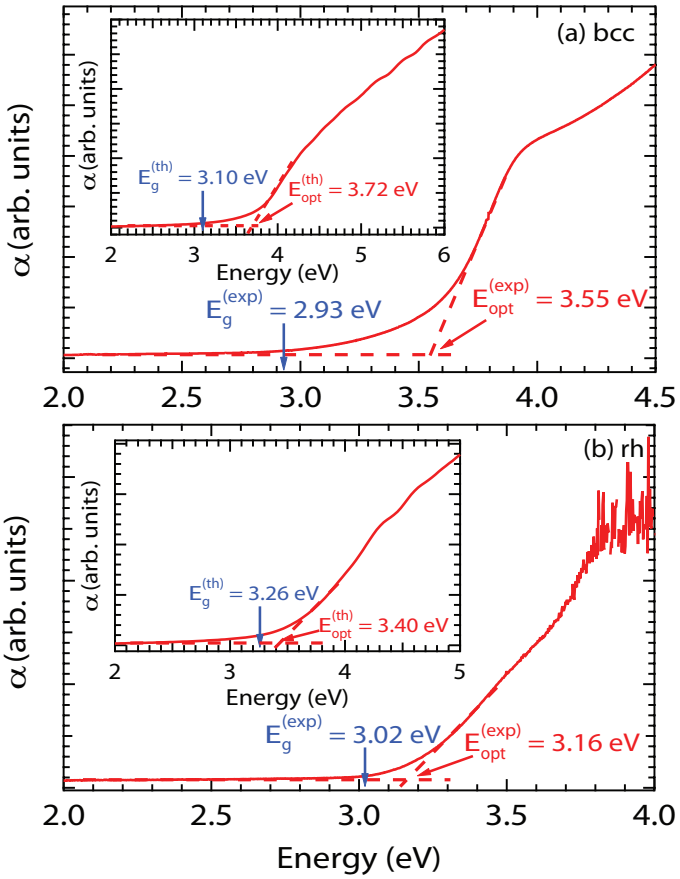

Figure 8.4: Experimental absorption coefficient, α, measured from (a) *bcc*–In_2O_3(001) and (b) *rh*–In_2O_3(0001). The calculated absorption coefficient for each polymorph is shown inset.

explanation has recently emerged. Walsh *et al.* [288] and Fuchs and Bechstedt [289] showed that, due to the symmetry of the bixbyite crystal structure and equal parity of the electronic states around the band extrema, optical transitions from the valence band maximum (VBM) to the CBM are forbidden within the dipole approximation. Furthermore, transitions from the valence bands somewhat below the VBM to the conduction band are also either forbidden, or have only very weak optical transition matrix elements. The result is evident in the calculated optical absorption spectrum, shown inset in Fig. 8.4(a), where a significant increase in the absorption coefficient is only observed at energies $\sim$0.5 to 1 eV above the fundamental band gap.

Consequently, experimental investigations have consistently reported a band gap of *bcc*–In_2O_3 that is significantly too high. Here, the term 'optical gap' is defined as the energy corresponding to the onset of significant optical absorption. This is determined by extrapolating the leading edge of the optical absorption coefficient to the baseline, as shown in Fig. 8.4(a), giving a value of $E_{\mathrm{opt}}^{(\mathrm{exp})} = 3.55 \pm 0.05$ eV for the experimentally determined room-temperature optical gap of the *bcc* polymorph.

This is slightly lower than the value of $\gtrsim$ 3.7 eV typically reported in previous studies. This difference is attributed largely to the different methods of analysis used in various cases. For example, performing, as is often done, an extrapolation of the square of the absorption coefficient for this sample to the baseline (not shown) gives a value of 3.68±0.05 eV, in approximate agreement with the lower limit of frequently determined values for the In_2O_3 optical gap. However, as this absorption onset is not due to interband transitions around the band extrema, there is no justification for using an α^2 extrapolation in this case, and the onset of significant absorption is therefore based here on the actual absorption coefficient, as described above. It is also necessary to point out that, from carrier statistics calculations including a non-parabolic conduction band dispersion, the Fermi level was estimated to lie only 0.02 eV above the CBM in this sample, in contrast to the often highly degenerate nature of this material. Consequently, the Moss-Burstein effect, which causes a shift of the onset of optical absorption to higher energies due to band filling, can be neglected here. This was not the case in all previous studies.

The same analysis was applied to the calculated absorption spectrum, shown inset in Fig. 8.4(a), giving an optical gap of $E_{\mathrm{opt}}^{(\mathrm{th})} = 3.72 \pm 0.10$ eV. This lies 0.62 eV above the calculated fundamental band gap of $E_{\mathrm{g}}^{(\mathrm{th})} = 3.10$ eV, indicating the effects of crystal symmetry on the dipole transition matrix elements discussed above. Applying the same difference between the optical and fundamental energy gaps for the experimental results, this allows the fundamental energy gap of *bcc*–In_2O_3 to be estimated as $E_{\mathrm{g}}^{(\mathrm{exp})} = 2.93 \pm 0.15$ eV. From Fig. 8.4(a), this energy agrees well with the weak onset of absorption of this sample, supporting this determination of the fundamental band gap. Note, Walsh *et al.* [288] reported that the onset of optical absorption does not occur until energies 0.81 eV above the fundamental band gap, suggesting a slightly larger shift between the fundamental and optical band gaps than determined here. However, lifetime broadening was not applied in the optical absorption coefficient calculations of Walsh *et al.*, as was included here, which decreases the value of the optical gap slightly. Consequently, a similar shift between the fundamental band gap and the onset of optical absorption as that

determined here would be expected.

The following points should be noted about this determination. First, due to the complexity of this system, the theoretical calculations of the absorption coefficient do not include QP effects, besides a rigid gap opening, or excitonic effects. While the experimental spectra do not show any indications of bound excitons, these effects could still cause a slight red-shift of the absorption edge. In contrast, QP effects would tend to cause a slight 'stretching' of the conduction and valence band electronic structure around the band gap [289], leading to a slight blue-shift of the absorption edge. The combination of these effects lead to some uncertainty in the determined fundamental band gap, as represented by the error given on this quantity. Additionally, the calculations are for a zero temperature limit, whereas the measurements were performed at room temperature. Broadening of the spectral features due to lifetime effects has been included in the calculations, but the band gap of semiconductors is also known to reduce in size with increasing temperature due to a mixture of lattice dilation effects and electron-phonon interactions [295]. Indeed, for the similar material SnO_2, the shift of the band gap between 0 K and room temperature is $\sim$0.2 eV [296]. Such a shift is not included in the independent QP approximation used to correct the band gap for calculating the theoretical absorption coefficient here. The above treatment, however, is not sensitive to the exact calculated band gap value; rather the comparison of the experiment with the theoretical calculations serves to account for the variation of transition matrix elements on the onset of optical absorption. The determination of the room-temperature band gap would therefore still be expected to hold. Indeed, the experimental value determined here being slightly lower than the calculated fundamental band gap is consistent with a reduction in band gap with increasing temperature.

The fundamental band gap determined here is slightly higher than the weak onset of absorption identified by Weiher and Ley [283] as due to indirect transitions, but which can now be understood as due to dipole forbidden or minimal dipole intensity transitions. However, Weiher and Ley analysed this absorption edge assuming that it had the spectral shape associated with indirect transitions in a parabolic

band semiconductor – both of these assumptions are not true for this absorption in In_2O_3, which could lead to significant inaccuracies in the extrapolated value for the onset of absorption. Also, the effects of Urbach tailing and lifetime broadening on this absorption onset, which could cause a pronounced shift between the extrapolated onset of such a weak absorption feature and the fundamental band gap, were not considered. These effects would lead to optical absorption at lower energies than would be expected from the band structure alone, further explaining why the weak onset of optical absorption determined previously is below the fundamental band gap value determined here. For degenerate samples with high concentrations of free electrons ($\sim 10^{20} - 10^{21}$ cm^{-3}) the weak absorption onset at low energies ($\sim$2.6 eV) observed previously has also been attributed to interconduction band transitions, as discussed in Ref. [289], providing a further possible mechanism to explain differences with some previous results.

The equivalent investigation for *rh*–In_2O_3 was also performed, as shown in Fig. 8.4(b). While the *rh* structure does not result in symmetry forbidden optical transitions around the band gap, the DOS close to the bottom of the conduction band is very small and the conduction band dispersion is non-parabolic [289], resulting in a more gradual onset of optical absorption than would be expected for a conventional direct band gap semiconductor characterised by parabolic dispersion relations. Indeed, performing the same analysis as for the *bcc* case discussed above, the optical gap is determined from the calculated absorption coefficient as $E_{\mathrm{opt}}^{(\mathrm{th})} = 3.40 \pm 0.10$ eV, 0.14 eV above the calculated fundamental band gap value of $E_{\mathrm{g}}^{(\mathrm{th})} = 3.26$ eV. Consequently, the experimentally observed optical gap of $E_{\mathrm{opt}}^{(\mathrm{exp})} = 3.16 \pm 0.05$ eV suggests a fundamental band gap of $E_{\mathrm{g}}^{(\mathrm{exp})} = 3.02 \pm 0.15$ eV, in reasonable agreement with previous studies [294]. Despite the large differences in the onset of optical absorption, the fundamental band gaps of *bcc*– and *rh*–In_2O_3 are therefore rather similar, consistent with theoretical predictions [289].

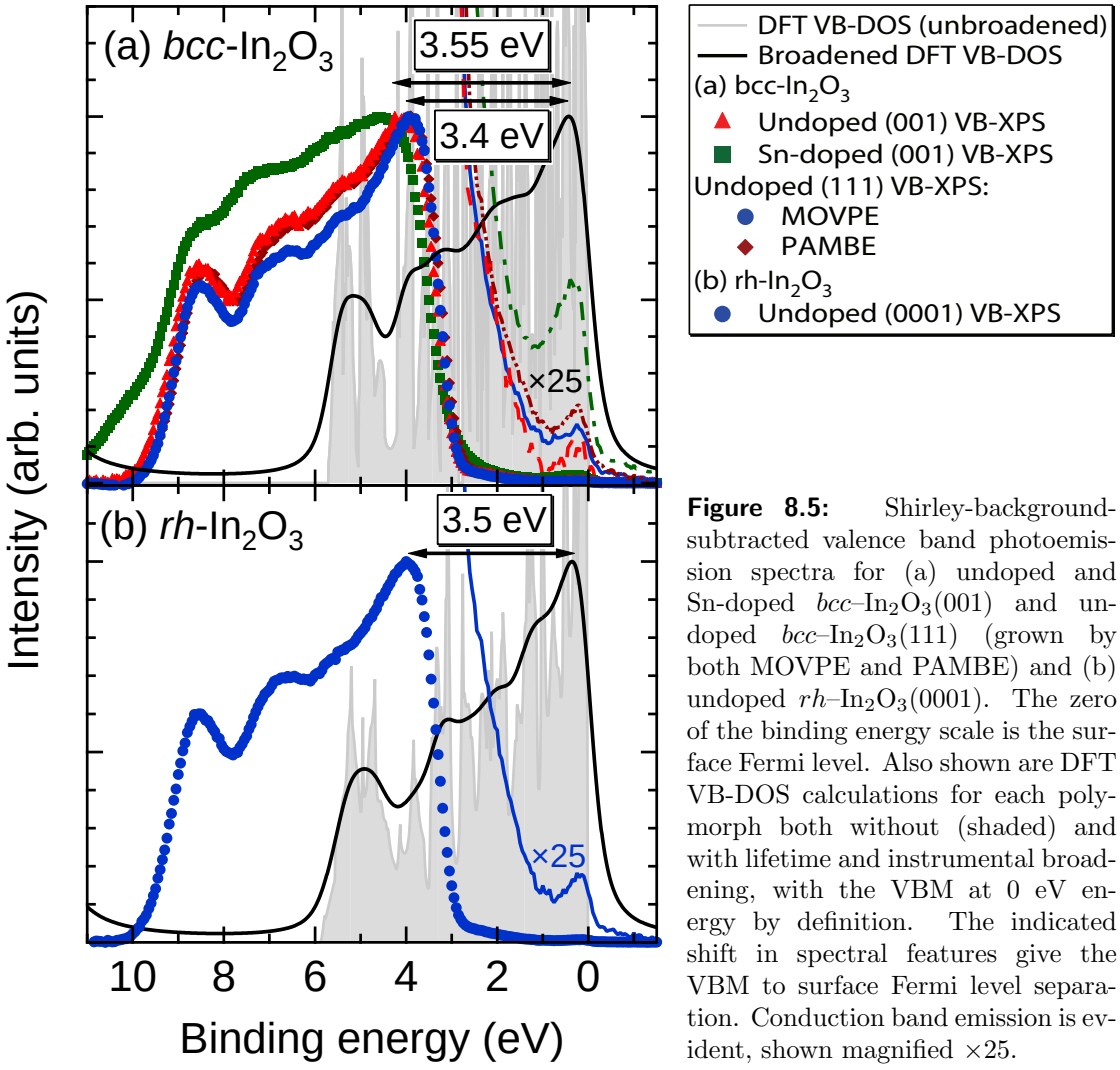

Figure 8.5: Shirley-background-subtracted valence band photoemission spectra for (a) undoped and Sn-doped *bcc*–In_2O_3(001) and undoped *bcc*–In_2O_3(111) (grown by both MOVPE and PAMBE) and (b) undoped *rh*–In_2O_3(0001). The zero of the binding energy scale is the surface Fermi level. Also shown are DFT VB-DOS calculations for each polymorph both without (shaded) and with lifetime and instrumental broadening, with the VBM at 0 eV energy by definition. The indicated shift in spectral features give the VBM to surface Fermi level separation. Conduction band emission is evident, shown magnified ×25.

8.4 Surface electronic properties

8.4.1 Results and analysis

Valence band photoemission spectra of undoped and Sn-doped *bcc*–In_2O_3(001), undoped *bcc*–In_2O_3(111), and undoped *rh*–In_2O_3(0001) are shown in Fig. 8.5. Some weak emission is also observed close to the Fermi level, above the valence band onset. This intensity has previously been attributed to emission from bulk conduction band states [288], and this is attributed here as the cause of the large peak in the heavily Sn-doped sample. However, the other samples investigated are nearly, or in fact are, non-degenerate in the bulk (see below), and so it is likely that there would be insufficient density of filled conduction band states in the bulk alone to

give rise to such a feature in the photoemission spectra. Further, due to the surface specificity of XPS, conduction band emission would not likely be visible if a pronounced depletion of carriers is present at the surface, as suggested in previous reports [290, 291]. If, however, the carrier density at the surface is higher than in the bulk, a peak would be expected in the photoemission spectra, as observed here, corresponding to conduction band emission from the near-surface region. This provides initial evidence that an accumulation of electrons may occur at the surface of both *bcc*– and *rh*–In_2O_3.

The VB-DOS from DFT calculations is also shown in Fig. 8.5. Due to the very shallow dispersion of the top valence band (see Figs. 8.2 and 8.3), there is a very sharp onset to the VB-DOS. However, this is considerably less steep in the experimental spectrum due to the effects of instrumental and lifetime broadening. Consequently, using a linear extrapolation of the leading edge of the valence band photoemission to determine the VBM to surface Fermi level separation, as has been performed in a number of previous investigations of In_2O_3 [288, 290, 291], results in a large underestimation. A more accurate determination of the VBM to surface Fermi level separation can therefore be obtained by comparisons of the positions of spectral features with those of the calculated VB-DOS which has been suitably broadened, provided that good agreement can be achieved between the photoemission spectrum and the broadened calculations with only a rigid shift of the binding energy scale to account for Fermi level differences. This is true here, as discussed in detail elsewhere [297]. Using this method of analysis, the VBM to surface Fermi level separation was estimated as 3.40 ± 0.05 eV for the undoped *bcc* samples, and 3.55 ± 0.05 eV for the heavily Sn-doped *bcc* sample. The difference in spectral shape of the valence band photoemission between the undoped and Sn-doped sample can be attributed to the influence of Sn 5*s* states on the VB-DOS. Taking a band gap of 2.93 eV, as determined above, the Fermi level therefore lies 0.47 eV (0.62 eV) above the CBM in the undoped (heavily Sn-doped) *bcc*–In_2O_3. Performing the same procedure for the *rh*–In_2O_3(0001) (Fig. 8.5(b)), the Fermi level was determined to lie 3.50 ± 0.05 eV above the VBM at the surface. While this is slightly higher

above the VBM than for the *bcc* case, the bulk band gap of the *rh* polymorph was also determined to be ~ 0.1 eV larger than that of *bcc*–In_2O_3 in Section 8.3. Consequently, the Fermi level pins at a very similar position into the conduction band (0.48 eV above the CBM) at the surface of the *rh*–In_2O_3 as it does for the undoped *bcc*–In_2O_3 samples.

To understand the surface electronic properties in detail, it is crucial to characterise those of the bulk. Hall effect measurements revealed an electron density (mobility) of 1.5×10^{18} cm^{-3} (11 cm^{2}V^{-1}s^{-1}) for the undoped PAMBE *bcc*–(111), 7.5×10^{18} cm^{-3} (32 cm^{2}V^{-1}s^{-1}) for the undoped PAMBE *bcc*–In_2O_3(001), 4.2×10^{20} cm^{-3} (27 cm^{2}V^{-1}s^{-1}) for the Sn-doped PAMBE *bcc*–In_2O_3(001), and 6.2×10^{18} cm^{-3} (55 cm^{2}V^{-1}s^{-1}) for the undoped MOVPE *rh*–In_2O_3(0001) samples. Single-field Hall effect results could not, however, be used to determine the carrier density in the MOVPE *bcc*–(111) sample due to the conducting buffer layer structure employed. IR reflectivity spectra were also measured, shown for undoped and Sn-doped *bcc*–In_2O_3(001), and undoped *rh*–In_2O_3(0001) in Fig. 8.6. The extended tail on the reflectivity from the Sn-doped sample is attributed to a heavily damped conduction electron plasmon, indicating a much higher plasma frequency in the Sn-doped than the undoped samples. The lack of observable Fabry-Pérot interference fringes within the measured spectral range for the *bcc*–samples is consistent with the 120 nm sample thickness, while the Fabry-Pérot fringes evident for the *rh*–sample allow a film thickness of 520 nm to be determined in this case. The reflectivity spectra of all samples were simulated using a two-oscillator dielectric theory model to account for lattice and free-carrier contributions. The transfer-matrix method discussed in Section 3.3 was used to model transmission through the In_2O_3 epilayer and buffer layers, reflections at the air/In_2O_3, buffer layer and substrate interfaces, and incoherent reflections within the substrate. The dielectric theory simulations showed good agreement with the experimental data (see Fig. 8.6), and from these the plasma frequency was determined to be 85 meV and 600 meV for the undoped and Sn-doped *bcc*–(001) samples, respectively, 140 meV for the MOVPE *bcc*–(111) sample, 50 meV for the PAMBE *bcc*–(111) sample, and 110 meV for the *rh*–(0001)

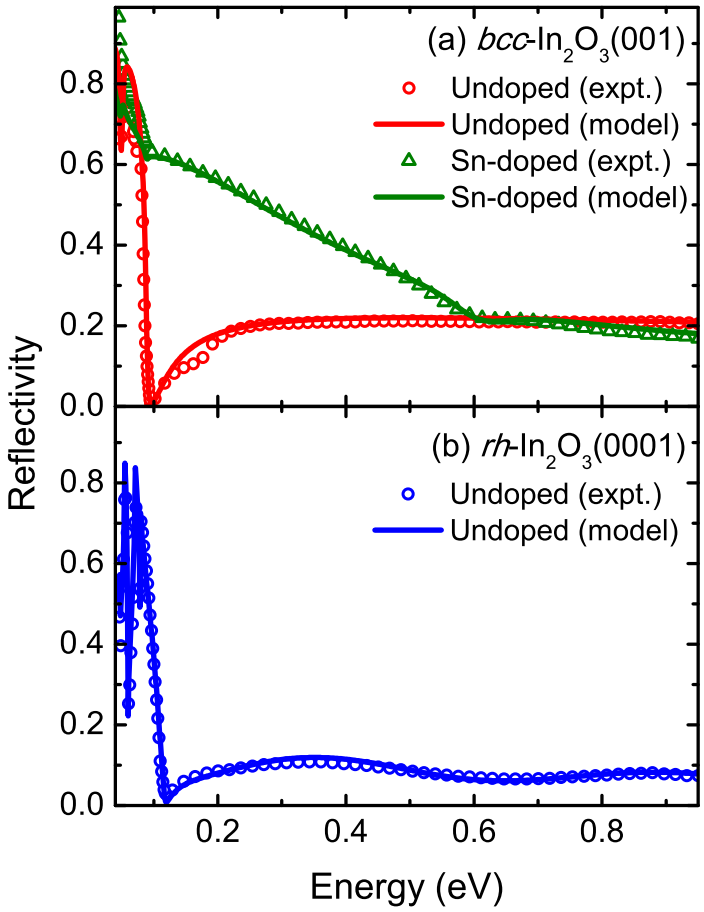

Figure 8.6: IR reflectivity spectra and dielectric theory simulations of (a) undoped and Sn-doped *bcc*–In_2O_3(001), and (b) undoped *rh*–In_2O_3(0001).

sample. These correspond to electron densities of 7×10^{18} cm^{-3} and 4×10^{20} cm^{-3} for the undoped and Sn-doped *bcc*–(001) samples, respectively, 2×10^{19} cm^{-3} for the MOVPE *bcc*–(111) sample, 2×10^{18} cm^{-3} for the PAMBE *bcc*–(111) sample, and 1×10^{19} cm^{-3} for the *rh* sample. These are in good general agreement with the Hall effect results. Non-parabolicity cannot be neglected for the conduction band dispersion of In_2O_3 [289]. Consequently, non-parabolic carrier statistics calculations (as discussed in Section 2.1.1) have been used to locate the bulk Fermi level 0.02 eV and 0.54 eV above the CBM for the undoped and Sn-doped *bcc*–In_2O_3(001) samples, respectively, 0.07 eV above the CBM for the undoped MOVPE *bcc*–(111) sample, 0.03 eV below the CBM for the undoped PAMBE *bcc*–(111) sample, and 0.03 eV above the CBM for the *rh* sample. Except for the deliberately Sn-doped sample, these are all almost, or actually are, non-degenerate, as stated above.

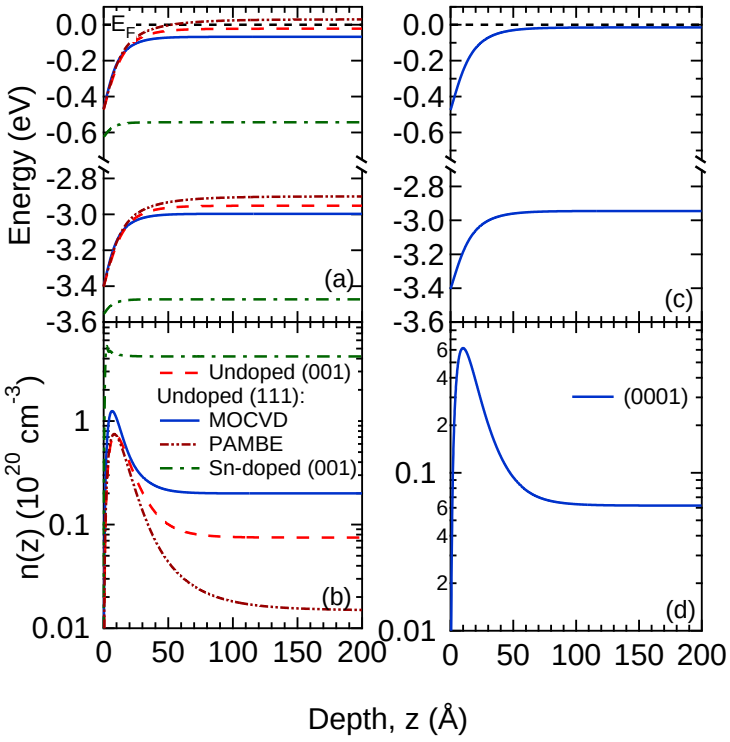

Figure 8.7: (a) [(c)] Band bending and (b) [(d)] carrier concentration profiles in the near surface region of undoped and Sn-doped *bcc* [undoped *rh*] In_2O_3.

8.4.2 Discussion

The above measurements indicate that the VBM to Fermi level separation is much larger at the surface than in the bulk of the undoped *bcc*– and *rh*–In_2O_3. This indicates a downward bending of the conduction and valence bands at the surface, leading to an increase in electron density in the near-surface region. The band bending and carrier concentration profiles as a function of depth below the surface have been calculated by solving Poisson's equation within a modified Thomas-Fermi approximation (MTFA), incorporating a non-parabolic conduction band, as described in Chapter 2.2.2. These are shown in Fig. 8.7, revealing a pronounced accumulation of electrons close to the surface, although as always, the carrier concentration still tends to zero right at the surface, as the wavefunctions must decay to zero amplitude here due to the potential barrier that the surface imposes. From the considerations presented in previous chapters, the surface electron accumulation observed here for undoped In_2O_3 results from a screening of the positive charge of unoccupied donor-like surface states. Indeed, the Poisson-MTFA calculations reveal a large positive surface state density of $(1.3 \pm 0.1) \times 10^{13}$ cm^{-2} and $\sim 1.2 \times 10^{13}$ cm^{-2} for the *bcc* and

rh polymorphs, respectively, associated with the electron accumulation. It should be noted that parameters such as the effective mass are not well known for *rh*–In_2O_3. The same ones as for *bcc*–In_2O_3 have been used here as a first approximation, but these numerical answers should be treated as somewhat approximate. Irrespective of this, however, these results provide clear evidence for an accumulation of electrons at the (0001) surface of undoped *rh*–In_2O_3, as well as at the (001) and (111) surface of undoped *bcc*–In_2O_3, and that this electron accumulation is not dependent on the growth technique, being present for both PAMBE and MOVPE-grown samples.

The surface electron accumulation observed here is in contrast to the depletion of electrons reported previously at In_2O_3 surfaces [290,291]. The recent revision of the band gap is an important factor in allowing the identification of electron accumulation; however, fundamentally, it is the comparatively low electron density in the bulk, resulting from the high growth quality, which means that the bulk Fermi level is sufficiently low to allow the intrinsic electron accumulation to be clearly observed here in In_2O_3. Without detailed information on the bulk Fermi level positions in the samples investigated in Refs. [290] and [291], it is not possible to comment further on whether any of those specific samples had low enough carrier densities to exhibit indium oxide's intrinsic electron accumulation.

8.5 The charge neutrality level

As discussed in previous chapters, the demarcation between surface states that are predominantly donor-like and acceptor-like can be identified as the CNL of the semiconductor. The existence of unoccupied donor-like surface states in this case means that the Fermi level is pinned slightly below the CNL at the surface. Consequently, the CNL must be located high relative to the band extrema in In_2O_3, > 0.47 eV above the CBM. This high relative location can be understood by considering the bulk band structure of In_2O_3. As for InN and CdO, also considered in this thesis, the band structure of In_2O_3 exhibits a particularly low Γ-point CBM compared to the average conduction band edge across the Brillouin zone, while it additionally possesses a shallow dispersion of the valence bands, as shown in Figs. 8.2 and 8.3.

As discussed in Chapter 4, the CNL is located close to the midgap energy averaged across the Brillouin zone, and would therefore be expected, from the calculated band structure, to lie above the CBM in In_2O_3, as inferred here experimentally.

To explore the position of the CNL further, Sn-doped *bcc*–In_2O_3(001) was investigated, in order to move the bulk Fermi level up towards the CNL. From the considerations of Chapter 5, the surface Fermi level must then pin closer to the CNL resulting in a smaller positive surface charge to maintain charge neutrality with the reduced space charge. As shown in Fig. 8.7, the heavily Sn-doped sample has a much reduced electron accumulation – the calculated surface-state density is an order of magnitude smaller than for the equivalent undoped sample – and the surface Fermi level is pinned higher than for the undoped samples. In this case, the surface Fermi level would be expected to be pinned only very slightly below the CNL, allowing an experimental estimate to be given for the location of the CNL: $E_{CNL} \sim 3.6$ eV above the VBM, and so consequently ~ 0.65 eV above the CBM in *bcc*–In_2O_3. A larger set of samples with a greater variation of bulk doping levels would be required to make a more accurate determination. The similarity of the bulk band structure of the *bcc* and *rh* polymorphs (see Figs. 8.2 and 8.3) will result in the CNL lying in a similar location for both cases, explaining the similar pinning position of the surface Fermi level above the CBM for both the *bcc* and *rh* polymorphs. This is supported by recent first-principles calculations which locate the CNL 0.54 eV above the CBM in *rh*–In_2O_3 [298].

The CNL lying above the CBM is unusual amongst conventional semiconductors. Consequently, surface electron accumulation is also unusual, and has in fact only previously been reported as an intrinsic property of the surface for InAs [39], InN [7], and CdO (this work, Chapter 4). It is interesting to compare the situation in the three In-containing materials which have been shown to exhibit electron accumulation; the band extrema relative to the CNL estimated here for In_2O_3, and those for these common-cation semiconductors are shown in Fig. 8.8(a). In In_2O_3, the CBM lies further below the CNL than in InAs, but not as far below as in InN, resulting in an areal density of unoccupied donor surface states associated with

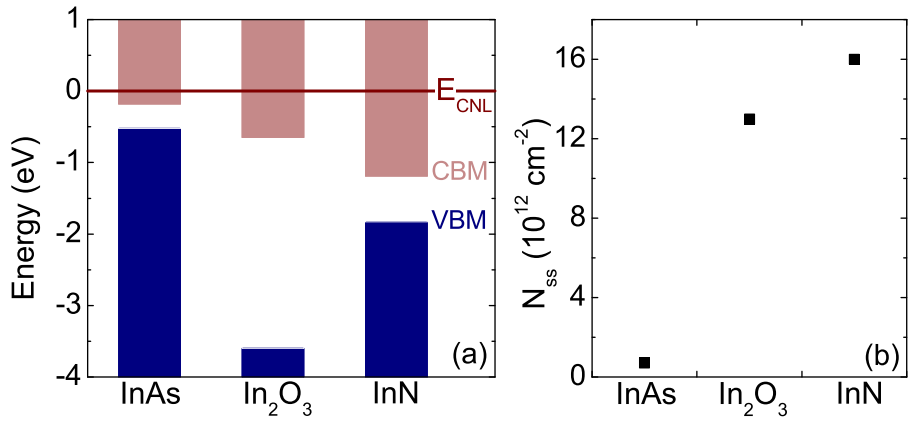

Figure 8.8: (a) Conduction and valence bands of InAs, In_2O_3 and InN relative to the CNL (InAs from Ref. [183]; In_2O_3 determined here; InN from Chapter 5), and (b) typical sheet density of unoccupied donor surface states associated with electron accumulation in InAs (from Ref. [39]), In_2O_3 (determined here) and InN (from Chapter 6).

the electron accumulation between those typical for InAs and InN, as shown in Fig. 8.8(b). An important factor explaining the CBM lying below the CNL in all of these In-containing compounds is the large size of the In atom, leading to a small s–s repulsion between the cation and anion s–orbitals due to the large cation-anion bond length. This, coupled with the large s–orbital energy separation, particularly with N and O, results in a low-lying cation s-like CBM compared to the average band edge across the Brillouin zone, resulting in the CBM lying below the CNL (*cf.* the chemical trends discussed in Section 5.4). Similar considerations would be expected to apply to other materials with a large size and electronegativity mismatch between the constituent cation and anion. In this thesis, this has been shown to hold for the II-O semiconductor CdO, but would also be expected for materials such as ZnO and SnO_2. Consequently, surface electron accumulation may also be expected in these materials, explaining a number of previous results [299, 300].

The position of the CNL relative to the band extrema also has implications for the bulk electronic properties of In_2O_3. As discussed in Chapter 4, native defects tend to drive the Fermi level in the bulk towards the CNL. As the CBM lies well below the CNL in In_2O_3, native defects favourably form as donors, increasing the Fermi level, while compensating acceptor defects will have higher formation energies. This is consistent with the formation energy calculations for native defects in In-rich In_2O_3 of Lany and Zunger [301], and provides an overriding band structure

explanation of the propensity for In_2O_3 to have a high background electron density even when nominally undoped. The range of Fermi level positions attainable by extrinsic doping is also intimately related to the CNL due to an increasing tendency for native defects to form compensating centres as the Fermi level moves away from the CNL. In In_2O_3, the n-type doping limit, with the Fermi level some way above the CNL, will therefore lie well above the CBM, meaning that it is possible to achieve extremely high n-type conductivities in this material by extrinsic doping (for example, $n \sim 10^{21}$ cm^{-3} for In_2O_3:Sn [9]). Thus, the CBM being located below the CNL in In_2O_3, combined with its relatively large fundamental band gap and dipole forbidden (minimal intensity) optical transitions between the CBM and VBM (high-lying valence bands) [288], explains the ability to obtain In_2O_3 with the usually contradictory properties of transparency and high conductivity, and hence its use as a TCO material.

8.6 Muonium in In_2O_3

From the considerations presented in this, and previous, chapters, hydrogen would also be expected to act as a shallow donor in In_2O_3. To test this prediction, a μSR study has been undertaken. In this experiment, a 100% spin-polarised beam of positive muons is implanted into the sample, which is held in a transverse magnetic field. The muon spin precesses in this field at the Larmor frequency, ν_L. The muon has a well defined lifetime of 2.2 μs, and decays into positrons preferentially in the direction of its spin. The muon precession can therefore be monitored by the 'forward-backward asymmetry' of the detected positrons. In addition, depolarization of the muon spins due to nuclear dipolar coupling can be probed. The finite lifetime of the muon limits the information attainable in practice to less than 15 μs, which results in information generally being obtained on isolated defect centres.

In addition to this diamagnetic signal, when a positive muon is implanted into a semiconductor, it can bind with an electron to form neutral muonium, $Mu^0 = [\mu^+, e^-]$. This can be treated as a light isotope analogue of hydrogen ($m_{Mu}/m_H \approx 1/9$), with the advantage that the muon has very well defined creation and decay

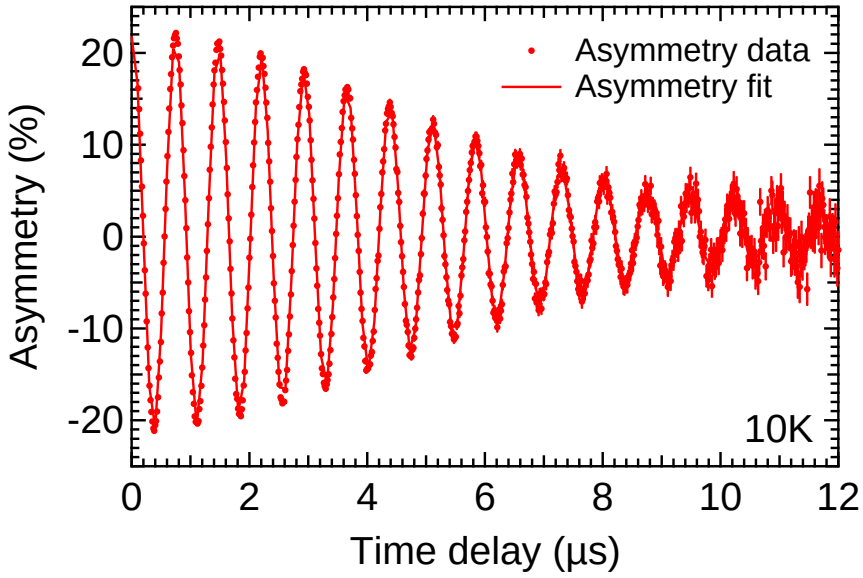

Figure 8.9: Time-domain asymmetry of the positron decay from a muon-implanted In_2O_3 powder sample at 10 K.

properties. Consequently, spectroscopic studies of muonium via muon spin rotation and relaxation (μSR) spectroscopy have emerged as a powerful tool to develop an understanding of the microscopic behaviour of hydrogen in materials [302–304]. The paramagnetic component, Mu^0, experiences a hyperfine field in addition to the applied transverse field, resulting in components that precess about the applied magnetic field at a frequency $\nu_L \pm \frac{A}{2}$, where A is the hyperfine splitting, in addition to the contribution from the diamagnetic state. The total measured asymmetry is the sum of these three components. In certain cases, this results in a clear beat pattern in the asymmetry as a function of time delay [302]. However, it is more usual that the paramagnetic component causes changes to the time-domain signals in a more subtle way that can only be elucidated by curve-fitting.

An example of the time-domain asymmetry data recorded from an In_2O_3 powder sample at 10 K is shown in Fig. 8.9. The measured asymmetries were simulated with three component fits to account for both positive and neutral muonium and depolarization (gaussian relaxation) effects. A small, but non-negligible, amplitude associated with Mu^0 was observed, with a hyperfine constant equal to 0.17 MHz. The amplitudes associated with the paramanetic Mu^0 and diamagnetic Mu^+ components, as a function of temperature, are shown in Fig. 8.10. As the signal associated

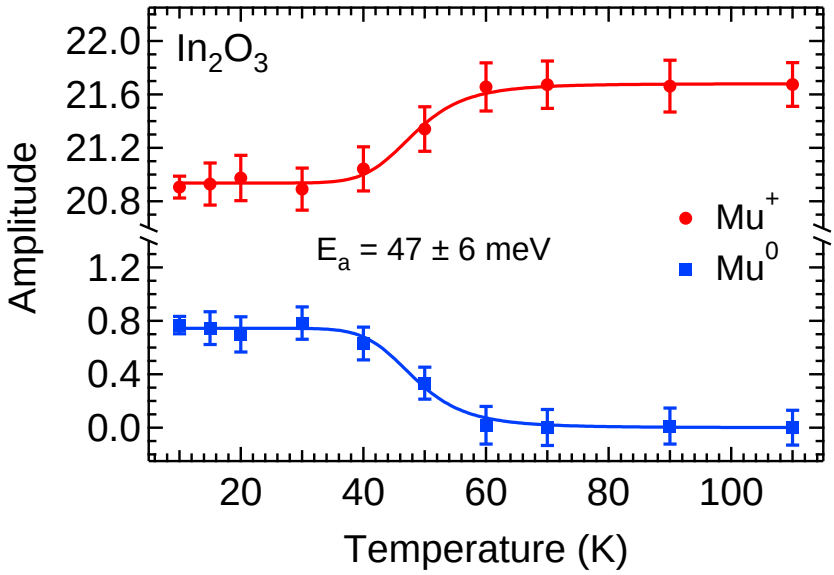

Figure 8.10: Temperature dependence of the amplitude assocaited with paramanetic Mu^0 and diamagnetic Mu^+ in In_2O_3.

with the Mu^0 component is quenched at around 50 K, this indicates that it is a shallow centre. In an ionization model [304], the fraction of ionized (f) and unionized ($1-f$) Mu can be fit by the functions

$$f = \frac{N \exp\left(-\frac{E_a}{k_B T}\right)}{1 + N \exp\left(-\frac{E_a}{k_B T}\right)} \tag{8.1a}$$

$$1 - f = \frac{1}{1 + N \exp\left(-\frac{E_a}{k_B T}\right)} \tag{8.1b}$$

where E_a is the activation energy and N is a density of states factor. Fitting the ampliludes in Fig. 8.10 according to this model yields an activation energy of only $E_a = 47 \pm 6$ meV. From thermal equilibrium arguments, this corresponds to a donor depth of $E_d = 2E_a = 94 \pm 12$ meV. However, it is unlikely that the electron occupations for Mu^0 and the conduction band reach a local equilibrium within a muon lifetime, and so the effective donor depth should be between these two values, $47 \leq E_d \leq 94$ meV.

The values determined from the fitting of the μSR data can be compared to simple estimates for a shallow donor within a hydrogenic model. The effective

shallow donor binding energy can be estimated from

$$R^* = \frac{(m^*/m_0)}{[\varepsilon(0)]^2}\text{Ryd}, \tag{8.2}$$

where Ryd = 13.6 eV is the Rydberg constant for hydrogen, to be 60 meV, in good agreement with the determined donor binding energy. Similarly, the effective shallow-donor radius can be estimated from

$$a^* = \frac{\varepsilon(0)}{(m^*/m^0)}a_0, \tag{8.3}$$

where $a_0 = 0.53$ Å is the Bohr radius, to be 1.35 nm. The expected hyperfine constant can be scaled from the value for free muonium of $A_0 = 4463$ MHz by

$$A^* = \left(\frac{a_0}{a^*}\right)^3 A_0, \tag{8.4}$$

giving an effective hyperfine splitting of 0.27 MHz. These simple estimates for the hyperfine splitting and donor binding energy are within a factor of two of those obtained from the experiment, strongly supporting the assignment of the Mu^0 signal as due to a shallow donor with a very extended wavefunction. Consequently, muonium, and by analogy hydrogen, form a shallow donor centre in In_2O_3, consistent with the expectations from the CNL position determined above. Hydrogen must therefore be considered as an additional potential cause of the propensity towards high n-type conductivity in In_2O_3, and indeed other TCOs. In fact, analysis of μSR data recorded from a SnO_2 sample revealed a very similar behaviour of muonium [305]. As for In_2O_3, a shallow donor centre was identified, although the activation energy of 18 ± 3 meV, and hyperfine splitting of 0.09 ± 0.02 MHz, were slightly lower than the values for In_2O_3, in agreement with the trends expected from simple model calculations within a hydrogenic model.

8.7 Conclusions

From comparisons of theoretical calculations and experimental measurements of the absorption coefficient, the fundamental band gap of *bcc*– and *rh*–In_2O_3 was determined as 2.93 ± 0.15 eV and 3.02 ± 0.15 eV, respectively. Using a combination of high-resolution XPS, IR reflectivity and Hall effect measurements, combined with

semiconductor space-charge calculations, single-crystalline undoped In_2O_3 has been shown to exhibit a pronounced electron accumulation at its surface, in contrast to the majority of other semiconductors. This was explained in terms of the low Γ-point CBM in In_2O_3 lying below the charge neutrality level. Increasing the bulk Fermi level towards the CNL by Sn-doping resulted in a drastic reduction of the electron accumulation, allowing the CNL to be located approximately 0.65 eV above the CBM. This explains not only the surface electron accumulation, but also both the propensity for n-type conductivity in undoped material and the ease of extrinsic n-type doping, providing an understanding of the normally conflicting properties of transparency and conductivity in In_2O_3. By investigations of the muonium analogue via μSR spectroscopy, hydrogen was also shown to be a donor in In_2O_3. This is consistent with the determined CNL position, and suggets hydrogen as another potential cause of the n-type conductivity in In_2O_3. The conclusions of this work extend to other transparent conducting oxide materials such as SnO_2 and ZnO.

Chapter 9

Quantized electron accumulation layers

9.1 Introduction

Throughout this thesis, it has been shown that if the charge neutrality level (CNL) lies above the conduction band minimum (CBM), the intrinsic state of the material is characterised by an accumulation of electrons at the surface, associated with a downward bending of the conduction and valence bands. This has been treated in a one-electron semi-classical manner, using the formalism discussed in Section 2.2.2. However, if the downward band bending is sufficiently deep and narrow, the resulting potential well causes the conduction band states normal to the surface to become quantized into a number of discrete levels [31]. This was first demonstrated from magnetoresistance measurements of an electron accumulation layer artificially created by applying a bias to a Si metal-oxide-semiconductor (MOS) system [306], and later confirmed by far-infrared inter-subband optical absorption measurements of this system [307]. Quantized states have also been observed in InAs and InN MOS structures by Tsui [308–310] and Veal *et al.* [311,312], and have been observed in native electron accumulation layers at InAs and InN surfaces by angle resolved photoemission spectroscopy (ARPES) measurements [313, 314]. As the downward band bending is in the direction normal to the surface, the quantization is in this direction only; the motion of carriers in the plane of the surface therefore remains free, and the subbands that form are two-dimensional. ARPES can then be used to image the parallel dispersion of these subband states [313].

The effective one-electron potential at a semiconductor surface, and corresponding variation in carrier density, is strictly described by a self-consistent solution of the Poisson and Schrödinger (PS) equations [315]. As the solution of the Schrödinger equation is dependent on the potential derived from a solution of Poisson's equation, this procedure is highly non-linear. Several methods have previously been employed to assist convergence of the self-consistent iteration. Baraff

and Appelbaum [315] and Ehlers and Mills [316] performed self-consistent Poisson-Schrödinger Hartree calculations employing a parameterized Morse potential, which allows a series solution of the Schrödinger equation to be made, without the need for full numerical solutions. Streight and Mills [317] employed a Fourier and a finite-difference method to determine self-consistent PS Hartree solutions for an electrically neutral finite semiconductor slab. The finite geometry of the slab makes achieving self-consistency easier, although the solutions do not necessarily apply to semi-infinite systems. The above schemes also assumed parabolic dispersion of the semiconductor bands.

Inaoka [318] employed a local-density-approximation (LDA) calculation within a semiconductor slab thick enough to ensure that the potential and carrier distribution at the surface of the slab is equivalent to that for a semi-infinite system. Non-parabolicity of the conduction band was approximated by modifying the value of the effective mass to that at the Fermi level for a non-parabolic (NP) dispersion. This approach was subsequently extended to include full conduction band non-parabolicity in self-consistent PS LDA solutions [319]. The incorporation of non-parabolicity, however, makes these calculations very computationally intensive.

As used in previous chapters of this work, an alternative approach to full self-consistent PS solutions is to solve Poisson's equation within a modified Thomas-Fermi approximation (MTFA), as discussed in Section 2.2.2. The MTFA approximation has been shown to be in excellent agreement with full self-consistent PS solutions for parabolic conduction-band dispersions [66, 320]. However, although this method generates one-electron potentials and charge profiles that are very similar to self-consistent PS solutions, it does not contain any information on the subband structure present when strong band bending at the semiconductor surface causes the conduction-3band states to become quantized. Here, a method combining the Poisson-MTFA formalism with a numerical solution of the Schrödinger equation for the resulting one-electron potential, to yield the conduction subband structure incorporating non-parabolicity, is derived. The calculations can be performed with relatively little computational cost, and these are shown to yield results in good

agreement with full self-consistent NP PS calculations. This is still a one-electron approximation. However, the carrier density in the electron accumulation layer can be very high, as seen in previous chapters. This raises the question of whether many-body effects are important for these quantized states. This chapter also presents initial investigations into these effects from a combination of ARPES measurements and theoretical calculations.

9.2 Experimental details

Single-crystalline InAs(111) samples were grown at the University of Sheffield, UK, to a thickness of 2 μm by molecular beam epitaxy (MBE) on GaAs(111)B. The InAs was doped with Si to a concentration of $n = 6 \times 10^{17}$ cm^{-3}. The samples were capped with a $\sim$100 nm thick layer of amorphous As before being removed from the growth chamber. Decapping was achieved in an ultra-high vacuum (UHV) preparation chamber connected to the ARPES spectrometer chamber by annealing the samples at $\sim$375°C for 1 h, following which a sharp (2×2) low energy electron diffraction (LEED) pattern was observed over a wide range of incident electron energies ($\sim$25 to 100 eV). The (2×2) reconstruction is known to be the favourable reconstruction of the clean InAs(111)B surface immediately following MBE growth, and can be described by a vacancy-buckling model [321].

Single-crystalline CdO(001) samples were grown at the Universitat de València, Spain, to a thickness of 500 nm by metal-organic vapour phase epitaxy on r-plane $(1\bar{1}02)$ sapphire substrates at a growth temperature of 400°C. Further details of the growth and materials characterisation are reported elsewhere [108]. The bulk carrier density (mobility) of the sample considered here was determined from single-field Hall effect and infrared (IR) reflectivity to be 2.0×10^{19} cm^{-3} (150 cm^{2}V^{-1}s^{-1}). Surface preparation was achieved by annealing in UHV in a preparation chamber connected to the ARPES spectrometer chamber for 2 h at 575°C. Following this, a sharp (2×2) LEED pattern was observed over a wide range of incident electron energies ($\sim$ 25 to 200 eV). The details of this reconstruction require further investigation.

ARPES measurements were performed as described in Chapter 3. A variety of photon energies and temperatures, within the range 16 to 60 eV and 60 to 450 K, respectively, were employed for the measurements.

9.3 Coupled Poisson-Schrödinger calculations

The bulk conduction band dispersion relations are calculated within the Kane [58] $\mathbf{k}\cdot\mathbf{p}$ non-parabolic scheme, as discussed in Section 2.1.1. The one-electron band bending potential is calculated within the Poisson-MTFA framework, discussed in Section 2.2.2, incorporating this non-parabolic conduction-band dispersion. The numerical solution of the Schrödinger equation for this one-electron potential proceeds via a Fourier-series representation [317, 319]. The band bending potential destroys the translational symmetry of the crystal. It is therefore appropriate to express the Schrödinger equation in terms of envelope functions made up of Wannier functions $\Psi(\mathbf{r}_\parallel, z)$ where $\mathbf{r}_\parallel$ [z] is the parallel [normal] component of the position vector. In this representation, the Schrödinger equation is given by [319, 322]

$$[E_c(-i\nabla) + V(z)]\,\Psi(\mathbf{r}_\parallel, z) = E\Psi(\mathbf{r}_\parallel, z), \tag{9.1}$$

where the eigenfunction for a subband j and a given parallel wavevector $\mathbf{k}_\parallel$

$$\Psi_{\mathbf{k}_\parallel,j}(\mathbf{r}_\parallel, z) = \frac{1}{\sqrt{A}}\exp(i\mathbf{k}_\parallel\cdot\mathbf{r}_\parallel)\psi_{\mathbf{k}_\parallel,j}(z), \tag{9.2}$$

where A is a normalization factor and $\psi_{\mathbf{k}_\parallel,j}(z)$ is the component of the eigenfunction normal to the surface for a given subband and parallel wavevector. E_c is the NP conduction band dispersion.

Imposing the boundary condition that the wavefunctions vanish at the surface ($z = 0$), and assuming a system of some length ℓ, such that the wavefunctions of the bound states have also decayed to zero by $z = \ell$, $\psi_{\mathbf{k}_\parallel,j}(z)$ can be expanded as a Fourier sine series

$$\psi_{\mathbf{k}_\parallel,j}(z) = \sum_{\nu=1}^{\infty}\sqrt{\frac{2}{\ell}}\,a_\nu^{\mathbf{k}_\parallel,j}\sin\left(\frac{\nu\pi}{\ell}z\right). \tag{9.3}$$

Substituting this into the Schrödinger equation (Eqn. 9.1) gives the matrix representation of the problem for a given $\mathbf{k}_\parallel$

$$\mathbf{M}^{\mathbf{k}_\parallel}\mathbf{a}^{\mathbf{k}_\parallel} = E^{\mathbf{k}_\parallel}\mathbf{a}^{\mathbf{k}_\parallel} \tag{9.4a}$$

where the matrix elements are given by

$$[\mathbf{M}]_{\nu\nu'} = E_c(k_\nu)\delta_{\nu\nu'} + \frac{2}{\ell}\int_0^\ell \mathrm{d}z\, V(z)\sin\left(\frac{\nu\pi}{\ell}z\right)\sin\left(\frac{\nu'\pi}{\ell}z\right) \tag{9.4b}$$

where $k_\nu = \sqrt{\mathbf{k}_\parallel^2 + (\nu\pi/\ell)^2}$ and $\delta_{\nu\nu'}$ is the Kronecker delta function. The eigenvalues and eigenfunctions of $\mathbf{M}$ can therefore be used to determine the confined subband energies and wavefunctions normal to the surface for a given one-electron potential, itself resulting from Poisson-MTFA calculations. In practice, the infinite sum in Eqn. 9.3 is truncated after an order ν_{max}, giving a $\nu_{max} \times \nu_{max}$ matrix in Eqn. 9.4. The value of ν_{max} required to ensure convergence of the eigenvalues is dependent on the depth and width of the surface potential well. Setting $\nu_{max} = 500$ was found to be sufficient for all cases considered here.

The Schrödinger equation has to be solved numerically for each value of parallel wavevector due to the conduction band non-parabolicity. However, in this method, this only has to be performed once for the one-electron potential calculated from the Poisson-MTFA formalism. This is in contrast to full self-consistent NP solutions where the Schrödinger equation has to be solved numerically (for each parallel wavevector) for multiple one-electron potentials in order to iteratively proceed towards a self-consistent solution, therefore proving significantly more computationally intensive than the coupled method presented here.

9.3.1 Verification of model

To verify the model developed here, the one-electron potential for a variety of surface-state densities and a set of subband dispersions calculated by this model for the electron accumulation layer at an InAs surface are compared to full self-consistent NP PS calculations of Abe *et al.* [319] in Fig. 9.1. The InAs parameters used are those employed by Abe *et al.* in their calculations.

The one-electron potentials and subband dispersions agree very well between the two calculation methods, confirming the validity of the NP coupled Poisson-MTFA/Schrödinger method as a good approximation to full self-consistent NP PS calculations. The calculations presented in the remainder of this chapter include higher surface-state densities than those considered by Abe *et al.* [319], as compared

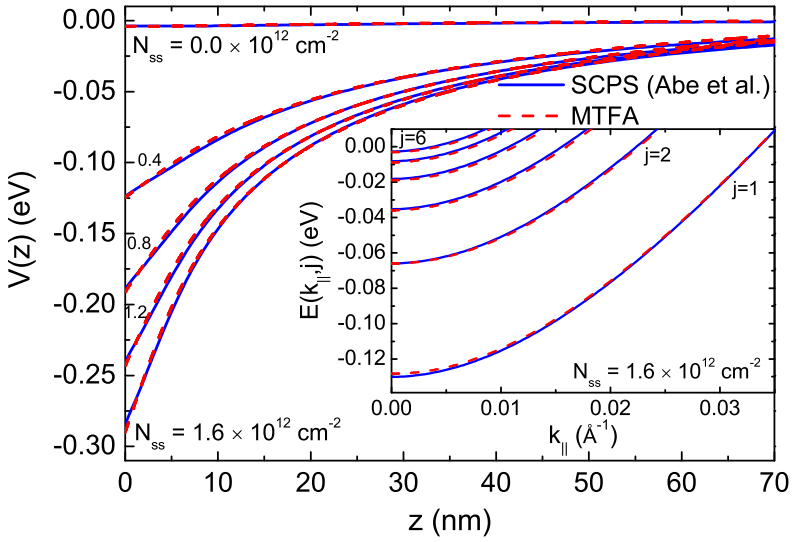

Figure 9.1: The one-electron potential, $V(z)$, as a function of depth below the surface, z, for InAs, using the material parameters in Ref. [319]. Self-consistent Poisson-Schrödinger (SCPS) calculations (solid lines, Abe *et al.* [319]) and Poisson-MTFA calculations (dashed lines, this work) are shown for surface sheet densities $N_{ss} = 0.0\times10^{12}$, 0.4×10^{12}, 0.8×10^{12}, 1.2×10^{12} and 1.6×10^{12} cm^{-2}, and a bulk carrier density $n = 1.3\times10^{16}$ cm^{-3}. For a surface sheet density $N_{ss} = 1.6\times10^{12}$, the calculated (SCPS and MTFA-Schrödinger approximation) subband dispersions are shown inset.

to here. However, comparison of the one-electron potentials shown in Fig. 9.1 does not show signs of increased deviation as the surface-state density is increased by over an order of magnitude. The agreement between the self-consistent NP PS calculations and the calculations presented here is therefore expected to hold for the higher surface-state densities used in the remainder of this work.

9.3.2 Example calculations for InN

As an illustration of the above model, the properties of a quantized electron accumulation layer in moderately doped ($n_b = 2.5 \times 10^{18}$ cm^{-3}) InN, for a typical surface-state density of $N_{ss} = 1.6 \times 10^{13}$ cm^{-2} (see Section 6.3), have been calculated here, as shown in Fig. 9.2. Two quantized states are obtained. The normal component of the eigenfunctions are shown superimposed on the subbands in Fig. 9.2(a). The wavefunctions are equal to zero at the surface ($z = 0$) due to the imposed boundary condition here. Also, the wavefunctions decay into the potential barrier, such that a long way from the surface they have zero amplitude. It is the peak of these wavefunctions close to the surface that is responsible for the peak in the carrier concentration in the accumulation layer (Fig. 9.2(b)). The parallel dispersion of the subbands is

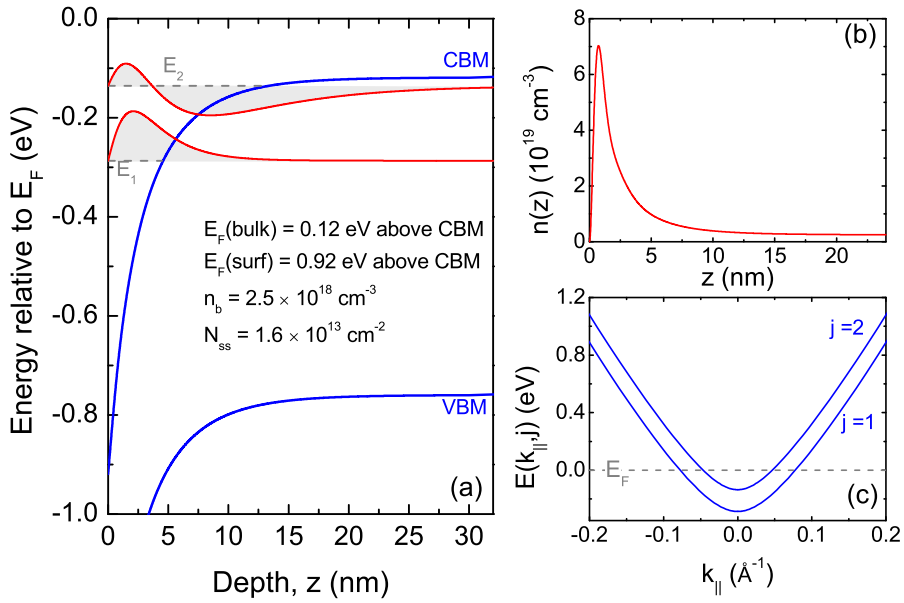

Figure 9.2: (a) Downward band bending at an InN surface with a surface sheet density $N_{ss} = 1.6 \times 10^{13}$ cm^{-2} and bulk carrier density $n_b = 2.5 \times 10^{18}$ cm^{-3} and (b) corresponding near-surface carrier density. Two quantized states form (E_1 and E_2) and their corresponding (a) wavefunctions and (c) parallel dispersion relations are shown.

also obtained from the model (Fig. 9.2(c)). Indeed, as the confining potential is only in the direction normal to the surface, the dispersions of the subbands actually form cones of the form shown in Fig. 9.4. The calculated dispersions become rather linear with increasing $k_{||}$, indicating a distinct non-parabolicity. However, this non-parabolicity is not simply described by a Kane-like dispersion, instead requiring the full numerical solution of the Schrödinger equation for different values of $k_{||}$.

Although the Fermi level is strongly pinned at clean InN surfaces, it is possible to induce changes in the pinning position in a number of ways. A large increase in bulk doping level increases the Fermi level pinning position (see Chapter 5), in order to maintain charge neutrality. The changes in measured conductivity of InN when exposed to a number of solvents and gases has been attributed to changes in the surface electronic properties [133, 323]. Additionally, the deposition on the surface of metals of varying electronegativity can cause a variation in the Fermi level pinning position [4]. For example, the deposition of small amounts of Cs on InAs(110) surfaces has been shown [324] to lead to a large enhancement of the electron accumulation. The variation in surface-state density and corresponding downward band bending associated with these modifications to the clean surface

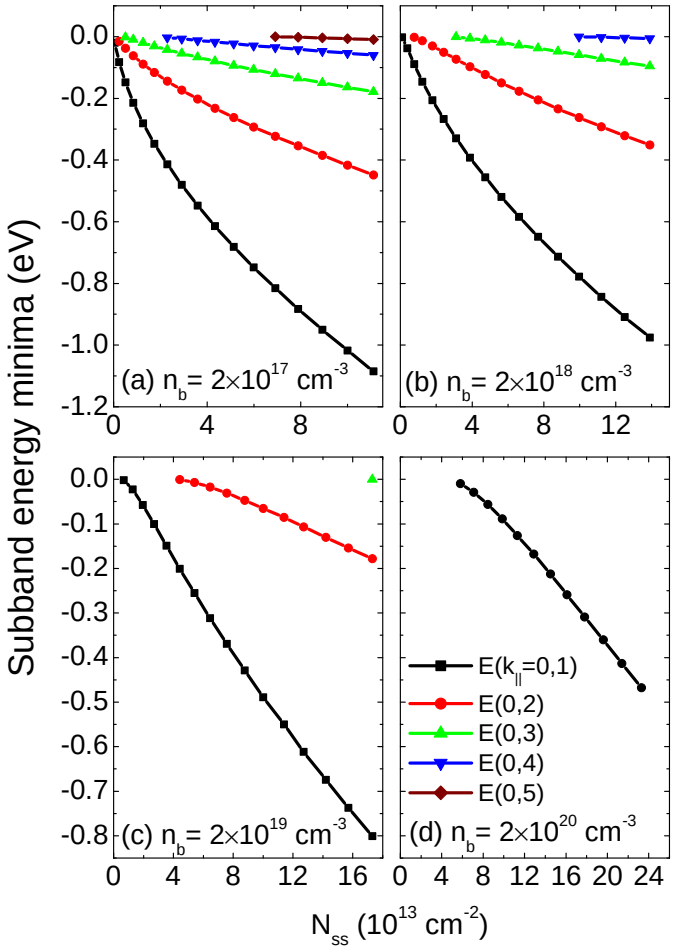

Figure 9.3: Variation in energy of the subband minima relative to the bulk CBM (top of the potential well) with surface-state density for a bulk carrier concentration of (a) 2×10^{17} cm^{-3}, (b) 2×10^{18} cm^{-3}, (c) 2×10^{19} cm^{-3} and (d) 2×10^{20} cm^{-3}. The points show the calculated subband energy minima for a downward band bending (right to left) of 3.3, 3.1, 2.9, 2.7, ... eV.

will cause a pronounced variation in the number and confinement energies of the subbands. This is represented by the variation in subband energy minima calculated for a variety of surface-state densities and bulk carrier densities, shown in Fig. 9.3.

With increasing surface-state density, the amount of downward band bending increases, and so the potential well becomes deeper at the surface. This causes the number of subbands bound within the well to increase, and the subbands to become confined deeper within the well. Conversely, with increasing bulk doping, fewer subbands are confined for a given amount of band bending. As the bulk doping level increases, the screening length becomes shorter, and so the potential well formed at the surface becomes narrower. This acts to increase the energy of the subband minima within the potential well, leading to fewer bound subbands for a given amount of downward band bending. By control of both the surface Fermi level pinning position and the bulk doping, it is therefore possible to control the

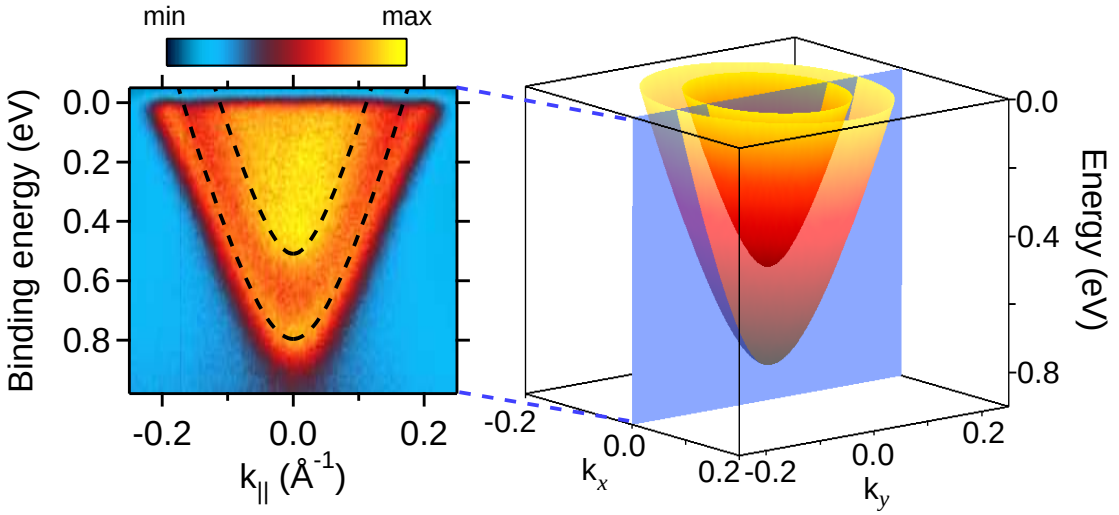

Figure 9.4: ARPES photocurrent intensity map of the parallel dispersion of two subbands in InN at 60 K (data from Colakerol *et al.* [314]). Sample preparation involved two 10 minute cycles of 500 eV Ar^+ ion bombardment and annealing at 300°C. The Fermi level is at 0 eV. Simulated non-parabolic (NP) subband dispersions for InN with a surface-state density of $N_{ss} = 8.1 \times 10^{13}$ cm^{-2} and bulk density of $n_b = 3.7 \times 10^{19}$ cm^{-3}, corresponding to a downward band bending of 1.8 eV, are shown (full two-dimensional dispersion shown on right, dispersion through measured energy-momentum cut shown on left as black dotted lines). The photoemission intensity is plotted on a false colour scale (shown above the photocurrent intensity map).

number and binding energies of the subbands within the potential well.

9.3.3 Comparison with experiment

Initially, this calculation scheme is used here to model previous experimental data. Colakerol *et al.* [314] have mapped the dispersion of subband states at InN surfaces using high-resolution ARPES. A photocurrent intensity map of the subband parallel dispersion is shown in Fig. 9.4. Simulations for InN with a surface-state density of $N_{ss} = 8.1 \times 10^{13}$ cm^{-2} and bulk density of $n_b = 3.7 \times 10^{19}$ cm^{-3}, corresponding to a downward band bending of 1.8 eV, result in two confined subbands with their minima located 0.80 eV and 0.51 eV below the Fermi level at the surface, in agreement with the experimental results.

The full two-dimensional dispersions resulting from these calculations, along with the parallel dispersions relative to the experimental ones, are shown in Fig. 9.4. At low parallel wavevector, there is good agreement between the calculated and experimental dispersions, although these diverge somewhat at higher wavevector. This may be due to small errors in the bulk conduction band-edge effective mass used,

failure of the Kane $\mathbf{k}\cdot\mathbf{p}$ bulk dispersion relations at higher wavevector, or neglecting the (albeit small) anisotropy of the conduction band dispersion in wurtzite InN. In addition, many-body effects may play an important role as discussed in detail below. Despite the slight divergence of the calculated and experimental dispersion at high parallel wavevectors, a distinct non-parabolicity is evident in both the experimental and model dispersions. The subband minimum momentum effective mass, determined from the calculated subband dispersions, is $0.080m_0$ and $0.055m_0$ for the first (E_1) and second (E_2) subbands, respectively.

It should be noted that, while good agreement was obtained between the measured and calculated dispersions, the required amount of downward band bending, and consequently the surface-state density, is significantly higher than that typically observed at clean InN surfaces (see Chapter 6). The reasons for this may be partly due to the surface preparation method, which involved Ar^+ ion bombardment and annealing at 300°C. Ar^+ ion bombardment has been shown [325] to preferentially sputter N, leading to an In-enrichment of the surface. Such an In-enrichment has been shown [326], in the similar case of InAs, to lead to an increase in the near surface carrier density; similar effects would be expected for InN, which may therefore increase the surface-state density over that of a clean surface prepared without ion bombardment and annealing. However, the required surface-state density to get agreement between these calculations and ARPES data was also rather large for another sample investigated by Colakerol *et al.* [314], which was prepared only by annealing. This suggests a more fundamental origin to the differences between the surface-state densities determined by different methods, stimulating the following investigation.

9.4 ARPES studies

The quantized conduction band states in a native electron accumulation layer are not only occupied, but also localized right at the surface of the semiconductor. This makes them ideally suited to being studied by ARPES, as evident from Fig. 9.4. Here, such measurements of the quantized surface electron accumulation layers of

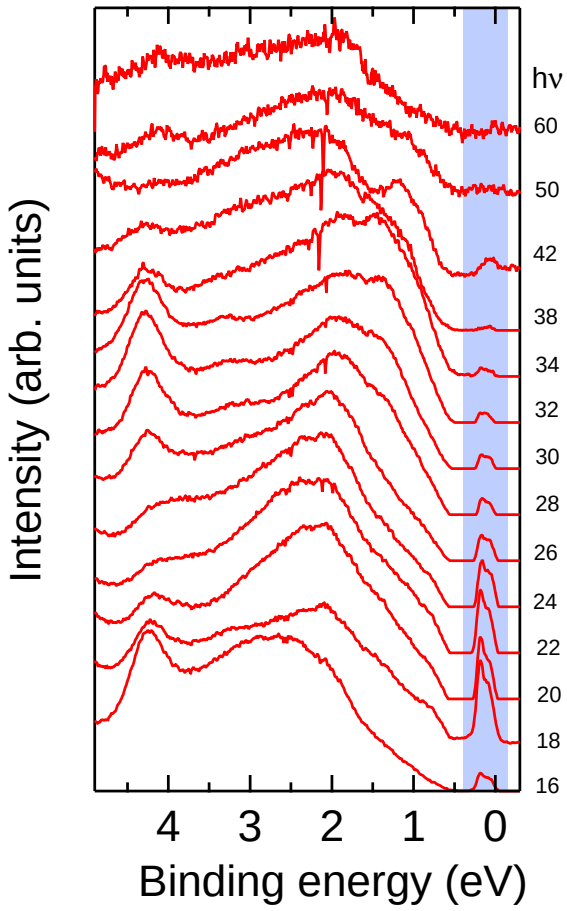

Figure 9.5: Normal emission EDCs recorded from a clean InAs(111) surface. The EDCs for different incident photon energies are vertically offset for clarity. The zero of the binding energy scale is the Fermi level at the surface. The shaded region indicates photoemission from quantized conduction band states.

InAs and CdO are reported.

A series of energy distribution curves (EDCs), recorded at room temperature in normal emission geometry from an InAs(111) surface as a function of incident photon energy, are shown in Fig. 9.5. As these spectra are taken in normal emission, the $\bar{\Gamma}$ point of the surface Brillouin zone is probed for all cases (see Section 3.1). However, with varying photon energy, the component of $k_\perp$ changes, and so these spectra effectively probe the Γ–L–Γ direction of the bulk BZ. Previous investigations have determined that photon energies of $\sim$20 eV and $\sim$44 eV probe the Γ-point of the bulk BZ for an InAs(111) sample [38, 321]. Of particular interest here are the states observable above the valence band maximum (VBM), represented by shading in Fig. 9.5. Similar features were previously observed by Olsson *et al.* [38], although only at photon energies very close to those probing the Γ-point of the bulk BZ. These features were interpreted as photoemission from states in the electron accumulation layer of InAs, but attributed to excitation from the centre of the bulk BZ. Here,

these states can be observed at almost all photon energies, indicating that they are not localized in $k_\perp$. This is further confirmed by their lack of dispersion with $k_\perp$, indicating their two-dimensional character. However, their amplitude is clearly enhanced close to the centre of the bulk BZ. The quantized electron accumulation layer states shown in Fig. 9.2 are only quasi-two-dimensional – they still 'see' a $k_\perp$ component due to the finite width of the potential well formed by band bending at the surface. Consequently, it is to be expected that some intensity variation occurs as a function of probing different $k_\perp$ in the photoemission measurements, with the highest cross-section for photoemission when probing close to the centre of the bulk BZ. These features are therefore ascribed here to emission from quantized conduction band states in the quasi-two-dimensional electron gas (Q2DEG) at the surface of InAs.

To investigate these states in detail, high-resolution ARPES measurements were performed at a photon energy of $h\nu = 20$ eV as a function of emission angle, and therefore, of parallel wavevector. The corresponding photocurrent intensity map is shown in Fig. 9.6. Two features can be observed - a clearly resolved lower band, and a rather diffuse inner band. The lower band is identified as a quantized subband state. The upper band may be a second quantized, but only weakly bound, subband state, or could be associated with photoemission from bulk conduction band states, as discussed further below. It is also possible that both of these features may be present, giving rise to the rather broad nature of this feature.

Using the model described in Section 9.3, it is possible to obtain subbands whose binding energies and dispersions accurately follow the experimental features. However, this requires a downward band bending of 0.4 eV, corresponding to a surface-state density of $N_{ss} = 6.1 \times 10^{12}$ cm^{-2}. This is very high in comparison with typical surface-state densities previously reported for InAs surface electron accumulation layers [39]. Indeed, from the onset of intensity in the normal emission spectra shown in Fig. 9.5 probing the Γ-point of the BZ, the VBM can be estimated to occur ~ 0.6 eV below the Fermi level at the surface, which corresponds to a downward band bending of only 0.1 eV, and a surface-state density of $N_{ss} = 1.0 \times 10^{12}$ cm^{-2},

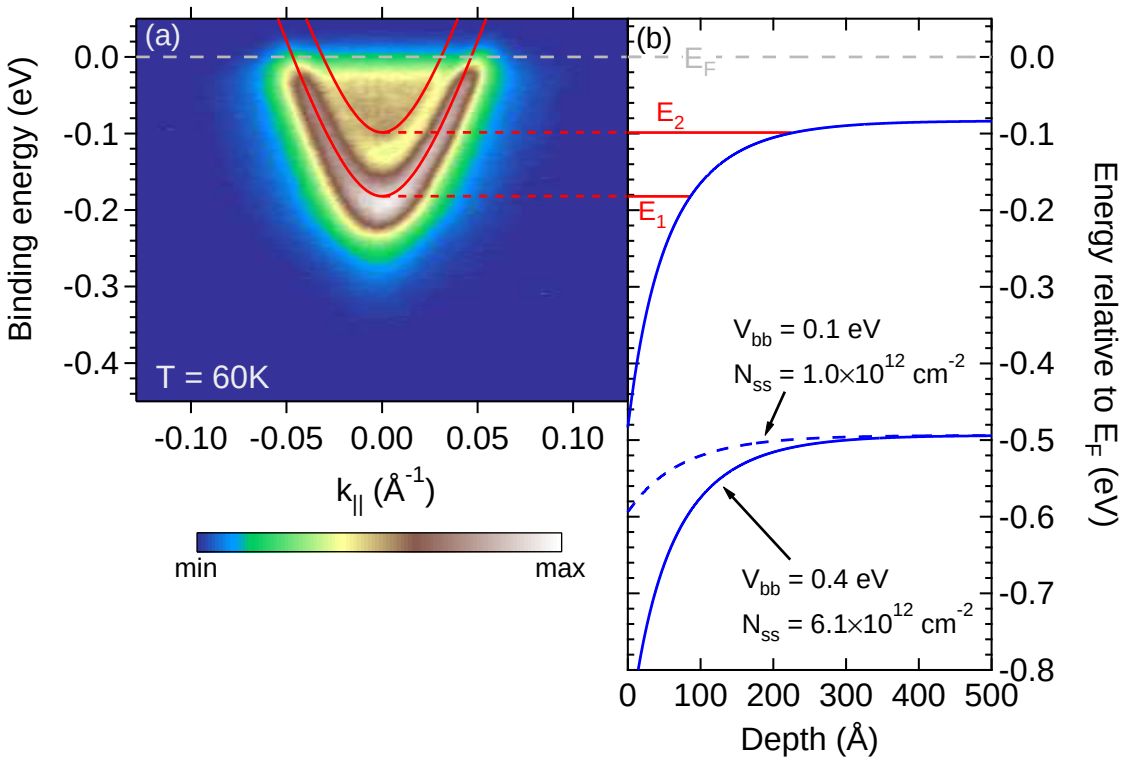

Figure 9.6: ARPES photocurrent intensity map of the parallel dispersion of quantized conduction band states at the surface of InAs(111), recorded at 60K. The Fermi level is at 0 eV. The photoemission intensity is plotted on a false colour scale (shown below the photocurrent map). Simulated NP subband dispersions for a surface-state density of $N_{ss} = 6.1 \times 10^{12}$ cm^{-2} and bulk density of $n_b = 6 \times 10^{17}$ cm^{-3}, corresponding to a downward band bending of 0.4 eV (shown in (b), solid blue lines) are plotted on top of the experimental dispersions (red lines). A downward band bending of the valence band of 0.1 eV, corresponding to the onset of valence band photoemission and the position of the In 4*d* core-levels, is also shown (dashed blue line).

significantly smaller than that required to simulate the ARPES dispersions. Such a downward band bending is represented in the valence band in Fig. 9.6(b).

This is also consistent with the core-level peak positions. The In 4*d* core levels, recorded in 'angle-integrated mode' at a photon energy of 70 eV, are shown in Fig. 9.7. The peak was fitted by two spin-orbit split *d* components ($\Delta E_{so} = 0.855$ eV) to account for the bulk core-level peak, and a surface core-level shift. The separation of the bulk and surface components was 0.28 eV, in agreement with previous studies of InAs(111)B–(2×2) [321]. The bulk component occurs at a binding energy of 17.46 ± 0.05 eV. Comparison with the VBM to In 4*d* separation determined previously [321] allows the Fermi level to be located 0.56 ± 0.05 eV above the VBM at the surface in this case, in agreement with the value determined from the normal-emission valence band EDCs. Consequently, there is a large discrepancy

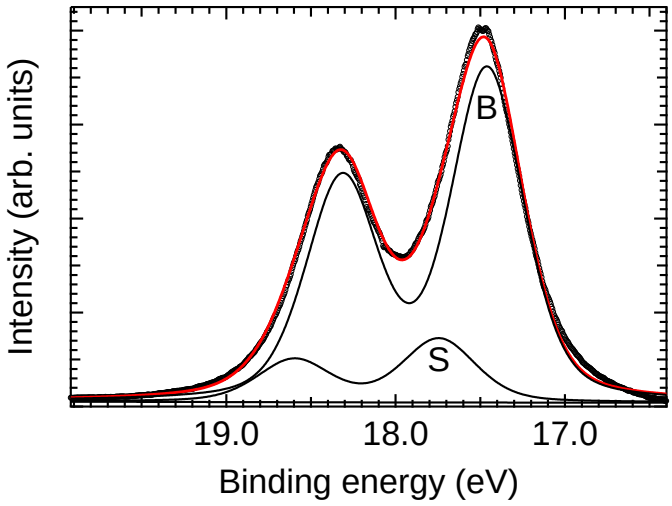

Figure 9.7: Angle-integrated In 4*d* core-level spectra, recorded at a photon energy of 70 eV. The peaks are fitted with a Shirley background and Voigt (mixed Lorentzian-Gaussian) lineshapes to account for bulk (B) and surface (S) components.

between the amount of downward band bending determined from core-level and valence band features and from simulation of the conduction subband features. While this may in part be due to the approximations made within the model (for example, the validity of the $\mathbf{k} \cdot \mathbf{p}$ dispersions in the degenerate electron accumulation layer), other effects, such as many-body interactions, may also be important. These are discussed further below.

An equivalent investigation was performed for the CdO(001) surface. From previous normal-emission measurements [327], photon energies of $\sim$ 30 eV and $\sim$85 eV can be taken as probing the Γ-point of the bulk BZ. High-resolution measurements are made here at the lowest of these two values, to ensure the highest $k_{\|}$-resolution. Quantized conduction band features were again observed, and an example measurement, performed at 80 K, is shown in Fig. 9.8. In this case, the dispersions extend over a larger binding energy, and the inner band has a more well defined dispersion, than was observed for InAs. It was possible to get reasonable agreement between calculated and measured dispersion relations using the model described above, as shown in Fig. 9.8. The agreement is not, however, as good as for InAs (Fig. 9.6), or indeed InN (Fig. 9.4), but it should be noted that the low-temperature band parameters are less well known for CdO than for these other materials. The calculations in this case required a downward band bending of 1.1 eV, corresponding to a surface-state density of $N_{ss} = 7.0 \times 10^{13}$ cm^{-2}. This is much higher than the values determined from valence band x-ray photoemission

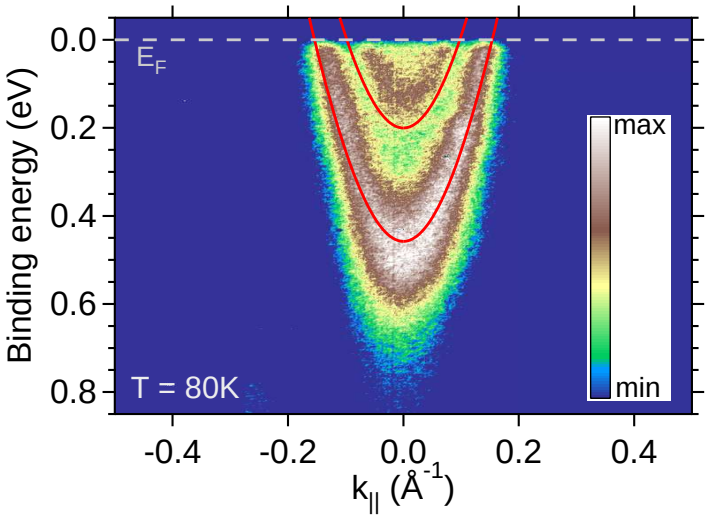

Figure 9.8: ARPES photocurrent intensity map of the parallel dispersion of quantized conduction band states at the surface of CdO(001) recorded at 80K. The Fermi level is at 0 eV. Simulated NP subband dispersions for a surface-state density of $N_{ss} = 7.0 \times 10^{13}$ cm^{-2} and bulk density of $n_b = 2 \times 10^{19}$ cm^{-3}, corresponding to a downward band bending of 1.1 eV, are plotted on top of the experimental dispersions. The photoemission intensity is plotted on a false colour scale (shown inset).

spectroscopy (XPS) measurements presented in Section 4.5 from another piece of the same sample, prepared under very similar conditions. This again suggests that other effects, such as many-body interactions, may play an important role here.

9.5 Many-body effects in an electron accumulation layer

As seen throughout this thesis, the electron density in a semiconductor surface electron accumulation layer can be very high. It therefore seems plausible that many-body interactions, such as electron-electron (e-e) and electron-phonon (e-ph) coupling, may become important. In particular, e-e interactions are known to lead to a reduction in the band gap of a semiconductor for highly degenerate bulk carrier concentrations [328]. In a two-dimensional system, many-body interactions can be much more important [329], as has previously been observed in optical investigations of semiconductor quantum well structures [329–331]. As discussed in Section 3.1.2, ARPES measures the quasiparticle electronic structure, and so many-body effects must be considered in the analysis of such data. In contrast, the valence band remains empty of holes both in the bulk and in the accumulation layer – it might therefore be expected that there is minimal change in many-body interactions between the bulk and surface for the valence band. In the previous section, it was shown that the amount of band bending in a semiconductor electron accumulation layer determined from an analysis of the relative positions of the VBM at the surface and

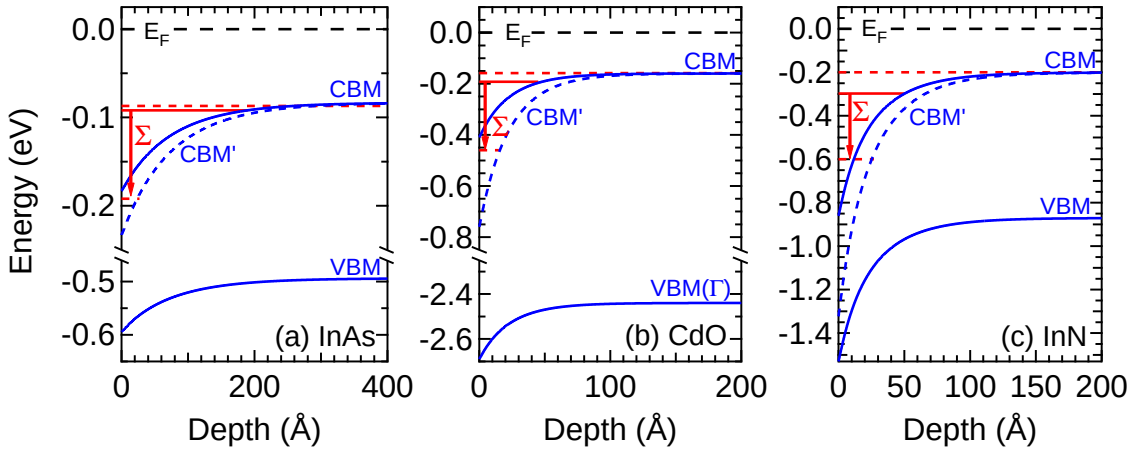

Figure 9.9: Bending of the CBM and VBM (solid blue lines) in (a) InAs, (b) CdO, and (c) InN, within the Hartree approximation, at 60 K, 80 K, and 177 K, respectively. The amount of band bending is determined from the VB onset in normal emission ARPES spectra and the position of the In 4*d* core levels for InAs, from XPS measurements of a sample prepared under identical conditions as for the ARPES measurements for CdO, and from XPS measurements of typical InN samples. The position of the calculated subband feature in each case is shown as a solid red line. The binding energies of the experimental subband features at $\bar{\Gamma}$ observed in the APRES spectra (measured here for InAs and CdO, from Ref. [314] for InN) are shown as dashed red lines. A schematic representation of the CBM bending, in the presence of many-body interactions, is shown as a dashed blue line.

in the bulk drastically underestimates the amount of band bending required to give quantized states at the binding energies identified by ARPES measurements. The following model is proposed here to explain these discrepancies: the VBM to surface Fermi level separation, and the subsequent solution of the band bending within the Poisson-MTFA formalism, defines the Hartree potential, that is, the band bending potential neglecting many-body effects on the conduction band. These many-body effects cause an increase in the binding energy of the quantized subband features by the electron self-energy, $\Sigma(\mathbf{k} = 0)$ – the many-body interactions effectively cause a band gap shrinkage within the electron accumulation layer, which causes the quantized state to occur deeper in the potential well than would be expected from the Hartree potential alone. This is represented in Fig. 9.9. It should be noted that this model is somewhat preliminary, and needs further experimental and theoretical verification. The results of initial measurements and calculations into this effect are, however, presented below.

9.5.1 Electron-electron interactions

To determine the Hartree potential for the InAs sample investigated above, the VBM to surface Fermi level separation was determined from the normal emission photoemission spectra, and the position of the In $4d$ levels, as discussed above. Calculations for this band bending are shown in Fig. 9.9(a), and result in a single quantized state $\sim$0.1 eV below the Fermi level. Two spectral features are observed in the ARPE spectra (Fig. 9.6(a)), and the positions of these at $\bar{\Gamma}$ are shown in Fig. 9.9(a) as dashed red lines. The topmost feature occurs at an energy very close to the calculated CBM position in the bulk of the semiconductor, and this is therefore attributed to emission from bulk conduction band states. The more deeply bound feature is associated with photoemission from a quantized state within the InAs accumulation layer. This state occurs 0.1 eV below the calculated subband feature for the Hartree potential. In the proposed model, this therefore corresponds to a subband renormalization by an electron self-energy of $\Sigma(\mathbf{k} = 0) = 0.1$ eV.

As discussed in Section 3.1.2, the measured ARPES intensity is directly related to the spectral function of the material. In particular, the Lorentzian linewidth of a momentum distribution curve (MDC) is directly proportional to the imaginary component of the self-energy. It is therefore of interest to investigate the properties of the MDCs here in some detail. A selection of MDCs of the states of interest are shown in Fig. 9.10(b). While the outer band is strong, the inner band shows only very weak features, as expected from the photocurrent intensity map. The following discussion is therefore limited to MDCs of the outer band. In particular, MDCs within the red boundary shown in Fig. 9.10(a) were considered in detail. In each case, a linear background was removed, following which the MDC was fitted by a single Lorentzian peak. The peak position and FWHM are shown in Fig. 9.10(c) and (d), respectively.

A small kink in the dispersion, can be seen in the MDC peak positions at around 0.1 eV below the Fermi level. At around this energy, there is also a slight peak, followed by a dip, in the MDC linewidth. This is somewhat analogous to the changes in MDC linewidth that have previously been associated with electron-

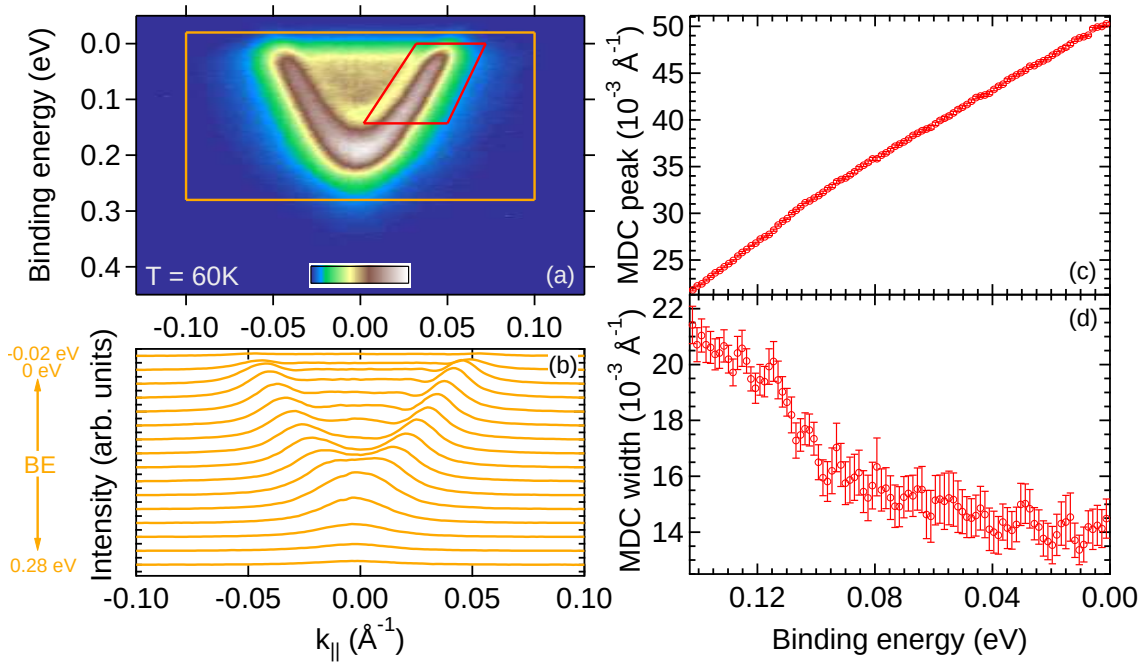

Figure 9.10: (a) ARPES photocurrent intensity map of the parallel dispersion of quantized conduction band states at the surface of InAs(111) at 60K, shown in Fig. 9.6(a). (b) A set of MDCs within the orange rectangle shown in (a). (c) Peak position and (d) Lorentzian FWHM of the MDCs in the red region of (a).

plasmon interactions in graphene [332]. Here, they are taken as evidence for an e-e interaction. Assuming no **k**-dependence of the electron self-energy (see below), the MDC analysis suggests a self-energy contribution of $\sim$0.1 eV from e-e interactions, in agreement with the value determined above from comparisons of the spectral features and model calculations.

A similar analysis was performed for CdO. From the VBM to surface Fermi level separation from XPS measurements (Chapter 4), the Hartree potential was calculated, as shown in Fig. 9.9(b). As for InAs, a single bound state within the surface quantum well was found, now slightly more deeply bound at 0.19 eV below the Fermi level. This is in contrast to the two clear spectral features observed in the experiment (Fig. 9.8), shown as red dotted lines in Fig. 9.9(b). However, as for InAs, the topmost feature occurs approximately at the CBM in the bulk, and is therefore attributed to photoemission from bulk states. The more deeply bound feature is ascribed to the quantized conduction band state, which lies $\sim$ 0.27 eV below the calculated state. An MDC analysis is also shown in Fig. 9.11. While

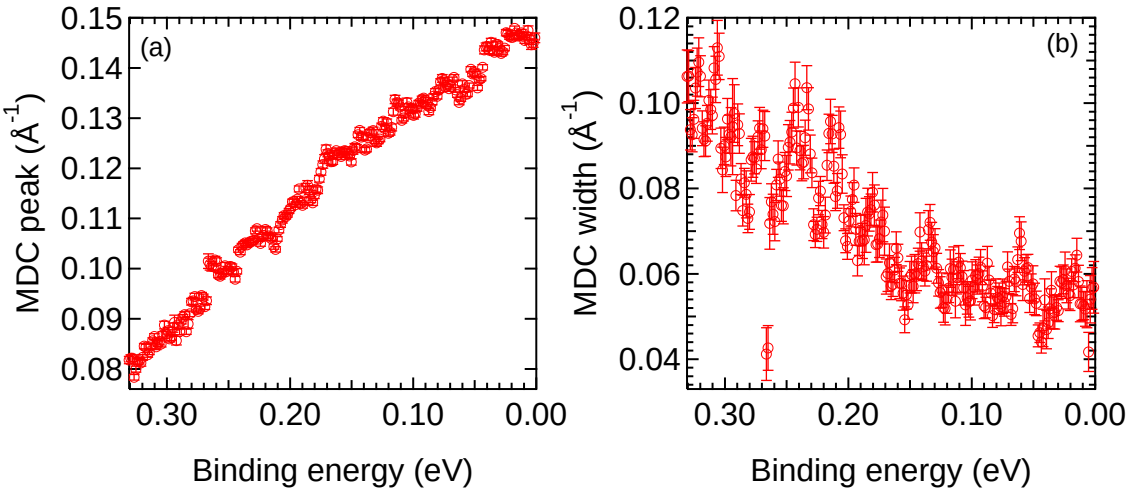

Figure 9.11: (a) Peak position and (b) Lorentzian width of MDCs of the outer subband feature from 0.33 eV binding energy to the Fermi level in CdO(001) at 80 K (see Fig. 9.8).

the data is more noisy than for the InAs case, an increase in width of the MDCs is just observable at ~ 0.25 eV below the Fermi level. This, and the comparison of the calculated and measured positions of the subband feature, both suggest a self-energy of $\sim$0.25 eV associated with e-e interactions in this case. This is higher than for InAs, as might be expected due to the higher density of carriers within the electron accumulation layer in CdO as compared to InAs.

Finally InN is considered. From the typical VBM to surface Fermi level separation determined in Chapter 6, the Hartree potential, for a bulk doping of $n = 6 \times 10^{18}$ cm^{-3}, is defined as shown in Fig. 9.9(c). At 177 K, this again gives one quantized state, located ~ 0.3 eV below the Fermi level. The ARPES results of Colakerol *et al.* [314], measured at 177 K from a sample ($n = 6 \times 10^{18}$ cm^{-3}) that was only annealed and not ion bombarded, gives measured spectral features 0.2 eV and 0.6 eV below the Fermi level at $\bar{\Gamma}$. The topmost feature can again be associated with photoemission from bulk conduction band states, while the shift in energy between the quantized state in the calculations and the experiment allows a self-energy of 0.3 eV to be estimated. This is the highest of all the materials considered, consistent with the highest surface-state density for InN, in comparison to CdO and InAs.

To validate the above considerations, it is of interest to calculate the expected

magnitude of the contribution from e-e interactions to the electron self-energy. The calculations here are based upon the formalism of Vinter [333, 334], originally developed to describe e-e interactions within the 2DEG of a Si MOSFET. Within the random phase approximation (RPA), the self-energy

$$\Sigma(\mathbf{k}, E) = i \iiint \frac{\mathrm{d}^2 q \, \mathrm{d}\omega}{(2\pi)^3} \frac{e^2}{2\varepsilon_0 \varepsilon(\infty) q} \frac{\varepsilon(\infty)}{\varepsilon(q,\omega)} G_0(\mathbf{k}-\mathbf{q}, E-\omega), \tag{9.5}$$

where $\varepsilon(\infty)$ describes the effective permittivity of the medium, and the permittivity function $\varepsilon(q,\omega)/\varepsilon(\infty)$ is derived from the polarizability of a 2DEG determined by Stern [335]. To account for image charge effects, the effective permittivity of the medium is assumed to be the mean of those in the semiconductor and the vacuum, as these calculations are being used here for a *surface* electron accumulation layer. The single-particle Green's function

$$G_0(\mathbf{k}, E) = \frac{\theta(|\mathbf{k}| - k_F)}{E - \xi(\mathbf{k}) + i\delta(0_+)} + \frac{\theta(k_F - |\mathbf{k}|)}{E - \xi(\mathbf{k}) - i\delta(0_+)} \tag{9.6}$$

where θ is the heaviside step function and $\xi(\mathbf{k}) = \hbar^2(k^2 - k_F^2)/2m_\parallel^*$. In Vinter's approach, a plasmon-pole approximation is introduced, where the self-energy is separated into separate components to account for exchange (an unscreened term) and correlation effects

$$\Sigma(k, E) = \Sigma_x(k) + \Sigma_c(k, E). \tag{9.7}$$

The details of this approximation are presented elsewhere [334]. The resulting exchange energy takes the form calculated by Stern [336], and is given by

$$\Sigma_x(k) = \begin{cases} \int_0^{k_F-k} \mathrm{d}q \, \frac{e^2}{4\pi\varepsilon_0\varepsilon(\infty)} - \int_{k_F-k}^{k_F+k} \mathrm{d}q \, \frac{e^2}{(2\pi)^2\varepsilon_0\varepsilon(\infty)} \left[\frac{\pi}{2} - \sin^{-1}\left(\frac{k^2+q^2-k_F^2}{2kq}\right)\right], & k < k_F \\ \int_{k-k_F}^{k+k_F} \mathrm{d}q \, \frac{e^2}{(2\pi)^2\varepsilon_0\varepsilon(\infty)} \left[\frac{\pi}{2} - \sin^{-1}\left(\frac{k^2+q^2-k_F^2}{2kq}\right)\right], & k > k_F \end{cases} \tag{9.8}$$

which is dependent on the sheet density of the 2DEG, $N = k_F^2/2\pi$. The correlation

energy

$$\Sigma_c(k,E) = \begin{cases} -\int_{k_F-k}^{k_F+k} \mathrm{d}q\, \Omega(q) \left\{ H\left[k_F^2, p_+\right] + H\left[(k+q)^2, p_-\right] - H\left[k_F^2, p_-\right] \right\} \\ \quad -\int_0^{k_F-k} \mathrm{d}q\, \Omega(q) H\left[(k+q)^2, p_+\right] & k < k_F \\ \quad -\int_{k_F+k}^{\infty} \mathrm{d}q\, \Omega(q) H\left[(k+q)^2, p_-\right], \\ -\int_{k-k_F}^{k+k_F} \mathrm{d}q\, \Omega(q) \left\{ H\left[k_F^2, p_+\right] + H\left[(k+q)^2, p_-\right] - H\left[k_F^2, p_-\right] \right\} \\ \quad -\int_0^{k-k_F} \mathrm{d}q\, \Omega(q) H\left[(k+q)^2, p_-\right] & k > k_F \\ \quad -\int_{k+k_F}^{\infty} \mathrm{d}q\, \Omega(q) H\left[(k+q)^2, p_-\right], \end{cases} \tag{9.9}$$

where

$$\Omega(q) = \frac{2m_\parallel^* e^2}{(2\pi)^2 \varepsilon_0 \varepsilon(\infty) \hbar} \frac{\omega_p^2}{\omega_q}, \tag{9.10}$$

$$p_\pm = -\frac{2m_\parallel^*(E \pm \hbar\omega_q)}{\hbar^2} - k_F^2. \tag{9.11}$$

The plasmon frequency [335]

$$\omega_p = \left[\frac{qNe^2}{2\varepsilon_0 \varepsilon(\infty) m_\parallel^*} \right]^{\frac{1}{2}}. \tag{9.12}$$

and

$$\omega_q^2 = -\frac{\omega_p^2}{(\varepsilon_0 \varepsilon(\infty)/\varepsilon(q,0)) - 1}. \tag{9.13}$$

The two-dimensional RPA result of Stern [335] is used to give

$$\frac{\varepsilon(q,0)}{\varepsilon(\infty)} = \begin{cases} 1 + \dfrac{e^2 m_\parallel^*}{2\pi\varepsilon_0 \varepsilon(\infty)\hbar^2} \dfrac{1}{q}, & q \le 2k_F \\ 1 + \dfrac{e^2 m_\parallel^*}{2\pi\varepsilon_0 \varepsilon(\infty)\hbar^2} \dfrac{1}{q} \left[1 - \sqrt{1 - \left(\dfrac{2k_F}{q} \right)^2} \right], & q > 2k_F. \end{cases} \tag{9.14}$$

For $k = k_F$, the correlation energy can be easily determined. However, for $k \neq k_F$, the calculation proceeds via a graphical solution of the Dyson equation [333]

$$E + \mu = \xi(\mathbf{k}) + \Sigma(k, E), \tag{9.15}$$

where the quasiparticle energy, E, is given relative to the chemical potential, μ.

Example calculations for the wavevector and density dependence of the electron self-energy in a 2DEG at an InAs surface are shown in Fig. 9.12. The total

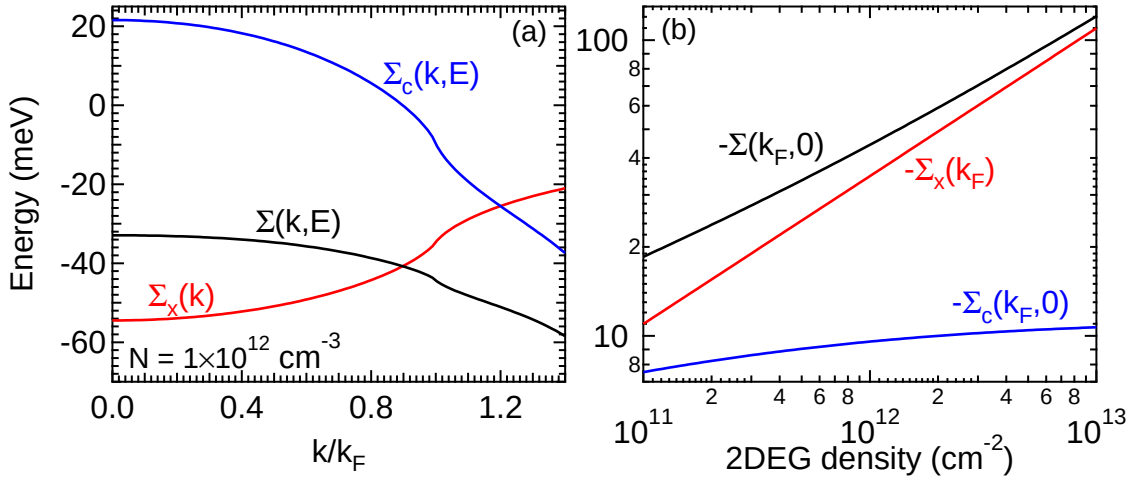

Figure 9.12: Self-energy calculations for InAs (a) for a 2DEG density of $N = 1 \times 10^{12}$ cm^{-2} as a function of k/k_F, and (b) at k_F as a function of the 2DEG density, N.

self energy varies by only $\sim$10 meV between the $\bar{\Gamma}$-point and the Fermi wavevector, validating the **k**-independence of the self-energy assumed above. The density of the Q2DEG in the current case can be estimated directly from the measured dispersions: the Fermi wavevector can be determined from the MDC peak position at the Fermi level (see Fig. 9.10(c)), and this can be converted into a 2DEG density via the relation

$$N = \frac{k_f^2}{2\pi}. \tag{9.16}$$

For the InAs sample investigated here, this corresponds to a 2DEG density of $N = 4 \times 10^{12}$ cm^{-2}. The electron self-energy for this 2DEG can be calculated to be 0.08 eV. This is in good agreement with the value of 0.1 eV determined experimentally above, particularly considering the approximations involved in this calculation scheme. Note, the experimental density of the Q2DEG is somewhat higher than the surface-state density resulting from Poisson-MTFA calculations for the Hartree potential. This is due to the lack of many-body interactions included within the calculation of the Hartree potential – the e-e interactions cause a shrinkage of the fundamental band gap, resulting in the bound subband lying further below the Fermi level. The carrier density associated with electron states in this subband is therefore higher than would be expected when neglecting the e-e interactions, leading to a higher density in the 2DEG, and correspondingly, a higher surface-state density to maintain charge neutrality.

From Fig. 9.11(a), the density of the Q2DEG in the CdO sample investigated here can be estimated as $N = 3.6 \times 10^{13}$ cm^{-2}, while from the measurements of Colakerol *et al.* [314], the density of the Q2DEG in InN can be estimated as $N \approx 5 \times 10^{13}$ cm^{-2}. Using the above method, the calculated electron self-energy is 0.41 eV and 0.50 eV for CdO and InN, respectively. These are both within a factor of two of the self-energy estimated from the experimental measurements presented above, providing some validation of the explanations presented here. Finally, it should be noted that the conclusions on electron accumulation presented in the preceding chapters of this thesis still hold. However, the reported downward band bending values and surface state densities are within the Hartree limit - the downward bending of the conduction band and density of electrons within the Q2DEG will therefore be slightly higher in the quasiparticle picture than the values that were reported.

9.5.2 Electron-phonon interactions

Given that e-e interactions seem to be important in the high carrier densities of surface electron accumulation layers, it seems likely that e-ph interactions would also be important. Electron-phonon interactions lead to a kink in the quasiparticle dispersion at an energy equal to the phonon energy below the Fermi level, and also lead to a narrowing of the MDC linewidth due to a decrease in the imaginary component of the self-energy close to the Fermi level [337]. In principle, it is therefore possible to extract information on e-ph coupling directly from the measured dispersion and MDC linewidths. However, from Figs. 9.10 and 9.11, these indications are not clear in this case.

It is also possible to obtain information on the e-ph coupling from the temperature dependence of the EDC linewidth of spectral features in the ARPES measurements [338]. It is generally assumed that the linewidth contribution from e-e interactions, and also e-ion or e-defect interactions, are independent of temperature. At a turning point in the electronic structure, the group velocity is zero, and the measured EDC linewidth directly gives the initial state linewidth [339]. The

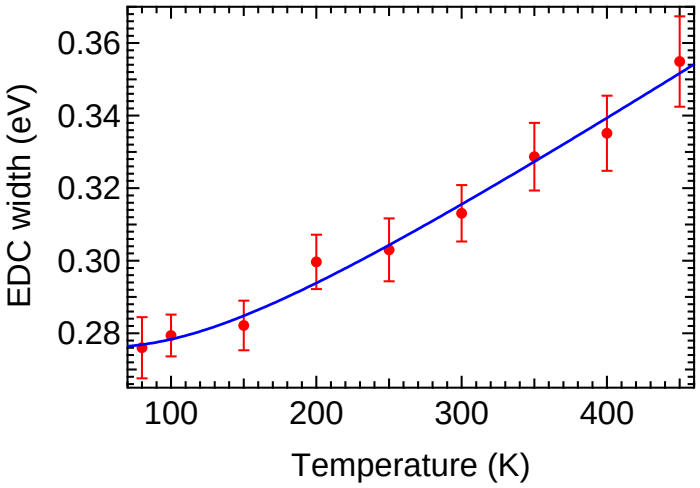

Figure 9.13: Temperature dependence of the Lorentzian width of EDCs of the quantized subband in CdO at $\bar{\Gamma}$, and a fit according to the Cardona model (Eqn. 9.17).

linewidths of the EDC at $\bar{\Gamma}$ in CdO are therefore considered here as a function of temperature, shown in Fig. 9.13.

As expected for e-ph coupling, the linewidth increases with increasing temperature. Cardona *et al.* [340, 341] have developed a model for the temperature dependence of the band gap in semiconductors due to e-ph interactions, and have extended this model to the temperature dependence of the linewidth that would be observed in ARPES measurements. In this model, the initial state linewidth

$$\Gamma(T) = \Gamma(0) + \frac{2\sigma(0)}{e^{\Theta/T} - 1}. \tag{9.17}$$

where $\Gamma(0)$ is the linewidth at $T = 0$, accounting for the temperature-independent linewidth contribution from e-e, e-d, and e-i interactions, $\sigma(0)$ is the linewidth contribution from zero-point phonons, and Θ is an effective average Debye temperature for acoustic and optical phonons. Fitting the temperature dependence of the CdO state linewidths using this model, shown in Fig. 9.13, gives the parameters $\Gamma(0) = 0.28$ eV, $\sigma(0) = 0.05$ eV, and $\Theta = 370$ K.

There are two particular points of interest. First, the zero-temperature linewidth is much larger than for InAs. While a full temperature-dependent analysis was not performed for InAs, the EDC linewidth at 60 K is only $\sim$0.07 eV. While it may be lower due to a lower density of defects and impurities, it is also consistent with a lower degree of e-e interactions, as found from the above analysis. Second, the effective Debye temperature of 370 K is similar, although slightly higher, than the bulk Debye temperature in CdO of $\sim$250 K [342].

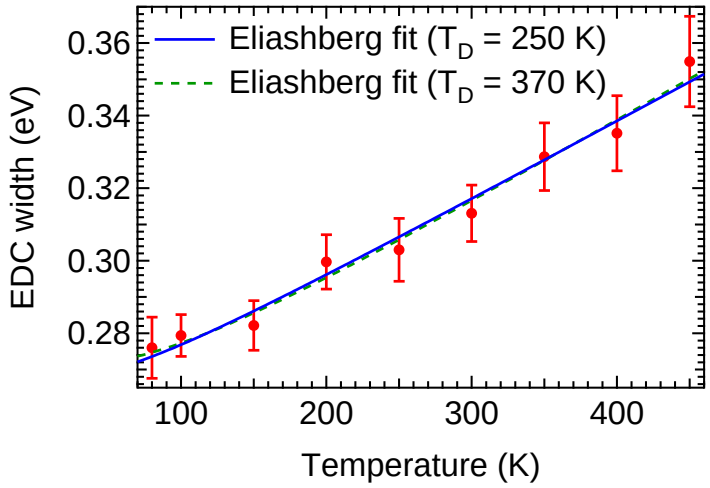

Figure 9.14: Temperature dependence of the Lorentzian width of EDCs of the quantized subband in CdO at $\bar{\Gamma}$, and a fit according to the Eliashberg model, within the Debye approximation (Eqns. 9.18 to 9.20), assuming a Debye temperature of 250 K and 370 K.

An alternative model often employed to describe e-ph interactions in solids, in particular metals [343], is the Eliashberg coupling function, $\alpha^2F(\omega)$. Within this model, the temperature dependent linewidth in the ARPE spectra is given by [338]

$$\Gamma(\omega,T) = \Gamma(0) + 2\pi\hbar \int_0^{\omega_m} \mathrm{d}\omega'\, \alpha^2F(\omega') \left[1 - f(\omega-\omega') + 2n(\omega') + f(\omega+\omega')\right] \quad (9.18)$$

where ω corresponds to the binding energy of the feature of interest, ω_m is the maximum phonon frequency, $f(\omega)$ is the Fermi-Dirac distribution function (Eqn. 2.22), and $n(\omega)$ is the Bose-Einstein distribution function

$$n(\omega) = \frac{1}{\exp\left[\beta(\omega-\omega_F)\right] - 1}, \quad (9.19)$$

where $\omega_F = 0$ for the Fermi level at 0 eV of the binding energy scale. Assuming the temperature is not too high, the Debye model can be used for the phonon spectrum [338], giving the Eliashberg coupling function

$$\alpha^2F(\omega) = \lambda \left(\frac{\omega}{\omega_D}\right)^2, \quad \omega < \omega_D, \quad (9.20)$$

where ω_D is the Debye frequency (corresponding to the Debye temperature), and λ is the electron-phonon coupling parameter, or mass-enhancement parameter. Above ω_D, the Eliahsberg function is zero.

The temperature dependence of the CdO EDC linewidth fitted using this model is shown in Fig. 9.14. A robust fit could not simultaneously be established for both the Debye temperature and e-ph coupling parameter. However, fixing the Debye temperature to that of the bulk (250 K) gives a zero temperature linewidth

and e-ph coupling parameter of $\Gamma(0) = 0.250 \pm 0.003$ eV and $\lambda = 0.40 \pm 0.02$, respectively. Instead, using the Debye temperature determined from the Cardona model discussed above (370 K), the fitted zero temperature linewidth and e-ph coupling parameter of $\Gamma(0) = 0.242 \pm 0.003$ eV and $\lambda = 0.43 \pm 0.02$, respectively, are very similar to those obtained using the bulk Debye temperature. This follows as the Debye temperature is not too high for CdO, so that the temperatures used in the measurements generally satisfy $T > 1/3T_D$, in which case the linewidth varies approximately linearly with temperature [338]

$$\Gamma(T > 1/3T_D) = \Gamma(0) + 2\pi\lambda k_B T, \tag{9.21}$$

independent of the Debye temperature. Consequently, the fits of the full Eliashberg coupling function within the Debye model are not sensitive to small changes in Debye temperature. Independent, therefore, of the Debye temperature used, the derived e-ph coupling parameter is reasonably strong, indicating that e-ph, in addition to e-e, interactions play a significant role in the quasiparticle electronic structure of a quantized semiconductor electron accumulation layer.

From the considerations presented here, these Q2DEGs present a novel system for investigating fundamental properties of many-body interactions. These systems also offer considerable flexibility. In the materials investigated in this thesis, the density of electrons in the Q2DEG varies by over an order of magnitude, providing the opportunity to probe many-body effects in a variety of different environments. Further, the density of electrons in the Q2DEG is known to be highly sensitive to adsorption of small quantities of elements such as Cs [324] or S [344] on the surface. This can even cause a Q2DEG to form where previously a carrier depletion layer existed [345]. This allows a unique opportunity to probe the carrier dependence of e-e and e-ph interactions by ARPES measurements without changing the properties of the host material (that is, Debye temperature, dielectric constant, band gap and band-edge effective mass). Such an investigation should be the subject of detailed further study.

9.6 Conclusions

The downward band bending of a surface electron accumulation layer was shown to lead to a confining potential, causing conduction band states to become quantized into two-dimensional subbands. A combined Poisson and Schrödinger calculation scheme, incorporating the effects of band non-parabolicity, was developed to describe the binding energy and dispersions of these quantized states within the Hartree limit. Angle-resolved photoemission spectroscopy measurements were made of these states at InAs and CdO surfaces. Many-body interactions, in particular electron-electron and electron-phonon coupling, were shown to be important in the electron accumulation layers, and were investigated via a combination of ARPES lineshape analysis and model calculations. This reconciles an apparent contradiction between the amount of band bending determined from analysis of the valence band maximum position at the surface and in the bulk, and the position and dispersion of quantized conduction subbands determined by ARPES. This work also demonstrates that quantized electron accumulation layers are a novel example quasi-two-dimensional system within which to investigate fundamental physics of many body interactions.

Chapter 10

Summary

This thesis has focussed on the electronic properties of a class of semiconductors identified here as *significantly cation-anion mismatched semiconductors* (SCAMS), due to the large size and electronegativity difference between the constituent cation and anion. Of potential cations for II-VI, III-V, and III-VI semiconductors, Cd and In have some of the highest atomic radii and lowest electronegativities, while O and N atoms are very small and highly electronegative. Consequently, combinations of these atomic species can be considered as model SCAMS, and three such compounds, CdO, In_2O_3, and InN, constitute the main materials investigated here.

The charge neutrality level (CNL) has been shown to be an important energy level in determining the electronic properties of defects, impurities and surfaces in these materials. In most conventional semiconductors, such as Si or GaAs, the CNL is located within the fundamental band gap (see Fig. 10.1). However, in CdO, In_2O_3, and InN, the CNL was shown here to be located within the conduction band, 0.39 eV, $\sim$ 0.65 eV, and 1.19 eV above the conduction band minimum (CBM), respectively, as shown in Fig. 10.1. This seemingly unusual location was explained from the band structure of typical SCAMS – the combination of a large cation and a small electronegative anion results in a very low CBM compared to the conduction band edge across the rest of the Brillouin zone. The CNL lies close to the mid-gap energy averaged across the Brillouin zone, and therefore above the CBM in these materials. For the specific case of InN, its position was rationalised within the chemical trends of common-cation and common-anion semiconductors. As a result of the low Γ-point CBM, lying below the CNL, the electronic properties of SCAMS are rather different to those of conventional semiconductors, as summarised below.

10.1 Native defects

Within the amphoteric defect model of Walukiewicz [51], native defects tend to drive the Fermi level towards an energy level termed the Fermi level stabilization

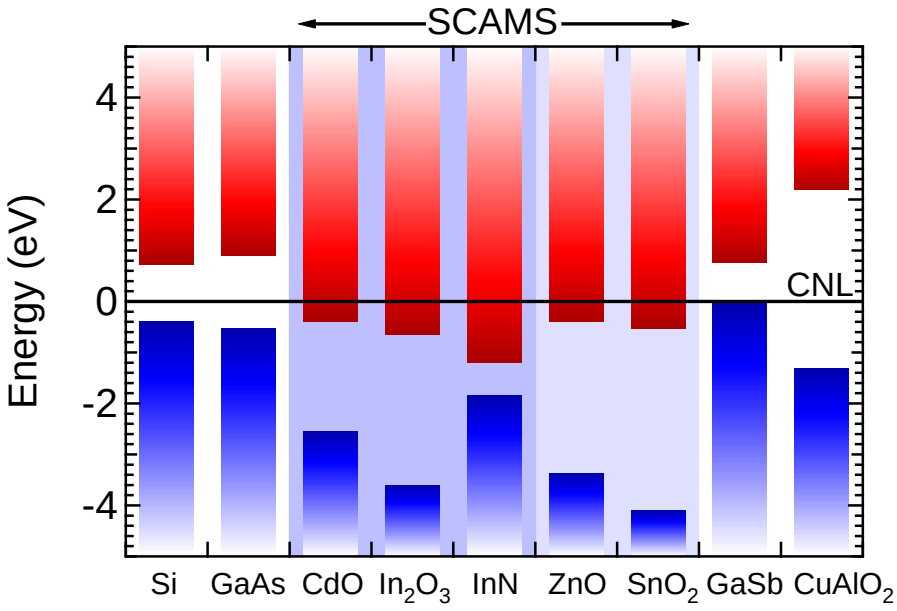

Figure 10.1: Band lineup of a number of semiconductors relative to the CNL. SCAMS are represented by shading. The darker shading indicates the primary materials investigated in this thesis. The bands are aligned from measured CNL positions (measured here for CdO, In_2O_3, and InN, from particle irradiation studies for Si, GaAs, and GaSb [183]), from measured valence band offsets for ZnO [346], and from calculations for SnO_2 and $CuAlO_2$ [347].

energy. It was argued here that this energy should be equal to the CNL, as it is virtual gap states (ViGS) that ultimately determine the charge state of deep defects, and the CNL lies at the branch point of these ViGS. Consequently, in conventional semiconductors, where the CNL lies within the band gap, native defects will tend to lower (raise) the Fermi level in n-type (p-type) material, as represented in Fig. 10.2. In contrast, for SCAMS where the CNL is located within the conduction band, the formation energy for donor-type native defects will remain lower than that of acceptor-type native defects until the Fermi level moves above the CNL (see Fig. 10.2). Consequently, native defects can be donors even in already n-type SCAMS. This was shown to be the case in CdO when native defects were deliberately introduced into n-type material by high-energy particle irradiation. The CNL positions determined here were also shown to be consistent with previous particle irradiation experiments in InN [177], and previous theoretical calculations for the formation energies of native defects in InN [190] and In_2O_3 [301].

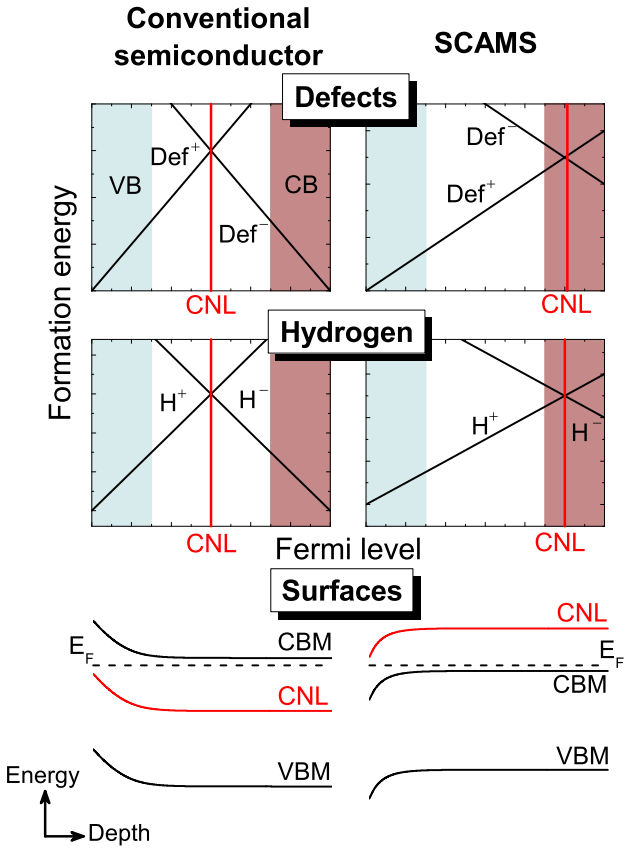

Figure 10.2: Schematic representation of formation energy as a function of Fermi level for donor (Def^+) and acceptor (Def^-) native defects, and donor (H^+) and acceptor (H^-) hydrogen, relative to the CNL, and band bending at the surface. All cases are illustrated for conventional semiconductors and for SCAMS.

10.2 Hydrogen

The donor/acceptor transition level for hydrogen [H(+/−)] was shown to be equivalent to the CNL, in agreement with previous theoretical arguments [25]. Consequently, as for native defects, H can be a donor even in n-type SCAMS, whereas the compensating charge state generally has the lowest formation energy in conventional semiconductors (see Fig. 10.2). Hydrogen was shown to be a donor in n-type CdO, while muon spin rotation spectroscopy measurements were used to show that muonium (Mu), and by analogy hydrogen, is a shallow donor in n-type In_2O_3. The CNL positions determined here are also consistent with previous measurements that H and Mu are both donors in InN [196, 197], and that Mu is a donor in CdO [117].

10.3 Surface electron accumulation

The surface electronic properties can differ markedly from those of the bulk. In the majority of semiconductors, a depletion of carriers results in the near surface

region. However, in SCAMS, the surface Fermi level pins slightly below the CNL, well into the conduction band. Consequently, a number of donor-type surface states will be unoccupied, and hence positively charged. In order to maintain charge neutrality, an increase in electron density, that is, an electron accumulation, occurs at the surface. This was shown to be the case in CdO, InN, and In_2O_3 investigated here. Furthermore, the low CBM, lying well below the CNL, was shown to lead to a strong pinning of the surface Fermi level, with a remarkable independence of the degree of surface electron accumulation observed as a function of surface orientation or bulk doping level, except for very high bulk concentrations. Electron accumulation was also shown to occur independent of the bulk polymorph of the material. For the InGaN system, where the CNL lies above the CBM in InN but below the CBM in GaN, a change from electron accumulation to depletion was observed with increasing Ga-composition. Similar changes were observed for the InAlN system. The electron accumulation was shown to persist at the surface of p-type InN, giving rise to an inversion layer, making it difficult to characterise the p-type bulk. Such an inversion layer would be expected at the surface of all p-type SCAMS. The strong downward band bending in the electron accumulation layer creates a confining potential well which was shown to result in quantized conduction band states. From a combination of angle-resolved photoemission spectroscopy measurements and model calculations, many-body interactions were shown to be important in the electron accumulation layer, where very high carrier densities can exist. Further work is needed to characterise these many-body effects in more detail.

10.4 Propensity for n-type conductivity

A combination of native defects tending to be donors, hydrogen acting as a donor, and a build up of carriers at the surface all contribute to the propensity for SCAMS to exhibit high unintentional n-type conductivity. Further, in InN, an increase in electron density approaching the InN/buffer layer interface was shown to be an additional source of conductivity, giving rise to a pronounced film-thickness dependence of single-field Hall effect results. In all cases, the CNL lying above the CBM can

be seen as the overriding reason for the unintentional n-type conductivity of these materials. In particular, for the relatively wide band gap oxide materials studied, this explains why they can be conducting while still being optically transparent, two normally conflicting properties, and hence their conventional use as transparent conducting oxides.

10.5 Consequences for other materials

While the position of the CNL does not guarantee a particular microscopic defect or surface state exists, it does describe tendencies for the charge character of the microscopic centres that are present. This is a particularly powerful guide when the CNL lies within one of the semiconductor bands, such as for SCAMS, and can therefore be used as a predictive tool. The band alignment of two further SCAMS, ZnO and SnO_2, determined from measured valence band offsets [346] and theoretical calculations [347], are shown in Fig. 10.1. In both of these cases, the CNL lies within the conduction band, as for the other SCAMS investigated here. This explains reported properties of these materials, such as their high unintentional conductivities, donor nature of H and Mu, and surface electron accumulation [102,300,302,305], as for the other SCAMS investigated here. As a contrasting example, the CNL can be located at or below the VBM, such as in GaSb, shown in Fig. 10.1, explaining its propensity for unintentional p-type conductivity, surface hole accumulation and the predictions of the acceptor nature of hydrogen even in p-type material [103,122]. Finally, while the oxides considered here all show a propensity for n-type conductivity, p-type conducting samples of $CuAlO_2$ have been realised [123]. Calculations locate the CNL in the lower half of the fundamental band gap for this material [347] (see Fig. 10.1), explaining why p-type conduction is achievable, in contrast to the other oxide materials investigated here. These results show that the CNL is a powerful tool for both explaining and predicting the electronic properties of a wide range of materials.

Bibliography

[1] Z. I. Alferov, Rev. Mod. Phys. **73**, 767 (2001).

[2] H. Kroemer, Rev. Mod. Phys. **73**, 783 (2001).

[3] K. von Klitzing, Rev. Mod. Phys. **58**, 519 (1986).

[4] W. Mönch, *Electronic properties of semiconductor interfaces*, Springer, Berlin, 2004.

[5] W. Shan, W. Walukiewicz, J. W. Ager, E. E. Haller, J. F. Geisz, D. J. Friedman, J. M. Olson, and S. R. Kurtz, Phys. Rev. Lett. **82**, 1221 (1999).

[6] K. M. Yu, W. Walukiewicz, J. Wu, W. Shan, J. W. Beeman, M. A. Scarpulla, O. D. Dubon, and P. Becla, Phys. Rev. Lett. **91**, 246403 (2003).

[7] I. Mahboob, T. D. Veal, C. F. McConville, H. Lu, and W. J. Schaff, Phys. Rev. Lett. **92**, 036804 (2004).

[8] T. J. Coutts, D. L. Young, X. Li, W. P. Mulligan, and X. Wu, J. Vac. Sci. Technol. A **18**, 2646 (2000).

[9] C. G. Granqvist and A. Hultker, Thin Solid Films **411**, 1 (2002).

[10] V. Heine, Phys. Rev. **138**, A1689 (1965).

[11] J. C. Inkson, J. Phys. C **13**, 369 (1980).

[12] W. Mönch, *Semiconductor surfaces and interfaces*, Springer, Berlin, 2001.

[13] S. Gasiorowicz, *Quantum physics*, Wiley, New York, 3^{rd} edition, 2003.

[14] Y.-C. Chang, Phys. Rev. B **25**, 605 (1982).

[15] C. Tejedor and F. Flores, J. Phys. C **11**, L19 (1977).

[16] J. Tersoff, Phys. Rev. Lett. **52**, 465 (1984).

[17] J. Tersoff, Phys. Rev. B **30**, 4874 (1984).

[18] J. Tersoff, Surf. Sci. **168**, 275 (1986).

[19] J. Tersoff, J. Vac. Sci. Technol. B **4**, 1066 (1986).

[20] M. Cardona and N. E. Christensen, Phys. Rev. B **35**, 6182 (1987).

[21] W. Mönch, J. Appl. Phys. **80**, 5076 (1996).

[22] A. Baldereschi, Phys. Rev. B **7**, 5212 (1973).

[23] D. R. Penn, Phys. Rev. **128**, 2093 (1962).

[24] J. Tersoff, Phys. Rev. B **32**, 6968 (1985).

[25] C. G. Van de Walle and J. Neugebauer, Nature **423**, 626 (2003).

[26] W. Walukiewicz, J. Vac. Sci. Technol. B **6**, 1257 (1988).

[27] Ç. Kılıç and A. Zunger, Appl. Phys. Lett. **81**, 73 (2002).

[28] I. E. Tamm, Physikal. Z. Sowjetunion **1**, 733 (1932), discussed in [12].

[29] W. Shockley, Phys. Rev. **56**, 317 (1939), discussed in [12].

[30] A. W. Maue, Z. Physik **94**, 717 (1935), discussed in [12].

[31] H. Lüth, *Surfaces and Interfaces of Solid Materials*, Springer, Berlin, 3rd edition, 1998.

[32] F. G. Allen and G. W. Gobeli, Phys. Rev. **127**, 150 (1962).

[33] W. Mönch, P. Koke, and S. Krueger, J. Vac. Sci. Technol. **19**, 313 (1981).

[34] G. W. Gobeli and F. G. Allen, Surf. Sci. **2**, 402 (1964).

[35] S. P. Svensson, J. Kanski, T. G. Andersson, and P.-O. Nilsson, J. Vac. Sci. Technol. B **2**, 235 (1984).

[36] A. Huijser and J. Van Laar, Surf. Sci. **52**, 202 (1975).

[37] W. E. Spicer, I. Lindau, P. E. Gregory, C. M. Garner, P. Pianetta, and P. W. Chye, J. Vac. Sci. Technol. **13**, 780 (1976).

[38] L. Ö. Olsson, C. B. M. Andersson, M. C. Håkansson, J. Kanski, L. Ilver, and U. O. Karlsson, Phys. Rev. Lett. **76**, 3626 (1996).

[39] M. Noguchi, K. Hirakawa, and T. Ikoma, Phys. Rev. Lett. **66**, 2243 (1991).

[40] W. Schottky, R. Stormer, and F. Waibel, Hoch Frequentztechnik **37**, 162 (1931), discussed in [41].

[41] G. Margaritondo, Rep. Prog. Phys. **62**, 765 (1999).

[42] J. Bardeen, Phys. Rev. **71**, 717 (1947).

[43] S. Kurtin, T. C. McGill, and C. A. Mead, Phys. Rev. Lett. **22**, 1433 (1969).

[44] W. E. Spicer, P. W. Chye, P. R. Skeath, C. Y. Su, and I. Lindau, J. Vac. Sci. Technol. **16**, 1422 (1979).

[45] W. Walukiewicz, J. Vac. Sci. Technol. B **5**, 1062 (1987).

[46] W. Mönch, Appl. Surf. Sci. **92**, 367 (1996).

[47] W. Mönch, On the present understanding of schottky contacts, in *Festköperprobleme (Adv. Solid State Physics)*, edited by P. Grosse, volume 26, pages 67–88, Braunschweig, 1986, Vieweg.

[48] W. Mönch, Phys. Rev. Lett. **58**, 1260 (1987).

[49] W. E. Spicer, I. Lindau, P. Skeath, C. Y. Su, and P. Chye, Phys. Rev. Lett. **44**, 420 (1980).

[50] H. Hong, R. D. Aburano, D.-S. Lin, H. Chen, T.-C. Chiang, P. Zschack, and E. D. Specht, Phys. Rev. Lett. **68**, 507 (1992).

[51] W. Walukiewicz, Appl. Phys. Lett. **54**, 2094 (1989).

[52] W. Walukiewicz, Phys. Rev. B **37**, 4760 (1988).

[53] W. Walukiewicz, Physica B **302-303**, 123 (2001).

[54] D. Khanal, J. Yim, W. Walukiewicz, and J. Wu, Nano Lett. **7**, 1186 (2007).

[55] P. Y. Yu and M. Cardona, *Fundamentals of Semiconductors*, Springer, Berlin, 3rd edition, 2005.

[56] B. K. Ridley, *Quantum processes in semiconductors*, Clarendon Press, Oxford, 1999.

[57] B. R. Nag, *Electron Transport in Compound Semiconductors*, Springer, Berlin, 1980.

[58] E. O. Kane, J. Phys. Chem. Solids. **1**, 249 (1957).

[59] P. Hohenberg and W. Kohn, Phys. Rev. **136**, B864 (1964).

[60] W. Kohn and L. J. Sham, Phys. Rev. **140**, A1133 (1965).

[61] M. S. Hybertsen and S. G. Louie, Phys. Rev. Lett. **55**, 1418 (1985).

[62] J. Heyd, G. E. Scuseria, and M. Ernzerhof, J. Chem. Phys. **118**, 8207 (2003).

[63] P. E. Blöchl, Phys. Rev. B **50**, 17953 (1994).

[64] J. Furthmüller, P. H. Hahn, F. Fuchs, and F. Bechstedt, Phys. Rev. B **72**, 205106 (2005).

[65] F. Fuchs, J. Furthmüller, F. Bechstedt, M. Shishkin, and G. Kresse, Phys. Rev. B **76**, 115109 (2007).

[66] G. Paasch and H. Übensee, Phys. Stat. Sol. B **113**, 165 (1982).

[67] H. Hertz, Ann. Physik. **31**, 983 (1887).

[68] A. Einstein, Ann. Phys. **17**, 132 (1905).

[69] K. Siegbahn, Rev. Mod. Phys. **54**, 709 (1982).

[70] C. N. Berglund and W. E. Spicer, Phys. Rev. **136**, A1030 (1964).

[71] S. Hüfner, *Photoelectron spectroscopy: principles and applications*, Springer, Berlin, 1995.

[72] S. Tanuma, C. J. Powell, and D. R. Penn, Surf. Interface Anal. **21**, 165 (1994).

[73] M. P. Seah and W. A. Dench, Surf. Interface Anal. **1**, 2 (1979).

[74] D. Briggs and J. C. Rivière, Spectral interpretation, in *Practical Surface Analysis Volume 1 – Auger and X-ray Photoelectron Spectroscopy*, edited by D. Briggs and M. P. Seah, pages 85–141, Wiley, Chichester, 2nd edition, 1990.

[75] D. A. Shirley, Phys. Rev. B **5**, 4709 (1972).

[76] F. J. Himpsel, Appl. Opt. **19**, 3964 (1980).

[77] J. E. Inglesfield and E. W. Plummer, *Angle-resolved photoemission: theory and current applications*, chapter 2 (The Physics of Photoemission), pages 15–61, Elsevier, Amsterdam, 1992.

[78] A. Damascelli, Z. Hussain, and Z.-X. Shen, Rev. Mod. Phys. **75**, 473 (2003).

[79] D. P. Woodruff and T. A. Delchar, *Modern techniques of surface science*, Cambridge University Press, Cambridge, 2nd edition, 1994.

[80] G. S. Herman, T. T. Tran, K. Higashiyama, and C. S. Fadley, Phys. Rev. Lett. **68**, 1204 (1992).

[81] R. A. Pollak, L. Ley, S. Kowalczyk, D. A. Shirley, J. D. Joannopoulos, D. J. Chadi, and M. L. Cohen, Phys. Rev. Lett. **29**, 1103 (1972).

[82] L. Ley, R. A. Pollak, F. R. McFeely, S. Kowalczyk, and D. A. Shirley, Phys. Rev. B **9**, 600 (1974).

[83] P. D. C. King, T. D. Veal, C. F. McConville, F. Fuchs, J. Furthmüller, F. Bechstedt, J. Schörmann, D. J. As, K. Lischka, H. Lu, and W. J. Schaff, Phys. Rev. B **77**, 115213 (2008).

[84] G. K. Woodgate, *Elementary Atomic Structure*, OUP, Oxford, 2^{nd} edition, 1980.

[85] G. Beamson, D. Briggs, S. F. Davies, I. W. Fletcher, D. T. Clark, J. Howard, U. Gelius, B. Wannberg, and P. Balzer, Surf. Interface Anal. **15**, 541 (1990).

[86] U. Gelius, B. Wannberg, P. Baltzer, H. Fellner-Feldegg, G. Carlsson, C. G. Johansson, J. Larsson, P. Mnger, and G. m. Vegerfors, J. Electron Spectrosc. Relat. Phenom. **52**, 747 (1990).

[87] M. P. Seah, Charge referencing techniques for insulators, in *Practical Surface Analysis Volume 1 – Auger and X-ray Photoelectron Spectroscopy*, edited by D. Briggs and M. P. Seah, pages 541–554, Wiley, Chichester, 2nd edition, 1990.

[88] S. V. Hoffmann, C. Sndergaard, C. Schultz, Z. Li, and P. Hofmann, Nuclear Instruments and Methods in Physics Research Section A **523**, 441 (2004).

[89] H. C. Casey, Jr. and F. Stern, J. Appl. Phys. **47**, 631 (1976).

[90] P. K. Basu, *Theory of Optical Processes in Semiconductors: Bulk and Microstructures*, OUP, Oxford, 2003.

[91] J. I. Pankove, *Optical Processes in Semiconductors*, Dover, New York, 1975.

[92] T. S. Moss, Proc. Phys. Soc. B **67**, 775 (1954).

[93] E. Burstein, Phys. Rev. **93**, 632 (1954).

[94] F. Urbach, Phys. Rev. **92**, 1324 (1953).

[95] G. Brooker, *Modern Classical Optics*, OUP, Oxford, 2002.

[96] C. Pickering, J. Phys. C **13**, 2959 (1980).

[97] C. C. Katsidis and D. I. Siapkas, Applied Optics **41**, 3978 (2002).

[98] M. Born and E. Wolf, *Principles of Optics*, CUP, Cambridge, 7th edition, 1999.

[99] N. W. Ashcroft and N. D. Mermin, *Solid State Physics*, Saunders College, Philadelphia, 1976.

[100] L. J. van der Pauw, Philips Research Reports **13**, 1 (1958).

[101] L. J. van der Pauw, Philips Technical Review **20**, 220 (1958).

[102] C. G. Van de Walle, Phys. Rev. Lett. **85**, 1012 (2000).

[103] A. Peles, A. Janotti, and C. G. V. de Walle, Phys. Rev. B **78**, 035204 (2008).

[104] A. Tsukazaki, A. Ohtomo, T. Onuma, M. Ohtani, T. Makino, M. Sumiya, K. Ohtani, S. F. Chichibu, S. Fuke, Y. Segawa, H. Ohno, H. Koinuma, and M. Kawasaki, Nature Mater. **4**, 42 (2005).

[105] P. H. Jefferson, S. A. Hatfield, T. D. Veal, P. D. C. King, C. F. McConville, J. Zúñiga-Pérez, and V. Muñoz-Sanjosé, Appl. Phys. Lett. **92**, 022101 (2008).

[106] T. Makino, Y. Segawa, M. Kawasaki, A. Ohtomo, R. Shiroki, K. Tamura, T. Yasuda, and H. Koinuma, Appl. Phys. Lett. **78**, 1237 (2001).

[107] S. Sadofev, S. Blumstengel, J. Cui, J. Puls, S. Rogaschewski, P. Schäfer, and F. Henneberger, Appl. Phys. Lett. **89**, 201907 (2006).

[108] J. Zúñiga-Pérez, C. Munuera, C. Ocal, and V. Muñoz-Sanjosé, J. Cryst. Growth **271**, 223 (2004).

[109] L. F. J. Piper, A. DeMasi, K. E. Smith, A. Schleife, F. Fuchs, F. Bechstedt, J. Zuniga-Pérez, and V. Munoz-Sanjosé, Phys. Rev. B **77**, 125204 (2008).

[110] J. E. Jaffe, R. Pandey, and A. B. Kunz, Phys. Rev. B **43**, 14030 (1991).

[111] A. Schleife, F. Fuchs, J. Furthmuller, and F. Bechstedt, Phys. Rev. B **73**, 245212 (2006).

[112] F. P. Koffyberg, Phys. Rev. B **13**, 4470 (1976).

[113] P. D. C. King, T. D. Veal, A. Schleife, J. Zúñiga-Pérez, B. Martel, P. H. Jefferson, F. Fuchs, V. Muñoz-Sanjosé, F. Bechstedt, and C. F. McConville, Phys. Rev. B **79**, 205205 (2009).

[114] G. P. Summers, E. A. Burke, and M. A. Xapsos, Radiat. Meas. **24**, 1 (1995).

[115] P. H. Jefferson, *Optoelectronic properties of highly mismatched semiconductor materials*, PhD thesis, University of Warwick, 2009.

[116] Y. Dou, R. G. Egdell, T. Walker, D. S. L. Law, and G. Beamson, Surf. Sci. **398**, 241 (1998).

[117] S. F. J. Cox, J. S. Lord, S. P. Cottrell, J. M. Gil, H. V. Alberto, A. Keren, D. Prabhakaran, R. Scheuermann, and A. Stoykov, J. Phys.: Condens. Matter **18**, 1061 (2006).

[118] A. Janotti and C. G. Van de Walle, Nature Mater. **6**, 44 (2007).

[119] P. D. C. King, T. D. Veal, H. Lu, S. A. Hatfield, W. J. Schaff, and C. F. McConville, Surf. Sci. **602**, 871 (2008).

[120] S. A. Chambers, T. Droubay, T. C. Kaspar, and M. Gutowski, J. Vac. Sci. Technol. B **22**, 2205 (2004).

[121] J. R. Chelikowsky and M. L. Cohen, Phys. Rev. B **14**, 556 (1976).

[122] T. D. Veal, M. J. Lowe, and C. F. McConville, Surf. Sci. **499**, 251 (2002).

[123] H. Kawazoe, M. Yasukawa, H. Hyodo, M. Kurita, H. Yanagi, and H. Hosono, Nature **389**, 939 (1997).

[124] K. Alberi, J. Wu, W. Walukiewicz, K. M. Yu, O. D. Dubon, S. P. Watkins, C. X. Wang, X. Liu, Y.-J. Cho, and J. Furdyna, Phys. Rev. B **75**, 045203 (2007).

[125] V. M. Polyakov and F. Schwierz, Appl. Phys. Lett. **88**, 032101 (2006).

[126] S. P. Fu and Y. F. Chen, Appl. Phys. Lett. **85**, 1523 (2004).

[127] V. M. Polyakov and F. Schwierz, J. Appl. Phys. **99**, 113705 (2006).

[128] V. M. Polyakov and F. Schwierz, Semicond. Sci. Technol. **21**, 1651 (2006).

[129] R. Ascázubi, I. Wilke, K. Denniston, H. Lu, and W. J. Schaff, Appl. Phys. Lett. **84**, 4810 (2004).

[130] V. Cimalla, B. Pradarutti, G. Matthus, C. Brckner, S. Riehemann, G. Notni, S. Nolte, A. Tnnermann, V. Lebedev, and O. Ambacher, Phys. Stat. Sol. B **244**, 1829 (2007).

[131] H. Ahn, Y.-P. Ku, C.-H. Chuang, C.-L. Pan, H.-W. Lin, Y.-L. Hong, and S. Gwo, Appl. Phys. Lett. **92**, 102103 (2008).

[132] H. Ahn, Y.-P. Ku, Y.-C. Wang, C.-H. Chuang, S. Gwo, and C.-L. Pan, Appl. Phys. Lett. **91**, 132108 (2007).

[133] H. Lu, W. J. Schaff, and L. F. Eastman, J. Appl. Phys. **96**, 3577 (2004).

[134] C.-F. Chen, C.-L. Wu, and S. Gwo, Appl. Phys. Lett. **89**, 252109 (2006).

[135] Y.-S. Lu, C.-C. Huang, J. A. Yeh, C.-F. Chen, and S. Gwo, Appl. Phys. Lett. **91**, 202109 (2007).

[136] Y.-S. Lu, C.-L. Ho, J. A. Yeh, H.-W. Lin, and S. Gwo, Appl. Phys. Lett. **92**, 212102 (2008).

[137] A. G. Bhuiyan, A. Hashimoto, and A. Yamamoto, J. Appl. Phys. **94**, 2779 (2003).

[138] H. Lu, W. J. Schaff, L. F. Eastman, and C. E. Stutz, Appl. Phys. Lett. **82**, 1736 (2003).

[139] V.-T. Rangel-Kuoppa, S. Suihkonen, M. Sopanen, and H. Lipsanen, Jpn. J. Appl. Phys. **45**, 36 (2006).

[140] R. Goldhahn, P. Schley, and M. Röppischer, Ellipsometry of indium nitride and related alloys, in *Indium Nitride and Related Alloys*, edited by T. D. Veal, C. F. McConville, and W. J. Schaff, CRC Press, Boca Raton, 2009.

[141] C. Persson and A. Zunger, Phys. Rev. B **68**, 073205 (2003).

[142] A. Tabata, A. P. Lima, L. K. Teles, L. M. R. Scolfaro, J. R. Leite, V. Lemos, B. Schöttker, T. Frey, D. Schikora, and K. Lischka, Appl. Phys. Lett. **74**, 362 (1999).

[143] P. A. Anderson, C. E. Kendrick, R. J. Kinsey, A. Asadov, W. Gao, R. J. Reeves, and S. M. Durbin, Phys. Stat. Sol. C **2**, 2320 (2005).

[144] J. Schörmann, D. J. As, K. Lischka, P. Schley, R. Goldhahn, S. F. Li, W. Löffler, M. Hetterich, and H. Kalt, Appl. Phys. Lett. **89**, 261903 (2006).

[145] J. G. Lozano, F. M. Morales, R. Garcia, D. Gonzalez, V. Lebedev, C. Y. Wang, V. Cimalla, and O. Ambacher, Appl. Phys. Lett. **90**, 091901 (2007).

[146] M. Ueno, M. Yoshida, A. Onodera, O. Shimomura, and K. Takemura, Phys. Rev. B **49**, 14 (1994).

[147] A. R. Smith, R. M. Feenstra, D. W. Greve, J. Neugebauer, and J. E. Northrup, Phys. Rev. Lett. **79**, 3934 (1997).

[148] J. E. Northrup, J. Neugebauer, R. M. Feenstra, and A. R. Smith, Phys. Rev. B **61**, 9932 (2000).

[149] G. Koblmüller, R. Averbeck, H. Riechert, and P. Pongratz, Phys. Rev. B **69**, 035325 (2004).

[150] D. Segev and C. G. Van de Walle, Surf. Sci. **601**, L15 (2007).

[151] T. D. Veal, P. D. C. King, P. H. Jefferson, L. F. J. Piper, C. F. McConville, H. Lu, W. J. Schaff, P. A. Anderson, S. M. Durbin, D. Muto, H. Naoi, and Y. Nanishi, Phys. Rev. B **76**, 075313 (2007).

[152] T. D. Veal, P. D. C. King, M. Walker, C. F. McConville, H. Lu, and W. J. Schaff, Physica B **401–402**, 351 (2007).

[153] T. L. Tansley and C. P. Foley, J. Appl. Phys. **59**, 3241 (1986).

[154] J. Wu, W. Walukiewicz, W. Shan, K. M. Yu, J. W. Ager III, S. X. Li, E. E. Haller, H. Lu, and W. J. Schaff, J. Appl. Phys. **94**, 4457 (2003).

[155] V. Y. Davydov, A. A. Klochikhin, R. P. Seisyan, V. V. Emtsev, S. V. Ivanov, F. Bechstedt, J. Furthmuller, H. Harima, V. Mudryi, J. Aderhold, O. Semchinova, and J. Graul, Phys. Stat. Sol. B **229**, R1 (2002).

[156] V. Davydov, A. Klochikhin, V. Emtsev, S. Ivanov, V. Vekshin, F. Bechstedt, J. Furthmller, H. Harima, A. Mudryi, A. Hashimoto, A. Yamamoto, J. Aderhold, J. Graul, and E. Haller, Phys. Stat. Sol. B **230**, R4 (2002).

[157] F. Bechstedt and J. Furthmüller, J. Cryst. Growth **246**, 315 (2002).

[158] J. Wu, W. Walukiewicz, K. M. Yu, J. W. Ager III, E. E. Haller, H. Lu, W. J. Schaff, Y. Saito, and Y. Nanishi, Appl. Phys. Lett. **80**, 3967 (2002).

[159] T. V. Shubina, S. V. Ivanov, V. N. Jmerik, D. D. Solnyshkov, V. A. Vekshin, P. S. Kop'ev, A. Vasson, J. Leymarie, A. Kavokin, H. Amano, K. Shimono, A. Kasic, and B. Monemar, Phys. Rev. Lett. **92**, 117407 (2004).

[160] F. Bechstedt, J. Furthmüller, O. Ambacher, and R. Goldhahn, Phys. Rev. Lett. **93**, 269701 (2004).

[161] T. V. Shubina, S. V. Ivanov, V. N. Jmerik, P. S. Kop'ev, A. Vasson, J. Leymarie, A. Kavokin, H. Amano, B. Gil, O. Briot, and B. Monemar, Phys. Rev. Lett. **93**, 269702 (2004).

[162] J. Wu, W. Walukiewicz, W. Shan, K. M. Yu, J. W. Ager III, E. E. Haller, H. Lu, and W. J. Schaff, Phys. Rev. B **66**, 201403(R) (2002).

[163] T. Hofmann, T. Chavdarov, V. Darakchieva, H. Lu, W. J. Schaff, and M. Schubert, Phys. Stat. Sol. C **3**, 1854 (2006).

[164] N. Miller, J. W. Ager III, and W. Walukiewicz, private communication.

[165] B. R. Nag, Phys. Stat. Sol. B **237**, R1 (2003).

[166] R. Goldhahn, P. Schley, A. Winzer, M. Rakel, C. Cobet, N. Esser, H. Lu, and W. Schaff, J. Cryst. Growth **288**, 273 (2006).

[167] D. Fritsch, H. Schmidt, and M. Grundmann, Phys. Rev. B **67**, 235205 (2003).

[168] D. Fritsch, H. Schmidt, and M. Grundmann, Phys. Rev. B **69**, 165204 (2004).

[169] P. Rinke, M. Winkelnkemper, A. Qteish, D. Bimberg, J. Neugebauer, and M. Scheffler, Phys. Rev. B **77**, 075202 (2008).

[170] I. Vurgaftman and J. R. Meyer, J. Appl. Phys. **94**, 3675 (2003).

[171] W. J. Schaff, H. Lu, L. F. Eastman, W. Walukiewicz, K. M. Yu, S. Keller, S. Kurtz, B. Keyes, and L. Gevilas, Electrical properties of InN grown by Molecular Beam Epitaxy, in *State-of-the-Art Program on Compound Semiconductors XLI and Nitride and Wide Bandgap Semiconductors for Sensors, Photonics, and Electronics V*, edited by H. M. Ng and A. G. Baca, volume 2004–06 of *The Electrochemical Society Proceedings Series, Honolulu, Hawaii, 3–8 October 2004*, pages 358–371, Pennington, NJ, 2004, Electrochemical Society.

[172] J. Finster, E. D. Klinkenberg, J. Heeg, and W. Braun, Vacuum **41**, 1586 (1990).

[173] P. D. C. King, T. D. Veal, P. H. Jefferson, C. F. McConville, H. Lu, and W. J. Schaff, Phys. Rev. B **75**, 115312 (2007).

[174] A. Uedono, S. F. Chichibu, M. Higashiwaki, T. Matsui, T. Ohdaira, and R. Suzuki, J. Appl. Phys. **97**, 043514 (2005).

[175] C. Rauch and F. Tuomisto, private communication.

[176] R. E. Jones, S. X. Li, L. Hsu, K. M. Yu, W. Walukiewicz, Z. Lillental-Weber, J. W. Ager III, E. E. Haller, H. Lu, and W. J. Schaff, Physica B **376**, 436 (2006).

[177] S. X. Li, K. M. Yu, J. Wu, R. E. Jones, W. Walukiewicz, J. W. Ager III, W. Shan, E. E. Haller, H. Lu, and W. J. Schaff, Phys. Rev. B **71**, 161201(R) (2005).

[178] J. Robertson and B. Falabretti, J. Appl. Phys. **100**, 014111 (2006).

[179] S.-H. Wei and A. Zunger, Appl. Phys. Lett. **72**, 2011 (1998).

[180] P. D. C. King, T. D. Veal, C. E. Kendrick, L. R. Bailey, S. M. Durbin, and C. F. McConville, Phys. Rev. B **78**, 033308 (2008).

[181] P. D. C. King, T. D. Veal, P. H. Jefferson, C. F. McConville, T. Wang, P. J. Parbrook, H. Lu, and W. J. Schaff, Appl. Phys. Lett. **90**, 132105 (2007).

[182] T. U. Kampen and W. Mönch, Appl. Surf. Sci. **117-118**, 388 (1997).

[183] V. N. Brudnyi, S. N. Grinyaev, and N. G. Kolin, Semiconductors **37**, 537 (2003).

[184] S. H. Wei, X. L. Nie, I. G. Batyrev, and S. B. Zhang, Phys. Rev. B **67**, 165209 (2003).

[185] S.-H. Wei and A. Zunger, Phys. Rev. B **60**, 5404 (1999).

[186] S.-H. Wei and A. Zunger, Appl. Phys. Lett. **69**, 2719 (1996).

[187] R. E. Jones, K. M. Yu, S. X. Li, W. Walukiewicz, J. W. Ager III, E. E. Haller, H. Lu, and W. J. Schaff, Phys. Rev. Lett. **96**, 125505 (2006).

[188] C. A. Mead and W. G. Spitzer, Phys. Rev. Lett. **10**, 471 (1963).

[189] K. M. Tracy, W. J. Mecouch, R. F. Davis, and R. J. Nemanich, J. Appl. Phys. **94**, 3163 (2003).

[190] C. Stampfl, C. G. Van de Walle, D. Vogel, P. Krüger, and J. Pollmann, Phys. Rev. B **61**, R7846 (2000).

[191] A. Janotti and C. G. Van de Walle, Appl. Phys. Lett. **92**, 032104 (2008).

[192] M. Higashiwaki, T. Inushima, and T. Matsui, Phys. Stat. Sol. B **240**, 417 (2003).

[193] J. Kim, E. Ikenaga, M. Kobata, A. Takeuchi, M. Awaji, H. Makino, P. Chen, A. Yamamoto, T. Matsuoka, and D. Miwa, Appl. Surf. Sci. **252**, 5602 (2006).

[194] S. Limpijumnong and C. G. Van de Walle, Phys. Stat. Sol. B **228**, 303 (2001).

[195] M. Losurdo, M. M. Giangregorio, G. Bruno, T.-H. Kim, S. Choi, A. S. Brown, G. Pettinari, M. Capizzi, and A. Polimeni, Appl. Phys. Lett. **91**, 081917 (2007).

[196] G. Pettinari, F. Masia, M. Capizzi, A. Polimeni, M. Losurdo, G. Bruno, T. H. Kim, S. Choi, A. Brown, V. Lebedev, V. Cimalla, and O. Ambacher, Phys. Rev. B **77**, 125207 (2008).

[197] E. A. Davis, S. F. J. Cox, R. L. Lichti, and C. G. Van de Walle, Appl. Phys. Lett. **82**, 592 (2003).

[198] C. S. Gallinat, G. Koblmüller, J. S. Brown, S. Bernardis, J. S. Speck, G. D. Chern, E. D. Readinger, H. Shen, and M. Wraback, Appl. Phys. Lett. **89**, 032109 (2006).

[199] J. Wu, W. Walukiewicz, S. X. Li, R. Armitage, J. C. Ho, E. R. Weber, E. E. Haller, H. Lu, W. J. Schaff, A. Barcz, and R. Jakiela, Appl. Phys. Lett. **84**, 2805 (2004).

[200] L. F. J. Piper, T. D. Veal, C. F. McConville, H. Lu, and W. J. Schaff, Appl. Phys. Lett. **88**, 252109 (2006).

[201] V. Cimalla, G. Ecke, M. Niebelschtz, O. Ambacher, R. Goldhahn, H. Lu, and W. J. Schaff, Phys. Stat. Sol. C **2**, 2254 (2005).

[202] V. Cimalla, V. Lebedev, F. M. Morales, R. Goldhahn, and O. Ambacher, Appl. Phys. Lett. **89**, 172109 (2006).

[203] V. Lebedev, V. Cimalla, T. Baumann, O. Ambacher, F. M. Morales, J. G. Lozano, and D. González., J. Appl. Phys. **100**, 094903 (2006).

[204] T. D. Veal, L. F. J. Piper, I. Mahboob, H. Lu, W. J. Schaff, and C. F. McConville, Phys. Stat. Sol. C **2**, 2246 (2005).

[205] Y. Ishitani, X. Wang, S.-B. Che, and A. Yoshikawa, J. Appl. Phys. **103**, 053515 (2008).

[206] H. Wang, D. S. Jiang, L. L. Wang, X. Sun, W. B. Liu, D. G. Zhao, J. J. Zhu, Z. S. Liu, Y. T. Wang, S. M. Zhang, and H. Yang, J. Phys. D: Appl. Phys. **41**, 135403 (2008).

[207] P. D. C. King, T. D. Veal, C. S. Gallinat, G. Koblmüller, L. R. Bailey, J. S. Speck, and C. F. McConville, J. Appl. Phys. **104**, 103703 (2008).

[208] P. D. C. King, T. D. Veal, and C. F. McConville, J. Phys.: Condens. Matter **21**, 174201 (2009).

[209] D. C. Look, H. Lu, W. J. Schaff, J. Jasinski, and Z. Liliental-Weber, Appl. Phys. Lett. **80**, 258 (2002).

[210] C. J. Lu, L. A. Bendersky, H. Lu, and W. J. Schaff, Appl. Phys. Lett. **83**, 2817 (2003).

[211] V. Gopal, E. P. Kvam, T. P. Chin, and J. M. Woodall, Appl. Phys. Lett. **72**, 2319 (1998).

[212] A. Kasic, M. Schubert, Y. Saito, Y. Nanishi, and G. Wagner, Phys. Rev. B **65**, 115206 (2002).

[213] D. Segev and C. G. Van de Walle, Europhys. Lett. **76**, 305 (2006).

[214] H. Lu, W. J. Schaff, L. F. Eastman, J. Wu, W. Walukiewicz, D. C. Look, and R. J. Molnar, Mat. Res. Soc. Symp. Proc. **743**, L4.10.1 (2003).

[215] H. Lu, W. J. Schaff, L. F. Eastman, J. Wu, W. Walukiewicz, V. Cimalla, and O. Ambacher, Appl. Phys. Lett. **83**, 1136 (2003).

[216] Y. Nanishi, Y. Saito, T. Yamaguchi, M. Hori, F. Matsuda, T. Araki, A. Suzuki, and T. Miyajima, Phys. Stat. Sol. A **200**, 202 (2003).

[217] L. F. J. Piper, T. D. Veal, M. Walker, I. Mahboob, C. F. McConville, H. Lu, and W. J. Schaff, J. Vac. Sci. Technol. A **23**, 617 (2005).

[218] E. Calleja, J. Grandal, M. A. Sánchez-Garcia, M. Niebelschütz, V. Cimalla, and O. Ambacher, Appl. Phys. Lett. **90**, 262110 (2007).

[219] S. Lazić, E. Gallardo, J. M. Calleja, F. Agulló-Rueda, J. Grandal, M. A. Sánchez-Garcia, E. Calleja, E. Luna, and A. Trampert, Phys. Rev. B **76**, 205319 (2007).

[220] C. S. Gallinat, G. Koblmüller, J. S. Brown, and J. S. Speck, J. Appl. Phys. **102**, 064907 (2007).

[221] G. Koblmüller, C. S. Gallinat, and J. S. Speck, J. Appl. Phys. **101**, 083516 (2007).

[222] C.-L. Wu, H.-M. Lee, C.-T. Kuo, C.-H. Chen, and S. Gwo, Phys. Rev. Lett. **101**, 106803 (2008).

[223] C. Stampfl and C. G. Van de Walle, Phys. Rev. B **57**, R15052 (1998).

[224] X. H. Lu, P. Y. Yu, L. X. Zheng, S. J. Xu, M. H. Xie, and S. Y. Tong, Appl. Phys. Lett. **82**, 1033 (2003).

[225] M. Murayama and T. Nakayama, Phys. Rev. B **49**, 4710 (1994).

[226] T. B. Fehlberg, C. S. Gallinat, G. A. Umana-Membreno, G. Koblmüller, B. D. Nener, J. S. Speck, and G. Parish, J. Electron. Mater. **37**, 593 (2008).

[227] G. Koblmüller, C. S. Gallinat, S. Bernardis, J. S. Speck, G. D. Chern, E. D. Readinger, H. Shen, and M. Wraback, Appl. Phys. Lett. **89**, 071902 (2006).

[228] R. L. Petritz, Phys. Rev. **110**, 1254 (1958).

[229] C. Swartz, R. Tompkins, N. Giles, T. Myers, H. Lu, W. Schaff, and L. Eastman, J. Cryst. Growth **269**, 29 (2004).

[230] W. Zawadzki and W. Szymańska, Phys. Stat. Sol. B **45**, 415 (1971).

[231] V. Lebedev, V. Cimalla, J. Pezoldt, M. Himmerlich, S. Krischok, J. A. Schaefer, O. Ambacher, F. M. Morales, J. G. Lozano, and D. González, J. Appl. Phys. **100**, 094902 (2006).

[232] Y. Liu, Y. Cai, L. Zhang, M. H. Xie, N. Wang, S. B. Zhang, and H. S. Wu, Appl. Phys. Lett. **92**, 231907 (2008).

[233] D. C. Look and J. R. Sizelove, Phys. Rev. Lett. **82**, 1237 (1999).

[234] H. Yamaguchi, J. L. Sudijono, B. A. Joyce, T. S. Jones, C. Gatzke, and R. A. Stradling, Phys. Rev. B **58**, R4219 (1998).

[235] J. Jasinski and Z. Liliental-Weber, J. Electron. Mater. **31**, 429 (2002).

[236] L. Hsu, R. E. Jones, S. X. Li, K. M. Yu, and W. Walukiewicz, J. Appl. Phys. **102**, 073705 (2007).

[237] Y. Ishitani, M. Fujiwara, X. Wang, S.-B. Che, and A. Yoshikawa, Appl. Phys. Lett. **92**, 251901 (2008).

[238] G. F. Brown, J. W. Ager, III, W. Walukiewicz, W. J. Schaff, and J. Wu, Appl. Phys. Lett. **93**, 262105 (2008).

[239] X. Wang, S.-B. Che, Y. Ishitani, and A. Yoshikawa, Appl. Phys. Lett. **90**, 151901 (2007).

[240] H. Lu, W. J. Schaff, L. F. Eastman, and C. Wood, Mat. Res. Soc. Symp. Proc. **693**, I1.5 (2002).

[241] V. Darakchieva, T. Hofmann, M. Schubert, B. E. Sernelius, B. Monemar, P. O. Å. Persson, F. Giuliani, E. Alves, H. Lu, and W. J. Schaff, Appl. Phys. Lett. **94**, 022109 (2009).

[242] J. W. L. Yim, R. E. Jones, K. M. Yu, J. W. Ager, III, W. Walukiewicz, W. J. Schaff, and J. Wu, Phys. Rev. B **76**, 041303(R) (2007).

[243] X. Wang, S.-B. Che, Y. Ishitani, and A. Yoshikawa, Appl. Phys. Lett. **91**, 242111 (2007).

[244] J. W. Ager III, N. Miller, R. E. Jones, K. M. Yu, J. Wu, W. J. Schaff, and W. Walukiewicz, Phys. Stat. Sol. B **245**, 873 (2008).

[245] P. A. Anderson, C. H. Swartz, D. Carder, R. J. Reeves, S. M. Durbin, S. Chandril, and T. H. Myers, Appl. Phys. Lett. **89**, 184104 (2006).

[246] L. T. Romano, M. Kneissl, J. E. Northrup, C. G. Van de Walle, and D. W. Treat, Appl. Phys. Lett. **79**, 2734 (2001).

[247] W. Walukiewicz, J. W. Ager III, K. M. Yu, Z. Liliental-Weber, J. Wu, S. X. Li, R. E. Jones, and J. D. Denlinger, J. Phys. D: Appl. Phys. **39**, R83 (2006).

[248] S. Nakamura, J. Vac. Sci. Technol. A **13**, 705 (1995).

[249] S. Nakamura, M. Senoh, S. ichi Nagahama, N. Iwasa, T. Yamada, T. Matsushita, H. Kiyoku, and Y. Sugimoto, Jpn. J. Appl. Phys. **35**, L74 (1996).

[250] S. Nakamura, Science **281**, 956 (1998).

[251] A. Martí and G. L. Araújo, Solar Energy Materials and Solar Cells **43**, 203 (1996).

[252] J. Wu, W. Walukiewicz, K. M. Yu, W. Shan, J. W. Ager III, E. E. Haller, H. Lu, W. J. Schaff, W. K. Metzger, and S. Kurtz, J. Appl. Phys. **94**, 6477 (2003).

[253] S. F. Chichibu, A. Uedono, T. Onuma, B. A. Haskell, A. Chakraborty, T. Koyama, P. T. Fini, S. Keller, S. P. DenBaars, J. S. Speck, U. K. Mishra, S. Nakamura, S. Yamaguchi, S. Kamiyama, H. Amano, I. Akasaki, J. Han, and T. Sota, Nature Mater. **5**, 810 (2006).

[254] F. A. Ponce and D. P. Bour, Nature **386**, 351 (1997).

[255] E. F. Schubert and J. K. Kim, Science **308**, 1274 (2005).

[256] K. Kajiyama, Y. Mizushima, and S. Sakata, Appl. Phys. Lett. **23**, 458 (1973).

[257] G. Martin, A. Botchkarev, A. Rockett, and H. Morkoç, Appl. Phys. Lett. **68**, 2541 (1996).

[258] C. F. Shih, N. C. Chen, P. H. Chang, and K. S. Liu, Jpn. J. Appl. Phys. - Part 1 **44**, 7892 (2005).

[259] C.-L. Wu, H.-M. Lee, C.-T. Kuo, S. Gwo, and C.-H. Hsu, Appl. Phys. Lett. **91**, 042112 (2007).

[260] Z. H. Mahmood, A. P. Shah, A. Kadir, M. R. Gokhale, S. Ghosh, A. Bhattacharya, and B. M. Arora, Appl. Phys. Lett. **91**, 152108 (2007).

[261] K. A. Wang, C. Lian, N. Su, D. Jena, and J. Timler, Appl. Phys. Lett. **91**, 232117 (2007).

[262] C.-L. Wu, H.-M. Lee, C.-T. Kuo, C.-H. Chen, and S. Gwo, Appl. Phys. Lett. **92**, 162106 (2008).

[263] C.-L. Wu, C.-H. Shen, and S. Gwo, Appl. Phys. Lett. **88**, 032105 (2006).

[264] C. G. Van de Walle and J. Neugebauer, Appl. Phys. Lett. **70**, 2577 (1997).

[265] S.-H. Wei and A. Zunger, Phys. Rev. Lett. **59**, 144 (1987).

[266] J. Wu, W. Walukiewicz, K. M. Yu, J. W. Ager III, E. E. Haller, H. Lu, and W. J. Schaff, Appl. Phys. Lett. **80**, 4741 (2002).

[267] J. Wu, W. Walukiewicz, K. M. Yu, J. W. Ager III, S. X. Li, E. E. Haller, H. Lu, and W. J. Schaff, Solid State Commun. **127**, 411 (2003).

[268] W. Terashima, S.-B. Che, Y. Ishitani, and A. Yoshikawa, Jpn. J. Appl. Phys. **45**, L539 (2006).

[269] R. Goldhahn, P. Schley, A. Winzer, G. Gobsch, V. Cimalla, O. Ambacher, M. Rakel, C. Cobet, N. Esser, H. Lu, and W. Schaff, Phys. Stat. Sol. A **203**, 42 (2006).

[270] P. Schley, R. Goldhahn, A. T. Winzer, G. Gobsch, V. Cimalla, O. Ambacher, H. Lu, W. J. Schaff, M. Kurouchi, Y. Nanishi, M. Rakel, C. Cobet, and N. Esser, Phys. Rev. B **75**, 205204 (2007).

[271] E. Dimakis, A. Georgakilas, M. Androulidaki, K. Tsagaraki, G. Kittler, F. Kalaitzakis, D. Cengher, E. Bellet-Amalric, D. Jalabert, and N. T. Pelekanos, J. Cryst. Growth **251**, 476 (2003).

[272] C. G. Van de Walle and D. Segev, J. Appl. Phys. **101**, 081704 (2007).

[273] C. Stampfl and C. G. Van de Walle, Phys. Rev. B **65**, 155212 (2002).

[274] G. Thomas, Nature **389**, 907 (1997).

[275] I. Hamberg and C. G. Granqvist, J. Appl. Phys. **60**, R123 (1986).

[276] N. G. Patel, P. D. Patel, and V. S. Vaishnav, Sens. Actuators B **96**, 180 (2003).

[277] K. Nomura, H. Ohta, K. Ueda, T. Kamiya, M. Hirano, and H. Hosono, Science **300**, 1269 (2003).

[278] A. Tsukazaki, A. Ohtomo, T. Kita, Y. Ohno, H. Ohno, and M. Kawasaki, Science **315**, 1388 (2007).

[279] A. P. Ramirez, Science **315**, 1377 (2007).

[280] Z. W. Pan, Z. R. Dai, and Z. L. Wang, Science **291**, 1947 (2001).

[281] Y. Li, Y. Bando, and D. Golberg, Adv. Mater. **15**, 581 (2003).

[282] D. Zhang, Z. Liu, C. Li, T. Tang, X. Liu, S. Han, B. Lei, and C. Zhou, Nano Lett. **4**, 1919 (2004).

[283] R. L. Weiher and R. P. Ley, J. Appl. Phys. **37**, 299 (1966).

[284] F. Matino, L. Persano, V. Arima, D. Pisignano, R. I. R. Blyth, R. Cingolani, and R. Rinaldi, Phys. Rev. B **72**, 085437 (2005).

[285] H. Odaka, S. Iwata, N. Taga, S. Ohnishi, Y. Kaneta, and Y. Shigesato, Jpn. J. Appl. Phys. **36**, 5551 (1997).

[286] O. N. Mryasov and A. J. Freeman, Phys. Rev. B **64**, 233111 (2001).

[287] P. Erhart, A. Klein, R. G. Egdell, and K. Albe, Phys. Rev. B **75**, 153205 (2007).

[288] A. Walsh, J. L. F. D. Silva, S.-H. Wei, C. Körber, A. Klein, L. F. J. Piper, A. DeMasi, K. E. Smith, G. Panaccione, P. Torelli, D. J. Payne, A. Bourlange, and R. G. Egdell, Phys. Rev. Lett. **100**, 167402 (2008).

[289] F. Fuchs and F. Bechstedt, Phys. Rev. B **77**, 155107 (2008).

[290] A. Klein, Appl. Phys. Lett. **77**, 2009 (2000).

[291] Y. Gassenbauer, R. Schafranek, A. Klein, S. Zafeiratos, M. Hävecker, A. Knop-Gericke, and R. Schlögl, Phys. Rev. B **73**, 245312 (2006), and references therein.

[292] C. Y. Wang, V. Lebedev, V. Cimalla, T. Kups, K. Tonisch, and O. Ambacher, Appl. Phys. Lett. **90**, 221902 (2007).

[293] A. Bourlange, D. J. Payne, R. G. Egdell, J. S. Foord, P. P. Edwards, M. O. Jones, A. Schertel, P. J. Dobson, and J. L. Hutchison, Appl. Phys. Lett. **92**, 092117 (2008).

[294] C. Y. Wang, V. Cimalla, H. Romanus, T. Kups, G. Ecke, T. Stauden, M. Ali, V. Lebedev, J. Pezoldt, and O. Ambacher, Appl. Phys. Lett. **89**, 011904 (2006).

[295] Y. P. Varshni, Physica **34**, 149 (1967).

[296] R. Summitt and N. F. Borrelli, J. Appl. Phys. **37**, 2200 (1966).

[297] P. D. C. King, T. D. Veal, F. Fuchs, C. Y. Wang, D. J. Payne, A. Bourlange, G. R. Bell, V. Cimalla, O. Ambacher, R. G. Egdell, F. Bechstedt, and C. F. McConville, Phys. Rev. B **79**, 205211 (2009).

[298] A. Schleife, F. Fuchs, C. Rödl, J. Furthmüller, and F. Bechstedt, Appl. Phys. Lett. **94**, 012104 (2009).

[299] D. Look, Surf. Sci. **601**, 5315 (2007).

[300] D. C. Look, B. Claflin, and H. E. Smith, Appl. Phys. Lett. **92**, 122108 (2008).

[301] S. Lany and A. Zunger, Phys. Rev. Lett. **98**, 045501 (2007).

[302] S. F. J. Cox, E. A. Davis, S. P. Cottrell, P. J. C. King, J. S. Lord, J. M. Gil, H. V. Alberto, R. C. Vilão, J. Piroto Duarte, N. Ayres de Campos, A. Weidinger, R. L. Lichti, and S. J. C. Irvine, Phys. Rev. Lett. **86**, 2601 (2001).

[303] S. F. J. Cox, J. Phys.: Condens. Matter **15**, R1727 (2003).

[304] S. F. J. Cox, J. L. Gavartin, J. S. Lord, S. P. Cottrell, J. M. Gil, H. V. Alberto, J. P. Duarte, R. C. Vilao, N. A. de Campos, D. J. Keeble, E. A. Davis, M. Charlton, and D. P. van der Werf, J. Phys.: Condens. Matter **18**, 1079 (2006).

[305] P. D. C. King, R. L. Lichti, Y. G. Celebi, J. M. Gil, R. C. Vilão, H. V. Alberto, J. Piroto Duarte, D. J. Payne, R. G. Egdell, I. McKenzie, C. F. McConville, S. F. J. Cox, and T. D. Veal, Phys. Rev. B **80**, 081201(R) (2009).

[306] A. B. Fowler, F. F. Fang, W. E. Howard, and P. J. Stiles, Phys. Rev. Lett. **16**, 901 (1966).

[307] A. Kamgar, P. Kneschaurek, G. Dorda, and J. F. Koch, Phys. Rev. Lett. **32**, 1251 (1974).

[308] D. C. Tsui, Phys. Rev. Lett. **24**, 303 (1970).

[309] D. C. Tsui, Phys. Rev. B **4**, 4438 (1971).

[310] D. C. Tsui, Phys. Rev. B **8**, 2657 (1973).

[311] T. D. Veal, L. F. J. Piper, M. R. Phillips, M. H. Zareie, H. Lu, W. J. Schaff, and C. F. McConville, Phys. Stat. Sol. A **203**, 85 (2006).

[312] T. D. Veal, L. F. J. Piper, M. R. Phillips, M. H. Zareie, H. Lu, W. J. Schaff, and C. F. McConville, Phys. Stat. Sol. A **204**, 536 (2007).

[313] V. Y. Aristov, G. Le Lay, V. M. Zhilin, G. Indlekofer, C. Grupp, A. Taleb-Ibrahimi, and P. Soukiassian, Phys. Rev. B **60**, 7752 (1999).

[314] L. Colakerol, T. D. Veal, H.-K. Jeong, L. Plucinski, A. DeMasi, T. Learmonth, P.-A. Glans, S. Wang, Y. Zhang, L. F. J. Piper, P. H. Jefferson, A. Fedorov, T.-C. Chen, T. D. Moustakas, C. F. McConville, and K. E. Smith, Phys. Rev. Lett. **97**, 237601 (2006).

[315] G. A. Baraff and J. A. Appelbaum, Phys. Rev. B **5**, 475 (1972).

[316] D. H. Ehlers and D. L. Mills, Phys. Rev. B **34**, 3939 (1986).

[317] S. R. Streight and D. L. Mills, Phys. Rev. B **37**, 965 (1988).

[318] T. Inaoka, Surf. Sci. **431**, 156 (1999).

[319] S. Abe, T. Inaoka, and M. Hasegawa, Phys. Rev. B **66**, 205309 (2002).

[320] H. Ubensee, G. Paasch, and J.-P. Zöllner, Phys. Rev. B **39**, 1955 (1989).

[321] L. O. Olsson, L. Ilver, J. Kanski, P. O. Nilsson, C. B. M. Andersson, U. O. Karlsson, and M. C. Håkansson, Phys. Rev. B **53**, 4734 (1996).

[322] J. M. Ziman, *Principles of the Theory of Solids*, Cambridge University Press, Cambridge, 1972.

[323] V. Lebedev, C. Y. Wang, V. Cimalla, S. Hauguth, T. Kups, M. Ali, G. Ecke, M. Himmerlich, S. Krischok, J. A. Schaefer, O. Ambacher, V. M. Polyakov, and F. Schwierz, J. Appl. Phys. **101**, 123705 (2007).

[324] V. Y. Aristov, G. L. Lay, P. Soukiassian, K. Hricovini, J. E. Bonnet, J. Osvald, and O. Olsson, J. Vac. Sci. Technol. B **12**, 2709 (1994).

[325] S. Krischok, V. Yanev, O. Balykov, M. Himmerlich, J. A. Schaefer, R. Kosiba, G. Ecke, I. Cimalla, V. Cimalla, O. Ambacher, H. Lu, W. J. Schaff, and L. F. Eastman, Surf. Sci. **566-568**, 849 (2004).

[326] G. R. Bell, C. F. McConville, and T. S. Jones, Appl. Surf. Sci. **104-105**, 17 (1996).

[327] L. F. J. Piper, L. Colakerol, P. D. C. King, A. Schleife, J. Zúñiga-Pérez, P.-A. Glans, T. Learmonth, A. Federov, T. D. Veal, F. Fuchs, V. Muñoz-Sanjosé, F. Bechstedt, C. F. McConville, and K. E. Smith, Phys. Rev. B **78**, 165127 (2008).

[328] K. F. Berggren and B. E. Sernelius, Phys. Rev. B **24**, 1971 (1981).

[329] G. Tränkle, H. Leier, A. Forchel, H. Haug, C. Ell, and G. Weimann, Phys. Rev. Lett. **58**, 419 (1987).

[330] C. Delalande, G. Bastard, J. Orgonasi, J. A. Brum, H. W. Liu, M. Voos, G. Weimann, and W. Schlapp, Phys. Rev. Lett. **59**, 2690 (1987).

[331] S. Das Sarma, R. Jalabert, and S.-R. E. Yang, Phys. Rev. B **39**, 5516 (1989).

[332] A. Bostwick, T. Ohta, T. Seyller, K. Horn, and E. Rotenberg, Nature Phys. **3**, 36 (2007).

[333] B. Vinter, Phys. Rev. Lett. **35**, 1044 (1975).

[334] B. Vinter, Phys. Rev. B **13**, 4447 (1976).

[335] F. Stern, Phys. Rev. Lett. **18**, 546 (1967).

[336] F. Stern, Phys. Rev. Lett. **30**, 278 (1973).

[337] C. Kirkegaard, T. K. Kim, and P. Hofmann, New Journal of Physics **7**, 99 (2005).

[338] B. A. McDougall, T. Balasubramanian, and E. Jensen, Phys. Rev. B **51**, 13891 (1995).

[339] J. E. Gayone, S. V. Hoffmann, Z. Li, and P. Hofmann, Phys. Rev. Lett. **91**, 127601 (2003).

[340] P. B. Allen and M. Cardona, Phys. Rev. B **27**, 4760 (1983).

[341] J. Fraxedas, M. K. Kelly, and M. Cardona, Phys. Rev. B **43**, 2159 (1991).

[342] H. Finkenrath, Cadmium oxide, in *Physics of II-VI and I-VII Compounds, Semi-Magnetic Semiconductors, Landolt-Börnstein: Numerical Data and Functional Relationships in Science and Technology. Group III: Crystal and Solid State Physics,*, edited by O. Madelung, M. Schulz, and H. Weiss, volume 17B, Springer, Berlin, 1982.

[343] G. Grimvall, *The Electron-Phonon Interaction in Metals*, North-Holland, Amsterdam, 1981.

[344] M. J. Lowe, T. D. Veal, A. P. Mowbray, and C. F. McConville, Surf. Sci. **544**, 320 (2003).

[345] P. D. C. King, T. D. Veal, M. J. Lowe, and C. F. McConville, J. Appl. Phys. **104**, 083709 (2008).

[346] T. D. Veal, P. D. C. King, S. A. Hatfield, L. R. Bailey, C. F. McConville, B. Martel, J. C. Moreno, E. Frayssinet, F. Semond, and J. Zúñiga-Pérez, Appl. Phys. Lett. **93**, 202108 (2008).

[347] B. Falabretti and J. Robertson, J. Appl. Phys. **102**, 123703 (2007).